X-RAY STUDY OF THE INTERMEDIATE MASS YOUNG STARS HERBIG AE/BE STARS

Hamaguchi Kenji

January 5, 2001

Abstract

We study the x-ray property of intermediate mass pre-main-sequence stars (PMSs) Herbig Ae/Be stars (HAeBes), mainly using the observational and archival data of the *ASCA* and *ROSAT* satellites. Among 39 HAeBes covered with 42 *ASCA* pointings, we detect 15 plausible x-ray counterparts. X-ray luminosities of the detected sources are in a high range of $L_{\rm X}$ $\sim 10^{30-32}$ ergs $\rm s^{-1}$ compared with those of low mass stars. This fact excludes the possibility that HAeBe x-ray emission comes from a low mass companion. Most sources with moderate photon counts (>1000 cts) show time variations. In particular, three HAeBes - MWC 297, TY CrA and VY Mon - exhibit flare-like time variations with long decay timescales (*e*-folding time $\sim$ 10−50 ksec). These flare shapes are quite similar to the flares of low mass protostars. In contrast, HR 6000 show a rapid variation with fast rise and fast decay ($\tau <2$ ksec). Each spectrum is successfully reproduced with an absorbed one or two temperature thin-thermal plasma (MeKaL) model. The temperature ranges between $kT \sim$ 1−5 keV, which is significantly higher than that of main-sequence OB stars ($kT <$ 1 keV).

For their x-ray origin, we test a few models for emission mechanisms of stellar x-rays - wind driven shock, wind-fed magnetosphere, accretion shock and magnetic activity. These models except for the magnetic activity cannot explain the plasma temperature, x-ray luminosity or time variability. Nevertheless, HAeBes are not thought to have solar type dynamo mechanism to amplify the magnetic field because they lack the convection zone on the stellar surface. We cannot find the $L_{\rm X}$ dependence on $v\ \sin i$ and $\omega\ \sin i$, that are indicators of the solar type dynamo. To find out the generating mechanism of the magnetic field, we investigate the evolutional variation of plasma temperature and x-ray luminosity. We then find that the plasma temperatures have a clear rising trend with increasing the absorption column density ($N_{\rm H}$), which traces the surrounding materials and hence the evolutional status of young stars. This indicates that younger stars have more violent high-energy activity. Whereas, the x-ray luminosity seems to depend more on stellar masses. We therefore plot the x-ray luminosity in the HR diagram together with additional samples in previous papers. We then find $L_{\rm X}$ drops after the age a few$\times 10^6$ yrs. Considering the circumstellar structure, our results favor the mechanism of large scale magnetic fields linking a star and its circumstellar disk.

Stars earlier than spectral type B reach to the main-sequence phase before a few $\times 10^6$ year-old. This indicates that young massive main-sequence stars still operate the magnetic activity. From several pieces of supporting evidence, we propose that the x-ray emission from B1−9 stars and hard tails seen in O stars originate in this magnetic activity. On the other hand, we find the hard x-ray emission from the giant molecular cloud core Monoceros R2. We suggest that it might come from progenitors of HAeBes. Finally, we draw a unified picture of x-ray activity on young stellar objects in view of the magnetic activity.

Contents

List of Figures

List of Tables

Chapter 1

Introduction

Intermediate mass stars ranging from $2M_\odot$ to $10M_\odot$ do not exhibit x-ray activity. This is due to the absence of physical processes which produce x-ray photons such as strong UV acceleration to drive high-speed stellar winds working in high mass stars and the surface dynamo to drive magnetic activity working in low mass stars. In the pre-main-sequence stage which is classified as Herbig Ae/Be stars (HAeBes), the UV fields are much weak because the temperature of the stellar surface is low, but the structure of the stellar inside is considered to be almost the same as that of the main-sequence phase. No x-ray activity, therefore, could be working on HAeBes according to the current theories.

Nevertheless the *ROSAT* satellite detected the x-ray emission from nearly half the members of HAeBes (Zinnecker and Preibisch 1994). Subsequent *ASCA* spectroscopy with hard x-ray efficiency demonstrated that x-ray plasma have quite a high temperature ($kT \sim$3 keV) in certain objects (Skinner and Yamauchi 1996; Yamauchi et al. 1998; Hamaguchi et al. 2000). More surprisingly, Hamaguchi et al. (2000) discovered a large x-ray flare from the HAeBe, MWC 297. These latest results strongly indicate the presence of high-energy activity on or around HAeBes. The x-ray activity is thought to drive outflow and jet phenomena seen around young stellar objects. X-ray study of HAeBes is thus crucial to grasp the origin of the high-energy activity and its effect on the circumstellar environments.

In this thesis, we perform a HAeBes survey using observational and archival data of the *ASCA* satellite. From the first systematic analyses of the spectral and timing information, we restrict the x-ray emission mechanism probable in the HAeBe system. HAeBes are characterized by a dynamically evolving system to the main-sequence phase. We investigate the evolutional dependence of the x-ray activity as well, by merging results from the *ROSAT* and *Einstein* satellites. This research gives us an important implication for the x-ray properties of post HAeBes, massive main-sequence stars, and pre HAeBes, protostars. By combining all these results, we finally draw an overall picture of stellar x-ray activity from protostars to the main-sequence phase.

This thesis consists of eight chapters. Chapter 2 describes a review of the HAeBe system and x-ray property of known stars. Chapter 3 describes an instrument overview about *ASCA* and *ROSAT*. The next two chapters contain the data analyzing procedure (Chapter 4) and the results of all individual sources (Chapter 5). Chapter 6 & 7 discuss x-ray emission mechanism of HAeBes, pre and post HAeBes. The conclusion of our survey is in the last chapter (Chapter 8).

Chapter 2

Review

2.1 Herbig Ae/Be Stars

2.1.1 Classification

Herbig (1960) made a catalogue of emission line objects which are candidate stars in the contracting phase between 3−20 $M_\odot$. The selection criteria in Herbig (1960) are as follows:

§1. spectral type A or B with emission lines,
§2. locating in an obscured region,
§3. accompanying a bright nebulousity.

The classified sources have been widely accepted as pre-main-sequence stars (PMSs) of intermediate mass, ie high mass counterparts of T-Tauri stars[1] (TTSs). They are now called Herbig Ae/Be stars. Recent sensitive surveys in near and far infrared wavelengths presented a few more candidates of intermediate mass PMSs which are not associated with nebulousity. To include these stars in the category, the criteria of Herbig Ae/Be stars were slightly modified as follows (cf. Waters and Waelkens 1998),

§1. spectral type A or B with emission lines,
§2. infrared (IR) excess due to hot or cool circumstellar dust or both,
§3. luminosity class III to V.

These new criteria are convenient to exclude classical Be stars and supergiants, which have similar photometric appearances to Herbig Ae/Be stars. Newly identified objects are especially called 'isolated Herbig Ae/Be stars'. We later abbreviate Herbig Ae/Be star to

---

[1] see Tsuboi (1999) for the evolution of low mass young stars

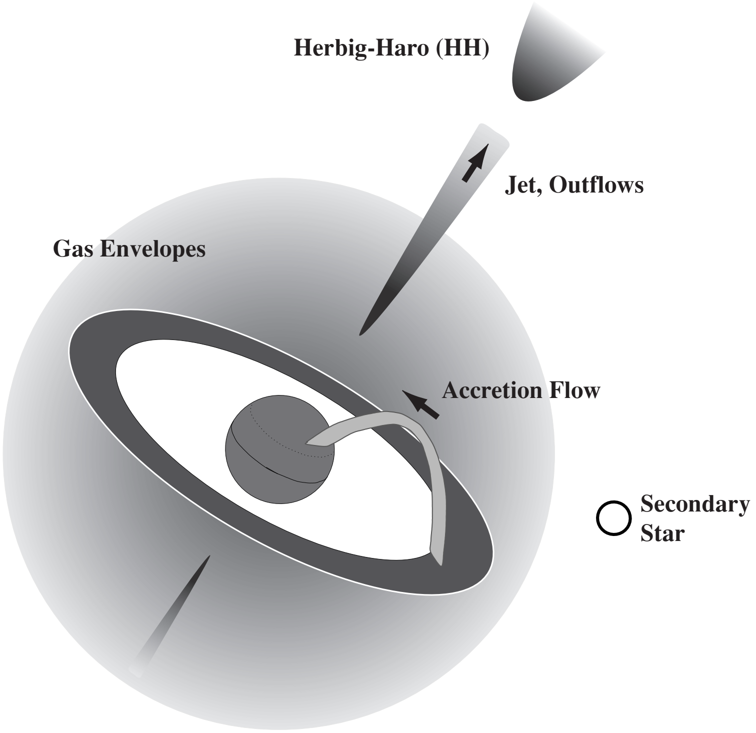

Figure 2.1: Schematic picture of the HAeBe system. This picture does not hold relative scale size.

'HAeBe' according as an usual manner.

2.1.2 Circumstellar Structure

Number of HAeBes observable in the sky is relatively small. This is because the birth ratio of HAeBes is not high and their PMS life time is about two orders as short as those of solar mass stars ($\sim 10^6$ yrs). These constraints make it difficult to figure out the circumstellar structure of HAeBes. However, infrared and radio observations have indicated several similarities between HAeBes and TTSs.

A schematic picture of the HAeBe system is displayed in Figure 2.1. The HAeBe system consists of a stellar main body, circumstellar disk and spherical gas envelope. Circumstellar materials in the disk gradually accrete onto the stellar body, and some of them are eliminated from the system seen as jets or mass outflows, which take away most of the angular momentum holding in the accreting gases. They collide with the ambient materials and form bow-shocks called Herbig-Haro objects. Most of the HAeBes ($P>85\%$, Pirzkal et al. 1997) accompanies companion stars, some of which are also HAeBes. Here we describe the detailed properties of each component.

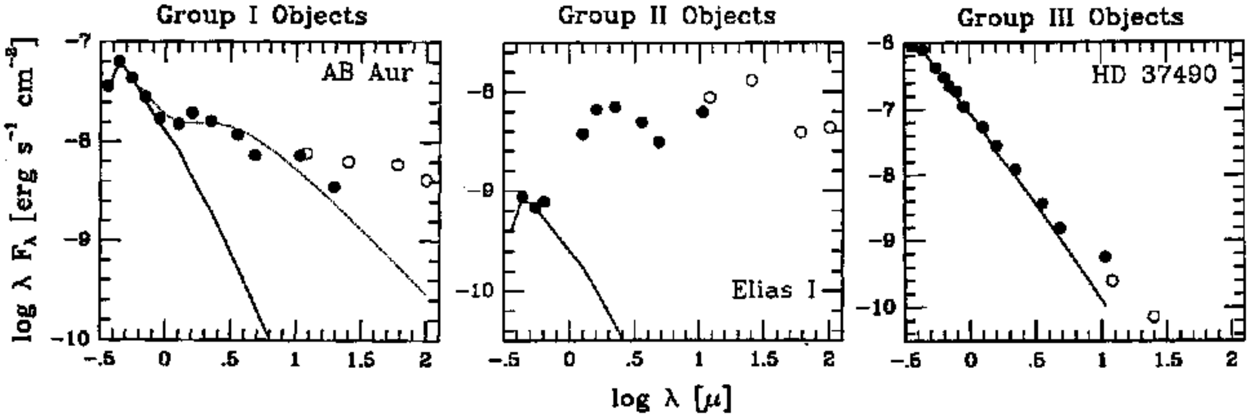

Figure 2.2: SEDs of three HAeBes in different groups (Hillenbrand et al. 1992).

Circumstellar Environments - Disks and Envelopes

Hillenbrand et al. (1992) classified spectral energy distribution (SED) of HAeBes into three groups according to the spectral shapes above $\lambda \sim 2.2\mu$m. By interpreting these SED shapes, they suggested each group has the following blackbody components (see also Figure 2.2),

Group I: star + geometrically flat, optically thick circumstellar accretion disk,

Group II: star + gas and dust which is not confined to a disk (envelope),

Group III: star without any excess emission.

Group III stars contain the highest mass stars and group I stars contain the next highest mass stars. They therefore concluded that the disks and envelopes of higher mass stars have shorter lifetimes than those of lower mass stars. Nevertheless, Hartmann et al. (1993) pointed out that the infrared excess regarded as the disk component can be explained by emission from spherical envelopes. Natta et al. (1993) also suggested the presence of envelope structure even for the Group I sources in the far infrared. Recent understanding is that the SEDs of Group I sources require the existence of both disks and envelopes. On the other hand, with the 1.3 mm radio continuum, Henning et al. (1998) evaluated the average density of the HAeBe cores to be 10^{5-8} cm^{-3} and those of the extended envelopes to be 10^{4-5} cm^{-3}. Fuente et al. (1998) found that the surrounding gases within 0.08 pc disperse in the time scale of 10^6 yrs.

Accretion Flows

Hillenbrand et al. (1992) deduced mass accretion rate of HAeBes to be high (M$_{acc} \sim 10^{-4--6}$ $M_\odot$ yr^{-1}) from excess emission over the standard disk blackbody. Skinner et al. (1993) and Hartmann et al. (1993), however, rebuted this result because the strong emission required for high accretion rate was not observed in the radio wavelength. UV excess is also a good

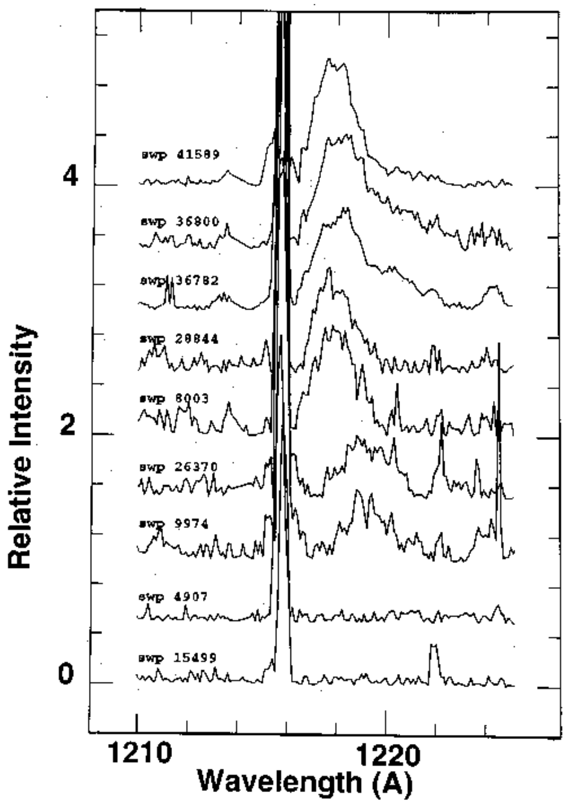

Figure 2.3: UV spectra around Lyman α emission line of HD 104237 (swp 41589, 36800, 36782), HD 163296 (swp 28844, 8003), HR 5999 (swp 26370, 9974), AB Aur (swp 4907) and HD 190073 (swp 15499) (Blondel et al. 1993). The strong line on 1216Å come from the geocoronal Lyman α emission. A redshift component of Lyman α emission ($\lambda \sim 1218$ Å) is seen in younger HAeBes (*upper*) but it is absent in elder HAeBes (*lower*).

estimator of mass accretion rate (Meeus et al. 1998; Valenti et al. 2000; Gullbring et al. 2000), but the estimate is not easy for HAeBes because UV radiation in stellar blackbody is dominant and moreover, the extinction of ISM strongly depends on $A_{\rm V}$ and adopted conversion ratio between $A_{\rm V}$ and $N_{\rm H}$. Blondel et al. (1993) derived low accretion rate ($\rm M_{acc} \sim 10^{-6--8}$ $M_{\odot}$ yr^{-1}) for Herbig Ae stars from red-shifted Lyman α emission lines using the IUE data (see Figure 2.3). This value is as many as those of T-Tauri stars but 3 orders of magnitude lower than those of active stars such as FU Ori and Z CMa. Assuming accretion geometry, they also suggested the faster infall velocity ($\rm v_{acc} \sim 600-2000$ km s^{-1}) than the free-fall velocity ($v_{ff} \sim 600$ km s^{-1}). This requires a certain acceleration mechanism in the inflow process.

Outflows & Stellar winds

Herbig-Haro (HH) outflows, including jets and CO outflows, are usually seen around YSOs (eg Levreault 1988). Outflows in HAeBes are qualitatively identical to, but a factor of two to three faster than, those of TTSs (v ~600−900 km s^{-1}, Mundt and Ray 1994). Outflow activity is usually seen in young HAeBes in 10^5-year-old, but collimated, bipolar outflow was also found from the elder HAe star HD 163296, whose age (1.5−10 Myrs) is ~10 times older than the age of TTSs showing outflow activity (Devine et al. 2000). Most HAeBe outflows

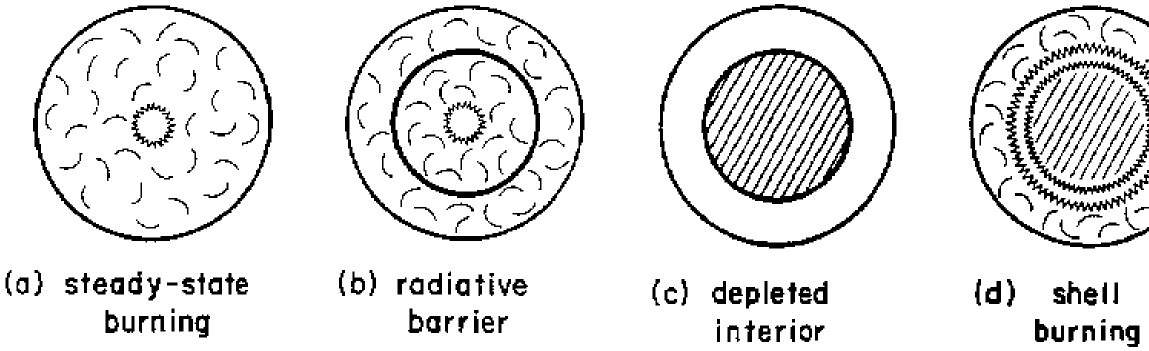

Figure 2.4: Schematic picture of deuterium burning in protostars (Palla et al. 1990). (a) At low masses, accreted deuterium is fed in a steady-state fashion to the burning center by convective eddies. (b) Eventually, a radiative barrier appears, cutting off the supply to the center. (c) The central region soon exhausts its deuterium and reverts to a radiatively stable state. (d) At higher mass, deuterium ignites as a shell source just outside the depleted central region.

(≈70%) are highly, but the rest are poorly, collimated (Mundt and Ray 1994).

From P-Cygni profiles of Hα and NaD lines, Finkenzeller and Mundt (1984) indicated that the stellar wind was accelerated within a few stellar radii and decelerated to the terminal velocity at larger distances (eg 20−50 R_*). Valenti et al. (2000) detected broad absorption features in UV spectra (eg C, O and Si), which are originated in wind materials. These features have a variety in strength even for stars with the same spectral type: some are blue-shifted and are not seen in early HBes. This absence on early HBe stars is interpreted as the highly ionization of circumstellar materials. On the other hand, the radio emission from HAeBes, which probably comes from stellar winds, is mostly thermal except for a few sources (eg TY CrA and EC95, Skinner et al. 1993; Smith et al. 1999).

2.1.3 Evolutional Status

In theoretical models a star is born in the upper right of the HR diagram, ie low $T_{\rm eff}$ & large $L_{\rm bol}$. It descends along nearly vertical track (Hayashi track) and then moves along a radiative track at almost constant luminosity when a radiative core develops. Finally, hydrogen ignites in the core, contraction is halted, and a star reach to the main-sequence phase (zero-age-main-sequence: ZAMS). Iben (1965) made numerical calculations of young stellar evolution in the HR diagram. He treated stars of masses ranging between $0.5-150M_\odot$, on the assumption that the initial state of stars is fully convective, with radii nearly two orders of magnitude larger than that of ZAMS. However, such a large amount of gases is not thought to be gathered in the initial phase. Palla and Stahler (1990) therefore set the stellar birthline much closer to the main-sequence branch. In their scenario, stars just below

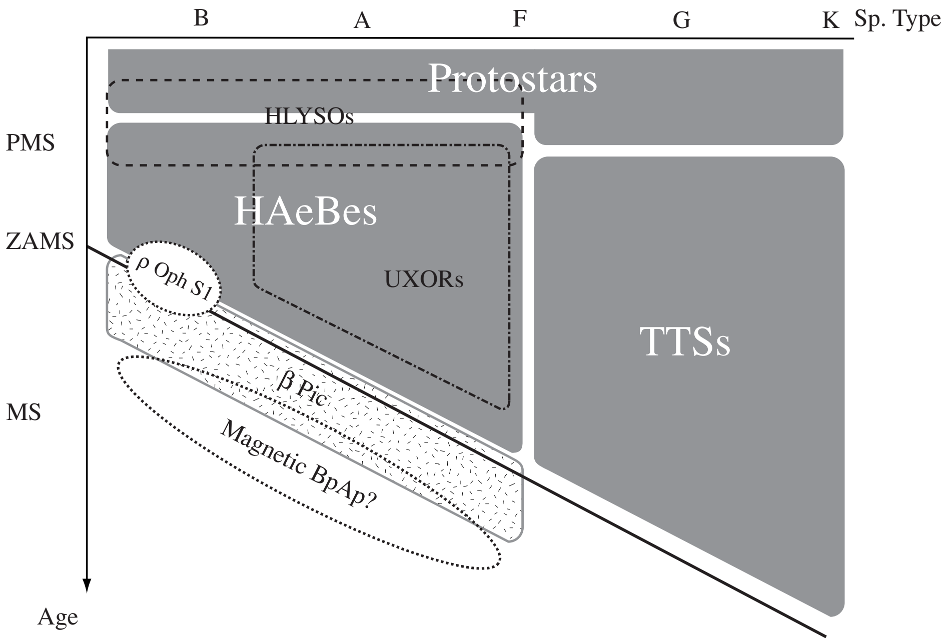

Figure 2.5: Evolutional status of each group of stars.

the birthline are fully convective, but they soon ignite deuterium burning, which makes the barrier to penetrate the convective eddy into the core and suppress the convection (see also Figure 2.4). During this phase, a weak convection occurs at the stellar surface but not so strong as to generate magnetic fields. The stellar inside soon turns to fully radiative and then reaches to ZAMS. HAeBes are a few times as young as the age estimated by Iben (1965) and stars larger than $8M_\odot$ already ignite the ordinary hydrogen burning in the core when they appear on the birthline.

2.1.4 Other Types of Stars Related to Herbig Ae/Be Stars

We briefly mention other stellar categories which are related to HAeBes. Their evolutional status is illustrated in Figure 2.5.

Classical Be stars: Classical Be stars are defined as the main-sequence or somewhat higher luminosity B-type stars with the Balmer emission lines, originated from circumstellar envelopes. This stellar category was first discovered in γ Cas and later called as 'classical' for distinguishing them with the HAeBe group. The Balmer lines and the polarization properties, called Be phenomena, are thought to relate with disks made by rapid axial rotation (v sin i $\sim$250 km s^{-1}). Be stars consist of 20% of the B-star population and is largest in the spectral type range B3–4 (Slettebak 1991).

β-Pic (Vega) type stars: The *IRAS* satellite found an excess emission from some main-sequence stars such as β Pictoris, Vega, and Fomalhaut (Walker and Wolstencroft 1988). A high resolution imaging, masking a stellar photosphere, revealed that this excess emission is originated in cool debris disks, probably made from cometary clumps. Though a part of them are later identified as isolated HAeBes, these stars now grouped in β-Pictoris type stars and thought to be in the phase between HAeBes and the main-sequence stars.

(Magnetic) Bp-Ap stars: Bp-Ap stars show chemically peculiar spectra and lie on the main-sequence branch. Some of them have magnetic fields and are especially called as magnetic Bp-Ap stars. From a *HIPPARCOS* survey of magnetic Ap stars, Hubrig et al. (2000) concluded that magnetic fields appear only in stars that have completed at least ~30% of their main-sequence lifetime. Nevertheless, a few HAeBes also have Bp-Ap characteristics (see Table 4.1) and the plausible magnetic Bp star S1 in ρ-Oph has characteristics of its youth (Andre et al. 1991).

High Luminosity Young Stellar Objects: High luminosity young stellar objects have $L_{\rm bol} \geq 1000\ L_{\odot}$ (HLYSOs), most of which are embedded infrared sources and thought to be progenitors of HAeBes (cf Mundt and Ray 1994).

UX Ori variables: UX Ori stars (UXORs) are defined as highly variable stars with deep irregular minima. A UXOR phenomenon is thought to occur by an occultation of patchy circumstellar dust clouds. 1/3 of HAe stars may be UXORs but no HBe shows UXOR phenomenon (see Natta et al. 2000).

A-shell type stars: A certain HAeBes coexist two types of line profiles in their spectra, one originating in the stellar photosphere and the other in the cooler shell (see Hauck and Jaschek 2000).

2.2 Stellar X-ray Emission

2.2.1 X-ray Emission from Main-Sequence Stars

Low mass Stars – Later than F5

X-ray emission from low mass MS stars like the sun exhibits occasional rapid x-ray flares (see Figure 2.6), and therefore is originated in the magnetic activity. The magnetic field is generated by the dynamo mechanism, powered by a coupled effect on surface convection and differential rotation ($\alpha - \omega$ dynamo). The role of stellar differential rotation can be seen in $L_{\rm X}$ dependence on the projected rotational velocity, v_{rot} sin i. $L_{\rm X}$ increases with v_{rot} sin i and reaches the saturation level at v_{rot} sin $i \sim 15$ km s^{-1} (log $L_{\rm X}/L_{\rm bol} < -3$, see also Figure

2.7). The level is also proportional to a square of a stellar radius (Fleming et al. 1989), which implys that $L_{\rm X}$ is proportional to the converting factor of magnetic loops on stellar disks. Through MS lifetime, low mass stars decay the x-ray luminosity owing to a systematic decline in the rotational speed by magnetic breaking (see Simon and Drake 1989). In the Pleiades cluster, however, the dependence of the x-ray luminosity on stellar age is not clearly seen (Stauffer et al. 1994).

Intermediate Mass Stars – Late B to F5 including β-Pic & Magnetic Bp-Ap Stars

Normal intermediate mass stars including β-Pic stars have the smallest x-ray luminosities. – log $L_{\rm X}$ (ergs s^{-1}) $\sim$ 28–30, (Panzera et al. 1999). This is due to deficiency of high energy activity. Even the above mentioned luminosity is suspected to come from a low mass companion. Whereas He-strong (Bp) stars have the x-ray emission level of log $L_{\rm X}/L_{\rm bol} \sim -7$ and He-week (Bp) and Si (Ap) stars have the emission level up to log $L_{\rm X}/L_{\rm bol} \sim -6$, but SrCrEu-type (Ap) stars emit no detectable x-rays (Drake et al. 1994). The He-strong star σ Ori E and the plausible magnetic Bp stars Rho-Oph S1 have incredibly high x-ray luminosity for B stars ($L_{\rm X} \sim 3\times10^{30}$ ergs s^{-1}, Montmerle et al. 1983; Drake et al. 1987). Followup radio observations of Rho-Oph S1 by Andre et al. (1988) and Andre et al. (1991) indicated the non-thermal radio spectrum, which can be simulated by a pole-on bipolar magnetic field of $\sim$ 2 kG on its stellar surface. A model proposed for magnetic Bp-Ap stars (Havnes and Goertz 1984) required that dense inner region with a chromospheric characteristic (n $\sim 10^{12}$ cm^{-3}, T $\sim 10^4$ K) extended out to 10 R_*. The radio and x-ray emission cannot penetrate such a thick envelope and hence would be originated in the outer magnetosphere (Andre et al. 1988).

High Mass Stars – OB Stars & Be Stars

MS OB stars produce almost constant x-ray emission ($kT < 1$ keV, log $L_{\rm X}$ (ergs s^{-1}) $\sim$ 32 and log $L_{\rm X}/L_{\rm bol} \sim -6 - -8$, Seward et al. 1979; Harnden et al. 1979; Long and White

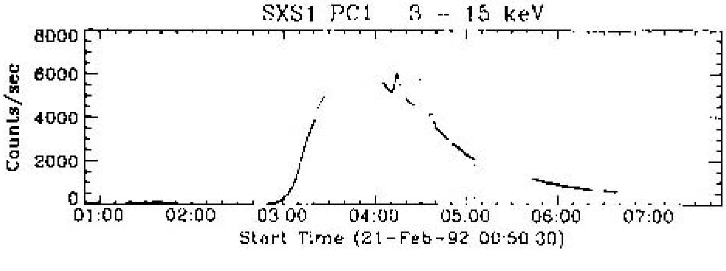

Figure 2.6: An x-ray flare from the sun in the *Yohkoh* soft x-ray band

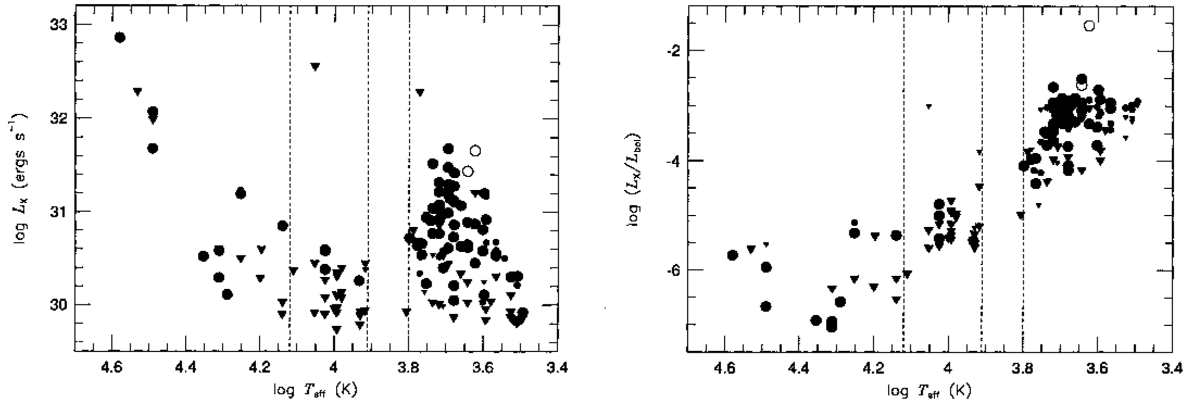

Figure 2.7: Log L_{X} (*left*) and log $L_{\mathrm{X}}/L_{\mathrm{bol}}$ (*right*) *vs.* effective temperature distribution in the Orion molecular cloud (Gagne et al. 1995)

1980; Chlebowski et al. 1989). Coronal x-ray emission like the sun was first proposed for the origin, but the strong mass loss log $\dot{M}$ ($M_{\odot}$ yr^{-1}) $\sim -5 - -7$ with $v \sim$ 1500–3000 km s^{-1} derived from P-Cygni profiles (Lamers and Leitherer 1993; Berghoefer and Schmitt 1994) required large N_{H}, which is not observed. Nordsieck et al. (1981) searched for, but did not find, optical lines characterizing coronal emission from two OB stars.

Lucy and White (1980) proposed a wind-shock model for OB stellar x-rays. In this model, line absorption of stellar radiation accelerates circumstellar materials and produce stellar winds. The winds confine ambient gases by ram pressure and form shocks (see Figure 2.8 *left*), which thermalize the gases and finally causes soft x-ray emission. This theory was strengthened by numerical calculations (Owocki and Rybicki 1984; Owocki and Rybicki 1985; Owocki and Rybicki 1986; Owocki et al. 1988) and the observational evidence of small time variations in ζ-Orionis (Berghofer and Schmitt 1994). Nevertheless conflicting results were reported as well, and therefore Usov and Melrose (1992) proposed an alternative emission mechanism – magnetic reconnection on current sheets of large magnetosphere (see Figure 2.8 *right*). The presence of magnetic fields on O stars was suggested from the non-thermal radio emission and the continuous variability in the blueshifted absorption of Si IV doublet lines (ζ Pup, Howarth et al. 1995). The x-ray emission mechanism on OB stars is under discussion, but it should be noted that latest high-resolution x-ray spectroscopy with *Chandra* and *XMM-Newton* suggests that x-ray line emission from massive MS stars originates from confined high density plasma well above 10^{12} cm^{-3}, with a mean velocity of $v \sim$700–1000 km/s (Schulz et al. 2000; Kahn et al. 2001).

Late B stars have different x-ray characteristics from O and early B type stars. In a survey of Grillo et al. (1992), 1545 B-type SAO stars with *Einstein*, early B-type stars between B0−B3 emit x-rays at the level above $L_{\mathrm{X}} > 10^{30}$ ergs s^{-1}, while late B-type stars tend to have fainter or no x-ray emission. Cassinelli et al. (1994) surveyed nearby MS B stars with *ROSAT* and found that the $L_{\mathrm{X}}/L_{\mathrm{bol}}$ ratio sharply decreases later than B1 down

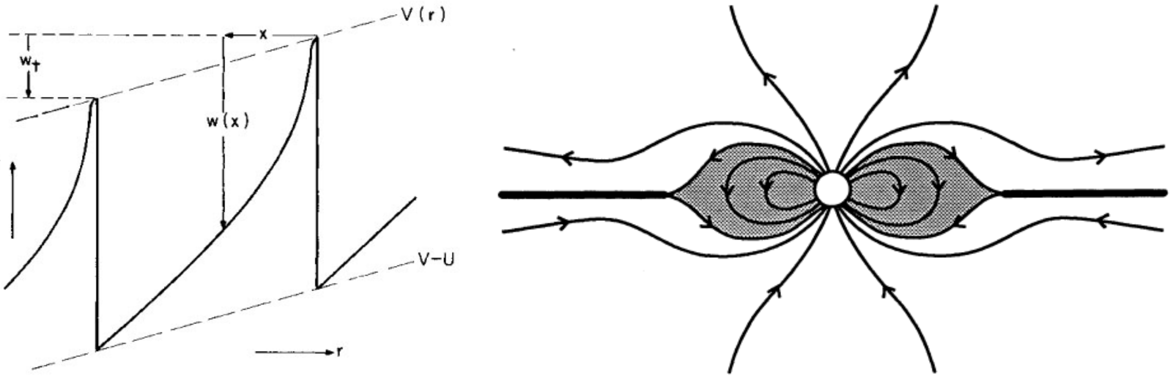

Figure 2.8: Shematic views of two x-ray emission models of massive MS stars. The left panel displays successive propagating shocks in the stellar wind (Lucy 1982). The holizontal and vertical axes show distance from a star and wind velocity, respectively. The right panel displays the configuration of magnetic fields (Usov and Melrose 1992). The magnetic reconnection fed by winds occurs on the equatorial plane.

to $L_\mathrm{X}/L_\mathrm{bol} \sim 10^{-9}$. On the other hand, Berghoefer et al. (1996) performed a complete survey of OB stars with the RASS and follow-up HRI data. they demonstrated that the canonical relation of $L_\mathrm{X}/L_\mathrm{bol}$ values ~ -7 is valid for stars earlier than B1-1.5 (see also the discussion 8.1), but such a clear relation is not seen later than B1-1.5. They also found that the detection rate decreases less than 10% below the spectral typoe.

The prototypical classical Be star, γ Cas, has normal x-ray luminosity of, but quite high temperature agaist, MS OB stars (L_X $\sim$$10^{33}$ergs s^{-1}, kT $\sim$10.6 keV). The x-ray emission would therefore come from a white-dwarf companion (Kubo et al. 1998). It is not known as whether the x-ray property is typical of classical Be stars.

2.2.2 X-ray Emission from Pre-Main-Sequence Stars

Low Mass Stars – T-Tauri Stars & Protostars

Low mass PMSs – TTSs and protostars – have more violent x-ray activity than low mass MS stars (Feigelson and Decampli 1981; Montmerle et al. 1983 for T-Tauri stars; Koyama et al. 1996; Kamata et al. 1997; Tsuboi et al. 2000 for protostars). Both types of stars are highly variable and exhibit large flares in the x-ray wavelength. From the similarity to the low mass MS stars, the x-ray emission from TTSs is probably originated in the magnetic activity enhanced by a coupled effect of deep convection and rapid rotation. Actually, the relation between L_X and v_{rot} sin i, an indicator of the solar-type dynamo, is seen for the T-Tauri membership of the Orion molecular cloud (Gagné et al. 1995), but it was not for the membership of Chameleon I cloud (Feigelson et al. 1993). On the other hand, protostars

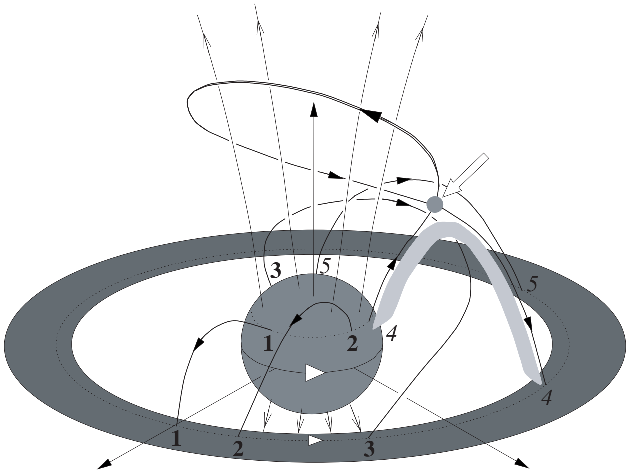

Figure 2.9: Schematic view of possible magnetic configuration between a star and its disk quoted from Montmerle et al. (2000). The solid lines describe a transition of magnetic fields in a sequence of No. 1 – 5, driven by rotating difference between a star and its disk.

cannot be thought to operate solar-type dynamo because they are fully convective and do not have an anchor point of the magnetic field. One of the most prausible model - the structure of the magnetic field linking a star and its disk (Koyama et al. 1996; Tsuboi et al. 2000; Montmerle et al. 2000, see Figure 2.9) - might explain the x-ray activity. This model assumes that magnetic fields perpendicular to the equatorial plane are inherently present. probably through the process of gathering interstellar magnetic fields during the gas infall. These magnetic fields are continuously twisted by the differential rotation between a star and its disk, and reconnect after one rotational difference, seen as an x-ray flare. In the numerical simulation by Hayashi et al. (1996), the reconnection accompanies a gas eruption, which could be later seen as outflows or jets.

Intermediate Mass Stars – Herbig Ae/Be Stars

Damiani et al. (1994) detected x-ray emission from 11 HAeBes out of 31 observed sources using *Einstein* (9/20 for Be stars, 1/8 for Ae stars and 1/3 for F0−F5 stars). They found that Be stars are more luminous than Ae stars. The luminosity function of Be stars is much different from, but that of Ae stars is similar to, low mass stars in Taurus-Aurigae. They therefore suggested that x-ray emission from Be stars arise in the same mechanism of MS OB stars while that of Ae stars might actually originate in low mass companions. The X-ray luminosity depends on the bolometric luminosity, which, they concluded, only see a different expression of $L_{\rm X}$ − spectral type relation because observed HAeBes are close to the MS track. They suggested a correlation between the x-ray luminosity and the terminal wind velocity but no correlation between the x-ray luminosity and the v_{rot} sin i. On the other hand,

Table 2.1: X-ray properties of giant molecular cloud cores

Target	ref.	kT (keV)	log L_X † (ergs s^{-1})	Band (keV)	Region
Monoceros R2	1	5.6 (4.7–7.0)	32.4	0.8–10	All GMC
NGC 6334	2	9.0 (7.2–12.3)	33.8	0.5–10	Five FIR cores
NGC 2264	3	4.4 (3.3–7.4)	32.2	0.7–10	IRAS 9 (Allen's source) or IRS1
W3	4	5.6 (4.6–7.3)	32.2	2–10	core
Orion Trapeisum	5	3.1 (2.9–3.2)	—	—	Trapesium region

†Absorption corrected luminosity for the energy band column. References: ^{1}this work (the subsection 6.1, see also Hamaguchi et al. 2000), ^{2}Sekimoto et al. (2000), ^{3}Nakano et al. (2000), values of hard component in the 2C model, ^{4}Hofner and Churchwell (1997), ^{5}Yamauchi et al. (1996).

Zinnecker and Preibisch (1994) detected x-ray emission from 11/21 HAeBes using *ROSAT*. They found a rising trend of L_X with $L_{\rm bol}$. In their estimation, there was no correlation with the spectral type or v_{rot} sin i, but a weak correlation with the wind velocity and a rather good correlation with the mass loss rate. They suggested that x-ray emission of HAeBes would originate in shocks of strong stellar winds to remnant circumstellar material.

Giant Molecular Cloud Cores – Massive Protostar Emission?

Massive stars go through their PMS age in the deep inside of GMC cores and reach to the MS stage in a very short time ($< 10^4$ yrs). Owing to the strong absorption by the surrounding gases, the beginning phase of massive stars is not seen in optical or even in near infrared. A theory predicts that massive stars larger than 10 $M_{\odot}$ cannot form from mass contraction of circumstellar gases but from the merging of smaller mass stars because strong radiation fields disperse accreting gases. The existance of massive protostars is therefore still doubted, but strong outflows and maser emission (OH, SiO) are generally observed around GMC cores. These phenomena suggest violent activities on very young massive stars.

Several massive young stars in the PMS phase, whose extinction exceeds over $A_V \sim 50$ ($N_H > 10^{23}$ cm^{-2}), were found in nearby GMC cores. Soft x-rays from massive PMSs undergo strong absorption so that hard x-ray imaging is the only tool to probe the x-ray activity. *ASCA* is the first satellite holding such capability. Though the spatial resolution is still limited to resolve crowded membership in GMC cores, *ASCA* have detected hard x-ray sources from the GMC core (Table 2.1). The next generation x-ray satellite *Chandra* has an excellent spatial resolution ($\sim$0.5$''$) in the *ASCA* band. Garmire et al. (2000) resolved all x-ray sources in the Orion cloud with *Chandra*, which includes the on-going massive star forming cite Becklin-Neugebauer/Kleinman-Low (BN/KL) region, but they did not detect x-ray emission from neither the IR luminous massive YSOs BN object nor the source i, showing strong outflow activity.

Chapter 3

Instruments

The atmosphere of the earth completely blocks cosmic x-ray radiation. Study of celestial x-ray sources thus requires an observation in the outer space. Fortunately, recent advance of space technology enabled continuous launch of spacecrafts for x-ray astronomy, and five satellites, *ASCA*, *XTE*, *Beppo SAX*, *Chandra* and *XMM-Newton* are now working (at Jan 5, 2001). In this chapter, we summarize the performances of two x-ray observatories *ASCA* and *ROSAT*, which led x-ray astrophysics in 1990s. We only mention subjects related to our analyses.

3.1 The *ASCA* Satellite

3.1.1 Outline

Advanced Satellite for Cosmology and Astrophysics - *ASCA* - is the 4th Japanese x-ray astronomy satellite developed by the Institute of Space and Astronautical Science (ISAS) in collaboration with domestic x-ray astronomy groups and American institutes MIT and NASA. *ASCA* was launched on February 20 1993 at the Kagoshima Space Center (KSC) with the M-3S-II rocket and put into an approximately circular orbit (perigee 520 km, apogee 620 km, inclination 30.1°, orbital period $\sim$96 min). *ASCA* worked properly until July 1999, but since then it has malfunctioned for an unexpected attack on air disturbance caused by an increase of solar activity.

ASCA carries four identical x-ray telescopes (XRT) and coupled focal plane detectors, two of which are the Solid-state Imaging Spectrometers (SISs) and the other two are the Gas Imaging Spectrometers (GISs). All these detectors run independently and output data at the same time. The schematic view of the *ASCA* satellite is shown in Figure 3.1. An introduction to *ASCA* is described in Tanaka et al. (1994).

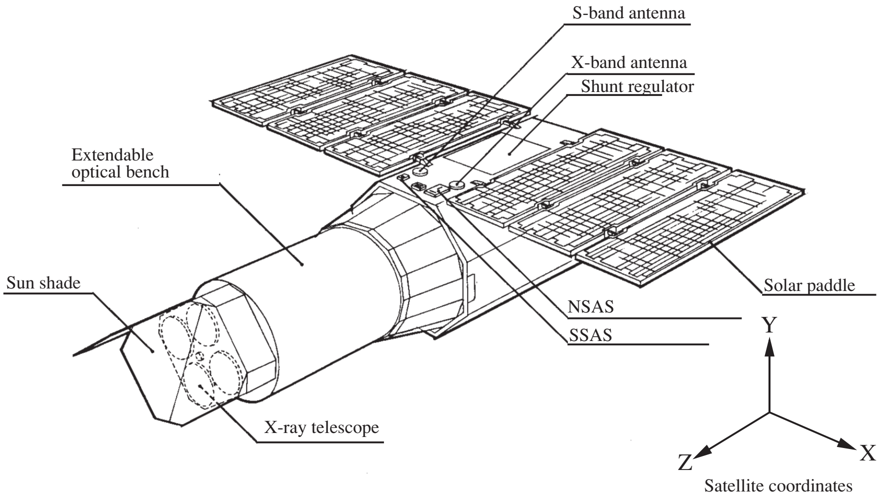

Figure 3.1: Schematic view of the *ASCA* satellite

The satellite attitude is controlled in three-axis with the stability less than 10″. Two star trackers calibrate the absolute pointings through observations, whose pointing accuracy was designed better than 12″ but later turned out to be around 40″ in onboard calibrations caused by thermal distortion of star trackers. From the constraint on power supply, orientation of the spacecraft is limited to the normal direction of solar paddle within 30° from the sun. This constraint limits the observable sky at one time and the entire sky is accessible every half year. Harsh environs on the *ASCA* orbit constrains the satellite operations. At first, whether satellite is in the sunshine or not, ie satellite day or night, decides the temperature of the spacecraft. Detector response, especially on SIS, is affected by the satellite temperature. Second, the radiation of cosmic particles not only degrades the quality of the data but also can damage detectors. South Atlantic Anomaly (SAA) is a region where the particle density is always high. During the passage of SAA, all detectors onboard *ASCA* are shut down.

The science data are first stored in onboard memories (Bubble data recorder; BDR) and then downloaded to the ground station at KSC and NASA deep space network (DSN). The storage capacity of BDRs is limited and thus the memory space of the science data written in a time is pre-programmed by each observing schedule. There are three memory modes; bit HIGH mode secures 32K bit memory space per second, bit MEDIUM does 4K bit and bit LOW does 1K bit. Overflowed data are discarded and thus an observer has to prepare a proper program met for observing targets and operational constraints.

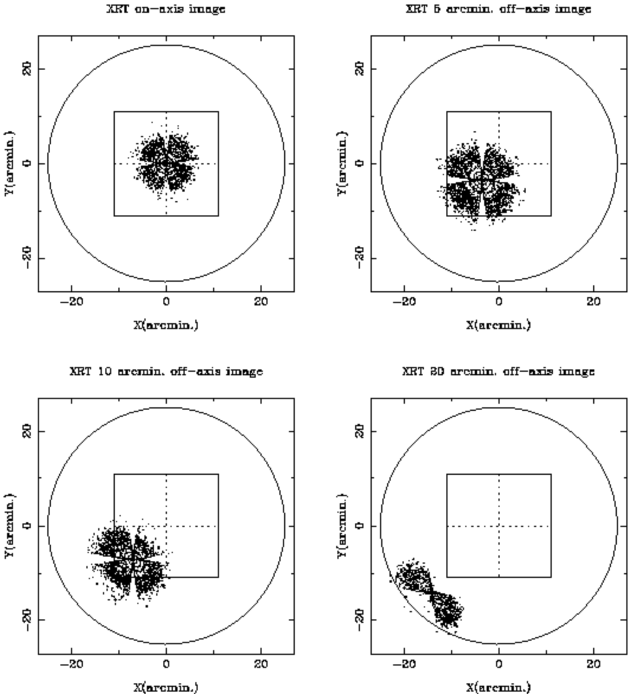

Figure 3.2: Point spread function of the *ASCA* XRT for four different off-axis angles. Inner boxes and outer circles represent the field of view of SIS and GIS respectively.

3.1.2 X-ray Telescope (XRT)

X-ray imaging telescopes utilize the optics of Wolter type I geometry, which focus x-rays through two mirrors of paraboloids and hyperboloids. *ASCA* XRTs are based on this optics as well, but they approximate these shapes to two flat conical surfaces made from thin aluminum foils. This simplification makes the spatial resolution modest (Half Power Diameter: HPD $\sim 3'$) but enables us to nest multiple mirrors (119 foils an XRT), which provides large collective area especially in the hard x-ray band. *ASCA* is thus the first satellite which holds the imaging capability of astronomical objects up to ~10 keV.

XRT has a cusped shape point spread function (*psf*) and concentrate 20% of parallel x-ray beams within a circle of $1'$ diameter. Ideal *psf* is radially symmetrical, but spokes connecting nested mirrors block part of x-ray beams and thus real *psf* looks like a butterfly shape (see Figure 3.2). As the characteristics of the Wolter I optics, *psf* is elongated to the direction perpendicular to the radial vector of XRT *fov*, which makes the spatial resolution in outer *fov* poor. XRT effective area decreases on the far side from the optical axis, depending on x-ray photon energy. This characteristic is called vignetting effect. See Serlemitsos et al. (1995) about the details of *ASCA* XRT.

Table 3.1: SIS and GIS detector performances

	Unit	SIS	GIS
Energy range	(keV)	0.4–10	0.7–10
Field of View		$20' \times 20'$	$50'$ $^{\dagger 2}$
Energy resolution (5.9 keV)	(eV)	130	460
Maximum Time Resolution	(sec)	$4^{\dagger 1}$	$60\mu^{\dagger 2}$

$^{\dagger 1}$ 1CCD mode, $^{\dagger 2}$ diameter, $^{\dagger 3}$ PH mode

3.1.3 Solid-state Imaging Spectrometer (SIS)

The Solid-state Imaging Spectrometers (SISs) are the first x-ray CCD cameras aboard astronomical x-ray satellites. CCD, the abbreviation of charge coupled device, is so called a μm pixel array of solid-state detectors. The detection process is as follows. An x-ray photon interacted in the depletion layer of a CCD generates large amount of electrons proportional to its photon energy. This electron cloud is collected at an electrode of an incident pixel by electric fields and conveyed to a readout gate according as a CCD control clock. The capacitor on the gate converts an electron charge to a signal voltage, which is amplified in a circuit. A readout system measures it with addressing the pixel position. A certain percentage of electron clouds, with many electrons or near pixel gaps, extend over plural pixels. Because cosmic particle events also generate huge electrons through multiple pixels, events are classified into 7 groups according to the pattern of 3×3 pixel pulse heights and 4 groups (grade 0,2,3,4) are adopted as x-ray events. The thickness of the depletion layer is $\sim$30 μm so that the SIS quantum efficiency drops above 6 keV. The soft x-ray efficiency (kT <1 keV) is better because insensitive layers above the depletion layer is thin. SIS sensitive band is therefore wider than GIS (0.4–10 keV: see Table 3.1).

Each of two SISs comprises four identical CCD chips (see Figure 3.3), which are cooled down on -60 °C by their Peltier coolers. One CCD chip covers a $11.1' \times 11.1'$ *fov* and needs 4 second a readout cycle. The readout module of each SIS sensor processes the output data of one CCD chip at one time so that the other CCD chips waits to be read and exposed on the focal plane. Exposure time per CCD frame is thus multiplied according as the number of working CCD chips. Because long exposure not only worsen the timing resolution but also causes increases of pile-up events and dark current noise, observers can select number of CCD chips to work, from 1, 2 and 4 CCD modes. Exposures of the selected modes are 4, 8 and 16 seconds, respectively. On the other hand, an observer can choose a data format from two modes according as the BDR capacity. Both data formats consist of the information about CCD ID, event pixel position and arrival time. The difference of these two modes is described like this.

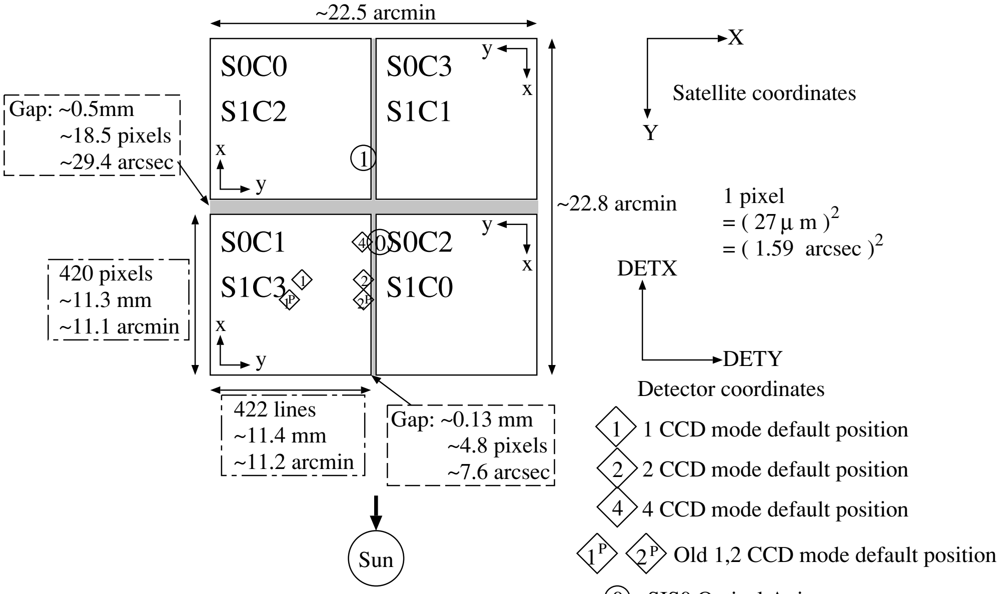

Figure 3.3: SIS chip configuration

FAINT: All the pulse heights of 3×3 pixels are transmitted to the ground. This mode can be only used for faint sources.

BRIGHT: An added pulse height of 3×3 pixels and its grade information are transmitted to the ground. Though event number memorable in BDRs is about four times as many as that of the FAINT mode, observers cannot re-process downloaded data on the ground.

Several problems have been found through onground and onboard calibrations. Properties of each problems and how to deal with them are summarized below.

Echo: A certain fraction of a pulse height is added on its right-side pixel (Otani and Dotani 1994). This false pixel height, linear to the real pixel height, is made in the processing of the Analogue Electronics (Yamashita 1995). This effect can be easily corrected if the event data is in the FAINT mode, but it cannot be corrected in the BRIGHT mode. Its response matrices correct the deviation from the real signal output.

Dark Frame Error (DFE): is to misestimate the mean pulse heights of CCD pixels without events (zero level of Dark frame; Otani and Dotani 1994). Onboard software calculate the zero level by averaging pixel pulse heights between -40 ADU and 40 ADU, but PH is asymmetrically distributed around zero level by the integration of

X-ray photons, charged particles and optical light leakages, which causes zero level to overestimate. In an orbital night, the DFE is stable (~3 ADU for 4CCD mode). In a satellite day, the mean DFE value is almost as same as in the night, but the fluctuation is typically doubled owing to the optical light leakage, and worsen when the bright Earth edge is within 25° from the SIS *fov* (~30 ADU at maximum). DFE is also severe during night-day terminators and the passage of SAA. DFE in the FAINT mode can be corrected at the ground data processing by averaging all PHs of corner pixels of an event in a certain time scale (Otani and Dotani 1994). There is no way to correct DFE for the BRIGHT mode and the effect is included in its response matrices.

Residual Dark Distribution (RDD): The zero level still has large scatters after the DEF correction, called "Residual Dark Distribution (RDD)" (Dotani et al. 1997). In a certain probability, charged particles on orbit damage some Si lattice. A CCD pixel holding a damaged lattice always output large charge currents in proportion to number of damaged lattice. The on-orbit frontend processor only stores the averaged zero-level of each 16×16 pixels. The residuals against the average zero-level remain. The RDD effect has been gradually worsen after launch by accumulating radiation damages. Charge currents stored in a pixel in an exposure is in proportion to the exposure time. The effect is still negligible in the 1-CCD mode, but it is significant in the 4-CCD mode data after 1995 (Yamashita 2000). The RDD correction method, which takes zero-level maps of each pixel in a certain interval, have been developed.

3.1.4 Gas Imaging Spectrometer (GIS)

Gas Imaging Spectrometers (GISs) are imaging gas scintillation proportional counters. The process of detecting x-ray photon is illustrated in Figure 3.4. An incident x-ray photon through the entrance window generates a photo electron cloud in the drift region. This cloud drifts to the scintillation region by weak electric fields, and then accelerates by the large voltage gap between the intermediate and ground meshes. In this process, electrons constituting the cloud excite Xe atoms, which emit recombination UV lines ($\lambda \sim 170$ nm). The imaging photo-multiplier tube installed under the gas cell collects these photons and converts anode signals to position data and signals of the last dynode to pulse-height and rise-time data. The drift region is thick enough and thus the quantum efficiency of hard x-rays is high (~100 %), while the entrance window absorbs soft x-rays. A method of rejecting cosmic particle background, using the information of the rise time duration of event signals, was established though onground calibrations. This method rejects ~90% of background events in 2–10 keV band. Among four system modes prepared for GIS operation, observers use the Pulse Height (PH) mode, which assigns the information of the pulse height, event position, rise time, event spread and timing data within 31 bit data length. The nominal bit assign is 10, 8, 8 and 5 bits for pulse height, x axis, y axis and rise time data, respectively. Details of the GIS detector are described in Ohashi et al. (1996) and Makishima et al.

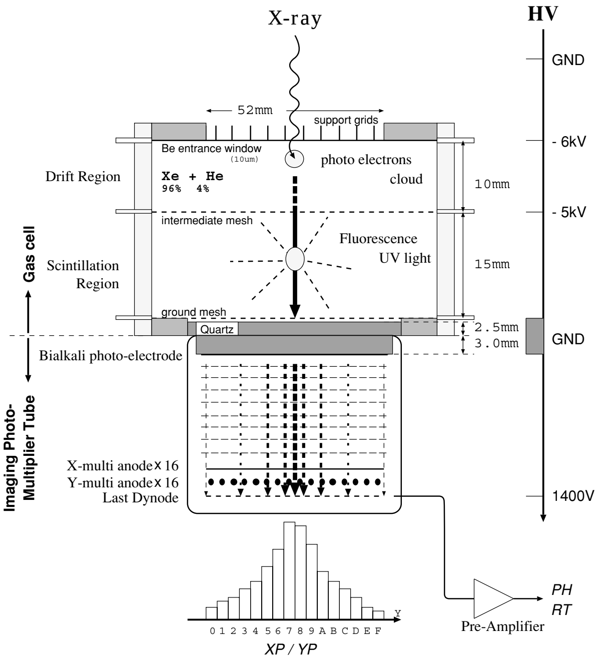

Figure 3.4: Schematic view of the GIS sensor system.

(1996).

GIS background levels occasionally flare up out of the passage of SAA. These phenomena are called "hard-flares" and "soft-flares". They were carefully studied by Ishisaki et al. (1997). Hard-flares occur on the periphery of SAA, probably caused by particles trapped in SAA. These events can be monitored with the H02 parameter including GIS house keeping data. While soft-flares do not accompany an increase of the H02 count. These events frequently occur in the south west to SAA and above Hawaii, probably caused by electrons entered through XRTs.

3.2 The *ROSAT* Satellite

3.2.1 Outline

ROSAT (acronym of Röntgensatellit) is the German x-ray satellite mainly developed by Max-Planck-Institut für extraterrestrische Physik (MPE) and launched into low Earth orbit on June 1990. *ROSAT* has one x-ray telescope (XMA) consisting of four Wolter I mirrors and three detectors, two identical position sensitive proportional counters (PSPC−B, PSPC−C) and one high-resolution imager (HRI). These detectors are switched on and off the focal plane of XMA. The sensitive energy bands of both detectors are between 0.1−2.4 keV, but

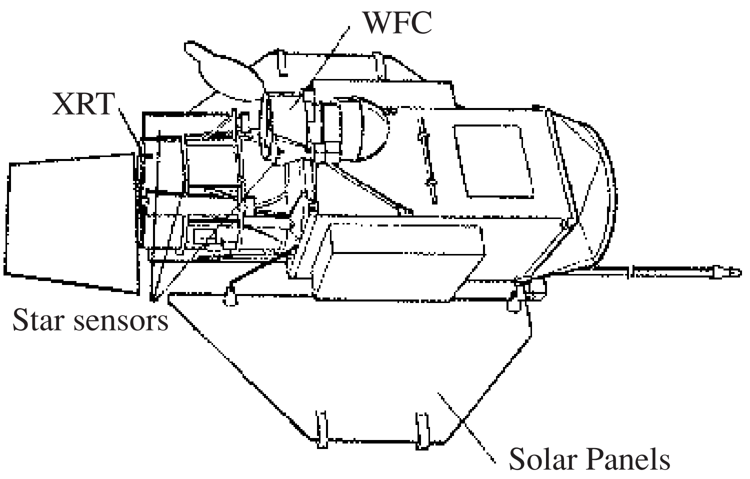

Figure 3.5: Schematic view of the *ROSAT* satellite.

the quantum efficiency between 0.3–0.4 keV is negligible owing to the absorption of window materials. The effective area of PSPC is about three times as large as that of HRI.

3.2.2 X-ray Mirror Assembly (XMA)

XMA is constructed from a zerodur block - a ceramic material - polished up to the ideal Wolter type I geometry. The highly smoothed mirrors focus soft x-rays below 2.4 keV within $2''$ radius circle on-axis. The *psf* however becomes less sharp with increasing off-axis angles. (See the dependence of *HPD* on off-axis angles in page 92 of Briel et al. 1994).

3.2.3 Position Sensitive Proportional Counter (PSPC)

PSPCs are multiwire proportional counters. These detectors provide modest energy resolution (27% FWHM at 1.5 keV) and relative time resolution down to ~130 μsec. The intrinsic spatial resolution is $\sim25''$ in the focal plane at 0.93 keV. At off-axis angles larger than about $20'$, the position resolution is dominated by XMA.

3.2.4 High Resolution Imager (HRI)

HRI comprises two cascaded microchannel plates (MCPs). A channel size of HRI is enough small to map XMA resolved x-ray sources. It has negligible energy resolution but provides relative time resolution down to 60 μsec. HRI has UV bandpass below ~4000Å, caused by enhanced transmission of the UV/ion shield (Zombeck et al. 1997; Berghöfer et al. 1999).

Chapter 4

Observation & Data Reduction

4.1 Target Selection

4.1.1 Data Retrieval

The et al. (1994) compiled a comprehensive catalogue of members and candidate members of HAeBes in previous articles. This catalogue comprises five categories ; i) Be and Ae stars historically recognized as true members or potential candidates of HAeBes, ii) Fe and emission line stars, iii) extreme emission line objects, iv) early type peculiar emission line stars listed by Allen and Swings (1976) and Dong and Hu (1991), v) non-emission line objects including β Pic and Vega type stars and vi) stars rejected as HAeBe candidates. We adopted i), ii) and v) as our HAeBe samples. The reason for adopting the categories ii) and v) is that these sources will fill the gap between HAeBes and TTSs or MSs. Whereas we did not adopt the categories iii) and iv). These members seem to be mainly on the Galactic plane and might be other types of stars such as classical Be stars or white dwarfs. In addition to i), ii) and v), we adopted few more samples from a few publications, which is lately recognized as HAeBes (Preibisch 1999; van den Ancker et al. 1997; van den Ancker et al. 1998).

In the *ASCA* guest observing programs (Announce of Opportunity: AO 1–7), we have observed several HAeBes, MWC 297, MWC 1080, V892 Tau and HAeBes in the R CrA cloud. For the other HAeBes observed with *ASCA*, we picked up the data from the *ASCA* archive - DARTS database provided by ISAS and W3 database by HEASARC. The observed HAeBes are shown in Table 4.1 and their observation logs are in Table 4.2, 4.3. On the other hand, we added the Monoceros R2 GMC (see also the section 8.2). Its log is listed in the same table of HAeBes.

4.1.2 Quantities of Fundamental Stellar Parameters

The fundamental parameters of HAeBes could have some uncertainties. Effective temperature of a HAeBe is measured from the blackbody component of the stellar core, but it is usually merged with disk and envelope components or contaminating lights from associating reflection nebula. The temperature therefore, especially on embedded sources, can have large uncertainties. Whereas the bolometric luminosity has another uncertain factor, distance. Almost all HAeBes are more than a hundred parsec away from the sun. Ground based telescopes do not have an accuracy to measure the distance from trigonometric parallax. Distances to most HAeBes are thus estimated from those of associating MS stars or clouds, but it is almost no way to prove the relationship between HAeBes and these objects. Some HAeBes have large uncertainties for distance in a factor to order (eg V921 Sco, see the subsection 5.1.8). The astrometry satellite *HIPPARCOS* launched in 1989 had an ability to measure the absolute sky coordinate of all stars with an accuracy of 2 milli-arcsec (Perryman et al. 1992; Walter and Sovers 2000). From the measurement of trigonometric parallax of the orbital diameter of the earth, *HIPPARCOS* can measure stellar distance up to $\sim$ 400 pc. We thus first rely on the results using the *HIPPARCOS* data (van den Ancker et al. 1997; van den Ancker et al. 1998; Bertout et al. 1999) and, if there is no information, refer to the latest articles.

Visible lights and X-rays are attenuated by the Interstellar medium (ISM) through different processes. Visible lights are absorbed or scattered by interstellar dusts. The extinction is basically continuous and prominent in short wave-lengths although some molecules make line absorptions. Degree of extinction is described with the attenuation ratio in V band ($A_{\rm V}$). Whereas x-ray lights are absorbed by photo-ionization with heavy elements such as carbon and oxygen (Morrison and McCammon 1983). The extinction is also continuous and effective in soft X-rays, ie long wave-lengths, and it also has sharp absorption edges at ionization energies of each absorbing element. Degree of extinction is described with the column density of hydrogen ($N_{\rm H}$), usually assuming solar values for chemical abundances. The relation between $A_{\rm V}$ and $N_{\rm H}$ depends on the ratio and size distribution of dust grains. A few authors derived empirical relations of these parameters, using optical and x-ray observations. We adopt the formula provided by Ryter (1996); $N_{\rm H} = 2.2 \times 10^{21}\ A_{\rm V}\ {\rm cm}^{-2}$.

In this article, we also show the physical parameters of HAeBes in Table 4.1. All parameters are referred to articles chosen by the above mentioned procedure. $T_{\rm eff}$ of some HAeBes is estimated from the spectral type (Tokunaga 2000).

Table 4.1: Stellar parameters of the observed Herbig Ae/Be stars

Object	R.A. (2000)			Dec. (2000)			d	Ref.	G	Sp. T	log T_{eff}	log L_{bol}	A_{V}	Bin.
	h	m	s	°	′	″	(pc)				(K)	($L_{\odot}$)		
BD+30 549	3	29	19.8	31	24	57	350	a		B8	4.08	$1.1^{\dagger1}$	1.9	
V892 Tau	4	18	40.6	28	19	17	160	i	II	A6	–	–	4.1	vis.
CoKu Tau 1	4	18	51.5	28	20	28	160	ii		M2	(3.55)	–	2.1	vis.
AB Aur	4	55	45.8	30	33	4	144	i	I	A0s	3.98	1.7	0.5	
IX Ori	5	34	40.8	−5	22	43	$460^{\dagger2}$	ii		K	–	–	0.5	
V372 Ori	5	34	47.0	−5	34	15	$460^{\dagger2}$	v		B9.5+A0.5	3.93	2.2	0.5	
YZ Ori	5	34	54.0	−5	3	30	$460^{\dagger2}$	ii		K5	3.64	0.0	0.2	
HD 36939	5	34	55.3	−5	30	22	$460^{\dagger2}$	v		B8-9	4.05	1.9	0.5	
HD245185	5	35	9.6	10	1	52	400	i		A2	3.96	1.3	0.1	
LP Ori	5	35	9.8	−5	27	53	$460^{\dagger2}$	v		B2	4.29	3.1	0.7	
MR Ori	5	35	17.0	−5	21	46	$460^{\dagger2}$	v		A2	3.93	1.9	1.6	
V361 Ori	5	35	31.4	−5	25	16	$460^{\dagger2}$	v		B1.5/B4	4.14	2.6	0.4	
T Ori	5	35	50.0	−5	28	42	460	i	I	A3	3.93	1.6	1.1	
V380 Ori	5	36	25.4	−6	42	58	460	i	I	B9-A0	3.97	$2^{\dagger3}$	1.4	IR
BF Ori	5	37	13.3	−6	35	1	430	i	I	A5-6	3.90	0.1	0.3	
MWC120	5	41	2.3	−2	43	1	500	i		A2p	3.95	1.3	0.03	
VY Mon	6	31	7.0	10	26	5	800	i		O9−B8	4.05	2.9	7.4	
VY Mon G2	6	31	8.2	10	26	1	800	v		A0s	(3.99)	4.0	1.6	
V590 Mon	6	40	41.3	9	48	1	800	i		B7	4.09	2.6	0.6	
LkHα 218	7	2	42.3	−11	26	10	1150	i	I	B9	4.03	2.1	1.5	
Z CMa	7	3	43.2	−11	33	6	1150	i		F6	3.80	3.4	2.8	IR
LkHα 220	7	4	5.4	−11	26	0	1150	i		B5	4.19	2.4	–	
HD76534	8	55	8.7	−43	28	0	830	i		B2n	4.34	3.9	1.2	
HD97048	11	8	3.3	−77	39	17	180	i	I	B9-A0ps	4.00	1.6	1.2	
HD97300	11	9	50.0	−76	36	48	188	v		B9	(4.03)	1.5	1.3	
T Cha	11	57	13.5	−79	21	32	66	ii		G2	3.77	0.1	1.6	
HD104237	12	0	5.1	−78	11	35	116	i		A4s	3.93	1.6	0.3	
IRAS12496	12	53	16.1	−77	7	2	200	i		A-F	(3.91)	1.7	12	
HR5999	16	8	34.3	−39	6	18	210	i		A5-7s	3.90	1.9	0.5	
HR6000	16	8	34.6	−39	5	34	241	a		B6	4.15	2.5	0.3	spec.
HD147889	16	25	24.3	−24	27	57	140	a		B2	4.34	3.3	3.3	
Hen 3−1191	16	27	14.2	−48	39	28	–	i		B0	–	–	–	
V921 Sco	16	59	6.9	−42	42	8	500	i	I	B4-5	(4.14)	3.0	7.1	
MWC297	18	27	39.6	−3	49	52	250	i	I	B1.5	(4.38)	4.5	8	
EC95	18	29	57.9	1	12	47	310	p		K0-K4	(3.65)	1.8	36	
S CrA	19	1	8.5	−36	57	20	130	ii		K6	(3.62)	−0.1	2.8	
HD176386	19	1	38.9	−36	53	27	122	v		B9	4.03	1.7	0.6	
TY CrA	19	1	40.8	−36	52	34	130	i	II	B7-9	(4.07)	1.8	1.0	
R CrA	19	1	53.7	−36	57	8	130	i	II	B8	(4.06)	2.1	1.9	spec.
T CrA	19	1	59.0	−36	58	0	130	ii	II	F0	(3.86)	0.9	1.7	
HD200775	21	1	36.9	68	9	48	429	i	I	B2.5	4.31	3.9	1.9	
MWC1080	23	17	26.1	60	50	43	2200	i	I	A0-3	(3.96)	3.9	4.4	vis.

Ref.: References [i/ii/v – listed in Table 1/2/5 in The et al. (1994), a – van den Ancker et al. (1997) or van den Ancker et al. (1998), p – Preibisch (1998)]. G: HAeBe Group defined by Hillenbrand et al. (1992), Sp.T: Spectral type [p: peculiar, s: shell-type], Bin.: binary [spec.: spectroscopic, vis.: visual, IR: infrared], Values in parenthesis is typical values of the spectral type and group. ^{†1}calculated from van den Ancker et al. (1998) assuming $d \sim$350 pc. ^{†2}distance to the Ori OB1 association ^{†3}intermettent value of Hillenbrand et al. (1992).

Table 4.2: *ASCA* observation log

Obs. ID	Abbr.	Seq. ID	Obs. Time									Mod. Value			
			Start Time						On Time			SIS		GIS	
			Date			Time						R.A.	Dec.	R.A.	Dec.
			y	m	d	h	m	s	h	m	s	(°)	(°)	(°)	(°)
SVS13	SVS13	23021000	95	8	30	13	28	11	58	37	20	–0.473	0.107	–0.186	–0.001
IC359	IC359	23009000	95	9	2	0	8	11	29	3	28	–0.055	0.163	0.239	0.026
SU Aur	SU Aur	23042000	95	2	25	4	43	23	31	48	16	0.750	–0.097	0.703	–0.080
ORION TRAPEZIUM	Ori Trap1	20004000	93	8	30	23	9	39	14	16	0	0.561	0.097	0.809	–0.128
TRAPEZIUM_I	Ori Trap2	25032000	97	9	23	17	0	11	27	10	56	–0.104	0.184	0.111	–0.006
TRAPEZIUM_II	Ori Trap3	25032010	97	9	30	13	3	21	30	37	52	–0.333	0.217	–0.128	0.041
TRAP_2_S1	Ori Trap4	25032020	98	9	20	5	41	12	31	34	40	–0.008	0.167	0.240	0.006
IOTA_ORIONIS_1	Iota Ori1	25035000	97	9	21	23	37	39	41	23	12	–0.049	0.169	0.189	0.000
IOTA_ORIONIS_2	Iota Ori2	25036000	97	10	6	21	4	23	20	16	32	–0.702	0.292	–0.520	0.134
L1641 NORTH	L1641N	21005000	94	3	13	23	6	38	27	4	32	–0.017	–0.153	–0.063	–0.133
LAMBDA ORI	Lamb Ori	21025000	94	3	12	3	56	3	14	14	56	0.220	–0.157	0.177	–0.135
Ori OB1B-3	Ori OB1	23019000	95	10	4	18	1	6	22	10	40	–0.789	0.279	–0.605	0.132
PSRJ0631+10	PSRJ0631	26007000	98	10	16	23	40	32	43	40	32	–0.778	0.332	–0.602	0.172
15 Mon	15 Mon	25015000	97	10	18	13	36	20	26	54	22	–0.721	0.363	–0.553	0.192
Z CMa	Z CMa	23014000	95	3	31	20	34	29	22	6	24	0.309	–0.295	0.278	–0.259
VELA SHRAPNEL BS	Vela Shrap	55030000	97	5	9	16	32	11	10	59	12	0.424	–0.259	0.378	–0.226
CHAMELEON_I_1	ChamI I	21009000	94	5	14	5	15	26	10	54	56	4.499	0.273	4.325	0.279
CHAMELEON_I_2	ChamI II	21009010	94	5	14	16	8	14	16	2	30	4.432	0.248	4.251	0.254
CHAMELEON_I_3	ChamI III	21009020	94	5	15	8	11	26	12	58	40	4.661	0.230	4.475	0.237
CHAMELEON_I_4	ChamI IV	21009030	94	5	15	21	10	5	12	25	4	4.609	0.208	4.417	0.215
CHAIBROWNDWARF	ChamI V	27017000	99	8	7	4	15	28	71	55	44	–0.045	–0.436	–0.017	–0.390
CHAMELEON_III	ChamIII	27002000	99	3	8	20	0	10	44	9	36	0.802	0.313	0.081	0.074
HD104237	HD104237	23003000	95	4	3	10	44	43	18	45	52	0.860	0.689	0.750	0.651
CHAMELEONII	ChamII	24000000	96	3	10	16	4	7	19	11	28	0.297	0.304	0.025	0.035
LUPUS3	Lupus3	24008000	96	2	22	21	33	47	27	6	40	0.369	0.086	0.620	–0.160
RHO-OPHIUCHI	Rho-Oph	20015010	93	8	20	2	19	34	20	26	40	0.481	–0.221	0.440	–0.194
GALACTIC RIDGE 10-7	Gal R 1	55003060	97	9	3	20	19	44	8	51	44	0.200	–0.146	0.131	–0.128
GAL_RIDGE1_3	Gal R 2	54004020	96	8	31	23	21	42	7	39	12	0.622	–0.148	0.566	–0.127
GAL_RIDGE1_4	Gal R 3	54004030	96	9	1	7	0	50	8	30	24	0.658	–0.147	0.602	–0.126
MWC297_N1	MWC297 1	21007000	94	4	8	0	2	0	13	51	12	–0.295	0.174	–0.068	0.021
MWC297_N2	MWC297 2	21007010	94	4	12	3	31	3	6	55	12	–0.585	0.180	–0.374	0.043
MWC297_N3	MWC297 3	21007020	94	4	12	23	53	26	12	37	20	–0.568	0.180	–0.355	0.042
SERPENS	Serp	25021000	97	4	13	23	47	14	68	23	23	–0.698†	0.165†	–0.489†	0.039†
R CrA1	R CrA 1	21001000	94	4	4	4	55	35	25	5	37	0.117	0.158	0.404	–0.037
R CrA2	R CrA 2	21002000	94	4	8	23	56	6	27	4	17	–0.139	0.184	0.129	–0.004
R CrA3	R CrA 3	24016000	96	4	5	1	39	40	44	30	9	0.192	0.150	0.481	–0.049
R CrA4	R CrA 4	24016010	96	10	18	3	25	59	8	33	20	–0.034	–0.155	–0.092	–0.136
R CrA5	R CrA 5	66017000	98	4	19	2	21	23	15	59	28	–1.195	0.057	–0.936	–0.034
R CrA6	R CrA 6	26018000	98	10	19	13	36	48	30	4	16	0.039	–0.150	–0.022	–0.137
HD200775	HD200775	23029000	95	11	17	0	48	22	30	33	4	2.126	0.001	2.015	0.014
MWC1080	MWC1080	21006000	93	12	8	6	3	34	23	52	32	2.566	0.211	2.488	0.222
Monoceros R2	Mon R2	25019000	97	3	9	6	27	31	57	23	44	0.627	–0.155	0.587	–0.133

Obs. ID: Observation ID, Abbr.: Abbreviation of Obs. ID, Seq. ID: Sequence ID, On time: On source time, Mod value: Modified value of an image coordinates presented by Gotthelf et al. (2000), †: the value in fa970413_2347.2359.

Table 4.3: Observing parameters of both SIS & GIS

Obs. ID	SIS							GIS		Memo
	Chip	Format		LD	RC	TS	Exp.	Mode	Exp.	
		Obs.	Ana.	(keV)			(ksec)		(ksec)	
SVS13	4	F/B	n.u.					PH	93.0	
IC359	4	F/B	B2	0.55	y	n	27.4	PH	37.8	SIS: 0.55–10 keV
SU Aur	2	F/B	B2		n	n	40.8	PH	45.0	
Ori Trap1	4	F/B	B		n	n	19.3	PH	18.0	
Ori Trap2	1	F/B	B				45.3[†1]	PH	8.2	
Ori Trap3	1	F/B	B		n	n	7.9	PH	49.8	
Ori Trap4	1	F/B	B		n	n	40.4	PH	35.9	
Iota Ori1	1	F/B	n.u.					PH	72.5	
Iota Ori2	1	F	n.u.					PH	24.6	
L1641N	4	F/B	n.u.					PH	34.6	
Lamb Ori	2/1	F	B2		n	n	21.8	PH	22.4	
Ori OB1	4	F/B	n.u.					PH	28.6	
PSRJ0631	1	F	n.u.					PH	81.6	GIS: 8-8-8-0-0-7
15 Mon	1	F	B2	0.48	n	n	36.6	PH	36.1	
Z CMa	1	F	B2		n	n	30.5	PH	37.6	
Vela Shrap	2	F	n.u.					PH	12.3	
ChamI I	4	F/B	B		n	y	8.5	PH	15.2	
ChamI II	4	F/B	n.u.					PH	13.9	
ChamI III	4	F/B	n.u.					PH	16.8	
ChamI IV	4	F/B	B2		n	y	12.6	PH	16.4	
ChamI V	2	F	B2		y	n	82.4	PH	75.0	
ChamIII	1	F	B2		n	n	62.5	PH	66.2	
HD104237	1	F	B2		n	n	29.9	PH	27.1	
ChamII	2	F/B	n.u.					PH	24.9	
Lupus3	4	F/B	B2	0.55→0.7	y	y[†2]	18.2	PH	41.3	SIS: 0.8–10 keV
Rho-Oph	4	F/B	n.u.					PH	41.1	
Gal R 1	4	F/B	n.u.					PH	9.7	
Gal R 2	4	F/B	B		y	n	12.2	PH	11.8	
Gal R 3	4	F/B	n.u.					PH	8.6	
MWC297 1	1	F	B2		n	n	10.5	PH	10.3	
MWC297 2	1	F	B2		n	n	5.3	PH	5.0	
MWC297 3	1	F	B2		n	n	12.9	PH	12.3	
Serp	4/2[†3]	F	B2	a	y	y	87.4	PH	89.9	SIS: 0.8–10 keV
R CrA 1	4	F/B	B		n	n	38.4	PH	39.4	
R CrA 2	4	F/B	B		n	n	35.5	PH	36.9	
R CrA 3	1	F	B2		n	n	65.2	PH	48.8	
R CrA 4	1	F	B2		n	n	10.6	PH	11.7	
R CrA 5	1	F	B2		n	n	17.1	PH	16.2	
R CrA 6	1	F	B2		n	n	31.5	PH	34.1	
HD200775	1	F	B2	0.45/0.55	n	n	46.0	PH	48.7	SIS: 0.55–10 keV
MWC1080	1	F	B2		n	n	36.1	PH	38.4	
Mon R2	4/2	F	B2	b	y	y	62.5	PH	70.6	

Chip: Chip mode, Format: SIS data format (Obs: observation, Ana: analysis, F: Faint, B: Bright, B2: Bright2, n.u.: not used), LD: Level Discri (a: s0[0.48→0.7], s1[0.55→0.69], b: 0.55→0.70/1.10), RC: RDD correction, TS: Telemetry Saturation, Exp.: Average exposure time, Mode: GIS mode, "subject1 / subject2" means "bit High / bit Medium & Low", [†1]Using an archived image, see Table 4.9, [†2]See Table 4.9. [†3]non-standard chips

Table 4.4: Calibration files used for the RDD correction

Obs. ID	Det.	Temp. °C	Chip	Used RDD map C0	C1	C2	C3
Serp	s0	−60.9	4	rdd9704_s0c0m4_t61_62	rdd9704_s0c1m4_t60_61	rdd9704_s0c2m4_t60_61	rdd9704_s0c3m4_t60_61
			2	rdd9702_s0c0m2_t61_62			rdd9702_s0c3m2_t61_62
	s1	−60.2	4	rdd9703_s1c0m4_t61_62	rdd9703_s1c1m4_t61_62	rdd9703_s1c2m4_t61_62	rdd9703_s1c3m4_t61_62
			2		rdd9702_s1c1m2_t60_61	rdd9702_s1c2m2_t60_61	
Gal R2	s0	−61.6	4	rdd9609_s0c0m4_t61_62	rdd9609_s0c1m4_t61_62	rdd9609_s0c2m4_t61_62	rdd9609_s0c3m4_t61_62
	s1	−61.6	4	rdd9609_s1c0m4_t61_62	rdd9609_s1c1m4_t61_62	rdd9609_s1c2m4_t61_62	rdd9609_s1c3m4_t61_62
HD200775†	s0	−61.3	2	rdd9511_s0c0m2_t60_61	rdd9511_s0c1m2_t60_61		
	s1	−60.9	2			rdd9511_s1c2m2_t0_60	rdd9511_s1c3m2_t0_60
ChamI V	s0	−61.6	2		rdd9908_s0c1m2_t61_62	rdd9908_s0c2m2_t61_62	
	s1	−61.4	2	rdd9908_s1c0m2_t61_62			rdd9908_s1c3m2_t61_62
Lupus3	s0	−61.4	4	rdd9603_s0c0m4_t61_62	rdd9603_s0c1m4_t61_62	rdd9603_s0c2m4_t61_62	rdd9603_s0c3m4_t61_62
	s1	−61.1	4	rdd9603_s1c0m4_t61_62	rdd9603_s1c1m4_t61_62	rdd9603_s1c2m4_t61_62	rdd9603_s1c3m4_t61_62
IC359	s0	−61.0	4	rdd9509_s0c0m4_t61_62	rdd9509_s0c1m4_t61_62	rdd9509_s0c2m4_t61_62	rdd9509_s0c3m4_t61_62
	s1	−60.5	4	rdd9509_s1c0m4_t61_62	rdd9509_s1c1m4_t61_62	rdd9509_s1c2m4_t61_62	rdd9509_s1c3m4_t61_62
Mon R2	s0	−60.2	4	rdd9703_s0c0m4_t61_62	rdd9703_s0c1m4_t61_62	rdd9703_s0c2m4_t61_62	rdd9703_s0c3m4_t61_62
			2	rdd9703_s0c0m2_t61_62	rdd9703_s0c1m2_t61_62	rdd9703_s0c2m2_t61_62	rdd9703_s0c3m2_t61_62
	s1	−59.6	4	rdd9703_s1c0m4_t61_62	rdd9703_s1c1m4_t61_62	rdd9703_s1c2m4_t61_62	rdd9703_s1c3m4_t61_62
			2	rdd9703_s1c0m2_t60_61		rdd9703_s1c2m2_t61_62	rdd9703_s1c3m2_t61_62

Det.: Detector, Temp.: CCD temperature, File names of maps are [map name].fits., †: RDD correction is not performed. See Table 4.9.

4.2 Reduction & Screening Methods of the *ASCA* Data

We used the *ASCA* archival data processed through the method, "revision2"[1]. All the observed quantities such as the arriving time, coordinate and pulse height of each event are listed in rev2 files. We thus did not perform further data processing before event selection unless the RDD correction is required. We processed events selection with the software package FTOOLS 4.2.

4.2.1 RDD Correction

We dealt with the RDD correction for SIS data taken after 1995 in 2 and 4 CCD FAINT mode, using the software package "correctrdd" (see the section 3.1.3). A pixel-height distribution on a RDD map depends on both observing date and CCD temperature, but RDD maps in some condition was not taken owing to the operational constraints. We thus searched for RDD maps taken under the same CCD temperature within 2 months before and after an observation, and if no RDD map exists, we used RDD maps taken under different CCD temperature. Used RDD maps are shown in Table 4.4.

For the RDD corrected data, we dealt with the DFE correction using "correctdfe" and then converted the data format to BRIGHT or BRIGHT2 modes using the softwares "f2b" or "f2b2" respectively, which simultaneously process the ECHO correction. These procedures are automatically done with the script "gordd.alpha" provided by GSFC.

4.2.2 Filtering Criteria

We referred selection criteria to the *ASCA* Data Reduction guide (*ASCA* ABC guide, Arida and ASCA team 2000) and applied the most lax values. We confirmed that our loose selection criteria do not affect the data quality, by investigating background levels in different cutoff energy. The criteria are listed in Table 4.5

4.2.3 Telemetry Saturated Data

Because dummy events from hot pixels increase in high CCD temperature ($T > -60°C$), we sometimes have to take telemetry saturation into account for SIS data These events have low PH and therefore can be rejected by the level discrimination in DP at the expense of low-energy photons during the observation. The *ASCA* calibration team set up the standard

---

[1] Revision2, or rev2 in short, is an improved analyzing method which do away with a lot of raw files made by observing mode changes and arrange in a few unfiltered event files for each observing mode. See ASCA Getting Started Guide (Pier and ASCA Processing Team) in detail

Table 4.5: Data selection criteria

	Unit	SIS	GIS
SAA		ex.	ex.
COE	[GeV]	4/6	4/6
SIS(GIS)_RBMF		ex.	ex.
T_SAA & T_DY_NT	[readout cycle]	4/inc.	inc.
SFR & HFR		inc.	ex./inc.
ELV	[degree]	5	5
BR_EARTH	[degree]	20	inc.
ANG_DIST	[degree]	0.01/inc.	0.01/inc.

Right values are criteria of R CrA 1–6, MWC 297 1–3, Serp and Mon R2
SAA: SAA passage, COE: Minimum of cutoff energy, SIS(GIS)_RBMF: SIS(GIS) radiation belt monitor flag, T_SAA(DY_NT): Time after passing through SAA (the day-night terminator), SFR: Soft flare region (G2_H0+G2_H2+G3_H0+G3_H2<45 & RBM_CONT<100), HFR: Hard flare region ($\mathrm{G2\_H0+G2\_H2+G3\_H0+G3\_H2}<0.45\times\mathrm{COR}^2-13\times\mathrm{COR}+125$) ELV: Elevation from the rim of the earth, BR_EARTH: Elevation from the bright earth, ANG_DIST: Maximum of angular distribution, ex.: excluding, inc.: including

discrimination level and *ASCA* duty scientists at KSC monitors telemetry saturation at *ASCA* contact passes, but some data cannot avoid being telemetry saturated. When the telemetry saturation occurs, events on the far side from readout gates are first discarded (see the section 3.1.1). We thus investigated whether events on a source position were discard or not, and only if these events were discarded, we removed telemetry saturated CCD frames.

4.2.4 Event Extraction

We removed SIS events associated with 'hot' and 'flickering' pixels using "sisclean" and then picked up all events of the *ASCA* grade 0234. We collected GIS events satisfying the normal criteria using "gisclean" (Ohashi et al. 1996).

4.3 Basic Procedure of Data Analyses

Event data are reduced to image, spectrum and light curve data with XSELECT. Further analyses are based on the XANADU software package provided by GSFC. This package comprises three tasks, XIMAGE for image analysis, XSPEC for spectral analysis and XRONOS for timing analysis. We used XIMAGE ver. 2.53, XSPEC ver. 9.0 and XRONOS ver. 4.02.

Table 4.6: *ROSAT* observation log

Target	Seq. ID	Obs. Time							Det.
		Start time						Exp.	
		y	m	d	h	m	s	sec	
CoKu Tau 1	RP200001A01	91	8	20	23	30	52	25,591	P
HD245185	RH202047N00	95	3	16	13	07	53	9,380	H
V380 Ori	RH900010A00	91	3	22	5	57	39	11,037	H
BF Ori	RH900010A01	92	3	14	2	24	42	4,835	H
MWC120	RP900189N00	91	9	19	20	05	57	24,154	P
VY Mon	RP900355N00	92	10	6	13	14	2	5,564	P
	RP900355A01	93	3	14	1	34	50	4,598	P
	RP900355A02	93	9	16	22	43	30	5,354	P
	RP900355A03	94	3	29	23	8	27	5,117	P
V590 Mon	RH200130A00	91	3	20	5	43	32	19,567	H
LkHa218	RP201011N00	93	4	22	17	38	19	19,665	P
LkHa220	RH202153N00	96	4	6	15	42	06	33,495	H
MWC 297	RH202048N00	95	9	28	21	28	37	1,089	H
HD200775	RH202319N00	97	8	11	19	51	22	4,799	H

Det.: P−PSPC, H−HRI,

This package is convenient in performing standard analyses but less flexible especially on image analyses. We then utilized the Display45 software package (ver. 1.90), which was originally developed by PEP4/SLAC group and optimized for *ASCA* data analyses by *ASCA* team members (Ishisaki et al. 1997).

4.3.1 Imaging Analysis

For each observation, we made whole x-ray band images of both SIS and GIS in the J2000 coordinate system (SIS: 0.5–10 keV, GIS: 0.8–10 keV). XSELECT automatically cuts off outer rim of GIS images in the sky coordinate, but some HAeBes are located on this outer rim. In this case, we analyzed GIS data using Display45. Gotthelf (1996) estimated position accuracy on SIS images at $\sim 40''$ (see the subsection 3.1.1). Gotthelf et al. (2000) found a systematic modulation of the *ASCA* absolute attitude by referencing AGNs, which depends on temperature of supports of the star trackers. New method reduces the position uncertainty to $\sim 12''$ for SIS. We used this latest method for all the imaging analyses.

We searched for an X-ray source above 5σ detection level around a optical position of a HAeBe. We simultaneously made use of *ROSAT* images for source identification because low mass stars are usually present around HAeBes. We first referred *ROSAT* images to Zinnecker and Preibisch (1994) and Preibisch (1998). For HAeBes not in these lists, we retrieved processed *ROSAT* images from HEASARC (rationalized data format: RDF, see Table 4.7). For HRI, there is only one total band image, while for PSPC there are three images energy-sliced in the total (im1), hard (im2) and soft band (im3). We basically used total band images.

For non-detected HAeBes, we determined upper-limit fluxes. We measured source

Table 4.7: RDF parameters of the *ROSAT* data

		PI		Energy	
		Low (ch)	High (ch)	Low (eV)	High (eV)
PSPC					
Total	(im1)	11	235	110	2360
Hard	(im2)	52	201	520	2020
Soft	(im3)	11	41	110	420
HRI					
Total	(im1)	1	16		

upper-limit counts in 99% confidence levels (3σ) from $20''$ half box for SIS and $40''$ half box for GIS, by taking background regions from a nearby source free region, using sosta package in XIMAGE. This upper-limit counts were converted to flux upper-limit assuming an absorbed thin-thermal model $kT = 1$ keV, abundance = 0.3 $Z_{\odot}$ and $N_{\rm H}$ estimated from $A_{\rm V}$. The assumption of plasma temperature, however, does not strongly affect the results because source flux is less dependent on plasma temperature (less than factor of two for typical temperature, $kT \sim 0.5-4$ keV, see Table 4.8). We also saw $L_{\rm X}$ values derived from *ROSAT* results in other articles and, if there is no article, estimate $L_{\rm X}$ from the *ROSAT* archival images with the ximage package. The method is basically the same as the method for the *ASCA* data, but the background level is estimated from surrounding regions ($12'$ $\times 12'$) with the 'background' command.

For detected sources, we normally took wider source regions with $2.5'$ or $3'$ radius circles for timing and spectral analyses (see Table 5.3). We selected background regions from nearby source free region or, when contaminating sources are present, a symmetrical region with respect to the contaminating sources.

4.3.2 Timing Analysis

We made source light curves for each detector by subtracting normalized background light curves using the "lcmath" package. We then merged light curves of same type of detectors, but we separately analyzed light curves of different types of detectors to avoid artificial gaps caused by the different time selection. All light curves were basically made in the whole energy band. Default minimum time bin is 2048s, but it is longer for weak sources. We tested time variability by the χ^2-test method.

Table 4.8: Flux converting ratio from the *ROSAT* and *Einstein* band to the *ASCA* band

kT	*ROSAT*			*Einstein*		
(keV)	0.5–10	2–10	4–10	0.5–10	2–10	4–10
0.5	0.69	0.010	0.00015	0.75	0.011	0.00016
1.0	0.73	0.087	0.0089	0.78	0.093	0.0095
2.0	0.97	0.36	0.11	0.90	0.33	0.10
5.0	1.57	0.95	0.52	1.32	0.80	0.43

Values are ratio of *ASCA* flux from a unit ROSAT (0.1–2.4 keV) or *Einstein* flux (0.16–3.5 keV).

4.3.3 Spectral Analysis

Spectral fittings were basically performed in 0.5–10 keV for SIS and 0.8–10 keV for GIS. Response matrix generators were made with "ascaarf" (ver. 2.81), sisrmg (ver. 1.1) for SIS. Whereas, standard GIS response matrices are used for GIS[2]. As for a plasma model, we adopt an absorbed thin-thermal plasma model because some sources clearly showed line features in their spectra. We used the MeKaL plasma code, which well treats fine structures of Fe−L lines (Mewe et al. 1995, see also Matsumoto 1998 Appendix B). Chemical abundances in the MeKaL model was fixed to $0.3Z_\odot$ because there are not enough photons to determine the chemical abundances. The stellar x-ray spectra taken by *ASCA* show low chemical abundance around 0.3 $Z_\odot$ (eg OB stars Kitamoto and Mukai 1996; Kitamoto et al. 2000; low mass MSs Tagliaferri et al. 1997; low mass PMSs Yamauchi et al. 1996; Kamata et al. 1997; Tsuboi et al. 1998). Though the reason is not known, the chemical abundance $0.3Z_\odot$ seems to be the most appropriate value for stellar x-rays. At first, we tried one-temperature thermal model, and when this model is rejected, we retried two-temperature model with common N_H.

SIS event data available through the level discrimination is complicated. Onboard frontend processors simply discard events of center pixel height under a programmed threshold value. Splitting events whose total pulse-heights exceed this values are also discarded. This degrades effective quantum efficiency just above this threshold energy. These effects are taken into account for making SIS response matrices, but the RDD correction makes this problem more complicated. As a criterion, we accepted a 10% error in quantum efficiency and briefly set the lowest fitting energy like this. We made a histogram of a used RDD map and then measured ΔPH including 90% of the total pixels. By approximating that the RDD distribution is symmetrical, we added ΔPH on the PH of level discrimination and determined it as the lower threshold energy.

---

[2] gis[23]v4_0.rmf

Table 4.9: Specific subjects related to observations and analyses

IC 359 ... 95% in the BRIGHT mode were operated during the satellite day. The data taken under this condition is less reliable so that the FAINT data were only analyzed.

L1641N ... GIS3 accidentally outputed the spectral column with only 7bit length. V380 Ori is near the calibration source in GIS3 so that the GIS2 data was only used.

PSRJ0631 ... The rise time bits were not assigned in the GIS event data format, in compensation for the precise determination of event arrival time for pulse detection. The background level is thus higher than that of ordinary observations.

Lupus3 ... The SIS telemetry saturation did not damage the data quality of HR 5999/6000. The BRIGHT mode data taken in the former observation, when the CCD temperature is relatively high, was terribly bad. The BRIGHT data was therefore discarded.

Gal R 2 ... For the first 5 ksec in the satellite-day condition, SIS was operated in the BRIGHT mode. XSELECT reported inconsistency in the OPTICS values for the SIS data.

Serp ... Background levels of both GIS detectors bursted up at 120 ksec. They were detected on the outer side of GIS and did not damage the EC 95 data.

R CrA 1 ... GIS3 outputed wrong PH values in lower 3 bits. The spectral bins were thus summed by 8 channels.

R CrA 4 ... The GIS2 front end processor stopped during the observation and more than half of GIS2 data were lost. A data station on ground failed to contact with *ASCA* at the end of the observation.

HD 200775 ... The observed exposure was shorter than the planned. The RDD correction was not processed because the quantum efficiency improved less than 4%.

Ori Trap2 ... For SIS, XSELECT did not run properly in the process of cleansis. We downloaded the screened event files from HEASARC. Its filtering criteria are thus HEASARC basis.

Ori Trap3 ... The exposure was far shorter than the planned because the down-link from *ASCA* failed by the antenna trouble at KSC.

ChamI IV ... SIS1 was saturated owing to hot CCD temperature ($T_{s1} \sim -59.3$°C) and completely lost the data around HD 97048, but SIS0 managed to keep them.

ChamI V ... Nonstandard CCD chips were used (S0/C1C2, S1/C3C0). The address discrimination of S0C2 for light leakage was mistakenly unset during the former one-thirds of the observation, but it did not affect the data analyses of HD 97048.

Gal 1 ... Stray light from a strong x-ray source covers the whole *fov* of both detectors

SVS13 ... During the former half of the observation, SIS data are saturated.

Chapter 5

Result I – Herbig Ae/Be Stars

This section describes the observing results of *ASCA* detected and non-detected HAeBes, separately in the ascending order of *right ascension*. The data of the imaging, timing and spectral analyses are summarized in Table 5.1, 5.2, 5.4 and 5.5.

5.1 Detected Sources

5.1.1 V892 Tau

V892 Tau, often designated as Elias 3-1, is located in the L1495E dark cloud. The stellar parameters are open to dispute; Strom and Strom (1994) quoted it as a B9 star of $L_{\rm bol}$ ~64.3 $L_\odot$, while Zinnecker and Preibisch (1994) quoted it as an A6e star of $L_{\rm bol}$ ~38 $L_\odot$. It shows an unusual infrared spectral with anomalous 3.43 μm and 3.53 μm features and an 11.2 μm emission peak. (eg Whittet et al. 1984; Hanner et al. 1994). Millimeter interferometry by di Francesco et al. (1997) certified the presence of a circumstellar disk with the mass of ~0.1 $M_\odot$. It has a companion star (Elias I NE) at ~4″ north east from V892 Tau, which would be a WTTS with $L_{\rm bol}$ ~0.3 $L_\odot$ (Skinner et al. 1993; Leinert et al. 1997; Pirzkal et al. 1997). Strom and Strom (1994) first reported the x-ray emission, but the $L_{\rm X}$ value is about twice as large as that estimated by Zinnecker and Preibisch (1994) ($\sim 2\times10^{30}$ ergs s^{-1}) from the same observing data. Zinnecker and Preibisch (1994) also measured the plasma temperature ($kT = 2.3\pm0.4$ keV) and the column density of hydrogen ($N_{\rm H} = 4.8\pm1.1 \times10^{21}$ cm^{-2}).

ASCA detect a strong x-ray source within the error circle of V892 Tau (Figure 5.1). In the SIS image, two other x-ray sources are seen close to V892 Tau. The bright one at ~2′ north-east from V892 Tau is V1023 Tau and the very faint one at 30″ south-east is V410 x-ray 7. V410 x-ray 7 is a reddened M0.5 pre-main-sequence star ($A_{\rm V}$ ~5.9; Briceño et al. 1998) probably belonging to the same nebulousity as V892 Tau, and it showed an x-ray

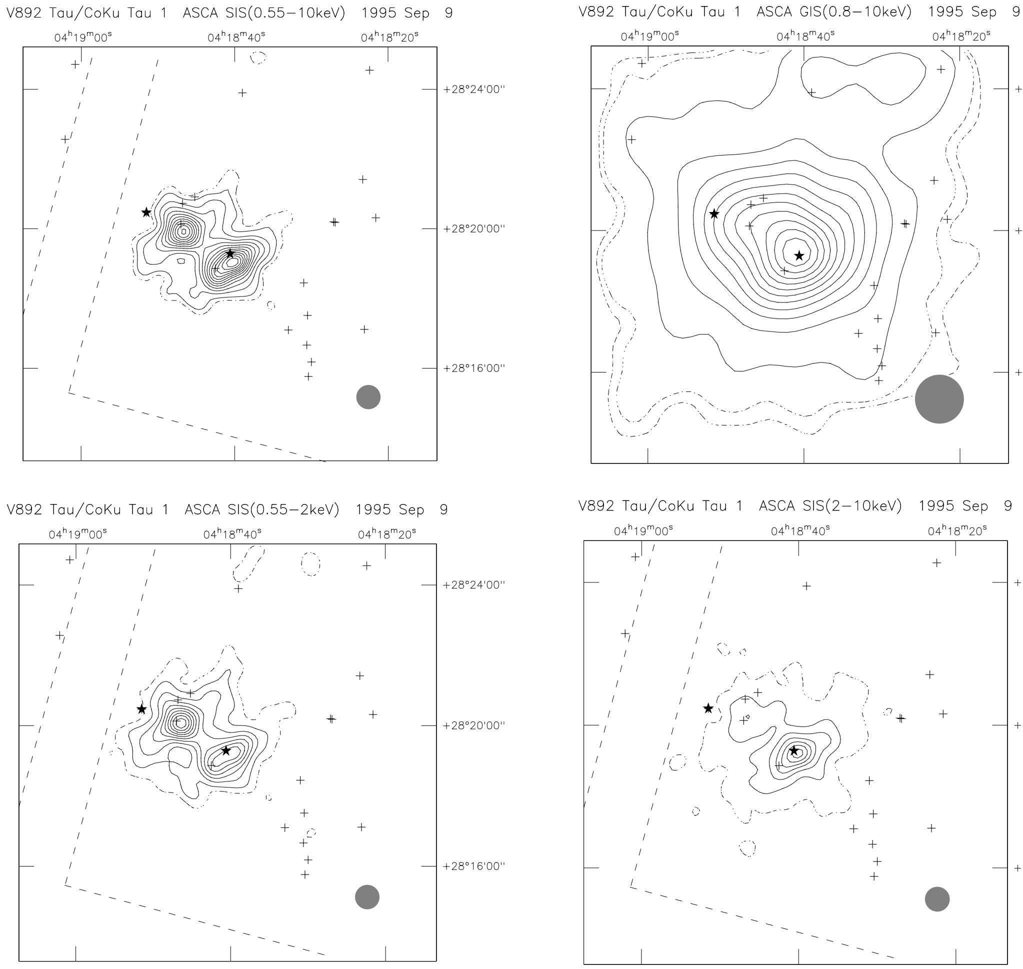
V892 Tau/CoKu Tau 1 ASCA SIS(0.55–10keV) 1995 Sep 9

V892 Tau/CoKu Tau 1 ASCA GIS(0.8–10keV) 1995 Sep 9

V892 Tau/CoKu Tau 1 ASCA SIS(0.55–2keV) 1995 Sep 9

V892 Tau/CoKu Tau 1 ASCA SIS(2–10keV) 1995 Sep 9

Figure 5.1: *ASCA* images of the V892 Tau/ CoKu Tau 1 field ($12' \times 12'$ *fov*: *upper left*: SIS total band, *upper right*: GIS total band, *lower left*: SIS soft band, *lower right*: SIS hard band, See the section 5.2.2 for CoKu Tau 1). These images are drawn with contours of total photon counts and smoothed with a Gaussian function of $\sigma \sim 2$ pixel. Solid-lines represent photon counts per pixel above the background level and are drawn by 0.4 cts/pixel/obs for SIS and 1.0 cts/pixel/obs for GIS. Dot-dash lines represent 5σ (SIS) and 3 & 5σ (GIS) detection levels, which are calculated from the Poisson-distributed photon error of selected background counts (see the table 5.3). Dash-lines in SIS images are CCD chip gaps and that in the GIS images (not in this figure). Star marks are the HAeBe positions (*center*: V892 Tau, *left*: CoKu Tau 1). Plus marks are optical or infrared source positions listed in the SIMBAD database. Each filled circle on the bottom right of each panel shows the typical error circle ($20''$ for SIS, $40''$ for GIS). The coordinate system is J2000.

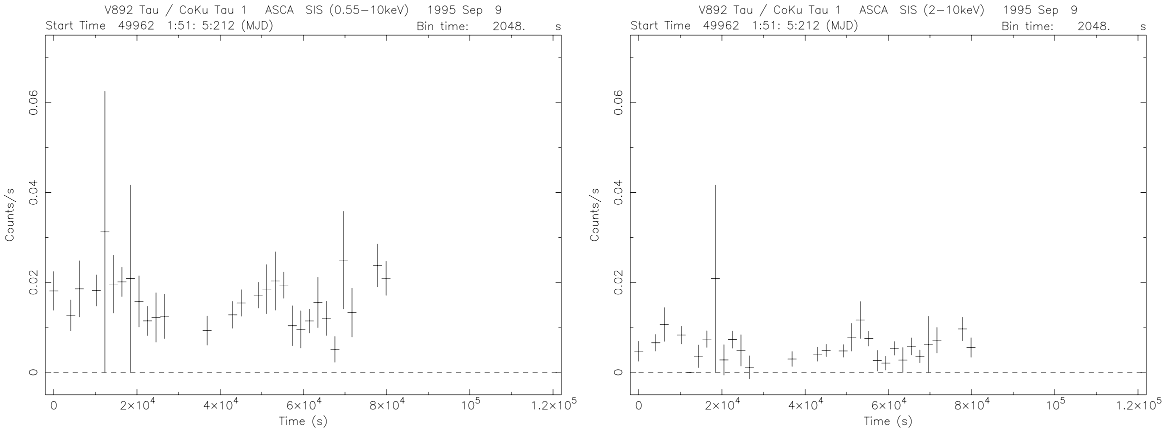

Figure 5.2: *ASCA* SIS light curves of V892 Tau after the background subtraction (*left*: total band, *right*: hard band). Vertical axes are averaged detector count rates and dotted lines are the zero level. 1 bin is 2,048 sec.

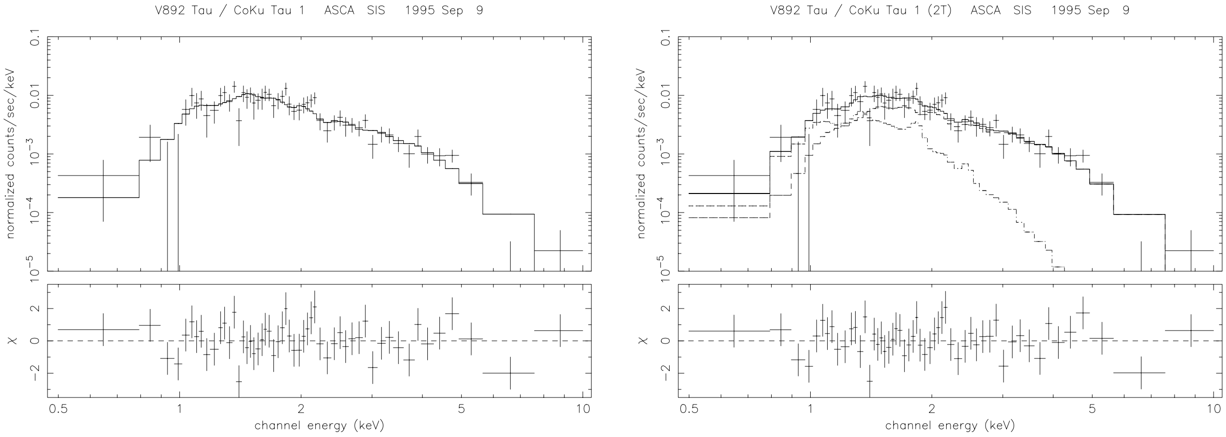

Figure 5.3: SIS spectra of V892 Tau (*left*: 1T component, *right*: 2T components including V410 x-ray 7). In each panel, the best-fit model is drawn with a solid line. Components in the 2T model is drawn with dotted lines. Each residual from the best-fit value is displayed in its lower section.

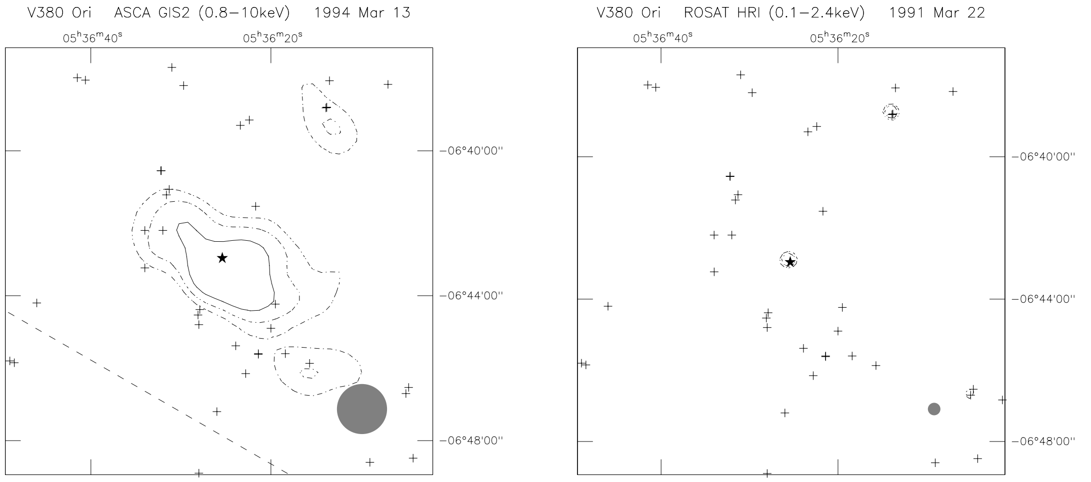

Figure 5.4: *ASCA* GIS (*left*) and *ROSAT* HRI (*right*) images of the V380 Ori field. Details of the *ASCA* image are the same as Figure 5.1, but the count rate per solid line is half (0.2 cts/pixel/obs for SIS and 0.5 cts/pixel/obs for GIS). In the *ROSAT* image, lines and symbols are used in the same manner. The image is smoothed with Gaussian function with $\sigma \sim$ HPD at the source position ($>8''$: binned pixel size). Solid-lines are drawn by 20 counts per 16×16 pixels (0.078cts/pixel). 3 and 5 σ levels are drawn with Dot-dash lines.

flare (Stelzer et al. 2000). Because GIS image cannot separate V1023 Tau from V892 Tau, we only proceed the SIS analyses. The peak of V410 x-ray 7 is obscured in the total band (0.55−10 keV), but it is clearly seen in the soft band (0.55−2 keV).

Figure 5.2 shows light curves of V892 Tau in the total band (0.55−10 keV). The source count rate seems to fluctuate within a factor of two, but it accepts a constant model within 90% confidence level. The spectrum can be reproduced with an absorbed 1T thermal model, but it obviously includes, at least, a component from V410 x-ray 7. The dominant source is V892 Tau in the hard band (2−10 keV, see Figure 5.1), Because the high energy part in the x-ray spectrum determines the plasma temperature, we fix the plasma temperature at the 1T best-fit values by regarding it as the temperature of V892 Tau. In the soft band, the peak counts of V892 Tau is 1.1 times as large as those of V410 x-ray 7. The soft band flux reduces to be half when $N_{\rm H}$ $\sim$1.8$\times$10^{22} cm^{-2}. We thus fix these parameters and add an absorbed 1T component. We then found an acceptable solution of kT. The luminosity of V410 x-ray 7, $L_{\rm X}$ $\sim$5$\times$10^{30} ergs s^{-1} (0.5−10 keV), is half of the *ROSAT* estimate in a quiescent state (Stelzer et al. 2000). We also made light curves in the hard band (2−10 keV) to minimize the contribution of V410 x-ray 7 (<10% from the peak flux). The light curves accept a constant model as well.

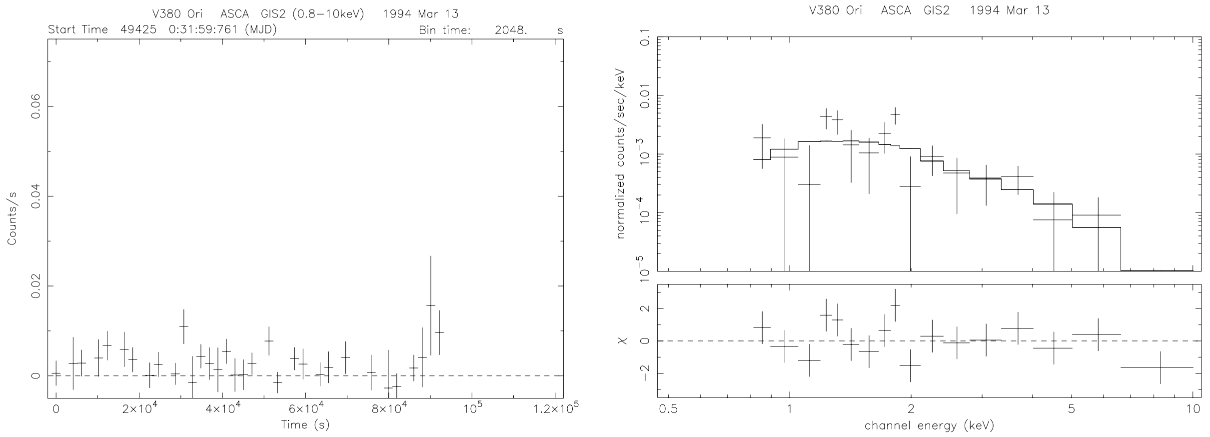

Figure 5.5: GIS light curves (*left*) and spectrum (*right*) of V380 Ori. Details can be seen in Figure 5.2, 5.3

5.1.2 V380 Ori

V380 Ori belongs to the star forming cloud L1641 (eg Strom et al. 1989). From a study of the multi-wave lengths in UV, optical and IR, V380 Ori is thought to be a B9–A0 star of 3.3−3.6 $M_\odot$, showing small amplification variability (Hillenbrand et al. 1992; Boehm and Catala 1995; Rossi et al. 1999; Herbst and Shevchenko 1999). It has a companion star 0.15″ apart from the primary (Corporon and Lagrange 1999). Recent study of V380 Ori is summarized in Rossi et al. (1999). The x-ray emission was detected with *Einstein* ($L_X \sim 1.1\times10^{31}$ ergs s^{-1}, Pravdo and Marshall 1981) and was confirmed with *ROSAT* ($L_X \sim 2.3\times10^{31}$ ergs s^{-1}, Zinnecker and Preibisch 1994). Damiani et al. (1994) evaluated the plasma temperature and absorption column density using the *Einstein* data ($kT \sim 1.1$ keV, $N_H \sim 7.4\times10^{21}$ cm^{-2}).

ASCA detect the x-ray emission from V380 Ori on the edge of GIS *fov* as a relatively faint source (Figure 5.4). There seems to be a small peak on the north tail of V380 Ori. but there is no source in *ROSAT* HRI. Light curves (Figure 5.5) show no apparent variability. In the spectrum (Figure 5.5), the best-fit temperature is relatively high ($kT \sim$3.2 keV), but it has a large error range from 0.65 keV to 11 keV. The luminosity is nearly the same as those of *Einstein* and *ROSAT*.

5.1.3 VY Mon & CoKu VY Mon/G2

Both VY Mon and VY Mon G2 are located at the 85″ south from the reflection nebular IC 446, which is illuminated by the B2.5 star IC 446 No.1 (eg Casey and Harper 1990).

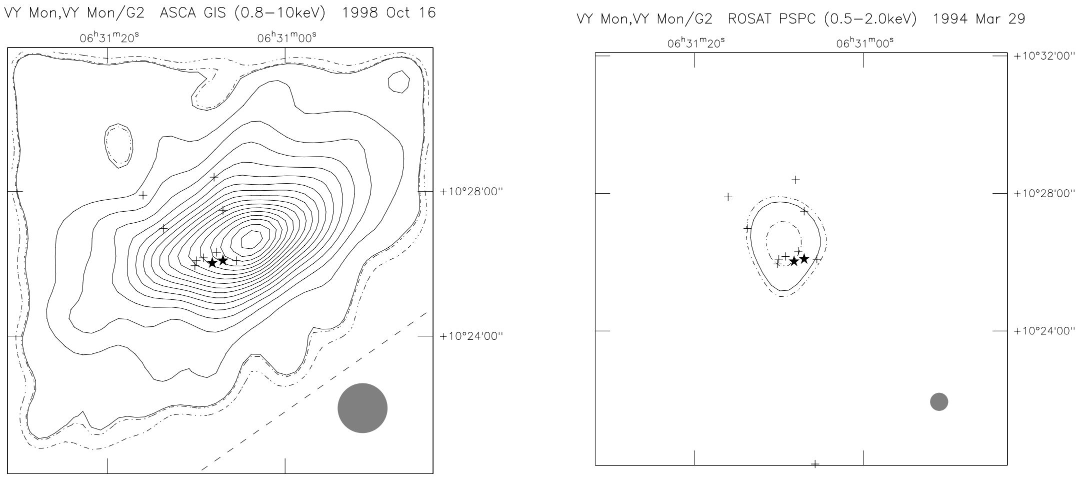

Figure 5.6: *ASCA* GIS (*left*) and *ROSAT* PSPC (*right*) images of the VY Mon region. Symbols are the same as Figure 5.1, 5.4, but the count rate per solid-line in the ASCA image is half (0.2 cts/pixel/obs for SIS and 0.5 cts/pixel/obs for GIS). The right star mark in each image is VY Mon and the left is CoKu VY Mon/G2. Five plus marks surrounding the star marks are VY Mon/G1, G4, G3, LkHα-274 and G5, anti-clockwise from right.

They form a small group of stars and are memberships of the Mon OB1 association (Cohen and Kuhi 1979; Testi et al. 1998). VY Mon is a O9−B8 star in the very young phase, ($\sim 5\times 10^4$ yrs, Casey and Harper 1990; The et al. 1994; Testi et al. 1999). It shows Algol-type variability and a highly reddening feature with large IR excess ($A_{\rm V}$ $\sim$7.4). CoKu VY Mon/G2 is a A0 shell-type star without emission line (Cohen and Kuhi 1979; The et al. 1994). X-ray emission from this region was first suggested with *Einstein* though the source significance was very small (S/N $\sim$2.5, Damiani et al. 1994). It is uncertain which was the x-ray source, but the emission was only detected in the *Einstein* hard band, suggesting the source is deeply embedded.

There are large discrepancy of the sky coordinate of VY Mon between the SIMBAD database and recent papers (Testi et al. 1998; Henning et al. 1998; Yudin and Evans 1998). This is probably because SIMBAD refers the coordinate to an old paper less reliable in absolute coordinate. We thus refer the absolute coordinate of VY Mon to the recent papers and determine the coordinates of other sources from the relative coordinates to VY Mon[1]. A strong x-ray source is detected in the VY Mon region (Figure 5.6). The separation from the optical position is about 40″, which is larger than the typical error ($\sim$24″) but acceptable for the GIS outer *fov*. *ROSAT* observed this region five times, but in each observation the off-axis angle at VY Mon is more than 30′ and the *HPD* is relatively large ($\sim$ 90″). No apparent

---

[1] The relative position to VY Mon is referred to Weintraub (1990) for CoKu VY Mon/G2, /G3, /G4 and to Herbst et al. (1982) for IC 446 and LkHa 274. There is no reference for CoKu VY Mon/G1 except for a figure in Cohen and Kuhi (1979). The relative coordinate is roughly measured from this figure.

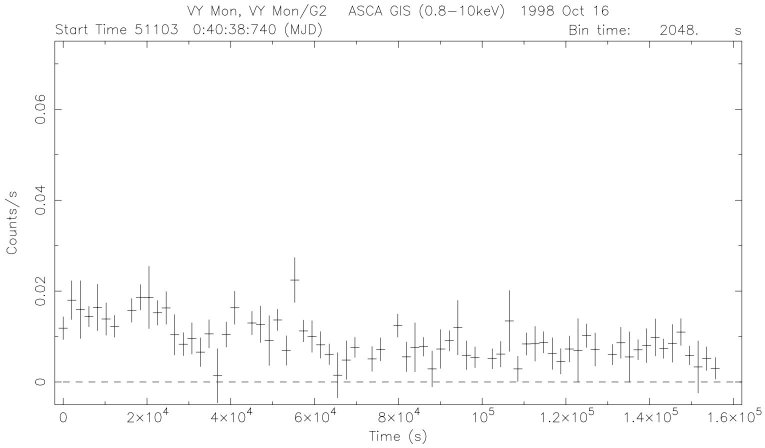

Figure 5.7: GIS light curves of VY Mon. See Figure 5.2 for details.

source appears in the *ROSAT* band and no significant variation occurs between observations (Figure 5.6 shows a hard band image taken in March 1994). X-ray emission concentrate on the stellar cluster in every observation, but we did not identify the counterpart even in the *ROSAT* images.

The light curve observed with *ASCA* gradually decreases with small fluctuations and becomes almost constant after $6{\times}10^4$ sec (Figure 5.7). We split the observation into two phases: $6{\times}10^4$ sec – high state (*before*) and low state (*after*). The low state spectrum rejects an absorbed 1T model in 90% confidence level, which is caused by a line-shaped structure at kT ~5 keV. We added a Gaussian component and found an acceptable fitting result. The line center energy is 5.1 keV, which is close to highly ionized Ca line energies. We thus tried an absorbed MeKaL model with free Ca abundance, but the Ca line appears lower than 5.1 keV and this model is rejected again. The line center energy corresponds to the Kα line of neutral vanadium, but this element is scarce in the universe. The x-ray luminosity in the low state is log $L_{\rm X}$ (ergs s^{-1}) ~32.2 (d ~800 pc), which is one of the largest luminosity among our HAeBe samples. On the other hand, the high state spectrum accepts an absorbed 1T model in 90% confidence level. The best-fit temperature is very high, kT ~6 keV. The 1T model assumes that there is only one plasma blob around a star, which is very hot during the high state and cools down in the low state. The fact that the emission measure varies less than 20% between two states supports this model (see also Figure 7.9). Another situation is also possible – two hot plasma components are present in the high state and one disappers in the low state. We also found an acceptable solution for the model, by adding the low state component. All fitting results showed a relatively small $N_{\rm H}$. The converted $A_{\rm V}$ value - ~$5{\times}10^{21}$ cm^{-2} ($A_{\rm V}$ ~2.5) - corresponding with VY Mon/G2, G3, G4. VY Mon/G3 and /G4 are classified as spectral types K−M (Cohen and Kuhi 1979). $L_{\rm X}$ of low mass stars are typically less than log $L_{\rm X}$ (ergs s^{-1}) ~30. VY Mon/G2 is the most plausible counterpart.

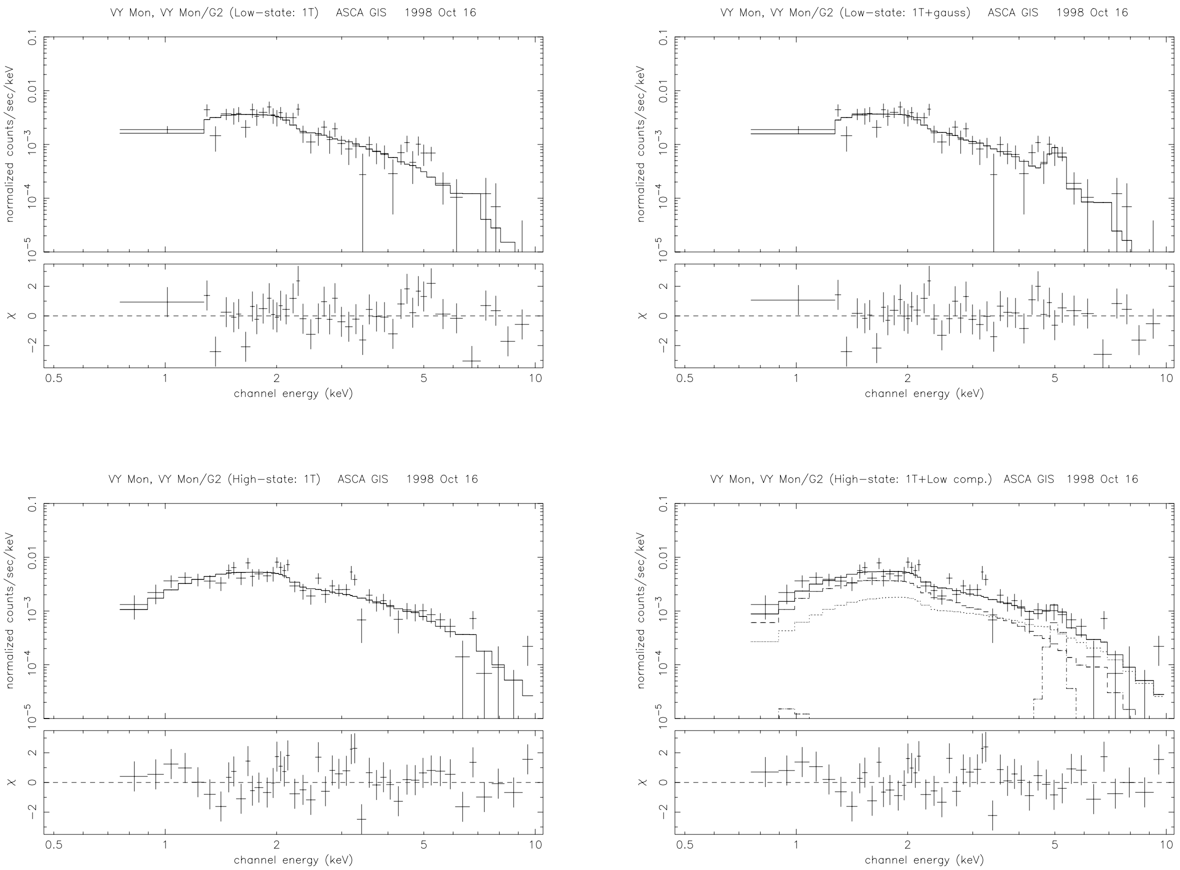

Figure 5.8: GIS spectra of VY Mon. Top panels show the spectra in the low state (*left*: an absorbed 1T best-fit model, *right*: adding a Gaussian component). Bottom panels show the spectra in the high state (*left*: an absorbed 1T best-fit model, *right*: adding the low state component).

5.1.4 T Cha

T Cha is in the dark cloud DC 300.2–16.8 locating between the Chameleon I and II clouds on the sky, but the distance measured with *HIPPARCOS* (d ~66 pc) is closer than the distances to the Chameleon I and II. T Cha is suspected to be a Weak-line T-Tauri star (Alcala et al. 1993). Hα lines show strong variability on a time scale of a day, sometimes accompanying with inverse P Cygni features (Alcala et al. 1993).

T Cha was detected as a strong x-ray source in the error circle. There is no optical counterpart other than T Cha and therefore T Cha is the most probable counterpart of the x-ray source. The flux is variable and seems to be gradually increasing through the

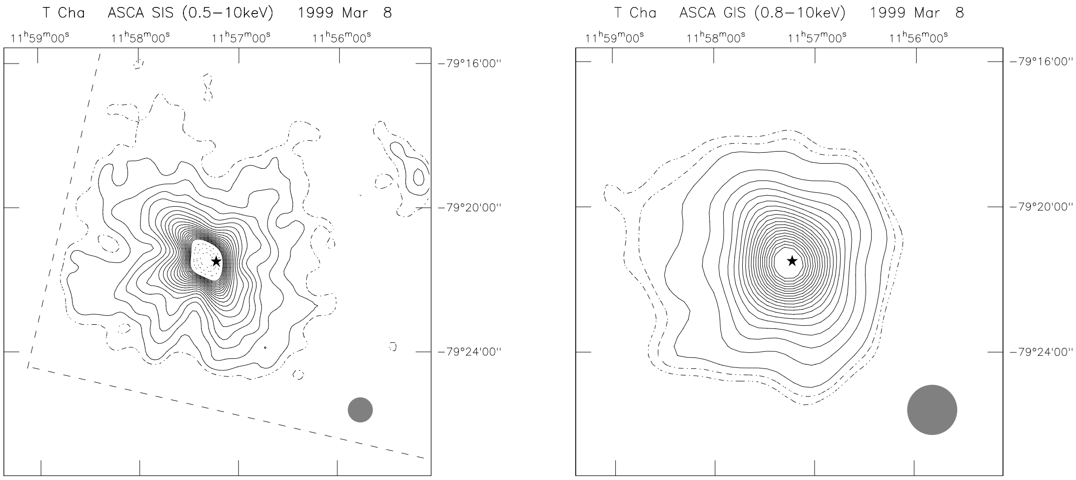

Figure 5.9: *ASCA* images (*left*: SIS, *right*: GIS) of the T Cha field. Symbols are the same as the captions in Figure 5.1, 5.4, but lines above 20 solid-lines in SIS are shown with dotted lines by 2cts/pixel/obs.

observation, with small flare like events (t ∼60, 130 ksec, Figure 5.10). The spectra are successfully reproduced with an absorbed 1T model (Figure 5.11). The log $L_{\rm X}/L_{\rm bol}$ value is the largest among the observed sources.

5.1.5 HD 104237

HD 104237, located in the Chamaeleon III dark cloud, is in the vicinity of the sun ($d \sim 116$ pc) and hence the brightest HAeBe star in the sky (V =6.6 mag, Hu et al. 1991). It is a slightly old star (Age ∼6.3 yrs) with the spectral type A4IVe+sh (Knee and Prusti 1996; van den Ancker et al. 1998). It shows P Cygni profiles of MgII lines but it does not have CO molecular outflows (Knee and Prusti 1996). It also emit several emission lines, indicative of the existence of a hot chromosphere (Hu et al. 1991). The X-ray emission was detected in the *ROSAT* all-sky survey as a relatively bright source (Alcala et al. 1995). The spectroscopic analysis with the *ASCA* deep observation have been performed by Skinner and Yamauchi (1996). Our data is the same as those of Skinner and Yamauchi (1996) so that the results is basically the same except for adopting the distance with *HIPPARCOS* (van den Ancker et al. 1998).

ASCA detect a strong x-ray source at the position of HD 104237 (Figure 5.12). There is no other counterpart within the error circle, and thus the x-ray source is identified as HD 104237. The x-ray flux fluctuates at the middle of the observation (Figure 5.13). A constant model is rejected in the 90% confidence level. Spectral fittings with an absorbed 1T model has large residual around 1keV (Figure 5.13). We thus tried an absorbed 2T model with common $N_{\rm H}$. Then the reduced χ^2 value greatly improves from 3.82 to 1.57,

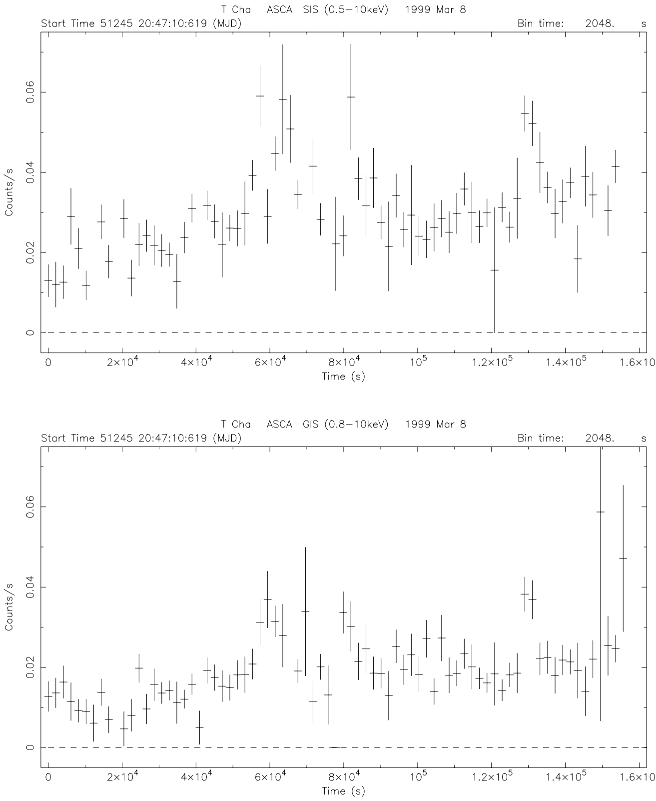

Figure 5.10: Light curves of T Cha (*top*: SIS, *bottom*: GIS). See Figure 5.3 for details.

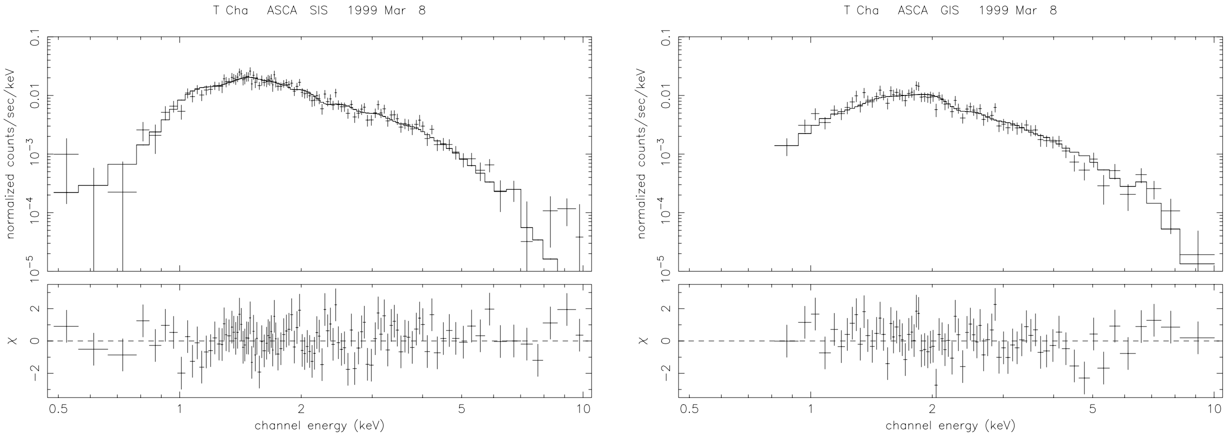

Figure 5.11: Spectra of T Cha (*left*: SIS, *right*: GIS). See Figure 5.3 for details.

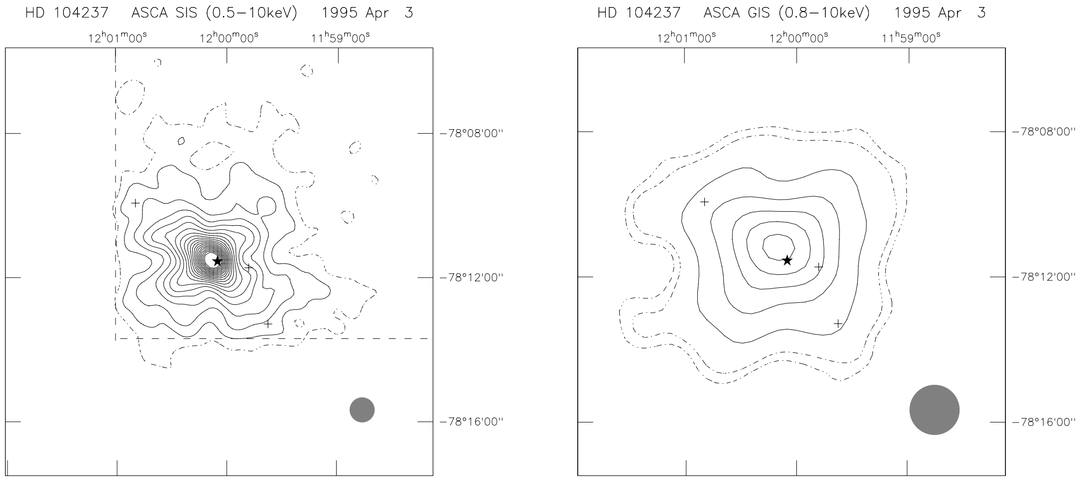

Figure 5.12: *ASCA* images of HD 104237 (*left*: SIS, *right*: GIS). For symbols, see Figure 5.1.

but the model is still rejected in the 90% confidence level. We also try other three models; 2T thermal model of free abundance with common N_{H}, 2T model with different N_{H} values, and 3T model with a common N_{H}, but their reduced χ^2 values do not improve. Skinner and Yamauchi (1996) showed acceptable results in the 2T and 3T model for the SIS spectrum. Bad reduced χ^2 values in our fittings could be responsible for the inconsistency between SIS and GIS. However, we could not find any systematic difference between these spectra.

5.1.6 IRAS 12496−7650

IRAS 12496−7650 is located in the Chameleon II Dark cloud. It is an embedded Herbig Ae star (Hughes et al. 1989) and is the most luminous far-infrared source in the Chameleon II cloud. Due to its extremely large extinction, the spectral type is not well established (A−F, Hughes et al. 1991). It is suggested to be the exciting source for the group of Herbig-Haro objects, HH 52-54, which places this object at the very young stage of stellar evolution (Cohen and Schwartz 1987).

We discover a highly absorbed x-ray source within $1'$ error radius at the position of IRAS 12496−7650 (Figure 5.15). Because no other cataloged source is present around there, the x-ray emission is most probably due to this peculiar object. We do not find any prominent x-ray variation within the limited photon counts (Figure 5.16). One important discovery is its very high absorption of about $N_{\mathrm{H}} \sim 1{\times}10^{23}$ cm^{-2}, which exceeds 5-times the estimated optical extinction of IRAS 12496−7650 (Figure 5.16, Hughes et al. 1991). The x-ray emitting region might be localized near to the star, and would be in a selected geometry to have large absorption, possibly due to the circumstellar disk.

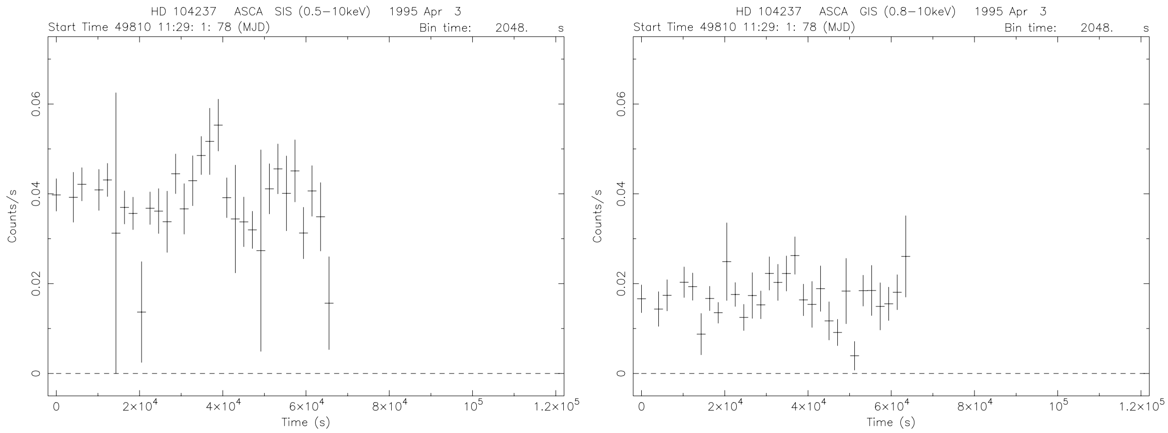

Figure 5.13: Light curves (*left*: SIS, *right*: GIS) of HD 104237. See Figure 5.2 for details.

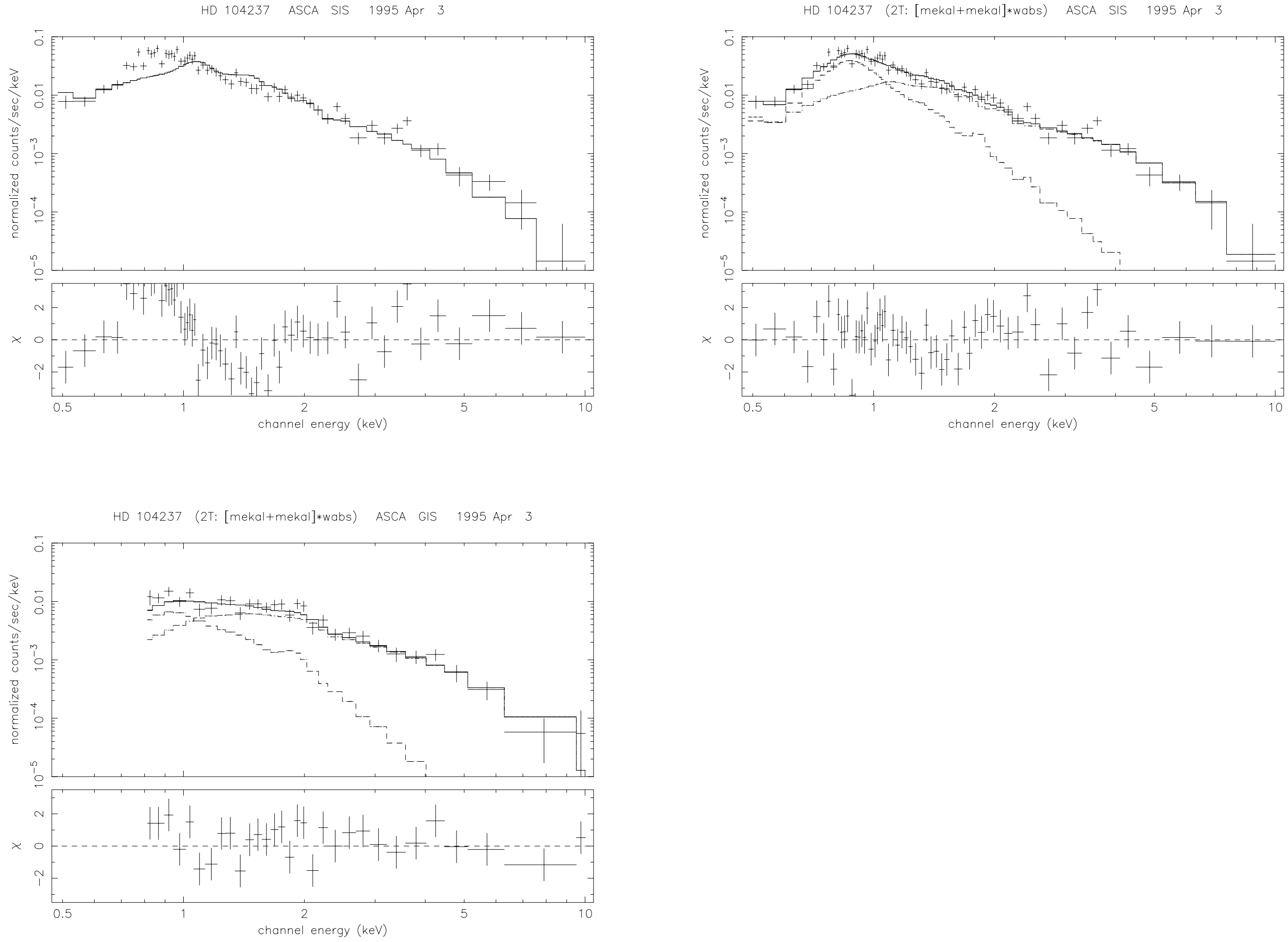

Figure 5.14: Spectra of HD 104237 (*upper left*: SIS 1T, *lower left*: SIS 2T, *lower right*: GIS 2T). See Figure 5.3 for details.

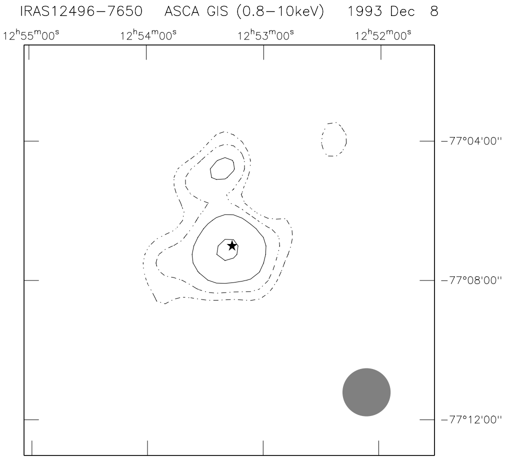

Figure 5.15: *ASCA* GIS image of IRAS 12496-7650. Symbols are the same as the caption in Figure 5.1. The count rate per solid-line is half (0.5 cts/pixel/obs).

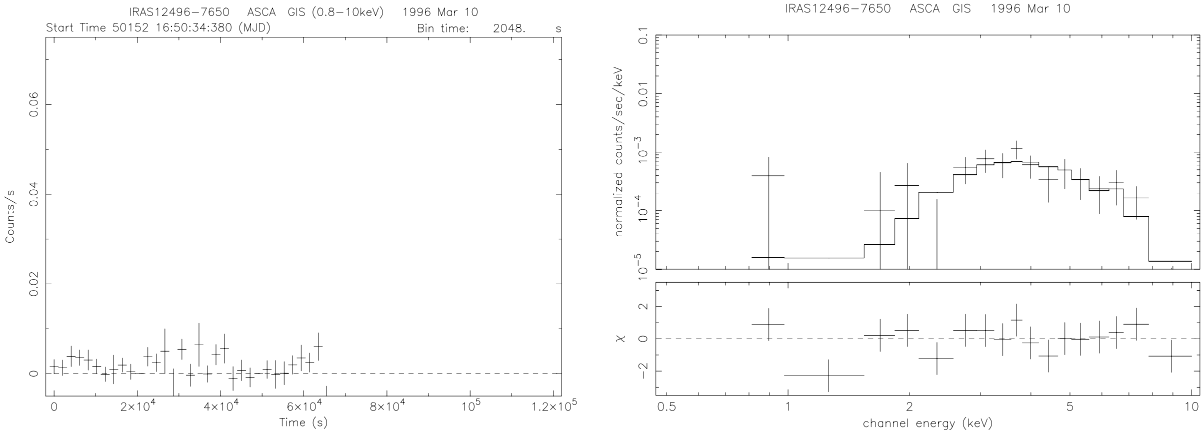

Figure 5.16: Light curves (*left*) and spectrum (*right*) of IRAS 12496–7650. See Figure 5.2, 5.3 for details.

5.1.7 HR 5999 / HR 6000

HR 5999 and HR 6000 are located in the center of the Lupus 3 subgroup and close to each other on the sky (∼45″). Both distances are approximately the same ; 210 pc for HR 5999 and 241 pc for HR 6000 (Bertout et al. 1999). HR 5999 and HR 6000 would be thus physically related to each other (Andersen et al. 1984)[2]. HR 5999 is a variable A5-7III/IVe star in 5×10^5-year-old (van den Ancker et al. 1998; Tjin A Djie et al. 1989). It is thought to have an accretion disk (eg The et al. 1996), which might cause photometrical and spectral variations. It also has a close companion at 1.3″ apart (Rossiter 3930, Stecklum et al. 1995), probably in the T-Tauri phase. On the other hand, HR 6000 is known to exhibit peculiar line features, which is recognized as abundance anomalies (Andersen et al. 1984; Castelli et al. 1985). These lines make it difficult to determine the spectral types and evolutional stage. From a model calculation, the spectral type was measured as late-B to early A (Castelli et al. 1985; Kurtz and Marang 1995). The detailed photometry and multi-band SED by van den Ancker et al. (1996) suggested the existence of a T-Tauri companion. Their paper interprets the abundance anomalous as a result of several atomic lines merging from the primary and secondary and concluded that the primary is a B6 star in a young main-sequence phase. However, the distance of HR 6000 was later modified to be 241 pc with *HIPPARCOS* (Bertout et al. 1999). This makes $L_{\rm bol}$ large and then HR 6000 should be a pre-main-sequence star of about $4M_\odot$. The x-ray emission of both HR 5999 and HR 6000 were first detected in the *ROSAT* observation as bright sources (Zinnecker and Preibisch 1994).

In both SIS and GIS images (Figure 5.17), HR 6000 was clearly seen as a strong source. Because HR 5999 is on the outskirts of the *psf* of HR 6000, only SIS could manage to detect a faint x-ray peak of HR 5999.

The light curves and spectrum (*top left* in Figure 5.18 and Figure 5.19) at the position of HR 5999 are made from the SIS data. We do not find any systematic difference between the SIS0 and SIS1 data. We think that the contamination from HR 6000 is satisfactory removed. The light curves of HR 5999 show no variable feature. The spectrum is successfully fit with a 1T thermal model. The best-fit $N_{\rm H}$ value is very small but its error range includes the converted $N_{\rm H}$ value from the relatively large $A_{\rm V}$ (∼0.5). The error bar of the temperature includes the hot component in the *ROSAT* spectra (kT ∼1.7 keV, Zinnecker and Preibisch 1994). The best-fit temperature derived with the *ASCA* data gets closer to the *ROSAT* value when we assume the same $N_{\rm H}$ ($N_{\rm H}$ $\sim7.5\times10^{20}$ cm^{-2}, 1T^f of HR5999 in Table 5.5). The light curves of HR 6000 show no time variation (*top right* in Figure 5.18) as well. For the spectrum (*top right* in Figure 5.19), we tried an absorbed 1-T thermal model but it is rejected because of having an excess in the hard energy band. We then analyzed the GIS data because GISs have better efficiency in the hard band and have longer exposure (see the

---

[2] The distance of ∼200 pc is far larger than the distance of the Lupus 3 cloud (140±20 pc; Hughes et al. 1993). They could be out of membership of the Lupus 3 cloud.

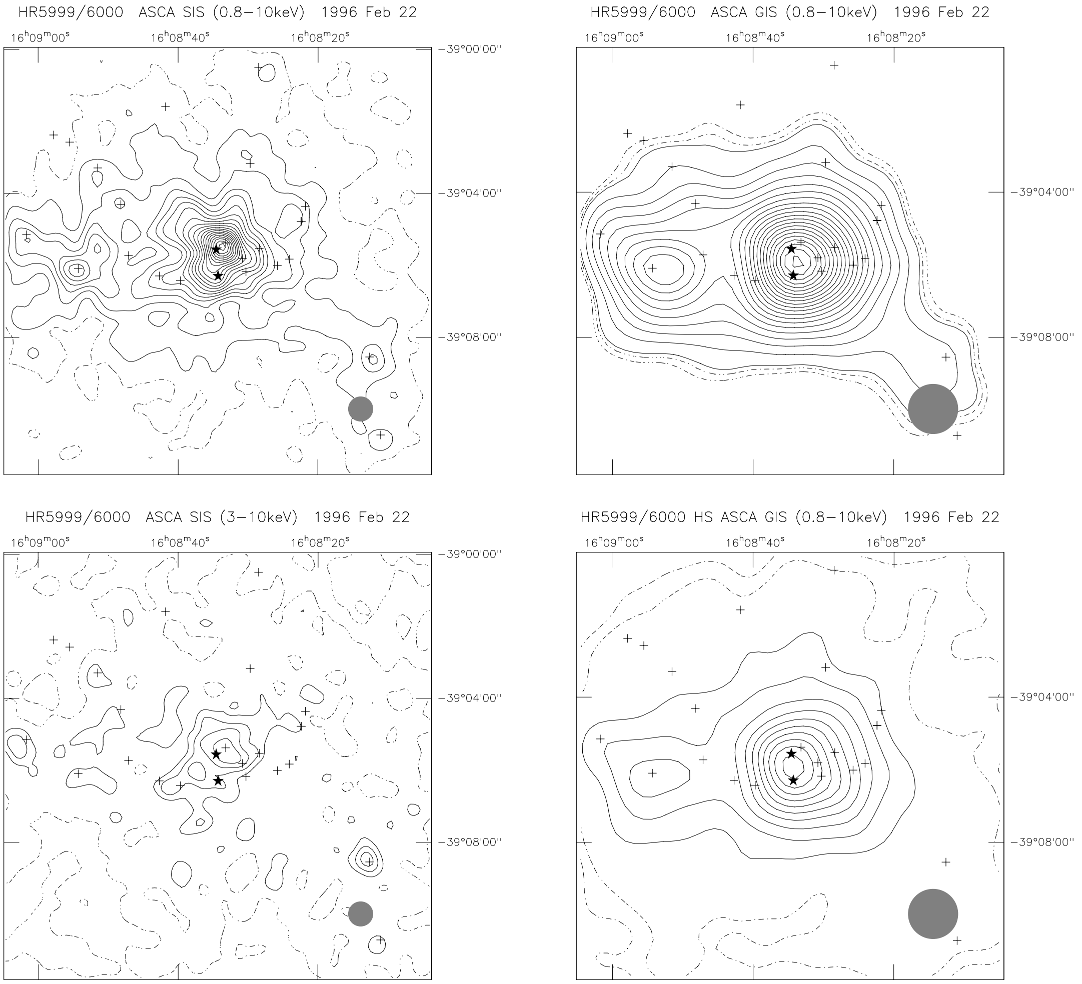

Figure 5.17: *ASCA* images (*left*: SIS, *right*: GIS) of HR 5999 (lower star mark) and HR 6000 (upper star mark). Top panels and a bottom left (3–10 keV) panel show images during the low state. A bottom right panel shows an image during the high state. Solid-lines of the SIS 3–10 keV images are drawn by 0.1cts/pixel/obs and those of the GIS high state image are drawn by 0.5cts/pixel/obs. See Figure 5.1 for symbols.

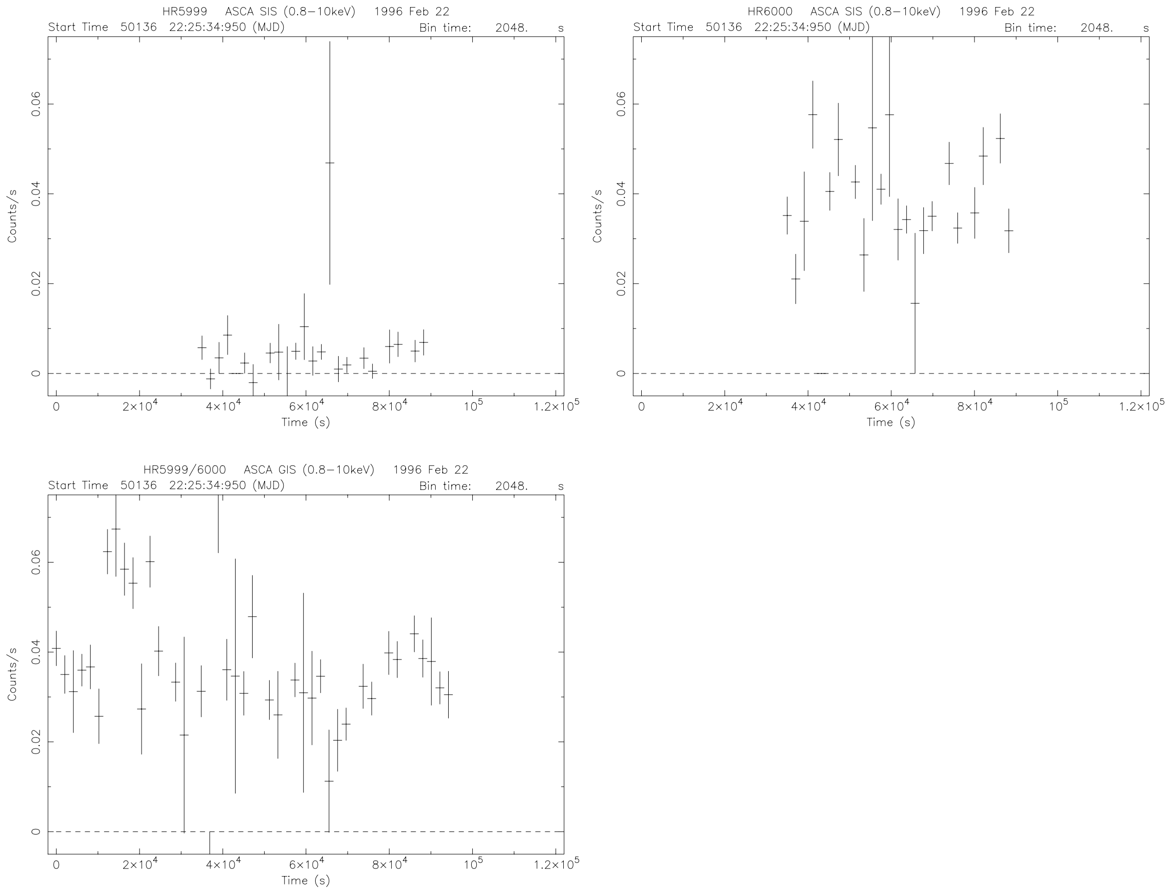

Figure 5.18: SIS light curves of HR 5999 (*top left*) and HR 6000 (*top right*) and the GIS light curve of HR 5999 + HR 6000. See the caption in Figure 5.2 for details.

table 4.9) At the beginning of GIS light curves (*bottom left* in Figure 5.18), the x-ray flux suddenly increased (τ_{inc} < 1,000 sec) by a factor of two, had a long plateau (τ_{pla} $\sim$1$\times$10^4 sec) and then rapidly decreased (τ_{dec} <1,000 sec). The flux level during the other period were almost constant. We call the period during the high as "high state" and the others as "low state". The low state includes the SIS exposure window. The x-ray peak position in the high state image is the same as in the low state (*bottom right* in Figure 5.17). HR 6000 is hence the most probable candidate of the variation source.

We made GIS spectra during the high and low state, separately (Figure 5.19). The GIS source region of HR 6000 inevitably includes HR 5999. We therefore made spectral fittings of GIS spectra adding the HR 5999 component in the model derived from the SIS spectrum though the flux of HR 5999 is almost negligible. The low state spectrum fit with an absorbed 1T thermal model has a distinct hard residual above 3 keV, which is not clearly seen in the SIS spectrum. We therefore checked the SIS hard band image above 3 keV. HR 6000 is then within the error circle of this hard peak though the T-Tauri stars CD-39 10894B is another

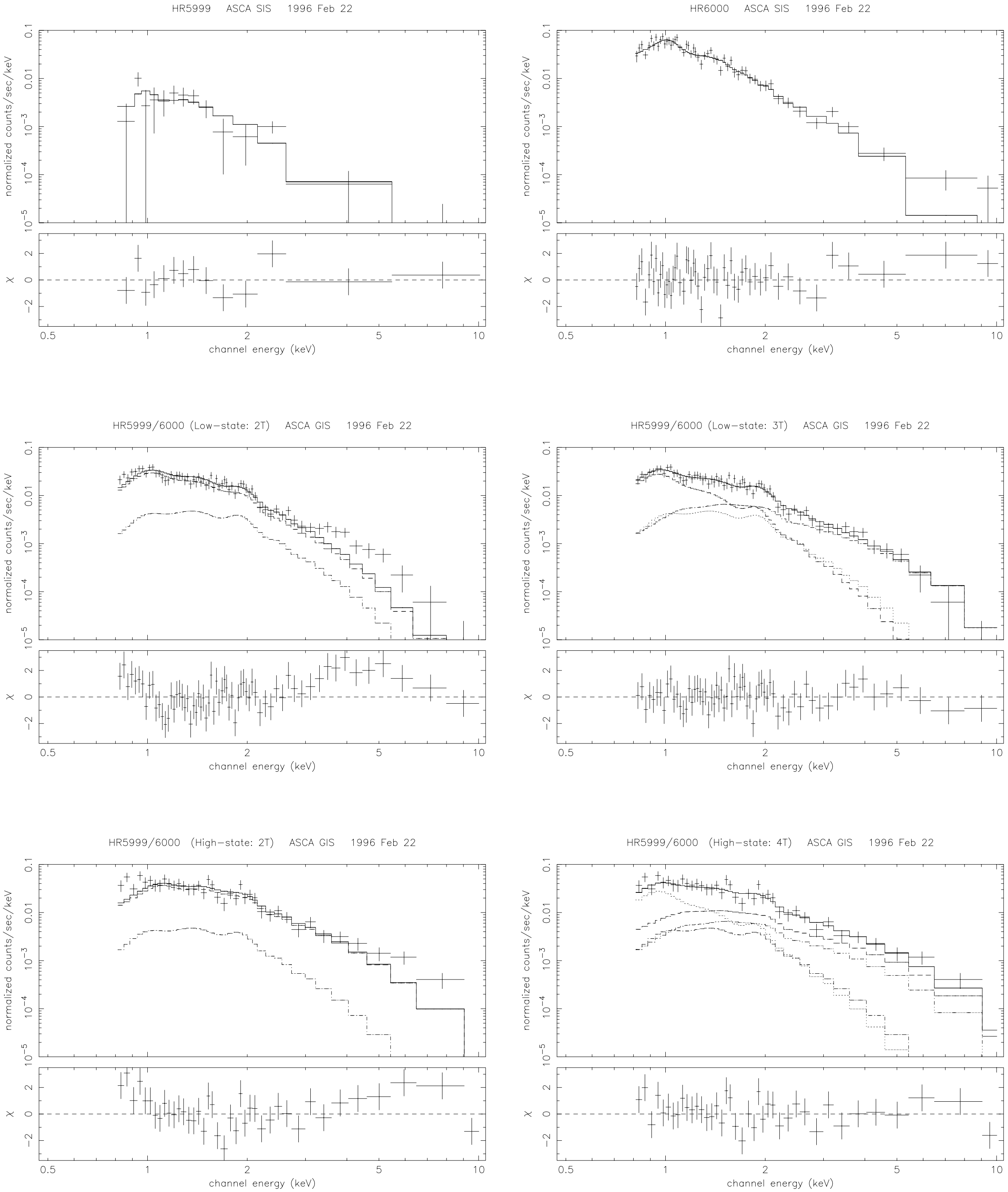

Figure 5.19: SIS spectra of HR 5999 (*top left*) and HR 6000 (*top right*) and GIS spectra of low state spectra (1T^h: *middle left*, 2T^{hi}: *middle right*) and high state spectra (1T: *bottom left*, 1T^h: *middle right*). See Figure 5.3 for details.

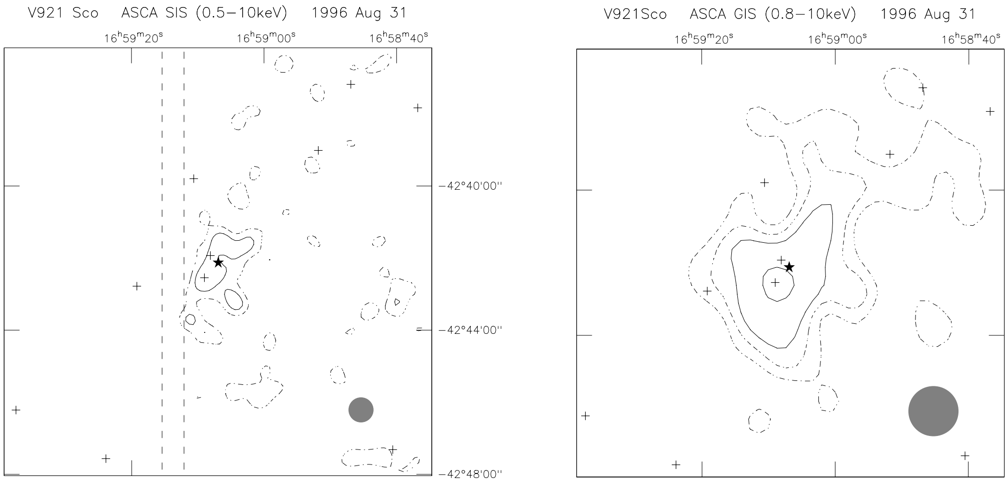

Figure 5.20: *ASCA* images (*left*: SIS, *right*: GIS) of V921 Sco. Meanings of symbols are the same as in Figure 5.1. The count rate per solid-line is half (0.2 cts/pixel/obs for SIS and 0.5 cts/pixel/obs for GIS).

candidate. We then gave an additional hard components with a common $N_{\rm H}$ and find an acceptable solution. We check the consistency of the derived model with the SIS spectrum and find that the SIS spectrum also has good agreement with the GIS spectrum above 1 keV. The reason for poor agreement below 1 keV is not sure but it could be due to the large uncertainty of the SIS response matrices in the soft band (see the subsection 3.1.3). We therefore adopt the fitting results derived from the GIS spectrum. The GIS images suggest that a source showing the flux increase is or lies around HR 6000. An absorbed 1T thermal model with the HR 5999 component has residue below 1 keV and above 4 keV, about the same flux during the low state. We therefore think that another plasma component is newly made or appears during the high state and soon disappears at the end. We fit the high state spectrum again with adding the low state component and find an acceptable solution. The $N_{\rm H}$ value is the same as that of HR 6000 during the low state, which indicates that the source is HR 6000 itself.

5.1.8 V921 Sco

V921 Sco, often called as CoD −42° 11721, is located on the galactic plane [(l, b) = (343.35, −0.08)]. Some papers classified it as a supergiant (eg Hutsemekers and van Drom 1990), but it is recently recognized as a young star. V921 Sco is embedded in a diffuse nebulousity, that spreads over $40'' \times 80''$ area. The distance to V921 Sco has large uncertainty from 200 pc (Pezzuto et al. 1997) to 2.6 kpc (Brooke et al. 1993). We adopt the distance of 500 pc derived from a ISO−SWS spectral analysis (Benedettini et al. 1998).

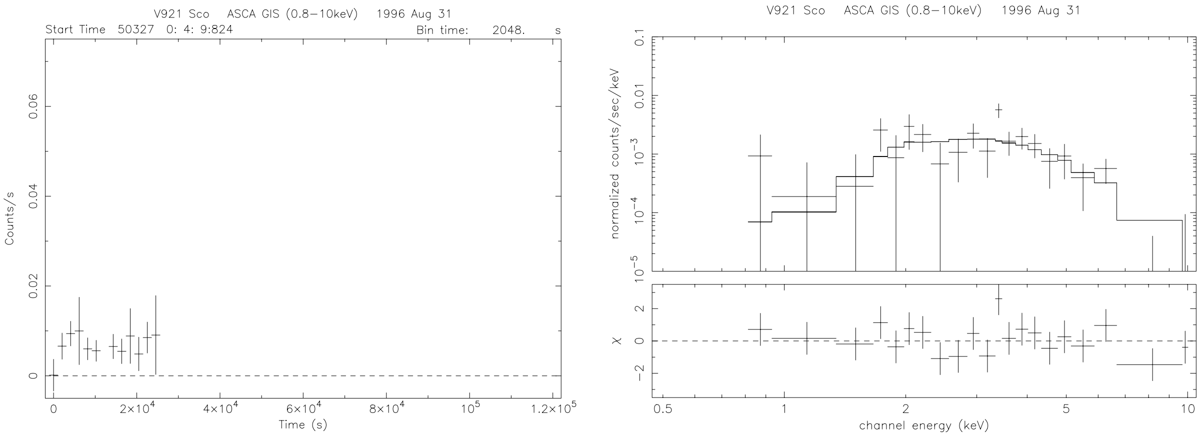

Figure 5.21: Light curves and spectra of V921 Sco. See Figure 5.2, 5.3 for details.

In the observation Gal R 2, a weak x-ray source is detected within both SIS and GIS error circles. The source in the SIS image seems to split into two humps, but it is uncertain as whether there are really two x-ray sources or simply made by limited photon statistics. In Gal R 3, GIS also detects a plausible x-ray emission at the position of V921 Sco with signal-to-noise ratio ~7.0 (0.8−10 keV), but the data quality is bad because V921 Sco is on the edge of GIS *fov*. We therefore only analyze the Gal R 2 data. The background subtracted light curves (Figure 5.21) do not show any time variation. The GIS spectrum (Figure 5.21) can be reproduced by an absorbed 1T model with an extremely large $N_{\rm H}$ ~5×10^{22} cm^{-2}. Even the lowest $N_{\rm H}$ is 1.5 times larger than the converted $N_{\rm H}$ from the largest $A_{\rm V}$ measurement (7.1). It is however comparable to the column density derived from a millimeter survey ($N_{\rm H}$ ~10^{23} cm^{-2}, Henning et al. 1998). The absorption corrected luminosity is quite large ($L_{\rm X}$ ~10^{32} ergs s^{-1}).

5.1.9 MWC 297

MWC 297 is a highly reddened star with extremely strong Balmer and silicate lines. Hillenbrand et al. (1992) reported that MWC 297 is a pre-main-sequence star with a spectral type of O9, at a distance of 450 pc and the age of ~3×10^4 years. Drew et al. (1997), however, predicted it to be a B1.5 zero-age main-sequence star at a distance of ~ 250 pc. They also argue that MWC 297 is a rapid rotator with v sin$i$ ~ 350 km/s. The visual extinction is accepted as 8−10 (McGregor et al. 1984; Hillenbrand et al. 1992; Porter et al. 1998) though Berrilli et al. (1992) and Hou et al. (1997) measured lower $A_{\rm V}$ (~3). *ROSAT* had an observation of this region with short exposure (~1089 sec) but detected no x-ray source.

A pointlike x-ray source is detected near MWC 297. Within the typical *ASCA* position

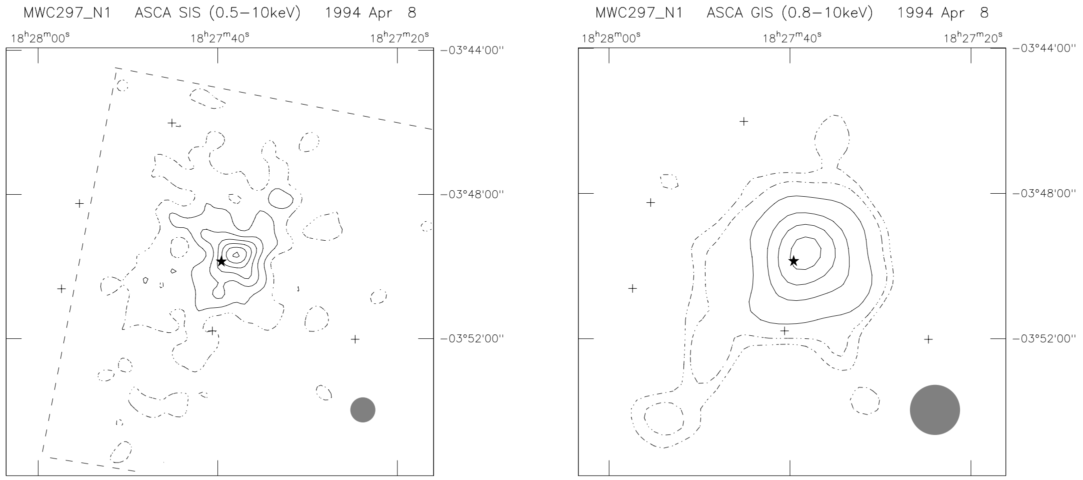

Figure 5.22: *ASCA* images of the MWC 297 field in the observation MWC 297 1 (*left*: SIS, *right*: GIS). Images of the other observations (MWC 297 2,3) are almost the same as this image. Symbols are the same as the captions of Figure 5.1. The count rate per solid-line is half (0.2 cts/pixel/obs for SIS and 0.5 cts/pixel/obs for GIS).

error, two objects MWC 297 and SH 2-62 are found from the SIMBAD database at the position of this x-ray source; SH 2-62 is a HII region surrounding the MWC 297 (Sharpless 1959; Chen et al. 1995). Figure 5.23 is the x-ray light curves in the full energy band. The flux in the first observation is found to be constant by the χ^2-test, but is increased by a factor of five at the beginning of the second observation, then gradually decreases exponentially to nearly the same flux of the pre-flare level at the end of the third observation. This short time variability indicates that the x-ray emitting region is compact, and hence is attributable to Herbig Be star MWC 297 rather than an extended object SH2-62. Here and after, we regard this source to be MWC 297. The time variability with an exponential-decay is similar to that of a flare from low mass stars. We accordingly regard that we observed a decay phase of an x-ray flare during the second and third observations, whereas the first observation fell on a quiescent phase. The on-set of the flare is between the first and second observations. We fitted the light curve to a constant plus exponential decay model and obtained the best-fit e-folding time of $\approx$ 5.6 $\times 10^4$ sec (see also Table 7.3).

The background subtracted SIS and GIS spectra for each observation are separately displayed in Figure 5.24. Acceptable fits with an absorbed 1T model are obtained for all the spectra of the three observations. The column density of hydrogen is consistent with a constant value during the three observations. The mean $N_{\rm H}$ value of $\approx 2.4 \pm 0.9 \times 10^{22}$ cm^{-2} is converted to the visual extinction of $\sim 10 \pm 4$ (Cardelli et al. 1988; Ryter 1996), which is in excellent agreement with the observed value of $A_{\rm V} = 8-10$. The plasma temperature in the quiescent phase of 2.7 keV is increased to 6.7 keV at the flare and then decreases to 3.2 keV. This would be the first detection of a flare for early-type stars, accompanied with

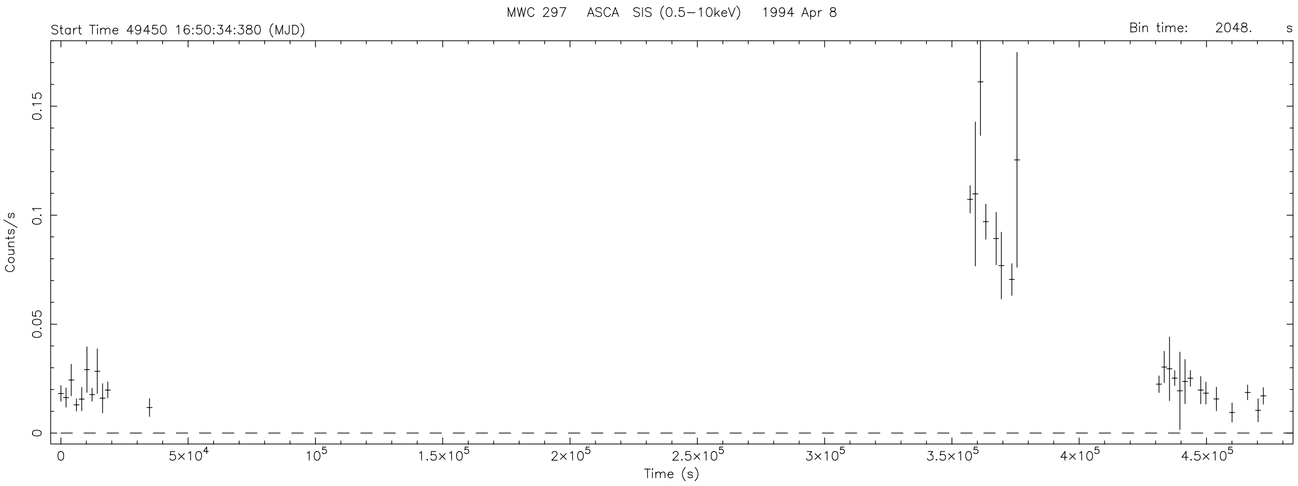

Figure 5.23: SIS light curves of MWC 297. The horizontal axis is longer than the light curves of the other sources. See also Table 5.4.

a plasma heating in the rising phase, and cooling in the decaying phase. The flare peak, however, is missed; we only detected x-rays after the on-set of the flare. Thus, the peak luminosity should be larger than 1.25×10^{32} ergs s^{-1}, which is the maximum value found at the beginning of the second observation. Then, the total energy released in the x-ray band is estimated to be more than 6.9×10^{36} ergs (0.4−10 keV).

5.1.10 EC 95

EC 95 is a member of the SVS4 IR stellar cluster in the Serpens star forming core (Strom et al. 1976; Strom and Strom 1994), which is one of the densest clustering region known (Eiroa and Casali 1989). Preibisch (1998) first reported the constant x-ray emission (X3) from it although they still leave the possibility of the other candidate EC 92. The very high visual extinction of both sources ($A_V \approx 25-35$ mag) made them suspect that the x-ray source has a large x-ray luminosity of about 10^{33} ergs s^{-1}. Preibisch (1999) analyzed a near-infrared spectroscopy with UKIRT and estimated that EC 95 is an extremely young intermediate mass star (Age $\sim 2\times10^5$ yrs; M $\sim 4\ M_\odot$), so called "proto-HAeBes". Radio observations have detected a point-like source around EC 95, which is named SH 68-2 (Rodriguez et al. 1980; Snell and Bally 1986). Smith et al. (1999) confirmed the source position of SH 68-2 within the error circle of EC 95 with VLA. They also found a falling spectrum and a time variation on a timescale of year, which suggests a gyrosynchrotron emission mechanism and hence a presence of magnetosphere on or around EC 95. They searched for, but found no evidence of, flaring activity and circular polarization.

Figure 5.25 shows total band images around EC 95. A point-like source is detected within the error circle of EC 95. In the SIMBAD database, there are 74 sources within 1.5′

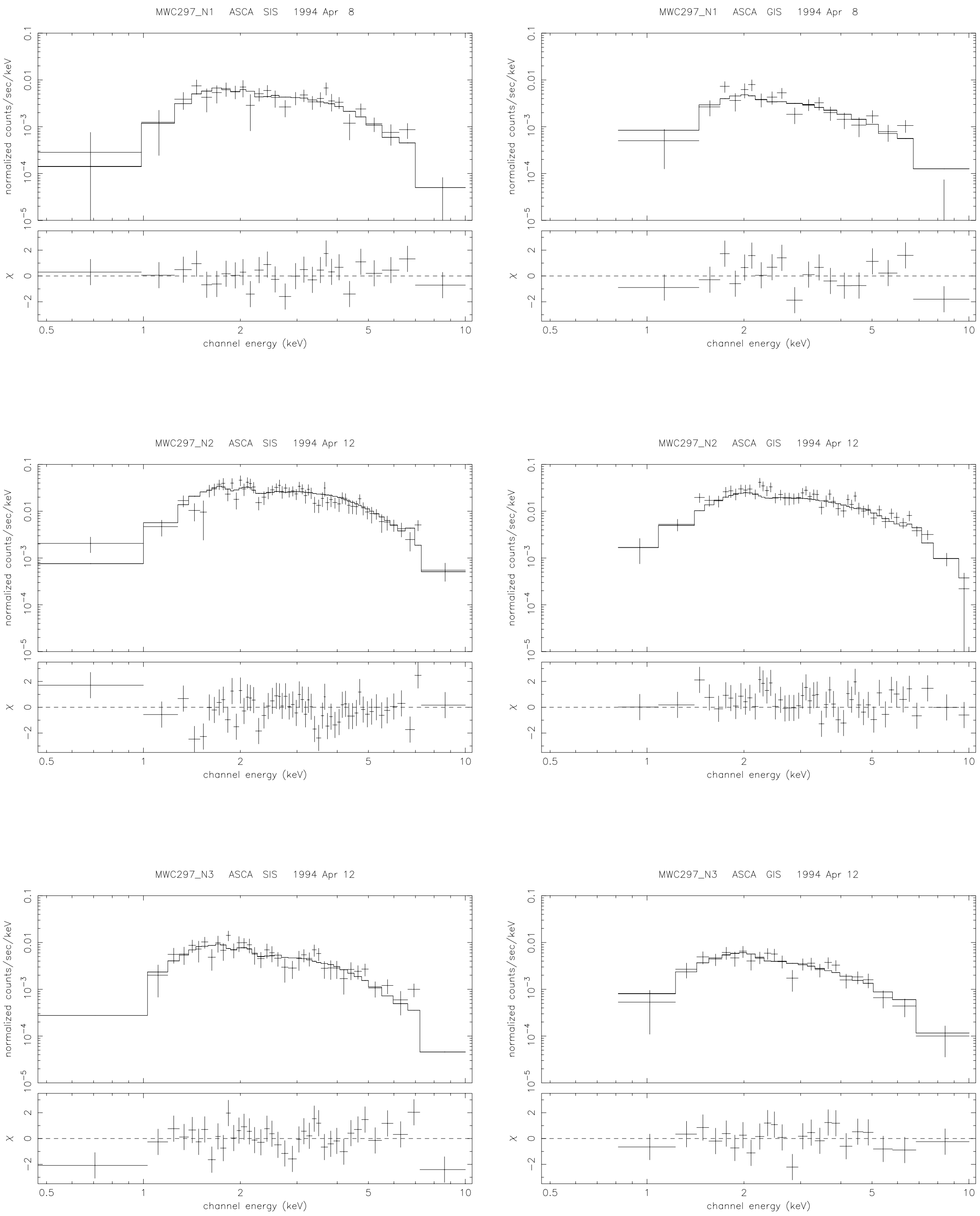

Figure 5.24: Spectra of MWC297 (*left*: SIS and *right*: GIS) from the first*(top)*, second*(middle)*, and third*(bottom)* observations. See Figure 5.3 for details.

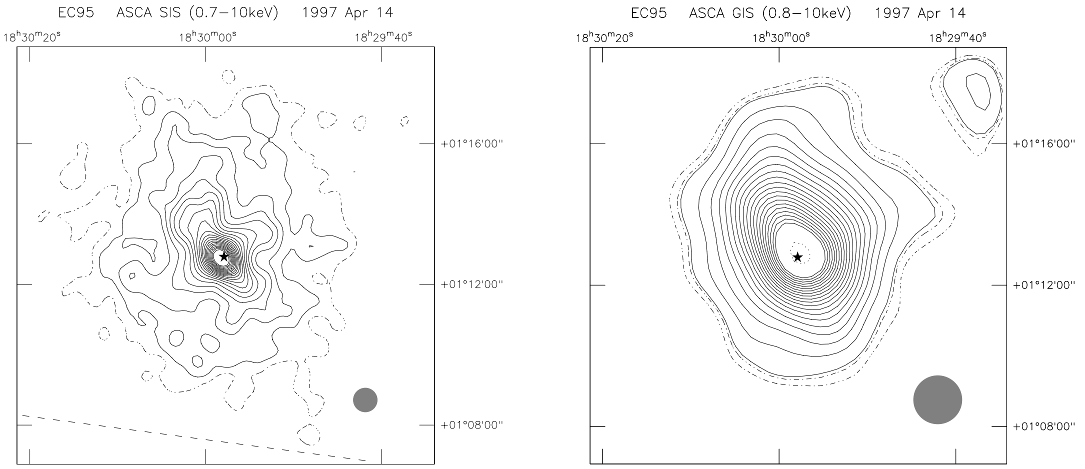

Figure 5.25: *ASCA* images (*left*: SIS, *right*: GIS) of the EC 95 field. See Figure 5.1 for symbols.

centered on the EC 95 although they include clouds, nebulousities and so on. A *ROSAT* HRI image with deep exposure of about 17 ksec (Preibisch 1998) displays only six sources within 15′ ×15′ squares and the nearest x-ray source is 20″ west from EC 95. We therefore identified the *ASCA* source as EC 95. Flare-like small fluctuation is clearly seen in SIS but less prominent in GIS (Figure 5.26). However both light curves reject a constant model over 99.9% probability. Both SIS and GIS spectra (Figure 5.27) are consistent with each other except for the model normalization, which is probably responsible for the CCD degradation (see the subsection 3.1.3). We thus vary each normalization parameter independently in the simultaneous fitting and derived its source flux from GIS parameters. The $N_{\rm H}$ value is one of the largest among HAeBes but about one fourth of the converted value from $A_{\rm V}$ ∼36. The plasma temperature is very high ($kT \sim$ 3.9keV), and the luminosity log $L_{\rm X}$ (ergs s^{-1}) ∼31.7 is large, but it is about an order as small as the *ROSAT* estimation assuming $A_{\rm V}$ ∼36 and kT ∼1−3keV. The count rate of *ROSAT* HRI in the *ASCA* observation is estimated at 2.8×10^{-3} cnts s^{-1}, which is about two times as large as the *ROSAT* result (Preibisch 1998). The difference between *ROSAT* and *ASCA* is therefore not due to time variation but simply due to the inconsistency of $N_{\rm H}$.

5.1.11 S CrA

S CrA is a K6 star in the CTTS phase (Herbig and Bell 1988), but The et al. (1994) quoted it at a potential candidate of a F-type PMS. It is thought to be extremely young, $\sim7\times10^4$ yrs. The mass is smaller than the sun, ∼0.55 $M_\odot$ (Olofsson et al. 1999). It has a companion star 1.4″ apart (eg Reipurth and Zinnecker 1993; Chelli et al. 1995; Prato and Simon 1997). The x-ray emission was detected with *ROSAT* as relatively strong source log $L_{\rm X}$ (ergs s^{-1})

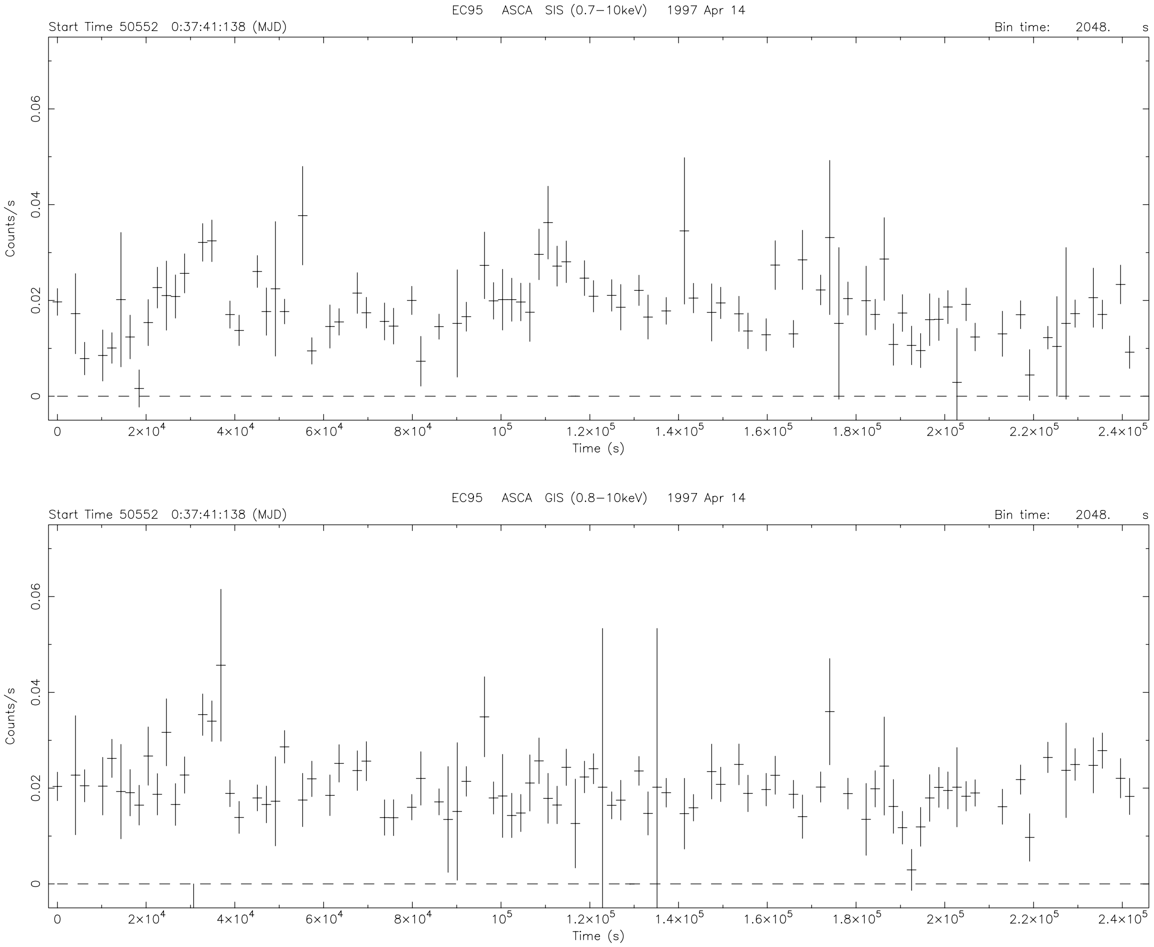

Figure 5.26: light curves of EC 95 (*top*: SIS, *bottom*: GIS). See Figure 5.2 for details.

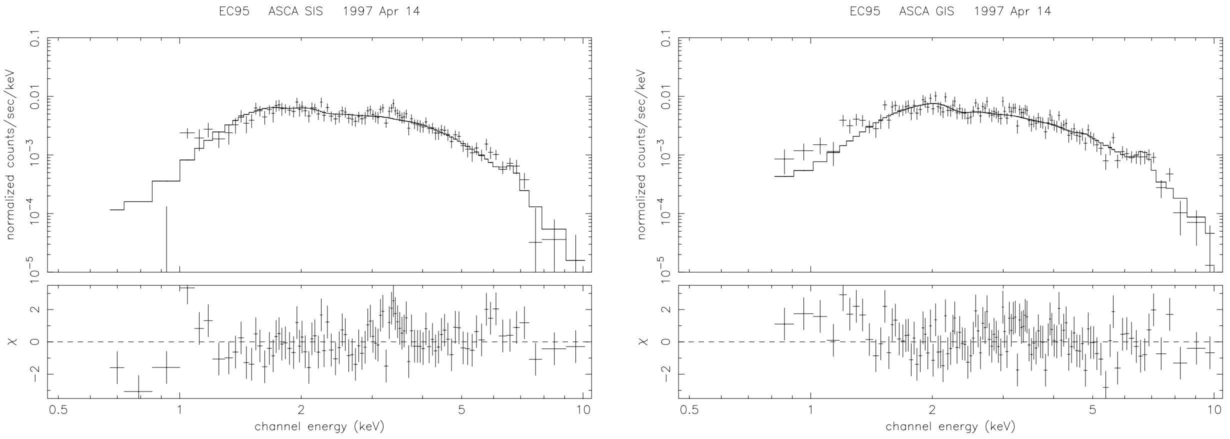

Figure 5.27: Spectra of EC 95 (*left*: SIS,*right*: GIS). See Figure 5.3 for details.

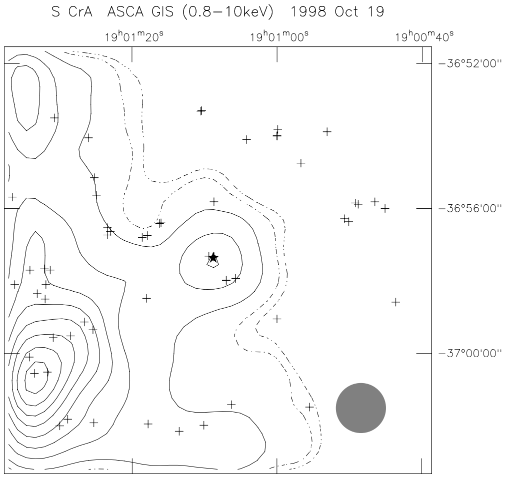

Figure 5.28: *ASCA* GIS image of the S CrA fields on Oct 1998 (R CrA6). The bright source at the south east is CrA1. See Figure 5.1 for symbols.

$\sim$30.1 (Carkner et al. 1998).

S CrA is on the *ASCA fov* in the 1st (SIS, GIS), 3rd(GIS), 4th(GIS) and 6th(GIS) observations. It locates near, and suffers strong contamination of, the bright soft x-ray source CrA1, but we find the significant x-ray emission at the position of S CrA (Figure 5.28) in the 1st, 3rd and 6th observations. The flux during the 1st observation is weak and therefore only the SIS can manage to detect the x-ray emission. A flare like variation is seen during the 6th observation though the photon count is too small. The plasma temperature is slightly high through the observations ($kT \sim$2 keV). The average flux goes up in an order between the 1st and 3rd observation, but it is constant after that.

5.1.12 TY CrA / HD 176386

TY CrA and HD 176386 belong to the R CrA cloud and illuminate the reflection nebula NGC 6726/7 (Graham 1991). TY CrA is $1'.1$ southwest northeast of HD 176386. The parallaxes of HD 176386 measured with *HIPPARCOS* is consistent with the distance of the R CrA cloud measured from associating early type stars. (Marraco and Rydgren 1981; de Zeeuw et al. 1999). TY CrA is a detached Herbig Be eclipsing binary with an orbital period of 2.88878 days (Kardopolov et al. 1981). The photometric variability associated with the eclipsing phenomena has been intensively studied by Casey et al. 1993,Casey et al. 1995 and Casey et al. 1998 [3]. From the orbital motion and the eclipsing feature, the primary star is estimated at 3.16$M_\odot$ located near the zero-age-main sequence stage and the secondary is at 1.64$M_\odot$ near the base of the Hayashi track. Both stars are consistent with an age of 3 Myr.

---

[3] The detailed photometry also suggests the presence of one more companions (Casey et al. 1998)

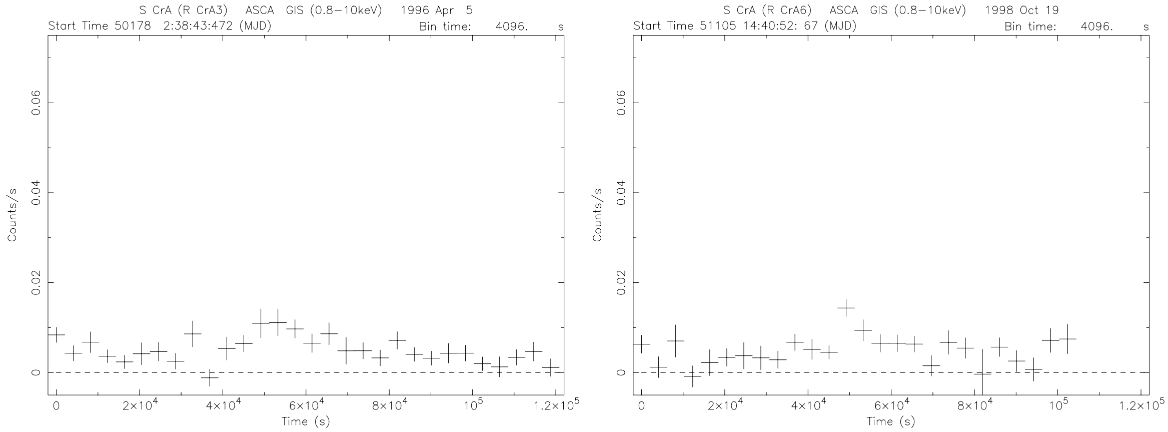

Figure 5.29: GIS light curves of S CrA in the 3rd and 6th observations. See Figure 5.2 for details.

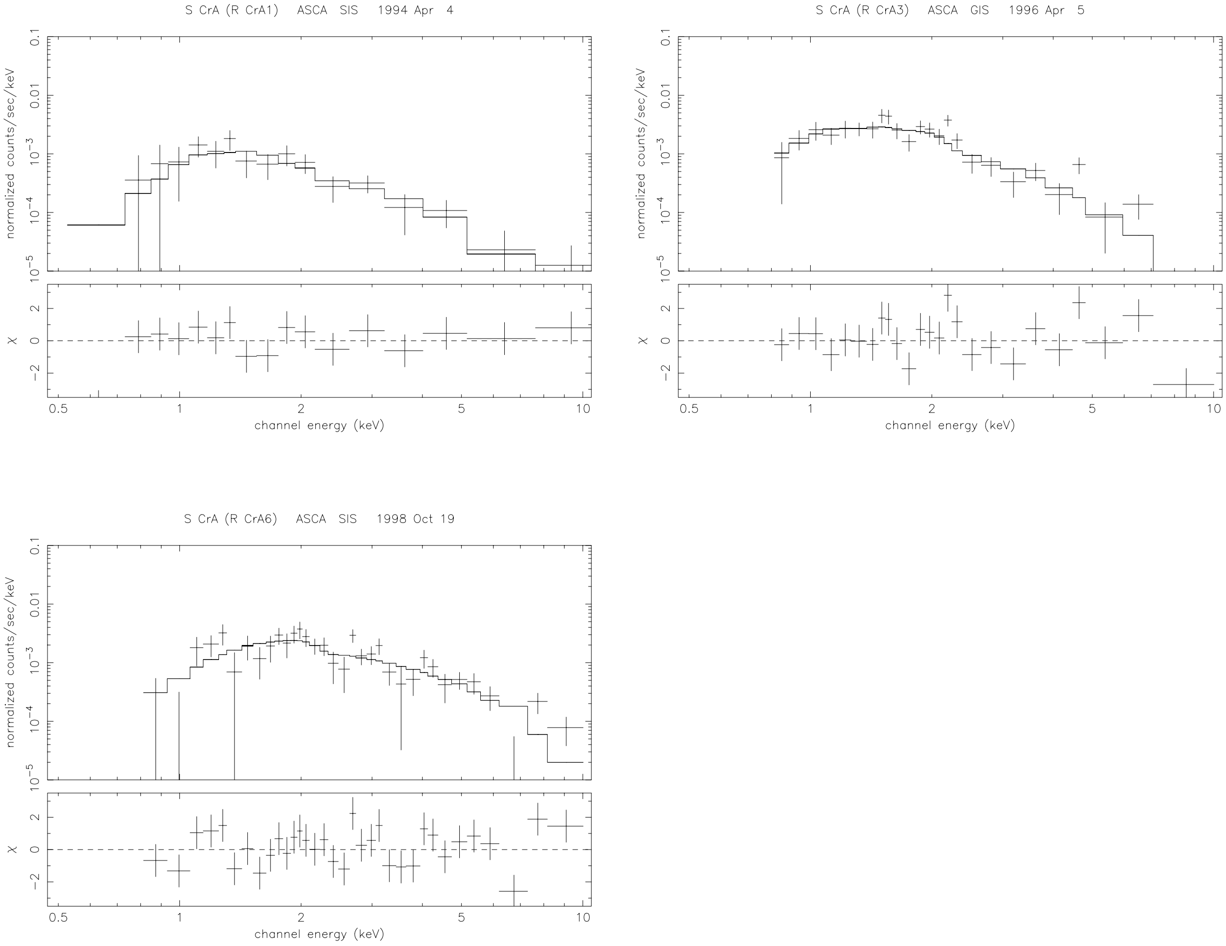

Figure 5.30: Spectra of S CrA in the 1st, 3rd and 6th observations. See Figure 5.3 for details.

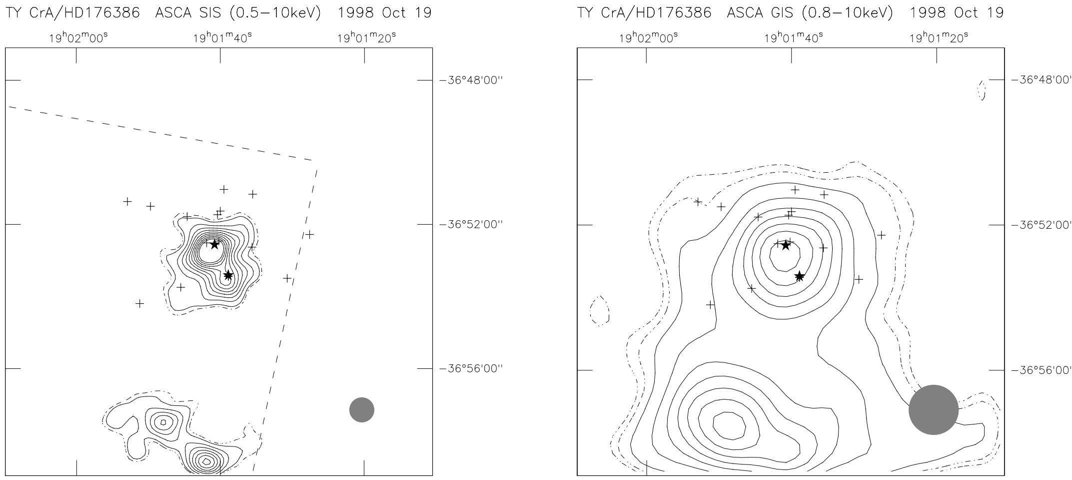

Figure 5.31: *ASCA* images (*left*: SIS, *right*: GIS) of the TY CrA/HD 176386 fields in Oct 1998 (R CrA6). See Figure 5.1 for symbols.

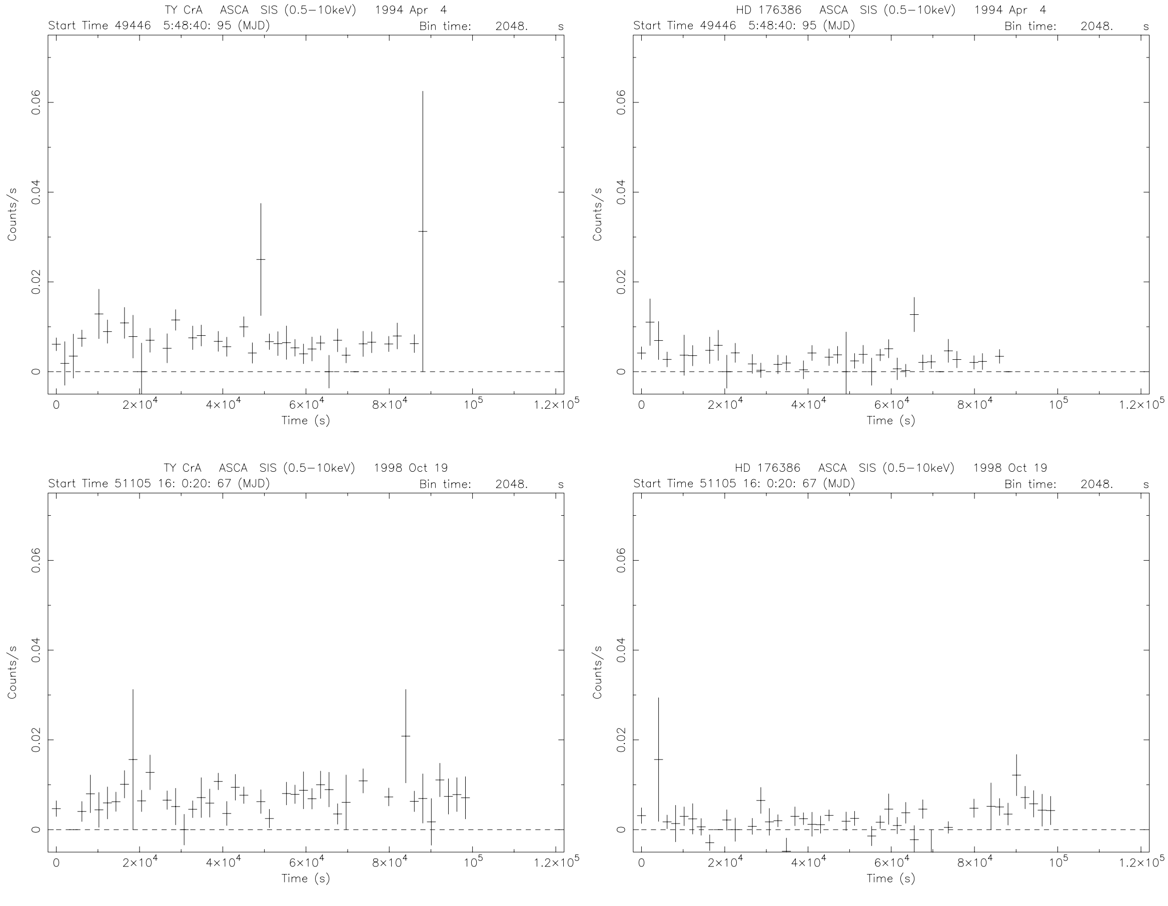

Figure 5.32: SIS light curves of TY CrA(*left*) and HD 176386(*right*) in the 1st(*top*) and 6th(*bottom*) observations. See Figure 5.2 for details.

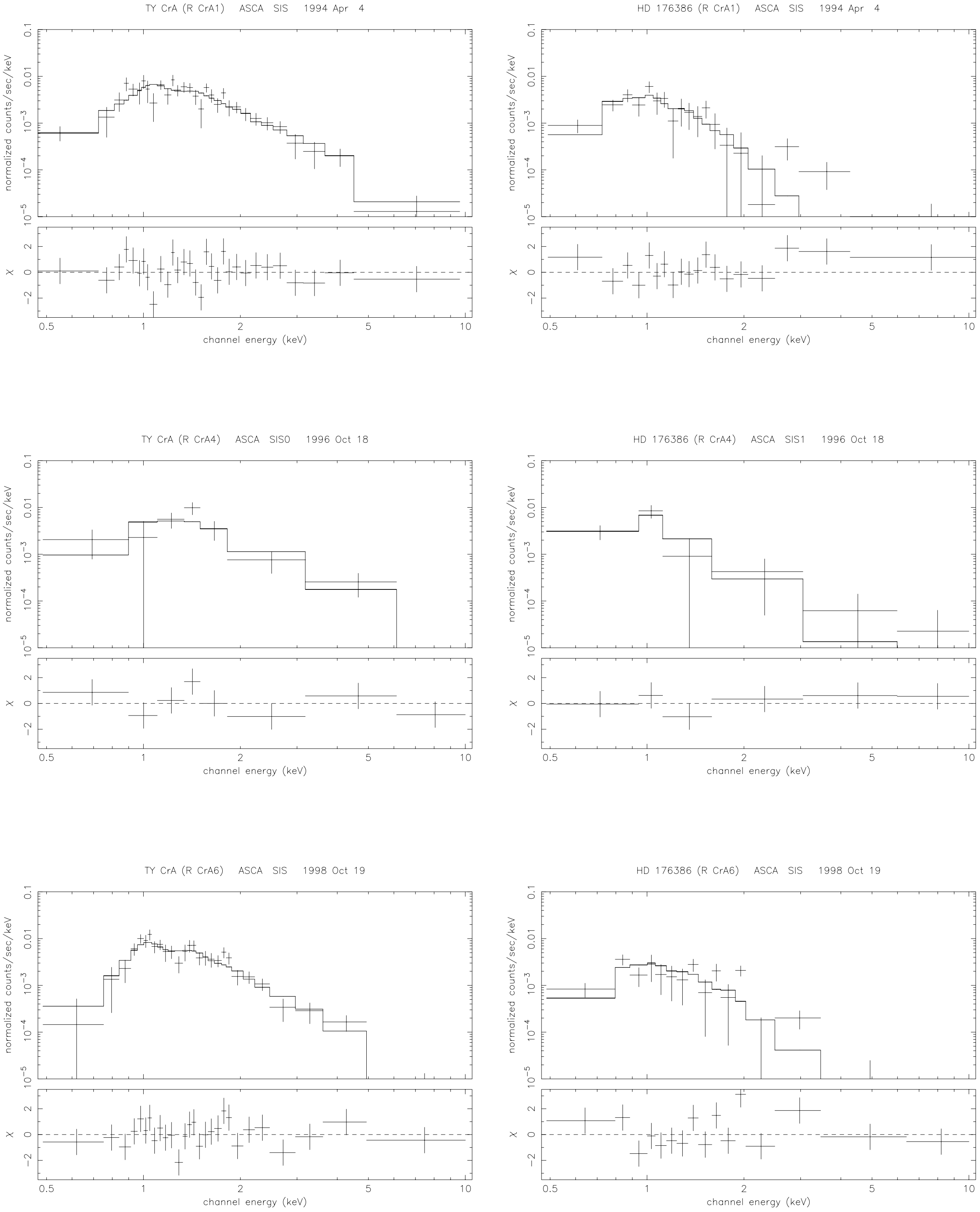

Figure 5.33: SIS spectra of TY CrA(*left*) and HD 176386(*right*) in the 1st(*top*), 4th(*middle*) and 6th(*bottom*) observations. See Figure 5.3 for details.

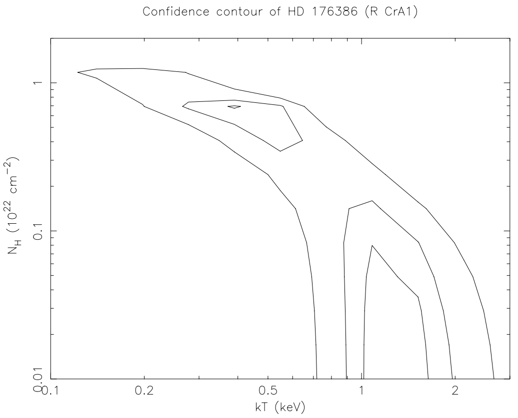

Figure 5.34: Confidence contour of the spectrum fitting parameters of HD 176386 (1st observation)

Whereas the spectral lines of the primary star is extremely narrow, indicative of an almost non-rotating star (v sin$i$ ~10 km s^{-1}). Spectral lines of the secondary is equivalent to v sin$i$ ~36 km s^{-1}, supporting the synchronous rotation (Casey et al. 1993; Lagrange et al. 1993). The time variations observed in the non-eclipsing phase are thought to originate in the dust obscurity of the circumbinary materials (Vaz et al. 1998), but the lack of the infrared excess indicates the absence of an optically thick disk (Casey et al. 1993). TY CrA is a non-thermal radio source (Skinner et al. 1993). Both *Einstein* and *ROSAT* detected the x-ray emission from TY CrA. *Einstein* also measured the plasma temperature and the absorption column density (kT ~1.04 keV, $N_{\rm H}$ ~ 5.5×10^{21} cm^{-2}, Damiani et al. 1994). On the other hand, HD 176386 is a B9.5 star with the age of 2.8 Myrs (eg Grady et al. 1993, Bibo et al. 1992). HD 176386 is thought to be close to ZAMS from these observational results; constant brightness in optical and near IR, extended mid-infrared emission indicating a presence of large inner cavity (Prusti et al. 1994), excess radiation only in far-IR (Bibo et al. 1992) and intermediate values of the accreting gas column densities and maximum accretion velocity (Grady et al. 1993).

ASCA detect the strong x-ray emission from TY CrA and HD 176386 and find no significant variation between observations. We show images in the 6th observation (Figure 5.31). Both sources are clearly seen in the SIS image but they are not in the GIS image. Because SIS only covers TY CrA and HD 176386 in the 1st, 4th and 6th observations, we first discuss the SIS results in detail and then mention the GIS results.

Figure 5.32 displays SIS light curves of TY CrA and HD 176386. The light curve of the 4th observation is excluded because of the very short exposure. We do not find any significant time variation and the constant model is accepted. All SIS spectra of both sources in Figure 5.33 are reproduced with an absorbed 1T thermal model. The best-fit values of the spectrum in HD 176386 had two local minima (Figure 5.34). A local peak with smaller

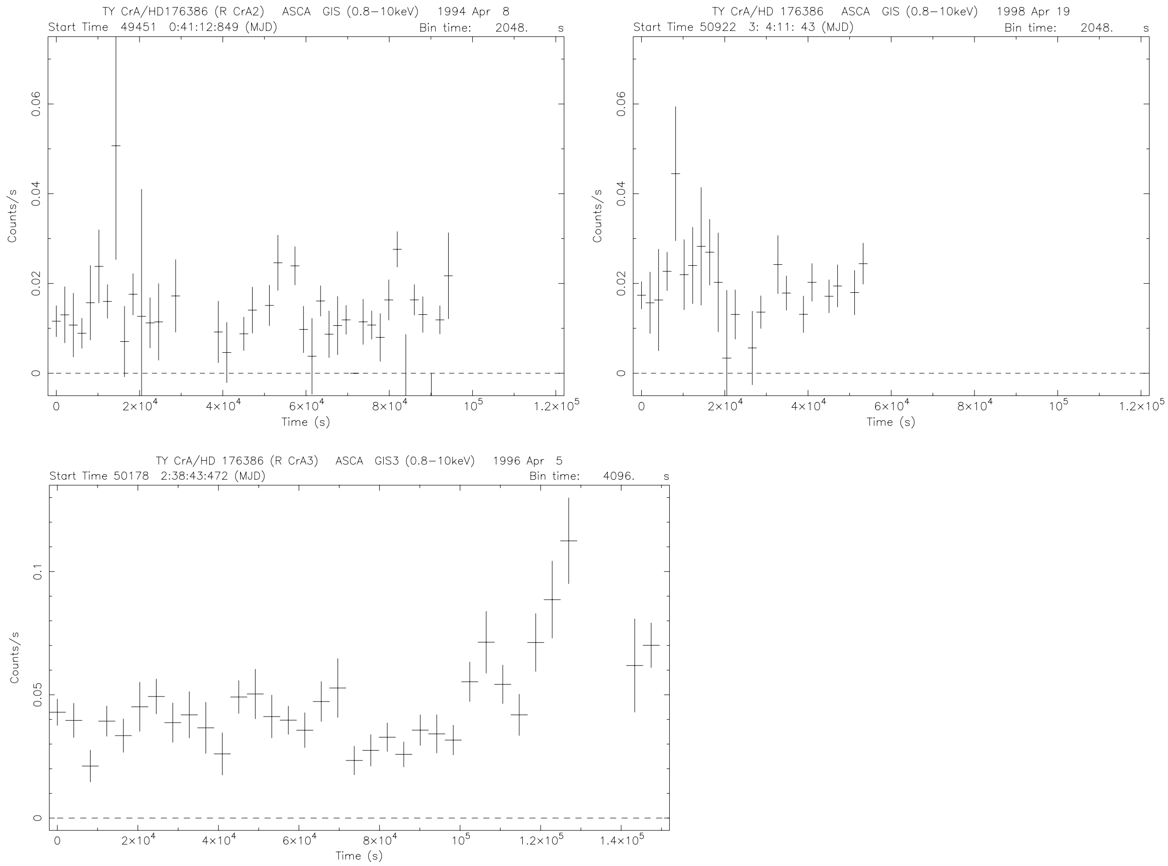

Figure 5.35: GIS light curves of TY CrA + HD 176386 in the 2nd (*top left*), 3rd (*bottom*) and 5th (*top right*) observations. The vertical scale of the bottom panel(3rd observation) is larger than the other panels. See Figure 5.2 for details.

$N_{\rm H}$ is consistent with the $A_{\rm V}$[4]. Because of the limitation of photon counts, statistical errors of the 4th spectra are quite large. $N_{\rm H}$ values of both sources in the 1st and 6th observations are about the same so that we also try the spectral fittings of 4th spectrum with fixing $N_{\rm H}$ value on the average of the 1st and 6th observations. Then the plasma temperature of TY CrA and HD 176386 are about the same as those in the other observations.

Figure 5.35 shows the GIS light curves of all observations, normalized by an effective area. The flux is almost constant except for the 3rd observation when the x-ray count rate began to increase at 100 ksec and is maximum at 120 ksec. The x-ray peak in the GIS

---

[4] Cardelli and Wallerstein (1989) measured the $R_{\rm V}$ value to the direction of TY CrA to be considerably higher than normal and derived relatively large $A_{\rm V} \sim 3.1$, compared with the Hillenbrand et al. (1992)'s estimation ($A_{\rm V}$ ~1.0). In the derivation of the $A_{\rm V} - N_{\rm H}$ relation (Ryter 1996), however, $R_{\rm V}$ is assumed to be the normal value, 3.1. We adopt the Hillenbrand et al. (1992)'s estimation.

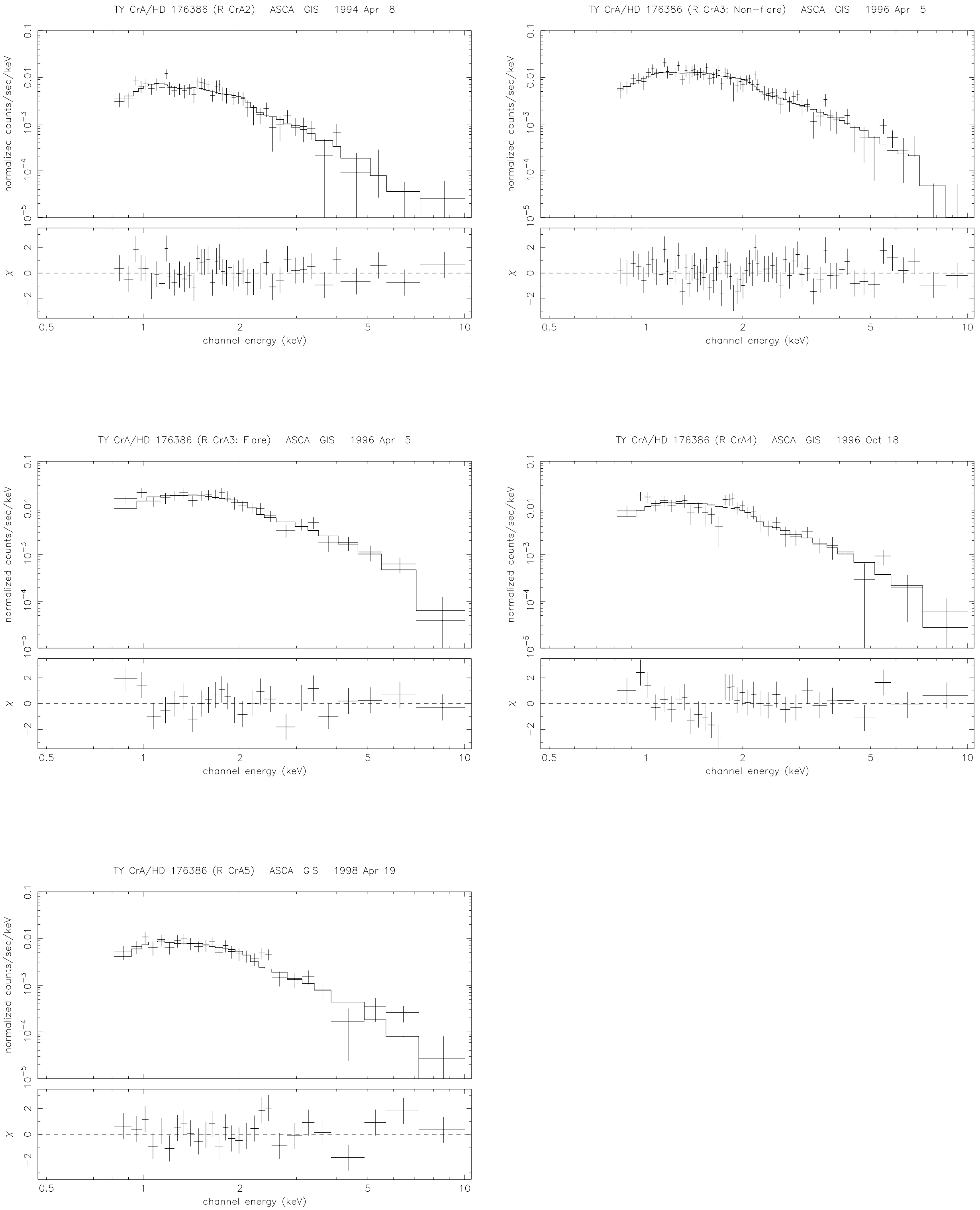

Figure 5.36: GIS spectra of TY CrA + HD 176386 in the 2nd(*top left*), 3rd in the low state(*top right*), 3rd in the flare state(*middle left*), 4th (*middle right*) and 5th(*bottom*) observations. See Figure 5.3 for details.

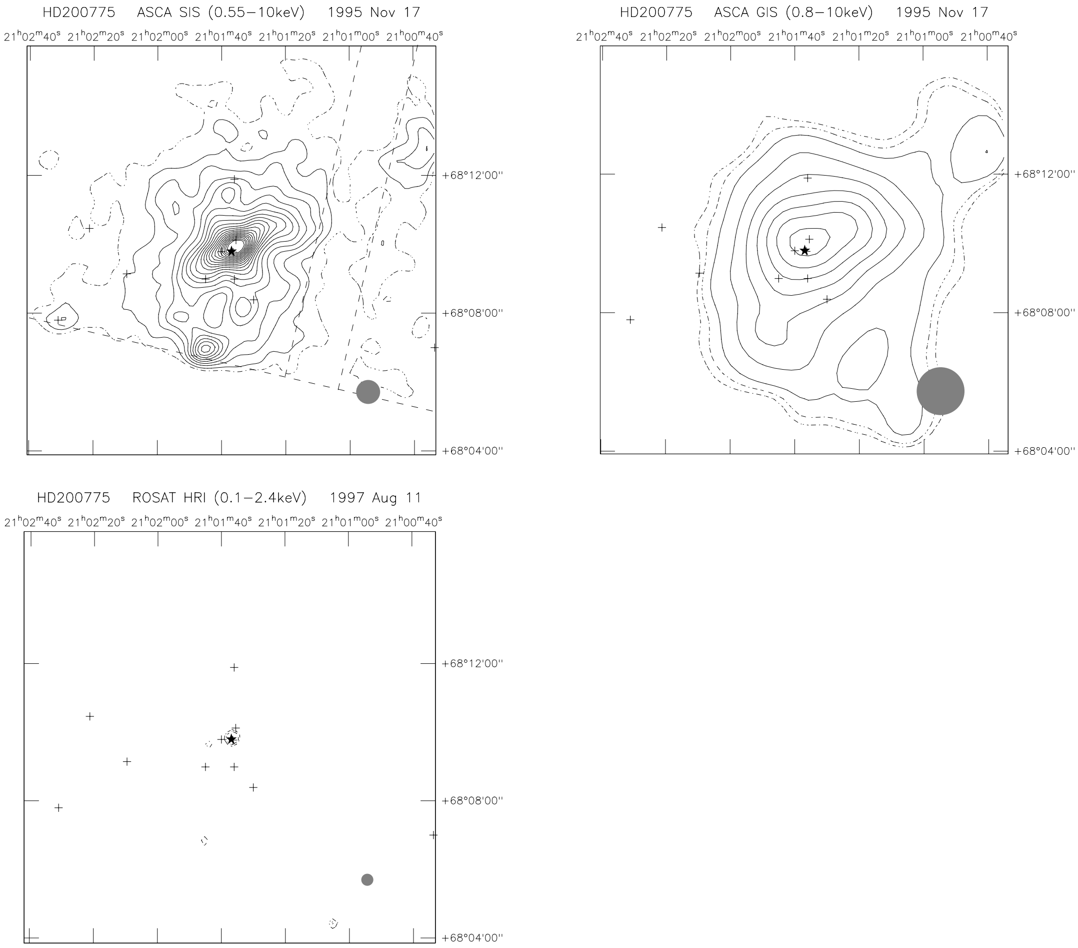

Figure 5.37: Images (*top left*: *ASCA* SIS, *top right*: *ASCA* GIS, *bottom right*: *ROSAT* HRI) of the HD 200775 field. See Figure 5.1, 5.4 for symbols.

image do not change during the flare state and thus the flaring source is probably TY CrA. Unfortunately, the data for about 20 ksec after the maximum is lost owing to the operational failure (see Table 4.9) so that we do not know the variable feature after the maximum. At 150 ksec, the flux decreases by half the maximum. All GIS spectra are reproduced with an absorbed 1T thermal model (Figure 5.36), but they really consist of two spectral components of TY CrA and HD 176386. The spectral parameters therefore do not reflect the plasma temperature itself but they represent the hardness of the merged x-rays. TY CrA is far luminous than HD 176386 above 1 keV. We thus think that GIS spectra is representative of the TY CrA component. The plasma temperature is about 2 keV, but it is higher during the flare state, which is clearly seen by adding the GIS2 data.

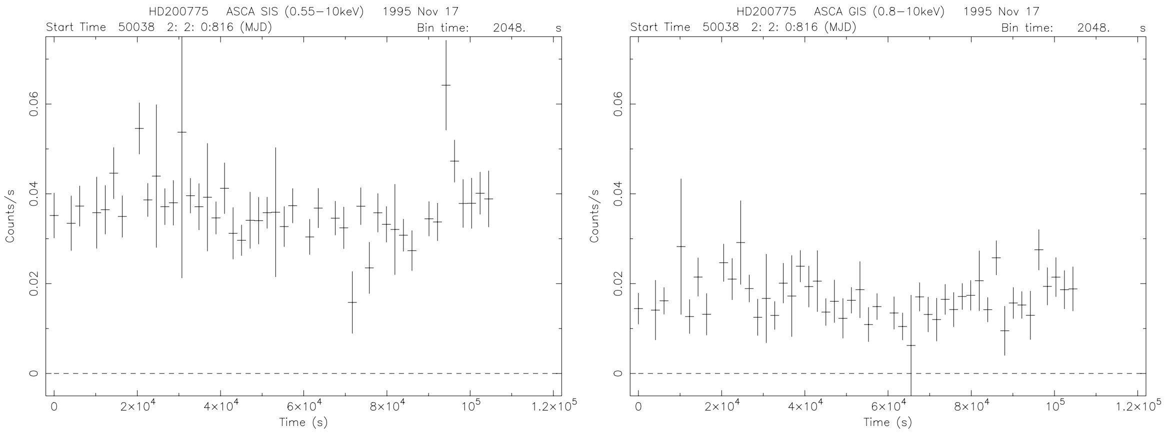

Figure 5.38: Light curves of HD 200775. See Figure 5.2 for details.

5.1.13 HD 200775

HD 200775 is a B2.5IVe star (see van den Ancker et al. 1998) illuminating the reflection nebula NGC 7023, The distance to HD 200775 was precisely measured with *HIPPARCOS* and determined at about 430 pc (van den Ancker et al. 1998; Benedettini et al. 1998). HD 200775 is in a biconical cavity that would have been swept away by energetic bipolar outflows, but there is no evidence of ongoing outflow activity (Fuente et al. 1998). From the comparison of the position in the HR diagram to an evolutional model, van den Ancker et al. (1997) estimated HD 200775 to be a very young star (~2×10^4 year). They however suggest that it could be in a post pre-main-sequence stage in 20M-year-old. It has a companion star 2.25″ apart (ΔK = 4.9 mag, Li et al. 1994; Pirzkal et al. 1997) and only eight surrounding sources within ~50″ (0.21 pc at 430 pc, Testi et al. 1999). *Einstein* detected relatively strong x-rays from HD 200775 and measured its plasma parameters at kT ~0.8 keV, $N_{\rm H}$ ~5×10^{21} cm^{-2} (Damiani et al. 1994).

In both SIS and GIS images (Figure 5.37), there is a pointlike source around HD 200775. The error circle includes one more optical source IRAS 21009+6758 to the north from HD 200775, but the *ROSAT* HRI image clearly shows the x-ray emission coming from HD 200775. IRAS 21009+6758 is thought to be a dusty cloud heated by UV radiation from HD 200775 (Whitcomb et al. 1981) and is not appropriate for an x-ray source.

The light curves (Figure 5.38) show no evidence of time variability. A flare-like event is seen at about 9.3 $\times10^4$ sec in the SIS light curve, but this is probably instrumental origin because it is only seen in SIS0. Figure 5.39 shows the spectra. In the spectral fittings we only use data bins above 0.73 keV because the level discrimination is set on a different value on each bit-rate data (see the subsection 4.3.3). We perform simultaneous fitting of both SIS and GIS spectra and first try the fitting with an absorbed 1T model, but it is rejected over the 99.9% confidence. The bad χ^2 values seems to be originated in several bumpy

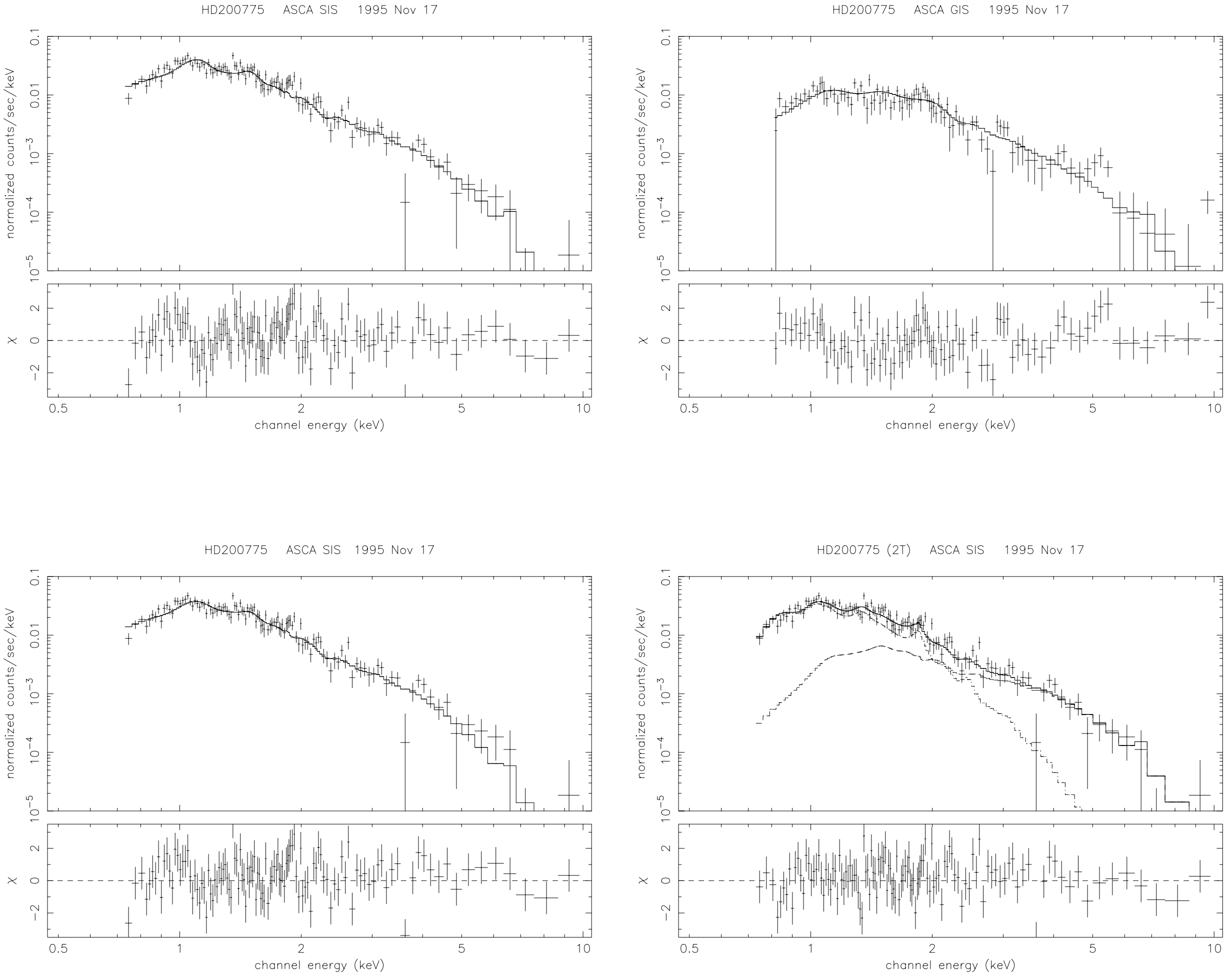

Figure 5.39: Spectra of HD 200775. Top panels show the 1T best-fit model of SIS (*left*) and GIS (*right*). Bottom panels show the SIS spectra of a 1T model with free abundance (*left*) and a 2T model (*right*). See Figure 5.3 for details.

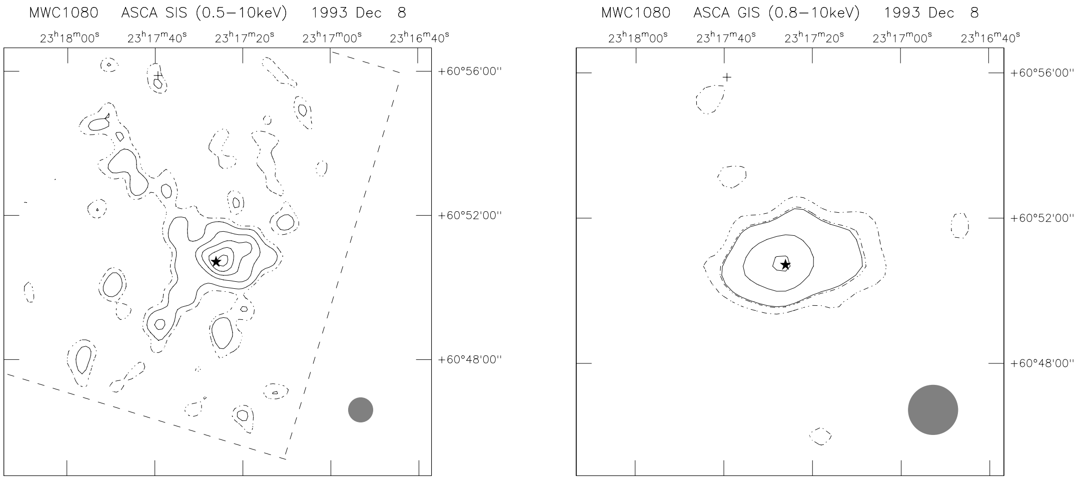

Figure 5.40: *ASCA* Images (*left*: SIS, *right*: GIS) of the MWC 1080 field. Details of symbols are the same as the captions of Figure 5.1,5.4, but the count rate per solid-line for the ASCA image is half (0.2 cts/pixel/obs for SIS and 0.5 cts/pixel/obs for GIS).

features at 4.2 and 5−6 keV (SIS) and 1.9, 3.1, 4.2 and 5.3 keV (GIS). We retry a spectral fitting with free abundance, but the reduced χ^2 value does not recover. The bumpy structure may be originated in several emission lines emanating from a different thermal component. We added one more thermal component with the common $N_{\rm H}$ (2T model in Table 5.5). Then, the reduced χ^2 value improves much though the fitting result is still rejected in the 90% confidence level. The $N_{\rm H}$ value in this 2T model is largely consistent with the visual extinction ($A_{\rm V}$ ∼1.92). We thus think that the excess of the χ^2 value is due to systematic errors. We also try the other 2T thermal models (i) with different $N_{\rm H}$ and (ii) setting the abundance parameter free. However these reduced χ^2 values are worse − 1.187 for (i) and 1.190 for (ii).

5.1.14 MWC 1080

MWC 1080 is an embedded star in the dark cloud Lynds 1238. The distance is measured at 2.2–2.5 kpc from the UVBR photometry of neighboring MS stars (Grankin et al. 1992) and the kinematic distance of the ^{13}CO molecular line (Canto et al. 1984). The spectral type is classified as B0e by Cohen and Kuhi (1979) using the He I emission lines, but the latter study using the other lines optimized for early-type stars indicated the spectral type to be early A with $A_{\rm V}$ ∼4.4 mag (Yoshida et al. 1992). MWC 1080 has a hierarchical multiple system. The primary star is an eclipsing binary with an orbital period of 2.8869 days (Grankin et al. 1992). It has a sub-arcsec companion (0.7″) which can also be a HAeBe, and another close companion 4.7″ apart (Leinert et al. 1997; Pirzkal et al. 1997). The binary system itself is surrounded by a small group of near-infrared stars (Testi et al. 1997). The CO molecular

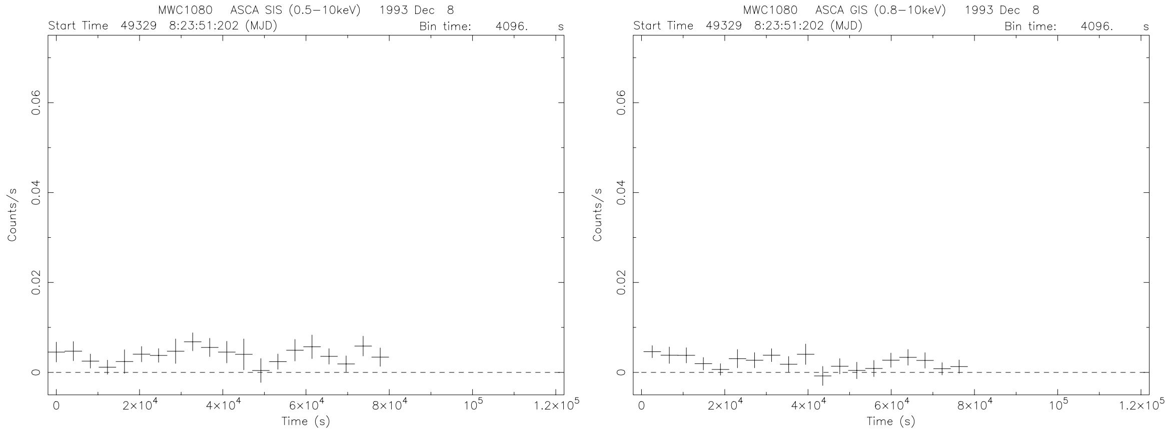

Figure 5.41: Light curves (*left*: SIS , *right*: GIS) of MWC 1080. See Figure 5.2 for details.

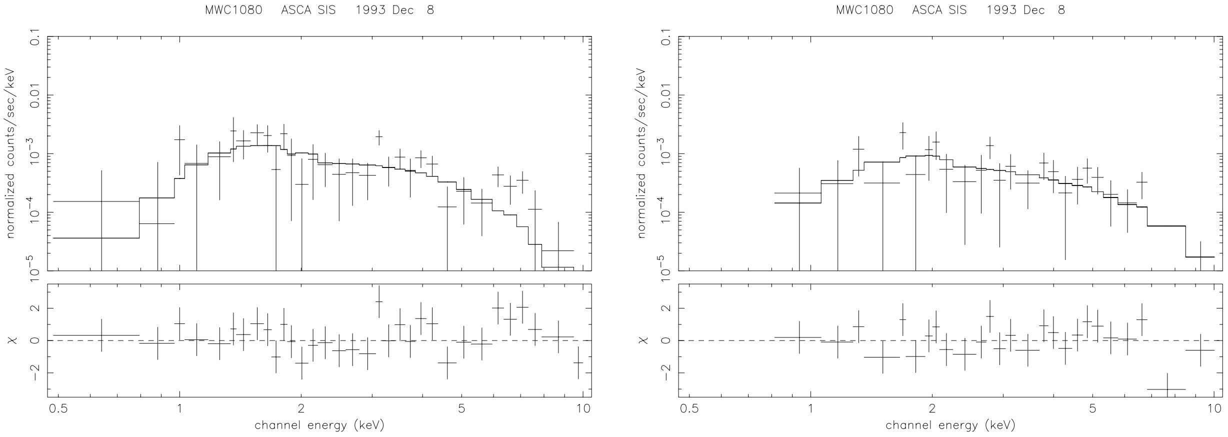

Figure 5.42: Spectra (*left*: SIS , *right*: GIS) of MWC 1080. See Figure 5.3 for details.

outflow were mapped by Canto et al. (1984) and Leinert et al. (1997). The blue- and red-shift components are concentric and centered on the star. It is thought to be a spherically symmetric appearing outflow. The spectrum shows the strong P-Cygni profile and the wind speed can be reached up to 1000 km s^{-1} (eg Yoshida et al. 1992). The spectrum also indicates the presence of ionizing winds (Benedettini et al. 1998). The X-ray emission was detected by Zinnecker and Preibisch (1994). The count rate detected by *ROSAT* was very small, but the x-ray luminosity is the largest among their samples log $L_{\rm X}$ (ergs s^{-1}) ∼32.

ASCA detect an x-ray source within the error circle of MWC 1080 as a relatively faint source (Figure 5.40). A fainter peak at the north east of this source can be another x-ray source. The source intensity (Figure 5.41) seems to oscillate periodically in a factor of four by about 40 ksec, but the constant fitting is also acceptable. The spectra could be reproduced with an absorbed 1T MeKaL model (Figure 5.42). The temperature is extremely high (kT $>$3.8 keV) and the absorption column density is modest ($N_{\rm H}$ $\sim$$10^{22}$ cm^{-2}), which is consistent with $A_{\rm V}$. A line-like excess is seen around 6.5 keV. When we put an additional component of Gaussian line with σ $\sim$0, the center energy is determined at 6.38 keV, corresponding to the neutral Fe. The total luminosity exceeds log $L_{\rm X}$ (ergs s^{-1}) $\sim$ 32 .

5.2 Non Detected Sources

5.2.1 BD+30°549

BD+30°549 is located in the NGC 1333 star forming region. In an *ASCA* GIS image, BD+30°549 suffered strongly contamination from GSC 2342359. The contamination is less significant in the SIS image, but the data quality is bad at the position of BD+30°549 by the telemetry saturation.

5.2.2 CoKu Tau 1

CoKu Tau 1 is classified as a potential HAeBe candidate in The et al. (1994). They did not quote its spectral type, but Strom and Strom (1994) estimated the spectral type at M2e so that it might be rather a low mass YSO. It exhibits bipolar outflows and accompanies a companion star (Padgett et al. 1999). *ASCA* and *ROSAT* PSPC detect no x-ray source around CoKu Tau 1 (Figure 5.1).

5.2.3 AB Aurigae

AB Aurigae is the brightest Herbig Ae star in the northern hemisphere (A0e: Bohm and Catala 1993). It is relatively close to the sun (d $\sim$144 pc, van den Ancker et al. 1998) and therefore have been well studied as a prototype of HAeBes. It has the photometric variability on the magnitude of one tenth, which could be caused by the changes of accretion rate or photospheric extinction (Skrutskie et al. 1996). Spectral lines, some of which have P-Cygni features, also exhibit high level variability with a periodic velocity modulation (Catala et al. 1999). It is surrounded by a circumstellar disk inclining of $\sim$76° (Mannings and Sargent 1997; Grady et al. 1999). There is no evidence of the presence of a companion star in the intensive binary searches (Leinert et al. 1997; Pirzkal et al. 1997; Testi et al. 1997). X-ray emission was first detected with *ROSAT* as a very faint source, log $L_{\rm X}$ (ergs s^{-1}) $\sim$29.5 (Zinnecker and Preibisch 1994).

AB Aurigae was fortunately within the *ASCA fov* of the SU Aurigae pointing (Figure

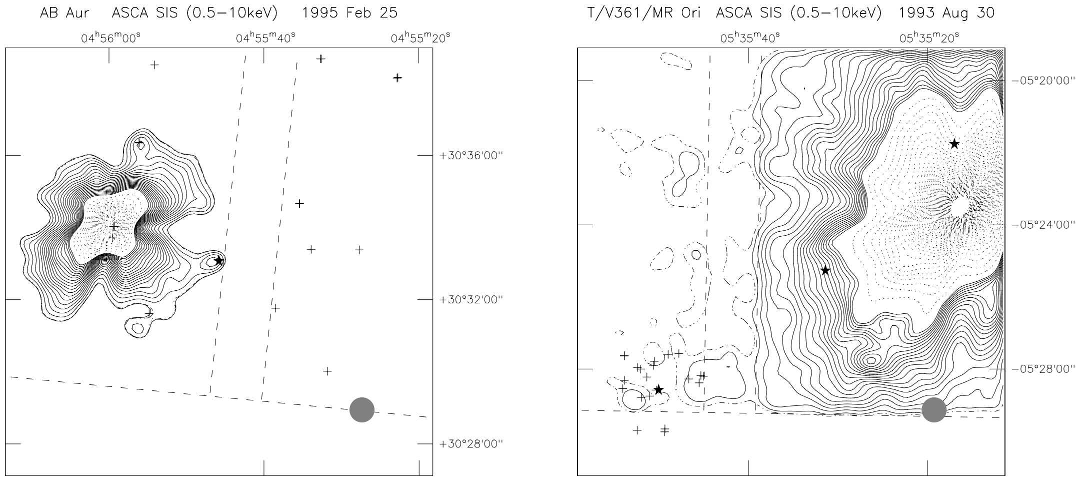

Figure 5.43: *ASCA* SIS images of the AB Aur (*left*) and T Ori (*right*) fields. For the T Ori field, Star marks are T Ori, V 361 Ori and MR Ori from left. Meanings of symbols are the same as Figure 5.1, 5.4, but lines above 20 solid-lines are shown with dotted lines by 2cts/pixel/obs. See Figure 5.1 for symbols.

5.43). SU Aurigae is $\sim 4'$ east from AB Aur and the brightest x-ray source in this region (Skinner and Walter 1998). The AB Aurigae region seems to have excess x-ray emission, but it is less significant merged with the emission of SU Aurigae – signal-to-noise ratio $\sim 1.5\sigma$ (0.5−10 keV), 2.0σ (0.5−2 keV).

5.2.4 MR Ori / V361 Ori / T Ori

V361 Ori is a B1.5 star in ZAMS or the β-Pic phase. It shows a large amplitude variable and has absorption line features in Hα and Mg, and inverse P-Cygni features in C_{IV} (Grady et al. 1996). Corporon and Lagrange (1999) did not conclude its binarity. *ROSAT* detected relatively strong x-rays, whose spectra suggest low-temperature plasma with a moderate absorption ($N_{\mathrm{H}} \sim 1.24 \times 10^{22}$ cm^{-2}, Gagné et al. 1995; Geier et al. 1995). MR Ori is an A2 star with $A_{\mathrm{V}} \sim 1.63$ (Gagné et al. 1995). *ROSAT* deep pointings determined the upper limit log L_{X} (ergs s^{-1}) <29.93. T Ori is located at about $10'$ south-east from the Orion Trapezium. Shevchenko and Vitrichenko (1994) noticed that T Ori would be an eclipsing binary with the period of 14.3 days, but Corporon and Lagrange (1999) did not find any eclipsing phenomenon. There is a plausible companion star at $7''.7$ from the primary star (Hillenbrand 1995; Leinert et al. 1997). The L_{X} upper limit was determined with *ROSAT* log L_{X} (ergs s^{-1}) <29.89 (Gagné et al. 1995).

In the *ASCA* SIS image (August 1993, Figure 5.43), x-rays from the Orion Trapezium strongly contaminate MR Ori and V361 Ori regions. On the other hand, we find no x-ray

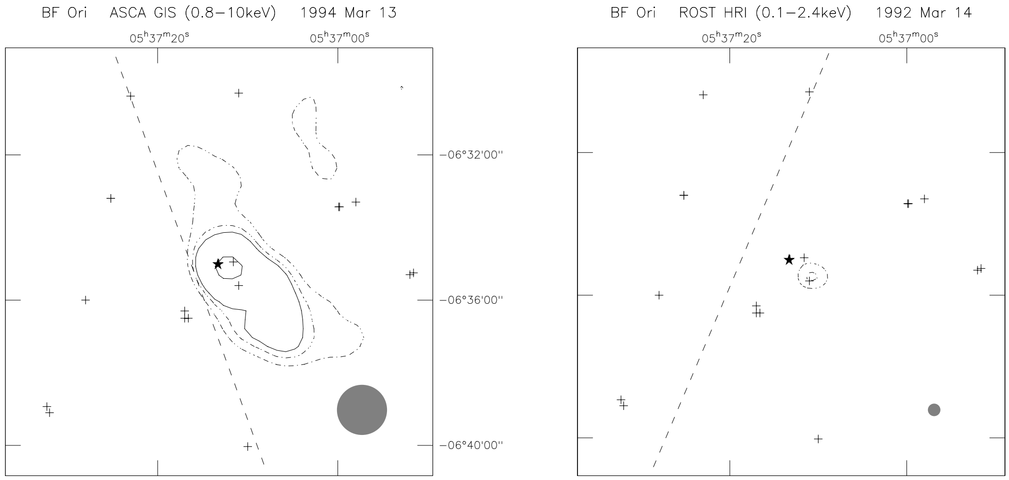

Figure 5.44: *ASCA* GIS(*left*) and *ROSAT* (*right*) images of the BF Ori field. See Figure 5.1 and 5.4 for symbols.

emission at the position around T Ori though there is small peak (S/N ∼4.3) at south-east from T Ori, which we identify as 648 in Ali and Depoy (1995) from a *ROSAT* image.

5.2.5 BF Ori

BF Ori is an isolated Herbig Ae star (A5−6IIIe) and showing β-Pic phenomenon (van den Ancker et al. 1998; de Winter et al. 1999). It is photometric variable with a large amplitude (Shevchenko et al. 1993). The distance is determined to be more than 210 pc with *HIPPARCOS* and estimated at ∼430 pc assuming a membership of the Orion OB1 c association (Warren and Hesser 1977; van den Ancker et al. 1998). A wing feature, inverse P-Cygni profiles and absorption lines indicate the presence of infalling materials (Welty et al. 1992; de Winter et al. 1999).

In the *ASCA* GIS image, we detect an x-ray source on BF Ori, but unsharp image on the edge of GIS allow another three candidates of the optical counterpart; [PC87b] 12, [VSS88] 3 and V865 Ori (error circle $\sim 1'$). In the *ROSAT* image, we find an x-ray source at the position of V865 Ori and not BF Ori. Pravdo and Angelini (1995) reported plausible x-ray detection of BF Ori with the same data, but the coordinate of BF Ori in Pravdo and Angelini (1995) is about $1'$ south west from the *HIPPARCOS* coordinate. We thus estimate the source upper-limit flux with the *ROSAT* data (See Table 5.2). We check the *ASCA* spectrum because BF Ori might be a hard x-ray source. However we find no enhancement above the *ROSAT* band so that we conclude that the x-ray emission only comes from V865 Ori.

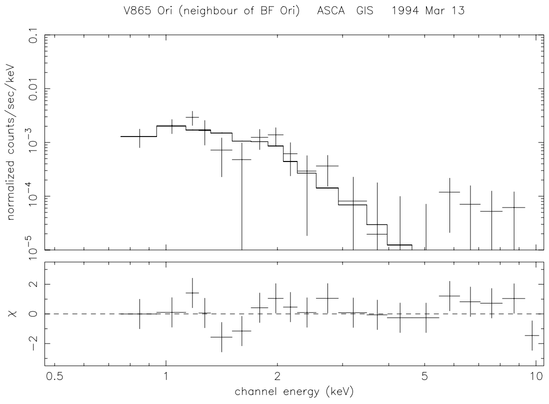

Figure 5.45: Spectrum of an x-ray source in the BF Ori field. See Figure 5.3 for details.

5.2.6 Z CMa / LkHα 218 / LkHα 220

Z CMa, LkHα 218 and LkHα 220 belong to the star forming region CMa R1-I (Shevchenko et al. 1999). Z CMa is classified as a member of the FU Ori class of variables. It is a binary with a separation of 0.1″, and both the primary and secondary are thought to be HAeBes (eg Leinert et al. 1997). It has a unique spectrum, dominated by its gaseous accretion disk (see intro. of Shevchenko et al. 1999) and showing a jet phenomenon. LkHα 218 showed the polarimetry in U and V (variable) band (Yudin and Evans 1998). *ROSAT* detected x-ray emission from Z CMa (Zinnecker and Preibisch 1994).

The x-ray emission is enhanced on a large region around Z CMa, LkHα 218 and LkHα 220, probably because weak x-ray emission from clustering sources form diffuse like image. A hard x-ray peak (2–10 keV) seems to be at Z CMa. Clear x-ray peaks are present around LkHα 218 and LkHα 220 as well, but these peaks are obscured and have another candidates. We therefore check the *ROSAT* data. The x-ray peak near LkHα 218 computed by the detect command $(\alpha, \delta) = (07^h02^m43^s.3, -11^\circ\ 27'\ 17'')$ has better coincidence with the variable star FZ CMa (sp. type: B2.5IV-V). On the contrary, there is no x-ray source around LkHα 220. Though Damiani et al. (1994) say that Einstein detect the x-ray emission from LkHα 218 of log $L_{\rm X}$ (ergs s^{-1}) ∼31.59, the x-ray source is probably PPM 713454 about 20″ south west from LkHα 218, which is also detected in the *ROSAT* image.

5.2.7 HD 97048

HD 97048 is an embedded B9−A0 star located in the Chameleon I dark cloud and associated with the reflection nebula Ced 111. Figure 2 in Comerón et al. (1999) helps us to grasp the surrounding environs. HD 97048 shows remarkable spectrum variability suggesting the intermittent phases of mass loss (Irvine and Houk 1977). It is one of the few stars with unusual 3.43 and 3.52 μm emission features. HD 97048 itself has no evidence of a binary star (Corporon and Lagrange 1999). Feigelson et al. (1993) surveyed the Chameleon I cloud with *ROSAT*, but they do not detect x-rays from HD 97048 due to the short exposure (~6 ksec). Zinnecker and Preibisch (1994) first detected its weak x-ray emission with a *ROSAT* deep pointing (~32 ksec).

ASCA observed the Chameleon I dark cloud two times. In each observation, we did not find clear evidence of the x-ray emission from HD 97048. In the GIS image of ChamI IV (May 1994, *top panel* in Figure 5.46), there is an x-ray source close to HD 97048, but we have another candidate HM16, which is a TTS surrounded by a dust shell (Feast and Glass 1973). In the SIS0 image, HD 97048 unfortunately drop on a chip gap. We, however, find a faint peak at $\sim 30''$ north from HD 97048. This can be the peak of HM 16 or an artificial peak made by the tail of HD 97048. We thus compared the SIS spectrum with the GIS spectrum. Both spectra accept an absorbed 1T thin-thermal model (Figure 5.47). The best-fit parameters are exactly alike; large absorption column density ($N_{\rm H}$ $\sim 4\times10^{22}$ cm^{-2}) and relatively high temperature (kT ~2 keV). The SIS flux is 75% of the GIS one but the error bars also include the GIS value. If the SIS peak is artificially made by the tail of HD 97048, the source region of SIS covers less than a quarter of the total effective area and the flux should be less than a quarter of the GIS one. We therefore conclude that the x-rays are not coming from HD 97048 but from probably HM16. Cambresy et al. (1998) estimated the $A_{\rm V}$ of HM16 at 5.3, which corresponds to $N_{\rm H} \sim 1.1\times10^{22}$ cm^{-2}, almost a quarter of the observed $N_{\rm H}$. The x-ray counterpart might be hidden another PMS nearby HM16. As for the timing analysis, a constant model is acceptable for both light curves.

In the GIS image of ChamI V (*bottom panel* in Figure 5.46), we find no bright source around HD 97048. In the SIS image, we see a small excess halfway between HD 97048 and HM16 though it is on a tail of SZ19. This source shows no evidence of time variation. The spectrum (Figure 5.47) is reproduced by an absorbed 1-T thermal model with relatively high temperature and moderate $N_{\rm H}$, which is not so large as the $N_{\rm H}$ of the source in ChamI IV and almost the same as the converted $N_{\rm H}$ of HM16, but larger than the converted $N_{\rm H}$ of HD 97048. It suggests that the x-ray emission mainly comes from HM16.

We do not find the clear evidence of x-ray emission from HD 97048, but we find the x-ray emission from an embedded source probably associated with HM16. The properties of HM16 is not well known, but Feast and Glass (1973) reports that the optical spectrum resembles the Herbig Be star R Mon. Intensive observations are needed for HM16.

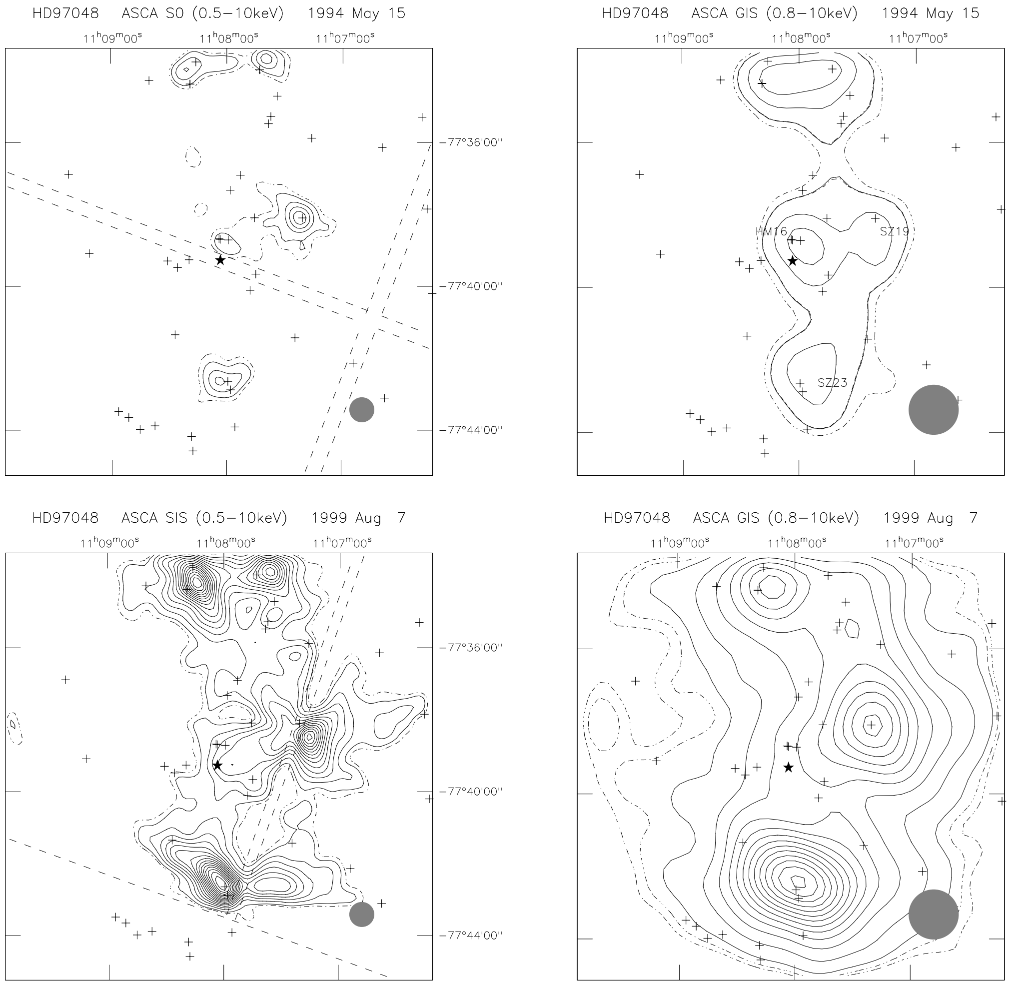

Figure 5.46: *ASCA* images of the HD 97048 field. Top panels are of ChamI IV (*left*: SIS, *right*: GIS) and bottom panels are of ChamI V (*left*: SIS, *right*: GIS). Names of surrounding sources are written in the upper right panel. Details of symbols are the same as the captions of Figure 5.1, but the count rate per solid-line of ChamI IV is half (0.2 cts/pixel/obs for SIS and 0.5 cts/pixel/obs for GIS).

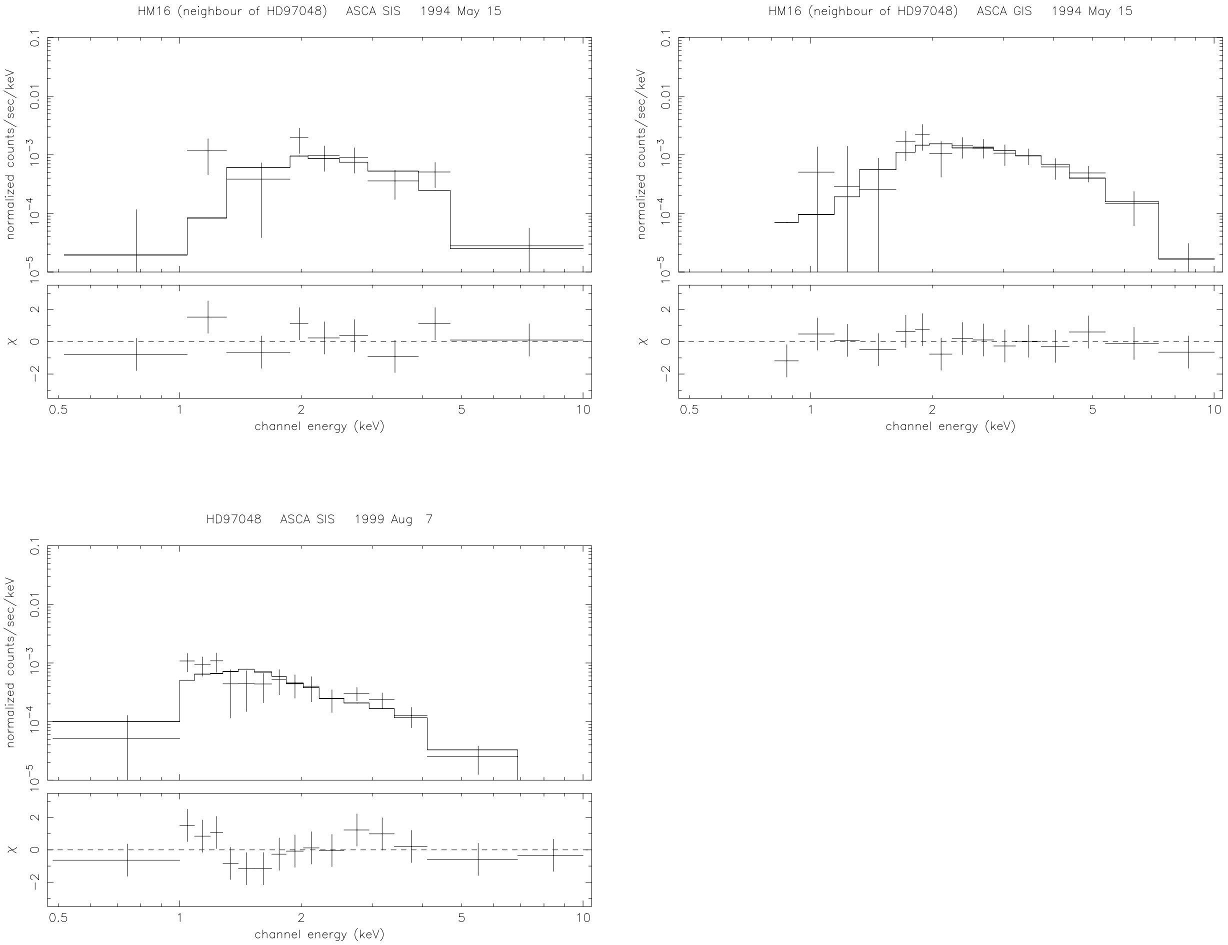

HM16 (neighbour of HD97048) ASCA SIS 1994 May 15

HM16 (neighbour of HD97048) ASCA GIS 1994 May 15

HD97048 ASCA SIS 1999 Aug 7

Figure 5.47: Spectra in ChamI IV(*top left*: SIS0, *top right*: GIS) and in ChamI V (*bottom left*: SIS). See Figure 5.3 for details.

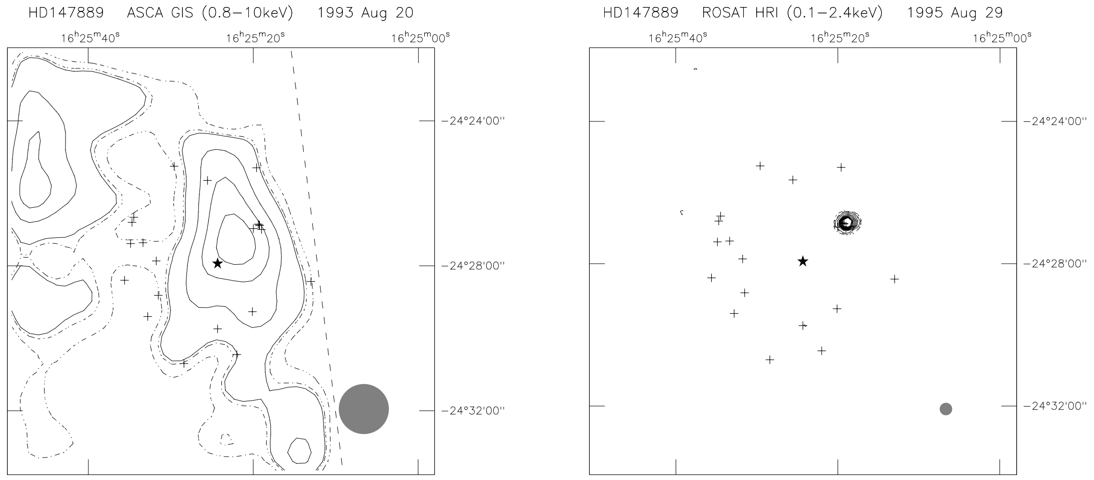

Figure 5.48: *ASCA* (*left*) and *ROSAT* HRI (*right*) images of the HD 147889 field. Meanings of symbols are the same as the captions of Figure 5.1, 5.4, but the count rate per solid-line for the ASCA image is half (0.2 cts/pixel/obs).

5.2.8 HD 97300

HD 97300 is located in the Chameleon I dark cloud at d ∼188 pc (Bertout et al. 1999). It is a B9 star near on the ZAMS in the HR diagram (Whittet et al. 1997). Feigelson et al. (1993) detected the weak x-ray emission corresponding to log $L_{\rm X}$ (ergs s^{-1}) ∼29.0. *ASCA* do not find any apparent x-ray source at the position of HD 97300. It is near on a bright x-ray source, which is just on a SIS chip gap. We at least confirm that no hard source is detected at HD 97300.

5.2.9 HD 147889

HD 147889 is located at a bright side of the Rho-Ophiucus dark cloud. van den Ancker et al. (1997) determined the distance at ∼140 pc using the *HIPPARCOS* data. They quoted that it might be a very young star (∼0.1 Myr). It has a double-lined feature in the optical spectrum, which suggests a spectroscopic binary of two B2 stars orbiting every ∼5 days (Haffner and Meyer 1995). The X-ray emission was not detected and only the upper limit is determined assuming $N_{\rm H}$ ∼0, log $L_{\rm X}$ (ergs s^{-1}) < 27.5 (Casanova et al. 1995).

ASCA detect an X-ray source at the position of HD 147889 (Figure 5.48). Because it is on the edge of GIS *fov* where the position uncertainty is large, we check *ROSAT* images in three observations from March 1991 to August 1995, which include a HRI deep pointing for ∼50 ksec. In all observations, we do not find any X-ray source in the HD 147889 region but two X-ray sources, the A2 star 2E 1622.3-2420 located at 100″ north-west and the Ae star V852 Oph located at 100″ south. The spectrum accepts an absorbed 1T model with

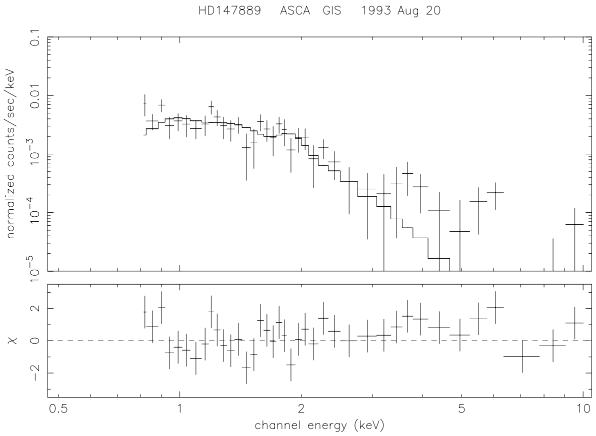

Figure 5.49: *ASCA* spectrum of the HD 147889 region. See Figure 5.3 for details.

slightly absorbed cool plasma ($N_{\rm H}$ ~5×10^{21} cm^{-2}, kT ~0.75 keV). Though a small residue is seen in the hard band, the flux is dominant in the *ROSAT* band (0.8−2 keV). It is probably originated in 2E 1622.3-2420 and V852 Oph.

5.3 Summary

With the *ASCA* satellite, 16 sources among 40 targets are detected above the 5 σ threshold (Table 5.1, 5.2). The detection rate (~ 38%) is smaller than the detection rate of a *ROSAT* survey (~ 52%, Zinnecker and Preibisch 1994) because the detection upper-limit is high due to source contamination from nearby bright sources (eg AB Aur, HD 97048 and Z CMa). Nevertheless, a few embedded sources (eg MWC 297 and V921 Sco) are detected with *ASCA* for the first time, thanks to its hard x-ray imaging capability. Number of detected sources on each spectral type is summarized in Figure 5.50. To see whether there is any bias effect against distance, we make a plot of distant *vs.* x-ray luminosity (Figure 5.51). There is no bright samples near from the sun, but when we see sources with same distance, the x-ray luminosity scatters in a wide range. We therefore do not think that samples are seriously affected by a bias effect against distance.

8 sources among 16 detected sources exhibited time variation (50%, Table 5.4). Because the sensitivity of the temporal time variation strongly depends on source intensity, we also see variability of the sources obtained above total 1000 photon counts through observations. Though the sample number decrease by eight, six sources are x-ray variable and the percentage of variable sources increases up to ~75%.

Every spectrum is successfully reproduced with an absorbed one or two temperature thin-thermal (MeKaL) model (Table 5.5). The plasma temperature ranges between kT $\sim$1$-$5 keV, which is significantly higher than main-sequence OB stars (kT <1 keV).

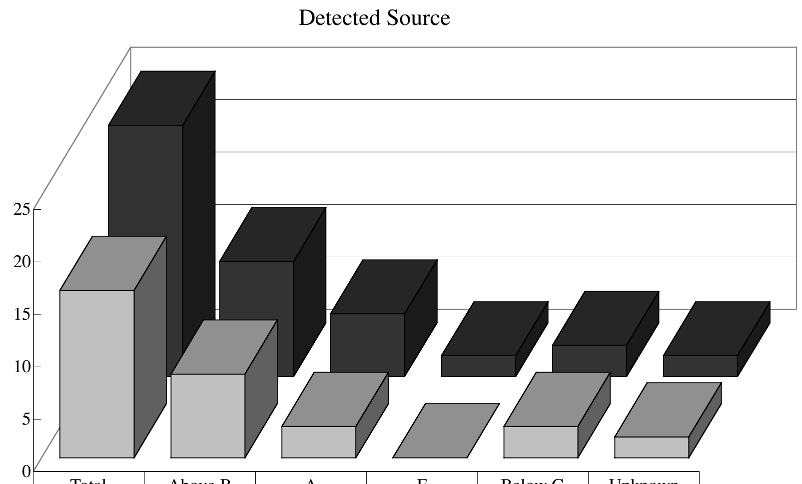

	Total	Above B	A	F	Below G	Unknown
▨ Detection	16	8	3	0	3	2
■ Non Detection	24	11	6	2	3	2

Figure 5.50: Number of detected sources in the *ASCA* survey. Sources with uncertain range in spectral type are grouped into the intermittent spectral type, but a few sources with wide uncertain range (eg IRAS 12496-7650) are grouped into the unknown. Spectral type below G includes the HAeBe progenitor EC95, but the others might be genuine low mass stars.

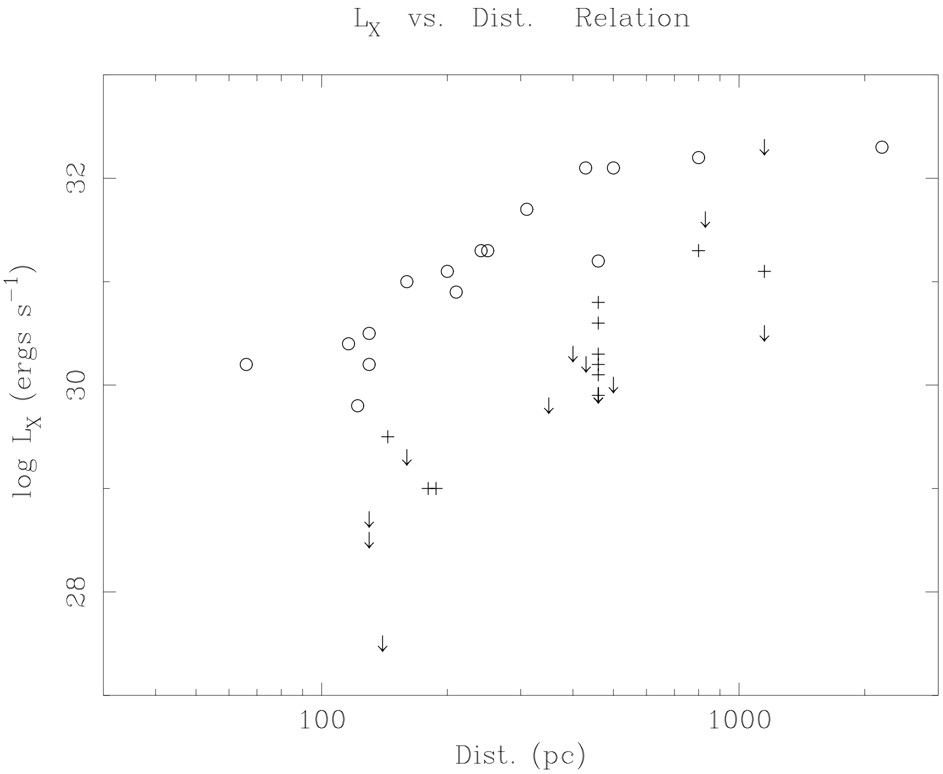

Figure 5.51: Distance *vs.* x-ray luminosity relation. Circles show the L_X values of the *ASCA* detected sources. Plus marks and arrows (upper-limit) show the values of the non-detected sources – L_X values are of the ROSAT estimates except for HD 76534, converted to the *ASCA* band assuming $kT = 2$ keV.

Table 5.1: *ASCA* detected sources

Objects	Obs. ID	Detected Position							Net count		
		R.A. (2000)			Dec. (2000)			Det.	SIS	GIS	Total
		h	m	s	°	′	″		cnts %	cnts %	cnts
V892 Tau	IC359	4	18	39.8	28	19	16	S	722 (59)	– (–)	722
V380 Ori	L1641N	5	36	23.8	−6	43	18	G2	– (–)	109^b(33)	109
VY Mon (/G2)	PSRJ0631	6	31	3.1	10	26	46	G	– (–)	338 (36)	338
T Cha	ChamIII	11	57	19.1	−79	21	30	S	4248 (76)	2509 (74)	6757
HD104237	HD104237	12	0	6.2	−78	11	29	S	2427 (84)	916 (74)	3343
IRAS12496-7650	ChamII	12	53	16.5	−77	7	6	G	– (–)	100 (31)	100
HR5999	Lupus3	16	8	34.9	−39	6	12	S	143 (48)	– (–)	143
HR6000	Lupus3	16	8	33.4	−39	5	25	S	1420 (95)	– (–)	1420
2HR†	Lupus3							G	– (–)	3146 (78)	3146
V921 Sco	Gal R 2	16	59	8.7	−42	42	30	G	– (–)	151 (38)	151
MWC297	MWC297 1	18	27	37.9	−3	49	36	S	353 (62)	257 (67)	610
	MWC297 2								1023 (79)	904 (87)	1927
	MWC297 3								528 (64)	349 (70)	877
EC95	Serp	18	29	58.3	1	12	43	S	3216 (75)	3679 (70)	6895
S CrA	R CrA 1	19	1	7.9	−36	57	11	S	122 (34)	– (–)	122
	R CrA 3								– (–)	337^b(65)	337
	R CrA 6								– (–)	421 (71)	421
TY CrA	R CrA 1	19	1	40.8	−36	52	31	S	524 (67)	– (–)	524
	R CrA 4								75^a(56)	– (–)	75
	R CrA 6								437 (71)	– (–)	437
HD176386	R CrA 1	19	1	38.7	−36	53	18	S	227 (49)	– (–)	227
	R CrA 4								45^a(52)	– (–)	45
	R CrA 6								228 (49)	– (–)	228
TYHD†	R CrA 1								– (–)	1488 (78)	1488
	R CrA 2								– (–)	676 (64)	676
	R CrA 3								– (–)	1585^c(78)	1585
	R CrA 4								– (–)	510 (73)	510
	R CrA 5								– (–)	543 (91)	543
	R CrA 6								– (–)	1029 (68)	1029
HD 200775	HD200775	21	1	34.9	68	10	1	S	3361 (85)	1641 (69)	5002
MWC 1080	MWC1080	23	17	24.0	60	50	43	S	273 (33)	185 (27)	458

Det.: Detector measuring source positions (S: SIS, G: GIS), Net count: background subtracted source counts [Parentheses – source event ratio defined as “source event / total event”, Total – Photon counts of SIS + GIS], †2HR/TYHD: GIS data merged with HR 5999 (TY CrA) and HR 6000 (HD 176386), a: s0 data, b: g2 data, c: g3 data

Table 5.2: *ASCA* non-detected sources

Objects	*ASCA*						*ROSAT*					
	Obs. ID	Intensity Upper limit Counts	Flux	Det.	log L_X	Note	Ref.	Intensity Counts	Flux	log L_X	log $\frac{L_X}{L_{bol}}$	Note
BD 30°549	SVS13	$2.1\ 10^{-2}$	$1.1\ 10^{-12}$	G	<31.2	con.	d			<29.8	< -4.9	
CoKu Tau 1	IC359	$4.4\ 10^{-2}$	$1.9\ 10^{-12}$	S	<30.8	con.	f	$<1.5\ 10^{-3}$	$<6.9\ 10^{-14}$	<29.3	< -4.3	con.
AB Aur	SU Aur	$3.1\ 10^{-2}$	$7.4\ 10^{-13}$	S	<30.3	con.	a			29.5	-5.7	
IX Ori	Ori Trap1	$2.5\ 10^{-2}$	$9.1\ 10^{-13}$	G	<31.4	con.	b			30.3	–	
V372 Ori	Ori Trap1	$3.5\ 10^{-2}$	$1.3\ 10^{-12}$	G	<31.5		b			30.3	-5.5	
YZ Ori	Ori Trap1	$1.8\ 10^{-2}$	$6.2\ 10^{-13}$	G	<31.2		b			30.7	-2.9	
HD 36939	Ori Trap1	$4.6\ 10^{-2}$	$1.7\ 10^{-12}$	G	<31.6		b			<29.9	< -5.6	
HD245185	Lamb Ori	$1.6\ 10^{-2}$	$3.3\ 10^{-13}$	S	<30.8		f	$<2.4\ 10^{-3}$	$<9.7\ 10^{-14}$	<30.3	< -4.6	
LP Ori	Ori Trap1	$3.6\ 10^{-1}$	$9.2\ 10^{-12}$	S	<32.4	con.	b			30.1	-6.6	
MR Ori	Ori Trap1	2.7	$9.4\ 10^{-11}$	S	<33.4	con.	b			<29.9	< -5.2	
V361 Ori	Ori Trap1	$9.8\ 10^{-1}$	$2.3\ 10^{-11}$	S	<32.8	con.	b			30.9	-5.4	
T Ori	Ori Trap1	$6.5\ 10^{-2}$	$1.6\ 10^{-12}$	S	<31.6	con.	b			29.9	-5.3	
BF Ori	L1641N	—	$5.8\ 10^{-13}$	G	<31.1	ano.	f	$<2.2\ 10^{-3}$	$<6.7\ 10^{-14}$	<30.2	< -3.5	
MWC120	Ori OB1	$9.5\ 10^{-3}$	$3.1\ 10^{-13}$	G	<31.0		f	$<2.7\ 10^{-3}$	$<3.3\ 10^{-14}$	<30.0	< -4.9	
V590 Mon	15 Mon	$4.8\ 10^{-2}$	$1.2\ 10^{-12}$	S	<32.0		f	$4.2\ 10^{-3}$	$2.4\ 10^{-13}$	31.3	-4.8	
LkHα 218	Z CMa	$9.9\ 10^{-2}$	$4.4\ 10^{-12}$	G	<32.8		f	$<3.7\ 10^{-2}$	$<1.2\ 10^{-12}$	<32.3	< -3.4	con.
Z CMa	Z CMa	$1.9\ 10^{-2}$	$8.9\ 10^{-13}$	S	<32.1		a			31.1	-5.8	
LkHα 220	Z CMa	$8.5\ 10^{-3}$	$2.8\ 10^{-13\dagger}$	G	<31.6	con.	f	$<7.0\ 10^{-4}$	$<2.2\ 10^{-14}$	<30.5	< -5.4	
HD76534	Vela Shrap	$1.0\ 10^{-2}$	$4.3\ 10^{-13}$	G	<31.6		n			–	–	
HD97048	ChamI V	—	$1.8\ 10^{-13}$	S	<29.8	ano.	a			29.0	-6.2	
HD97300	ChamI I	$5.1\ 10^{-2}$	$2.3\ 10^{-12}$	G	<31.0	con.	c			29.0	-6.1	
HD147889	Rho-Oph	—	$1.7\ 10^{-12}$	G	<30.6	ano.	e			<27.5	< -9.4	
Hen 3-1191	Gal R 1	$2.3\ 10^{-2}$	$7.5\ 10^{-13\dagger}$	G	–		n			–	–	
R CrA	R CrA 1	$1.4\ 10^{-1}$	$5.2\ 10^{-12}$	S	<31.0	con.	a			<28.7	< -7.0	
T CrA	R CrA 1	$4.0\ 10^{-2}$	$1.5\ 10^{-12}$	S	<30.5	con.	a			<28.5	< -6.0	

ASCA data – Intensity upper limit [Counts : cnts s^{-1}, Flux: ergs $cm^{-2}\ s^{-1}$]: 3σ level or count rate of detected events within selected regions for contaminated sources (Counts), estimated from $20''$ half-box for SIS and $40''$ for GIS. Unabsorbed flux upperlimit in the *ASCA* band (Flux, 0.5–10 keV) caluculated using the PIMMS package, assuming thin-thermal plasma of $kT \sim$1.3keV and $N_{\rm H}$ converted from $A_{\rm V}$., Log $L_{\rm X}$ [ergs s^{-1}]: unabsorbed luminosity in the *ASCA* band, Det.: Detector measured count rate (S: SIS, G: GIS)., Note: sources marked "con." suffer x-ray contamintion from nearby sources., sources marked "ano." are identified as the other objects (BF Ori: V865 Ori, HD 97048: $11^h7^m58^s.5$, $-77°\ 39'\ 13''$, HD 147889: 2E 1622.3-2420 and V852 Oph)., † assuming $N_{\rm H} = 0.0$.

ROSAT data – Ref.: Reference of x-ray luminosity, [a: Zinnecker and Preibisch (1994), b: Gagné et al. (1995), c: Feigelson et al. (1993), d: Preibisch (1997), e: Casanova et al. (1995), f: this work, n: no *ROSAT* pointing observation.], Intensity [Counts: cnts s^{-1}, Flux: ergs $cm^{-2}\ s^{-1}$]: 3σ upper limit or count rate of detected events using the PIMMS package (Counts), and unabsorbed flux in the *ROSAT* band (Flux, 0.1–2.4 keV) calculated using the PIMMS package, assuming thin-thermal plasma of $kT \sim$1.3keV and $N_{\rm H}$ converted from $A_{\rm V}$., Log $L_{\rm X}$ [ergs s^{-1}]: unabsorbed luminosity in the *ROSAT* band (0.1–2.4 keV)., Note: "con." suffer x-ray contamintion from nearby sources.

Table 5.3: Selected regions for event extraction

Target	Det.	Source	Background	
V892 Tau	S	c_3	sym V1023 Tau	*sr* includes V410 x-ray 7.
V380 Ori	G	c_3	a_3_6	
VY Mon	G	e_4.5_2.5	*sf* (sym optical axis)	
T Cha	S	c_3	*sf*	
	G	c_3	a_3_6	
HD 104237	S	c_2.5	whole chip ex. *sr*	
	G	c_3	a_3_6	
IRAS 12496	G	c_3	a_3_6	
HR 5999	S	e_.66_.25	sym HR 6000	optimized to reduce HR 6000
HR 6000	S	e_2_.66	*sf*	ex. of the HR 5999 peak
HR 5999+6000	G	c_2.5	sym GSC 07851-00426[†]	
V921 Sco	G	c_3	a_3_6	
MWC 297	S	c_3	a_3_4.4	
	G	c_3	a_3_6	
EC 95	S	c_3	b_9_3	
	G	c_3	a_3_6	
TY CrA	S	e_.74_.53	sym HD 176386	
HD 176386	S	e_.64_.42	sym TY CrA	
TY CrA+HD	G	c_2.5	sym the protostars	*sf* *br* for 6th obs.[†2].
S CrA	S	c_1.5	sym CrA 1	
HD 200775	S	c_2.5	*sf*	
	G	c_3	sym the SE source	
MWC 1080	S	c_2.5	*sf*	
	G	c_3	a_3_6	
AB Aur	S	c_1	sym SU Aur	
HD 97048[†3]	S	c_0.5	b_1.27_1.27	*br* the other tail of SZ19
	G	e_1.25_1.63	symax SZ19 SZ23	ex. of the SZ19 peak
HD 97048[†4]	S	c_.67	c_.67[†5]	small *sr* to reduce SZ19
HD 147889	G	c_3	e_3_7.5	sym DoAr21
Mon R2	G	c_5	*sf*	

c_*num*: *num* arcmin radius circle centered on a target, e_*num*1_*num*2: ellipse with *num*1 arcmin long and *num*2 arcmin short axes. a_*num*1_*num*2: annular circle with *num*1 arcmin inner and *num*2 arcmin outer radius centered on a target, b_*num*1_*num*2: *num*1 arcmin × *num*2 arcmin box sym: symmetrical region with respect to *sth*, symax: symmetrical region with respect to the axis between *sth*1 and *sth*2, nu: not used, *sr*: source region, *br*: background region, *sf*: source free region

[†] GSC 07851-00426: the x-ray luminous T-Tauri star located at the east from HR 6000, [†2] to avoid the flare contamination of CrA 3 and V702 CrA, [†3] CHAI_III, [†4] CHAIBROWN, [†5] There is the brown dwarf Hα3 at the another tail of SZ19 of the same CCD chip, whose x-ray emission *ROSAT* detected by Neuhauser and Comeron (1998). The background is therefore selected from another CCD chip (S0C2/S1C0).

Table 5.4: Result of *ASCA* timing analyses

Objects	St.	Det.	Bin (sec)	Constant Fittings		
				Mean (cnts s^{-1})	$\Delta\chi^2$	Var.
V892 Tau		S	2048	1.5 10^{-2}	1.42 (27)	n
		S^H	2048	5.2 10^{-3}	1.13 (27)	n
V380 Ori		G2	2048	2.4 10^{-3}	0.94 (33)	n
VY Mon (/G2)		G	2048	8.9 10^{-3}	1.69 (70)	y
T Cha		S	2048	2.9 10^{-2}	3.88 (69)	y
		G	2048	1.7 10^{-2}	2.75 (74)	y
HD104237		S	2048	4.0 10^{-2}	1.38 (30)	n
		G	2048	1.6 10^{-2}	1.58 (29)	y
IRAS12496		G	2048	1.6 10^{-3}	1.00 (30)	n
		G	4096	1.7 10^{-3}	1.22 (16)	n
HR5999		S	2048	3.4 10^{-3}	1.08 (21)	n
HR6000		S	2048	3.8 10^{-2}	2.39 (21)	y
2HR		G	2048	3.6 10^{-2}	3.70 (39)	y
V921 Sco		G	2048	6.3 10^{-3}	0.51 (11)	n
MWC297	1	S	2048	1.7 10^{-2}	0.81 (10)	n
	1	G	2048	1.2 10^{-2}	0.87 (10)	n
	2	S	2048	5.0 10^{-2}	1.84 (7)	n
	2	G	2048	8.7 10^{-2}	3.11 (6)	y
	3	S	2048	1.5 10^{-2}	1.18 (13)	n
	3	G	2048	1.0 10^{-2}	5.68 (13)	y
EC95		S	2048	1.7 10^{-2}	2.13 (88)	y
		G	2048	2.0 10^{-2}	1.81 (93)	y
S CrA	1	S	2048	1.1 10^{-3}	2.40 (35)	y
	3	G	4096	3.8 10^{-3}	2.52 (33)	y
	6	G	4096	5.2 10^{-3}	2.11 (25)	y
TY CrA	1	S	2048	6.4 10^{-3}	0.79 (34)	n
	4	S	2048	5.8 10^{-3}	1.09 (12)	n
	6	S	2048	6.7 10^{-3}	0.90 (39)	n
HD176386	1	S	2048	2.8 10^{-3}	0.83 (33)	n
	4	S	2048	4.4 10^{-3}	0.40 (12)	n
	6	S	2048	2.1 10^{-3}	1.21 (39)	n
TYHD	1	G	2048	1.4 10^{-2}	1.67 (36)	y
	2	G	2048	1.3 10^{-2}	1.42 (37)	y
	3	G	4096	4.0 10^{-2}	3.14 (33)	y
	4	G	2048	1.5 10^{-2}	1.79 (14)	y
	5	G	2048	1.8 10^{-2}	0.84 (21)	n
	6	G	2048	6.7 10^{-3}	0.90 (39)	n
HD200775		S	2048	3.6 10^{-2}	1.32 (45)	n
		G	2048	1.6 10^{-2}	1.04 (47)	n
MWC1080		S	4096	3.6 10^{-3}	0.64 (19)	n
		G	4096	2.3 10^{-3}	0.78 (18)	n
X-ray sources identitified as other objects						
BF Ori		G	2048	1.8 10^{-3}	1.30 (33)	n
HD97048	2	S0	2048	1.9 10^{-3}	0.71 (13)	n
	2	G	2048	3.9 10^{-3}	1.14 (18)	n
	3	S	4096	1.1 10^{-3}	0.86 (47)	n
	3	S	8192	1.1 10^{-3}	0.78 (24)	n
HD147889		G	2048	4.5 10^{-3}	1.44 (32)	n

St.: Number of observation ID., Det.: detector (S: SIS, G: GIS, ^{H}hard band [2-10 keV])., Bin.: binning time scales of light curves., Mean: average count rates derived from constant fittings., $\Delta\chi^2$: parentheses show the degree of freedom., Var.: sources showing time variation above 90% confidence level. 2HR/TYHD: GIS data merged with HR 5999 (TY CrA) and HR 6000 (HD 176386),

Table 5.5: Result of *ASCA* spectral analyses

Objects	St.	Det.	ML	kT	$E.M.$	N_{H}	$\Delta\chi^2$	Flux	L_{X}	L_X/L_{bol}
V892 Tau		S	1T	2.0 (1.6–2.5)	54.0 (53.9–54.1)	1.2 (0.9–1.6)	0.99 (51)	1.22	—	—
		S	2T	2.0 (fix)	54.0 (fix)	1.8 (fix)	0.87 (54)	1.02	31.0	–4.4
				0.5 (0.3–0.7)	54.3 (53.9–55.4)	1.7 (1.2–2.8)		0.20	31.3^{†1}	—
V380 Ori		G2	1T	3.2 (0.7–11.0)	54.1 (53.9–54.3)^{†0}	0.0 (0.0–1.5)	1.31 (14)	0.59	31.2	–4.4
		G2	1T^{f}	2.4 (1.3–6.1)	54.2 (54.0–54.4)	0.3 (fix)	1.25 (15)	0.68	31.2	–4.3
VY Mon (/G2)	LS	G	1T	2.9 (2.0–4.6)	55.1 (55.0–55.3)	0.6 (0.2–1.0)	1.40 (42)	1.21	32.2	–5.4^{†4}
	LS	G	1T^{g†2}	2.2 (1.6–3.3)	55.2 (55.0–55.4)	0.8 (0.4–1.2)	1.23 (40)	1.18	32.2	–5.4^{†4}
	HS	G	1T	6.0 (3.8–12.3)	55.2 (55.1–55.3)	0.4 (0.1–0.8)	1.29 (45)	2.49	32.4	–4.1^{†4}
	HS	G	1T^{ls}	20.3 (3.0–)	54.8 (54.7–55.2)	0.6 (0.0–2.5)	1.28 (45)	1.24	32.1	–4.4^{†4}
T Cha		SG	1T	2.0 (1.9–2.2)	53.2 (53.2–53.3)	1.1 (1.0–1.3)	0.94 (183)	1.24	30.2	–3.5
HD104237		SG	1T	2.1 (—)	53.3 (—)	0.0 (—)	3.82 (89)	—	—	—
		SG	2T	0.7 (0.6–0.7)	52.9 (52.8–53.1)	0.1 (0.0–0.2)	1.57 (87)	0.43	29.9	–5.2
				4.0 (3.3–4.8)	53.1 (53.0–53.1)	c		0.93	30.2	–4.9
IRAS12496		G	1T	2.0 (0.9–7.2)	54.1 (53.4–55.3)	13 (6.2–24)	0.93 (14)	0.29	31.1	–4.2
HR5999		S	1T	0.9 (0.6–1.7)	53.9 (53.5–54.3)	0.7 (0.0–1.2)	1.15 (11)	0.37	30.9	–4.6
		S	1T^{f}	1.6 (1.2–2.4)	53.5 (53.4–53.6)	0.1 (fix)	1.27 (12)	0.44	30.4	–5.1
HR6000		S	1T	1.4 (1.2-1.4)	54.2 (54.2–54.3)	0.0 (0.0–0.1)	1.53 (51)	2.01	31.1	–5.0
2HR	LS	G	1T^{h}	1.2 (0.9–1.3)	54.2 (54.2–54.4)	0.0 (0.0–0.3)	1.63 (62)	—	—	—
	LS	G	2T^{h}	0.7 (0.5–0.9)	54.1 (54.0–54.3)	0.0 (0.0–0.2)	0.74 (61)	1.64	31.1	–5.0^{†5}
				3.2 (2.4–5.0)	53.9 (53.7–54.1)	c		1.22	30.9	–5.2^{†5}
	HS	G	1T	1.8 (1.5–2.3)	54.5 (54.4–54.5)	0.0 (0.0–0.1)	1.70 (37)	4.14	31.5	–4.6^{†5}
	HS	G	1T^{h}	4.0 (2.5–8.2)	54.0 (53.9–54.1)	0.0 (0.0–0.3)	0.96 (37)	1.87	31.1	–5.0^{†5}
V921 Sco		G	1T	2.8 (1.1–9.1)	55.0 (54.6–56.1)	4.9 (2.3–14)	0.96 (18)	1.14	32.1	–4.5
MWC297	1	SG	1T	3.4 (2.4–5.1)	54.2 (54.1–54.4)	2.4 (1.8–3.1)	0.92 (43)	1.18	31.3	–6.8
	2	SG	1T	6.5 (4.7–9.6)	54.9 (54.8–55.0)	2.5 (2.1–2.8)	1.04 (105)	9.23	32.1	–6.0
	3	SG	1T	3.4 (2.6–4.8)	54.2 (54.1–54.3)	1.9 (1.5–2.4)	0.89 (63)	1.31	31.3	–6.7
EC95		SG	1T	3.9 (3.5–4.4)	54.5 (54.5–54.6)^{†3}	2.3 (2.0–2.5)	1.20 (205)	1.97^{†3}	31.7	–3.7
S CrA	1	S	1T	2.9 (1.2–13.5)	52.5 (52.3–52.6)^{†0}	0.6 (0.2–1.3)	1.68 (14)	0.11	29.5	–3.9
	3	G	1T	2.4 (1.4–4.0)	53.4 (53.2–53.6)	0.2 (0.0–0.7)	1.69 (22)	0.99	30.4	–3.1
	6	G	1T	4.7 (2.4–45.2)	53.1 (52.9–53.4)	1.0 (0.2–1.9)	1.37 (31)	0.59	30.3	–3.2
TY CrA	1	S	1T	1.8 (0.8–2.3)	53.4 (53.3–53.5)	0.3 (0.1–0.5)	1.02 (28)	0.76	30.4	–5.1
	4	S	1T^{f}	1.8 (1.2–3.4)	53.5 (53.3–53.7)	0.4 (fix)	1.33 (5)	0.89	30.5	–4.9
	6	S	1T	1.2 (1.0–1.4)	53.7 (53.5–53.8)	0.6 (0.3–0.9)	0.87 (25)	0.82	30.6	–4.8
HD176386	1	S	1T	1.3 (1.0–1.8)	52.8 (52.7–52.9)	0.0 (0.0–0.2)	0.90 (16)	0.32	29.8	–5.5
	1	S	1T^{f}	1.1 (0.7–1.4)	52.9 (52.8–53.0)	0.1 (fix)	1.07 (17)	0.39	29.8	–5.4
	4	S	1T^{f}	1.0 (0.7–1.5)	53.0 (52.8–53.2)	0.0 (fix)	0.56 (4)	0.50	30.0	–5.3
	6	S	1T	1.9 (1.3–2.8)	52.9 (52.8–53.9)	0.0 (0.0–0.2)	1.93 (13)	0.39	29.8	–5.4
	6	S	1T^{f}	1.6 (1.2–2.3)	53.0 (52.9–53.1)	0.1 (fix)	1.91 (14)	0.48	29.9	–5.3
TYHD	1	G	1T	2.1 (1.9–2.4)	53.6 (53.6–53.6)	0.0 (0.0–0.1)	1.87 (26)	1.86	—	—
	2	G	1T	1.7 (1.2–2.0)	53.6 (53.6–53.8)	0.0 (0.0–0.5)	0.66 (41)	1.74	—	—
	3LS	G3	1T	2.6 (2.1–3.1)	53.7 (53.6–53.7)	0.0 (0.0–0.1)	0.79 (65)	2.43	—	—
	3HS	G3	1T	3.0 (2.4–3.8)	53.8 (53.8–53.9)	0.0 (0.0–0.2)	0.88 (22)	3.87	—	—
	4	G	1T	2.5 (2.0–3.3)	53.6 (53.5–53.6)	0.0 (0.0–0.2)	1.18 (30)	1.92	—	—
	5	G	1T	2.1 (1.3–2.6)	53.7 (53.6–53.9)	0.0 (0.0–0.4)	0.98 (25)	2.26	—	—
	6	G	1T	1.7 (1.4–1.9)	53.5 (53.5–53.6)	0.0 (0.0–0.2)	1.03 (64)	1.49	—	—
HD200775		SG	1T	1.7 (1.6–1.9)	54.5 (54.5–54.6)	0.1 (0.0–0.2)	1.39 (211)	1.11	31.5	–6.0
		SG	2T	0.5 (0.4–0.6)	55.2 (55.1–55.4)	0.9 (0.8–1.1)	1.18 (210)	0.59	32.1	–5.3
				2.7 (1.9–4.1)	54.3 (54.1–54.5)	c		0.47	31.3	–6.2
MWC1080		SG	1T	10.0 (3.8–)	55.1 (55.0–55.3)	1.0 (0.3–2.2)	1.02 (56)	0.26	32.3	–5.1
X-ray sources identitified as other objects										
BF Ori		G	1T	0.8 (0.5–1.9)	54.5 (54.0–55.0)	0.0 (0.0–0.9)	0.85 (17)	0.45	—	—
HD97048	2	S0	1T	1.4 (0.4–12.2)	54.2 (53.2–56.1)	4.2 (0.9–10)	1.14 (6)	0.42	—	—
	2	G	1T	2.2 (1.2–5.2)	53.9 (53.5–54.5)	3.5 (1.5–7.0)	0.34 (12)	0.55	—	—
	3	S	1T	2.8 (1.7–6.0)	53.1 (52.9–53.4)	0.7 (0.3–1.5)	0.85 (13)	0.23	—	—
HD147889		G	1T	0.8 (0.6–1.6)	53.8 (53.5–54.1)	0.5 (0.0–0.7)	1.13 (36)	0.82	—	—

St.: Number of observation ID & status (HS: high or flare state, LS: low state), Det.: Detector (S: SIS, G: GIS, SG: SIS+GIS), ML: Model [1T: 1-temperature, 2T: 2-temparature, $^{h/g/ls}$: adding the components of HR5999/Gaussian/low-state, ^{f}: fixing N_{H} value, ^{i}: two temperature model with independent N_{H}, kT [keV], $E.M.$ [log, cm^{-3}], N_{H} [10^{22}cm^{-2}] Parentheses show 90% confidence level, $^{\Delta}\chi^2$: Parentheses denote number of degree of freedom (d.o.f), Flux[10^{-12} ergs cm^{-2} s^{-1}]: observed flux in the *ASCA* band (0.5–10keV), L_{X} [log, ergs s^{-1}]: absorption corrected xray luminosity in the *ASCA* band, $L_{\mathrm{X}}/L_{\mathrm{bol}}$ [log], 2HR/TYHD: GIS data merged with HR 5999 (TY CrA) and HR 6000 (HD 176386), c: common N_{H} values with the above column, $^{\dagger0}N_{\mathrm{H}}$ is fixed in the error estimate. ^{†1}The distance of V410 X-ray 7, ^{†2}Best-fit parameters of the gaussian component [center energy, 5.10keV (4.86-5.30), σ ~0.0, flux includes the gaussian component], ^{†3}GIS value, $^{\dagger4}L_{\mathrm{bol}}$ value of VY Mon G2, $^{\dagger5}L_{\mathrm{bol}}$ value of HR 6000,

Chapter 6

Result II – Giant Molecular Cloud

6.1 Monoceros R2 Giant Molecular Cloud

The Monoceros R2 giant molecular cloud ($d = 950$ pc) shows recent high mass star formation activities, including a compact HII region (Downes et al. 1975), H_2O and OH masers (Knapp and Brown 1976) and a well-developed molecular outflow (Loren 1977). In the core region, there are three luminous compact near-infrared objects with PMS characteristics (Beckwith et al. 1976). Infrared spectra of IRS2 and IRS3 show deep absorption in the water-ice band (eg Willner et al. 1982), which is a signature of young embedded sources such as the Becklin-Neugebauer object. *ROSAT* observed the Monoceros R2 cloud and detected 41 X-ray reliable sources (Gregorio-Hetem et al. 1998) but *ROSAT* found no X-ray source from the core.

Figure 6.1 shows *ASCA* images of the Monoceros R2 GMC core. Gray scale images show the SIS medium band (*left*: 2−4 keV) and the SIS hard band (*right*: 4−10 keV). Though the *ASCA* spatial resolution is limited, we can see at least three x-ray peaks in these images, which correspond to IRS1 and source d (medium band) and IRS 2 (hard band). No peaks have soft x-ray counterparts, suggesting them to be deeply embedded in the cloud core.

In hard band light curves, we found a hard X-ray flare during the latter half of the observation (Figure 6.2). The light curves in the soft band show no variable feature, which means that the flaring source is deeply embedded. The flare shows a fast-rise and an exponential-decay with the e-folding time of $\sim 1.8 \times 10^4$ sec. The peak count rate reaches almost three times as large as the quiescent level. The strongest source during the flare is identical to the hard source during the quiescent state, ie probably IRS 2.

The left panel of Figure 6.3 shows a GIS spectrum during the quiescent state. This spectrum has a line like feature at ~6.5 keV and can be reproduced with an absorbed bremsstrahlung model with a Gaussian line (Table 6.1). The plasma temperature is very

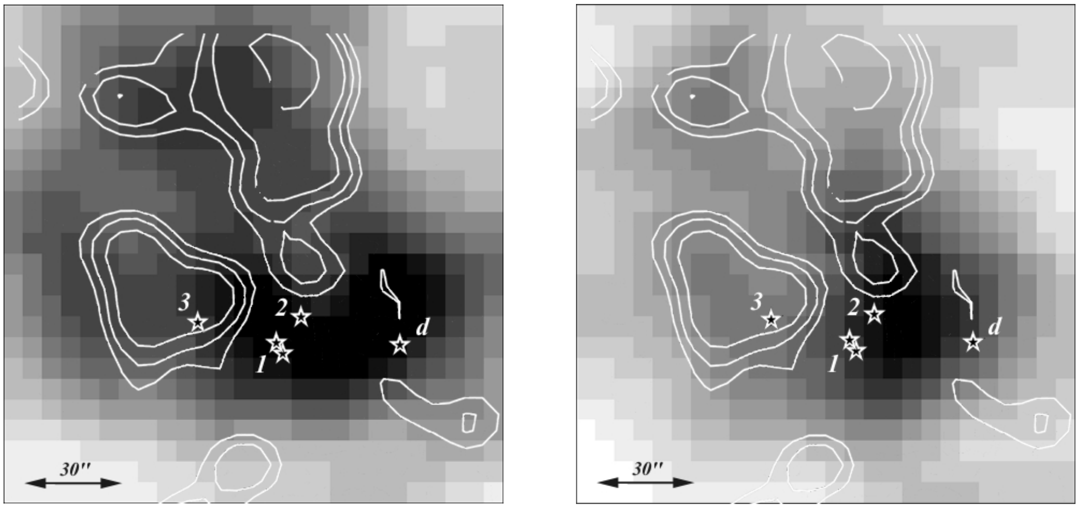

Figure 6.1: *ASCA* images of the Monoceros R2 giant molecular cloud core (*left*: 2−4 keV, *right*: 4−10 keV). Massive YSO candidates IRS1, 2, 3 and source *d* are shown by star marks. White contours represent the *ROSAT* PSPC flux (soft band: 0.1–2.4keV).

high, kT ∼5.6±1.0 keV. Line center energy is 6.58±0.20 keV in the 90% confidence level. This error range leaves possibility of both neutral iron (6.4 keV) and Helium-like iron (6.7 keV) origins. The x-ray luminosity is typical of GMCs, $L_{\rm X}$ (0.8−10 keV, ergs s^{-1}) ∼32.6 (see also Table 2.1). The right panel of Figure 6.3 shows a spectrum of the flare component, which takes the quiescent spectrum as its background. The spectrum seems to have Fe, Ca and marginal Ar lines and is successfully reproduced with an absorbed thermal bremsstrahlung model with three Gaussian lines (Table 6.1). Line emissions from Ar and Ca materials has never been detected in YSO spectra, and such a clear detection implys the richness of these materials. The flare temperature is also very high, kT >5.3 keV. The absorption column density is very large ($N_{\rm H}$ ∼5.6×10^{22} cm^{-2}), and almost equal to that of low mass protostars. The flare luminosity, log $L_{\rm X}$ (0.8−10 keV, ergs s^{-1}) ∼32.4 on average, is one of the largest among previously detected YSO flares.

The flare spectrum shows a certain peculiar feature. The quantities of line center energy for both Fe and Ca are significantly lower than those calculated in a thin thermal plasma model. We do not find any systematic error in calibration data (^{55}Fe radioactive source), which is obtained during observations. We tentatively fit the flare spectrum with an absorbed Raymond-smith model with free redshift parameter, and then find an acceptable result when z = 0.072. One possibility is a flare from an hidden AGN. Certainly, log $L_{\rm X}$ (ergs s^{-1}) ∼43.5 at z = 0.072 is typical of AGN flares, but the flare source is strongly associated with the cloud core and its chance probability is extremely low. We thus try another model, assuming non-ionization equilibrium plasma (NEI). We adopt an absorbed masai89 model with free abundances for Fe and Ca materials and one solar fixed for the other materials. This model

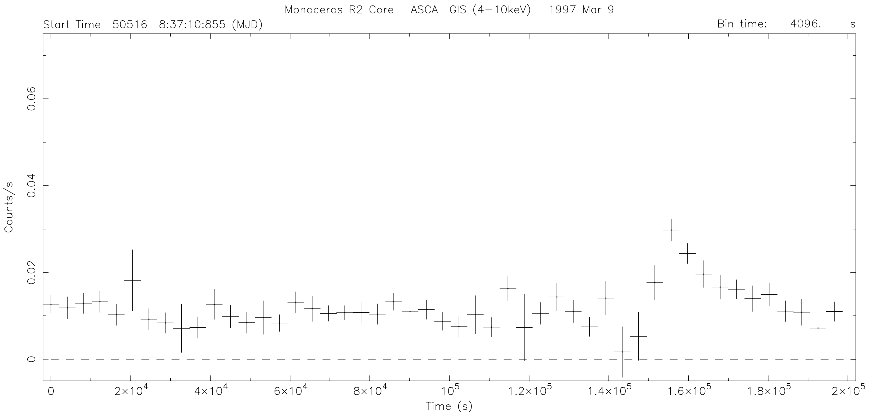

Figure 6.2: Hard band light curves of the Monoceros R2 core (4–10 keV).

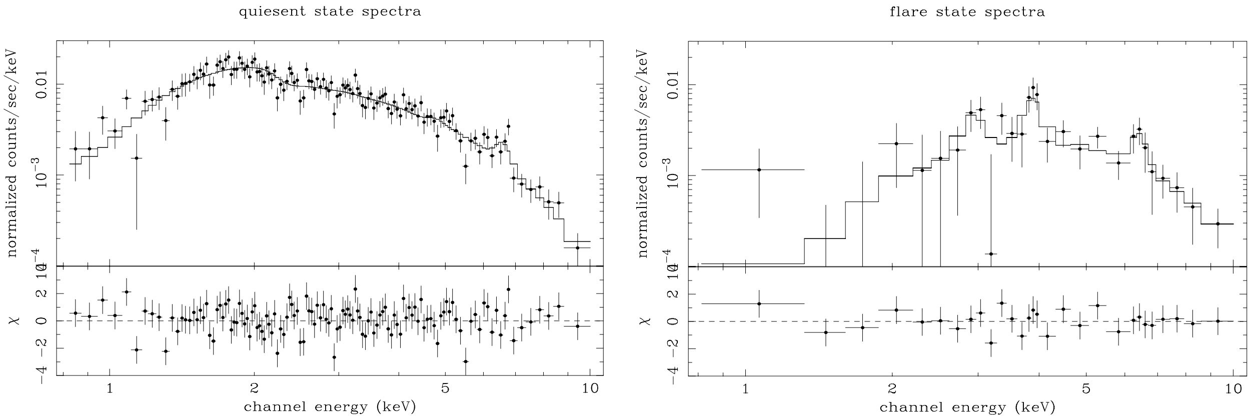

Figure 6.3: Quiescent and flare state spectra of the Monoceros R2 core.

Table 6.1: Spectral parameters of the x-ray emission from the Monoceros R2 core

			quiescent state		flare state	
temperature	kT	[keV]	5.62	(4.67–6.95)		(5.3–)
absorption	N_H	[10^{22}cm^{-2}]	1.31	(1.13–1.50)	5.59	(2.9–14.2)
Fe line	Energy	[keV]	6.58	(6.37–6.72)	6.41	(6.21–6.64)
Ca line	Energy	[keV]			3.85	(3.76–3.93)
Ar line	Energy	[keV]			2.90	
χ^2/d.o.f			1.06		0.78	

Notes. Errors listed in parentheses are quoted for 90% confidence level

well reproduce Fe and Ca line features when log nt = 10.09, but Ca is extremely over-abundant against the solar value. Shu et al. (1996) suggest that calcium-aluminum-rich inclusions (CAIs) condense near the X-point. We might see an x-ray flare occurred in such a region.

Chapter 7

Discussion I – X-ray Emission Mechanism

This chapter discusses the relation of x-ray properties of HAeBes to stellar parameters and studies the characteristic behavior on each individual HAeBe. The final goal is to reveal the x-ray emission mechanism.

7.1 Could the X-ray Emission Come from a Low Mass Companion?

Large fraction of HAeBes is thought to be visible or spectroscopic binaries (P >85%, Pirzkal et al. 1997). Though not a few companions are higher mass stars (eg MWC 1080), low mass companions are generally much fainter than HAeBes in the optical wavelength and are not easy to be detected. Therefore almost all HAeBes could possess a low mass companion. Because the x-ray luminosity of a low mass star constitutes a large portion in the bolometric luminosity compared with a high mass MS star (low mass: log $L_{\rm X}/L_{\rm bol} <-3$, High mass: log $L_{\rm X}/L_{\rm bol} \sim -6 - -8$, see the section 2.2), a detected x-ray source cannot be easily identified with a HAeBe itself even if no companions are found. Zinnecker and Preibisch (1994) have already mentioned that the luminosity of unresolved T-Tauri companions, log $L_{\rm X}$ (ergs s^{-1}) $\sim$28–30, cannot explain the *ROSAT* samples, but we discuss the possibility in detail.

We estimate the low mass contribution of x-ray emission if a HAeBe has a low mass companion. Binary formation theories say that the primary and secondary stars are simultaneously form in a molecular cloud, which suggests that low mass companions of HAeBes would be in protostar or TTS phases (Age $\sim 10^5 - 10^7$ yrs). This picture is supported by the observational evidence of the eclipsing binary TY CrA by Casey et al. (1998), in which they estimated both of primary and secondary at $\sim$3M-year-old. We then refer to the x-ray luminosity function of optically selected low mass PMSs. Neuhaeuser et al. (1995) performed a complete survey of TTSs in the Taurus Aurigae region using the RASS data. They investigated the x-ray luminosities of optically selected TTSs and provided luminosity functions of both CTTSs and WTTSs. In their survey, they found significant difference of the functions between CTTSs and WTTSs, but deep pointings of the Chameleon I cloud with *ROSAT* (Feigelson et al. 1993) and the ρ-Ophiuchi with *Chandra* (Imanishi et al. 2001) indicated that the x-ray luminosity does not evolve from protostars to WTTSs. This discrepancy might be due to the limited detection efficiency for CTTSs with relatively large absorption. We thus adopt the luminosity function of WTTSs in Figure 2 of Neuhaeuser et al. (1995)[1]. We measured 90% of optically selected WTTSs below $L_{\rm X}$ $\sim$$10^{30}$ ergs s^{-1} (0.1$-$2.4 keV). For the typical WTTS temperature (kT $\sim$0.5$-$2 keV), the x-ray flux in the *ASCA* band is almost as same as that in the *ROSAT* band (see Table 4.8). The detection rate of our survey is $\sim$40 % and almost all the detected samples exceed $L_{\rm X}$ $\sim$$10^{30}$ ergs s^{-1}. We again cannot explain the HAeBe luminosity with a T-Tauri low mass companion.

Nevertheless we should cope with a complex problem for *ASCA* results, especially on the GIS data. A clustering survey of HAeBes by Testi et al. (1999) indicated that early Be stars generally associated several low mass stars, while late Be and Ae stars did not. *ASCA psf* would cover many low mass stars around a HAeBe. We therefore evaluate possible flux contribution of these members. Testi et al. (1998) estimated that HAeBes accompanied at most 30 TTSs within 0.21 pc, corresponding to from 17$''$ (d $\sim$2.5 kpc) to 270$''$ (d $\sim$160 pc). There could be $\sim$10 low mass stars within the typical *ASCA* resolution (r $\sim$20$''$). From Neuhaeuser et al. (1995), we estimated the average $L_{\rm X}$ of WTTSs to be log $L_{\rm X}$ (ergs s^{-1}) $\sim$29.5[2], which is largely as same as the average $L_{\rm X}$ value in the Chameleon I cloud log $L_{\rm X}$ (ergs s^{-1}) $\sim$29.2 (Feigelson et al. 1993). The estimated luminosities from low mass clusters are up to log $L_{\rm X}$ (ergs s^{-1}) <30.5. This is less than 10% of the x-ray luminosity of HBes.

7.2 X-ray Emission Mechanism

We find that x-ray emission from a HAeBe probably comes from HAeBes itself. We then discuss four plausible x-ray emission mechanisms on stars. This procedure traces the method by Skinner and Yamauchi (1996).

7.2.1 Stellar Wind

The stellar wind model is proposed by Lucy and White (1980) and Lucy (1982) to explain the observed x-ray features of O stars (see the section 2.2.1). This model assumes a complicated

---

[1] The graph shows the value in the Kaplan-Meier estimator. The detection rate of WTTS is 37%

[2] $L_{\rm X} \sim 10^{29.7}$ ergs s^{-1} at Kaplan-Meier estimator 0.5, and the WTTS detection rate $\sim$66%

situation; the presence of successive shocks in the wind. Here we simplify this problem as whether the observed stellar wind has enough kinetic energy to generate the x-ray emission of HAeBes. We investigate this possibility in two ways; i). $L_{\rm X}$ *vs.* total kinetic energy in stellar winds, ii). thermal energy *vs.* kinetic energy in a unit volume.

For the estimate of i), we adopt the wind kinetic luminosity defined as $L_{\rm kin}$ =1/2$\dot{M}$ $V_{\rm term}^2$. Figure 7.1 shows $L_{\rm kin}$ *vs.* $L_{\rm X}$. All $L_{\rm X}$ are far below $L_{\rm kin}$ so that the wind can constantly produce the observed luminosity.

For the estimate of ii), we made a graph of the wind velocity *vs.* the plasma temperature (Figure 7.2). we refer the wind velocity to Nisini et al. (1995) and Blondel et al. (1993). All observed kT values are far larger than maximum temperatures produced from the wind velocity. The wind velocity has to exceed $v \sim 1000$ km s^{-1} to heat gases up to $\sim$ 2 keV. Such a high velocity wind is only seen in O stars. The stellar wind, therefore, cannot produce the observed HAeBe temperature.

7.2.2 Accretion Shock

We estimate the maximum plasma temperature heated up by the mass accretion process, which is the origin of the UV excess emission from YSOs (eg Gullbring et al. 2000). We assume that accreting gases have free-fall velocity on stellar surface. Then the equation is as follows,

$$3nkT = \frac{GM_* n m_p}{3R_*}$$

where n: electron (proton) density, m$_p$: proton mass, M$_*$: stellar mass, R$_*$: stellar radius. The derived temperature $kT \sim$0.5−1 keV does not explain the typical temperature of HAeBes ($kT \sim$2 keV). Moreover the maximum temperature should be smaller than the derived value because gases fall from the inner edge of a circumstellar disk and the gas velocity should be slower than the free-fall velocity. The accretion shocks therefore cannot explain the plasma temperature of HAeBes.

Blondel et al. (1993) reported that Lyman α emission from a few HAeBes is red-shifted by $v_{\parallel} \sim$600−900 km s^{-1}. They suggested accretion velocity can be up to $v \sim 800 - 2000$ km s^{-1}, assuming the accreting geometry(see also the subsection 2.1.2). This is much faster than the typical free-fall velocity and these accreting gases can be heated up by $kT \sim$7 keV when $v \sim$2000 km s^{-1} and can explain the temperature of HAeBes. If this accreting velocity is real, a certain gas accelerating mechanism is needed.

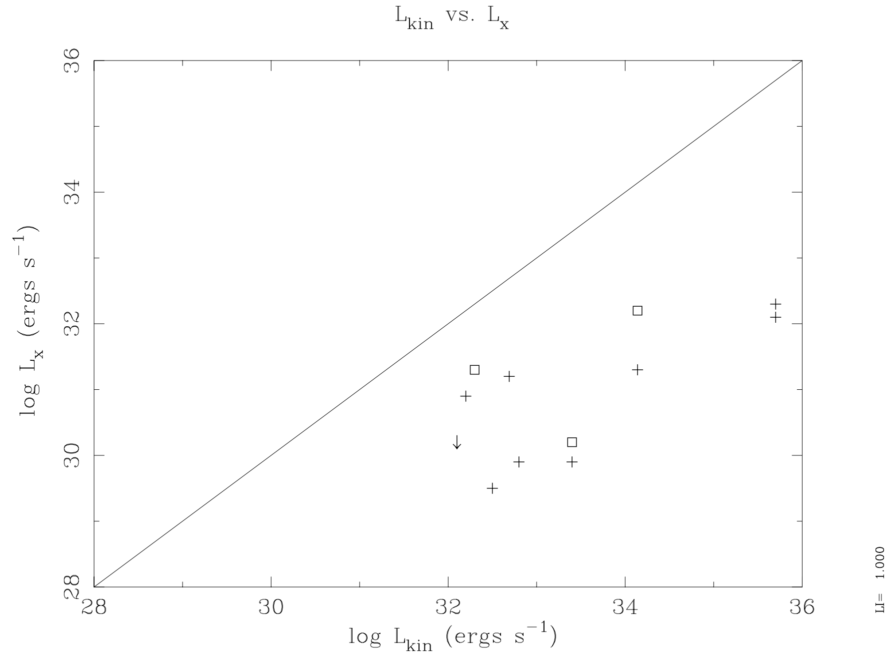

Figure 7.1: Wind kinetic luminosity and x-ray luminosity relation. Square plots mean high temperature components in the 2T models. L_{kin} of HD 104237 and HR 5999 are intermittent values.

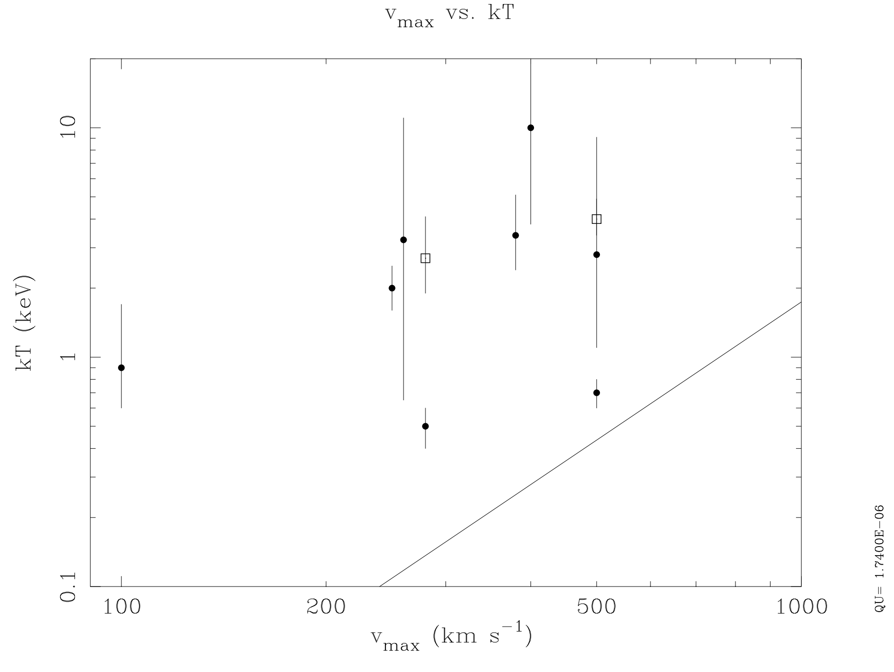

Figure 7.2: Terminal velocity (v_∞) *vs.* plasma temperature relation. Square plots mean high temperature components in the 2T models. The line denotes the plasma temperature when whole kinetic energy is converted to the thermal energy ($3kT=\frac{1}{2}m_p v_\infty^2$, m_p: proton mass).

7.2.3 Wind-fed Magnetosphere

A model by Usov and Melrose (1992) assumes successive occurrence of magnetic reconnection on the equatorial plane by dragging the magnetic field out with stellar winds (see the subsection 2.2.1 and Figure 2.8). This model does not assume the presence of a circumstellar disk and therefore is not appropriate for the structure of HAeBes. An x-ray emission model, matching the circumstellar structure of HAeBes, is developed by Babel and Montmerle (1997). This model suggests that wind-shock in the magnetosphere can efficiently heat up gases. Because simulated stellar parameters are optimized in the magnetic Ap star, IQ Aur, the wind velocity is faster than, and the mass loss rate is much smaller than, those of HAeBes. In this simulation, the plasma temperature mainly depends on the wind velocity and the x-ray luminosities depends on the mass-loss rate. HAeBes satisfy the latter condition, but plasma temperature produced by the HAeBes wind (v <500 km s^{-1}) is below kT $\sim$1 keV, which is lower than the observed HAeBe temperature. This model does not seem to account for the x-ray emission from HAeBes as well.

7.2.4 Magnetic Activity on the Stellar Surface

Magnetic activity on or near stars seems to be the most plausible mechanism to explain the HAeBe x-ray emission. High percentage of our observed sources were x-ray variable (see the subsection 5.3) and a few sources, MWC 297, HR 6000, VY Mon and TY CrA, show flare like time variations, similar to TTS flares. The presence of an azimuthal magnetic field structure on a HAe is also suggested by time covariation of emission lines with stellar rotational period in the optical wavelength (AB Aur: MgII 2795Å, Praderie et al. 1986; HeI 5876Å, Boehm et al. 1996). In the next section, we discuss the magnetic activity on HAeBes in details.

7.3 X-ray Properties Related to the Magnetic Activity

After this section, we add HAeBe samples observed with *ROSAT* (Zinnecker and Preibisch 1994). We also add the x-ray emitting PMS candidate SSV 63E+W discovered with *ASCA* (Ozawa et al. 1999). The x-ray source SSV 63E+W would be either the Class I protostar candidates SSV 63E or SSV 63W, which are located in the HH 24-26 region in the Orion cloud. Zealey et al. (1992) mention the evolutional age to be less than 10^6 yrs, estimating that SSV 63E to be in the pre-main-sequence stage and the mass $1.5M_\odot$ <M<$5M_\odot$ from its reddening factor.

Table 7.1: Physical Parameters of Herbig Ae/Be stars

Targets	R$_*$ ($R_\odot$)	Mass ($M_\odot$)	Wind Vel. (km s^{-1})	log $\dot{M}$ ($M_\odot$ yr^{-1})	log $L_{\rm kin}$ (ergs s^{-1})	v sin$i$ (km s^{-1})	W(Hα) (Å)	F$_{1.3mm}$ (mJy)
BD+30 549	0.8							
V892 Tau	4.0		250				20.6	490
CoKu Tau 1	2.7							
AB Aur	2.5	2.4	260	−8.0	32.5	140	26.3	430
IX Ori	–					15		
V372 Ori	6.0	3.3				125	2.5	
YZ Ori	1.7							
HD 36939	2.4					275	1	
HD245185	1.9					150		
LP Ori	3.1	3.6				100	0.5	
MR Ori	3.9							
V361 Ori	3.6					50		
T Ori	3.0			−8.0	32.8	100		130
V380 Ori	3.8	3.3	260	−7.9	32.7	200	71.0	<20
BF Ori	0.6	2.0		−8.8	32.1	100	3.7	<70
MWC120	2.0					120		<12
VY Mon	7.0						50	
VY Mon G2	36.3						21	
V590 Mon	4.2			−8.5	32.3		47	
LkHa218	3.2	3.8					31.9	
Z CMa	40.0					<130	24.8	489
LkHa220	2.1	4.0						
HD76534	6.2					110	14.3	
HD97048	2.1	2.5				140	51.1	451
HD97300	1.7	2.5						<91
T Cha	1.1	1.1				48		
HD104237	2.7	2.3	500	−8.9, −6.7	32.3, 34.5			66
IRAS12496	3.5							522
HR5999	4.9	3.2	100	−8.4, −6.8	31.4−33.0	180		<40†
HR6000	3.0							<40†
HD147889	3.1	7.5						
Hen 3−1191	–							
V921 Sco	5.6		500	−5.5	35.7			270
MWC297	9.9	10	380			350	102.6	110
EC95	12.7	4						
S CrA	1.6	0.6						328
HD176386	2.0	2.3						
TY CrA	2.0	3.2				10	2	130
R CrA	2.9	3.0		−8.0				
T CrA	1.8	1.5		−8.6		40		
HD200775	7.0	10	280	−6.6	34.1	60	17.7	<20
MWC1080	35.1		400	−5.3	35.7	200	94.2	

Reference: Radius– Caliculated from $T_{\rm eff}$ and $L_{\rm bol}$ (see the subsection 7.3.2). Mass– Hillenbrand et al. (1992), Bibo et al. (1992), Boehm and Catala (1995), Casey et al. (1998), Drew et al. (1997), van den Ancker et al. (1997), van den Ancker et al. (1998), de Winter et al. (1999), Shevchenko et al. (1999), Preibisch (1999), Olofsson et al. (1999). Wind Vel.– Nisini et al. (1995), Benedettini et al. (1998). Log $\dot{M}$, log $L_{\rm kin}$– Damiani et al. (1994), Benedettini et al. (1998). v sin$i$– Grady et al. (1993), Boehm and Catala (1995), Drew et al. (1997), Casey et al. (1998).van den Ancker et al. (1998), Corporon and Lagrange (1999). W(Hα)– Damiani et al. (1994), Reipurth et al. (1996), Corcoran and Ray (1998). F$_{1.3mm}$– Wendker (1995) (22,500 or 23,000MHz). †HR5999 and HR6000 are not resolved.

Table 7.2: Other HAeBes

Objects	$T_{\rm eff}$	$L_{\rm bol}$	$L_{\rm X}$	$L_{\rm X}/L_{\rm bol}$
	K	$L_{\odot}$	ergs s^{-1}	
LkHα 101	–	4.1	<31.4	<−6.3
LkHα 349	4.15	3.1	30.9	−5.8
AFGL 4029	–	4.3	<31.8	<−6.2
LkHα 198	4.28	2.1	<30.5	<−5.2
V376 Cas	3.86	2.3	<30.0	<−5.9
BD +46° 3471	3.92	2.1	31.2	−4.5
LkHα 257	–	–	<30.4	—
GU CMa	4.32	3.6	<30.4	<−6.8
LkHα 234	4.14	2.7	<30.7	<−5.6
ω Ori	4.28	4.3	<29.6	<−8.3
LkHα 215	4.11	2.7	31.1	−5.2

All values are in logarithmic scales and referred to Zinnecker and Preibisch (1994). $T_{\rm eff}$ is the typical values of class V stars.

7.3.1 $L_{\rm X}$ *vs.* $L_{\rm bol}$ Relation

Figure 7.3 shows the $L_{\rm X}$ *vs.* $L_{\rm bol}$ relation. About half sources are in the range of $-4<$ log $L_{\rm X}/L_{\rm bol} <-6$. This is an intermediate range between massive MSs and the saturation level of low mass stars. We also plotted the $T_{\rm eff}$ *vs.* $L_{\rm X}/L_{\rm bol}$ relation in Figure 7.4. Here we omit sources whose $T_{\rm eff}$ values are not known. Sources near the saturation level of low mass stellar x-rays (log $L_{\rm X}/L_{\rm bol} < -3$) are concentrated in the region of log $T_{\rm eff}$ (K) <3.8, which corresponds to later than K type stars. One of them S CrA is really a low mass star, but the other three are the promising HAeBes EC95, T Cha and SSV63E+W. This fact implys that the x-ray emission mechanism during the very young phase is similar to low mass stars. The $L_{\rm X}/L_{\rm bol}$ values gradually decrease as stellar effective temperature increases.

7.3.2 Standard Dynamo Mechanism

The x-ray luminosities of low mass stars have a clear relation to the projected rotational velocity (v_{rot} sin i), that is the characteristics of the standard dynamo activity (see the section 2.2.1). The same relation is expected for HAeBes as well if the standard dynamo works on HAeBes on contrary to star forming theories. Figure 7.5, 7.6 show the dependence of log $L_{\rm X}$ and log $L_{\rm X}/L_{\rm bol}$ values on v_{rot} sin$i$. We cannot see any clear correlation between these quantities. The $L_{\rm X}/L_{\rm bol}$ values saturate at the level of log $L_{\rm X}/L_{\rm bol} \sim -3$ above v_{rot} sin$i$ > 15 km/s in low mass MSs (Stauffer et al. 1994). All our samples rotate faster than this boundary, but the quantities of log $L_{\rm X}/L_{\rm bol}$ scatter in the range between −4 and −6. There seems to be no saturation level.

The standard (solar) dynamo, is believed to be a type of $\alpha\Omega$ dynamo, which couples the α effect and differential rotation Ω. The $L_{\rm X}$ and $L_{\rm X}/L_{\rm bol}$ values should be really dependent on Ω and not on v_{rot}. We do not know the exact value of differential rotation Ω, but Ω could

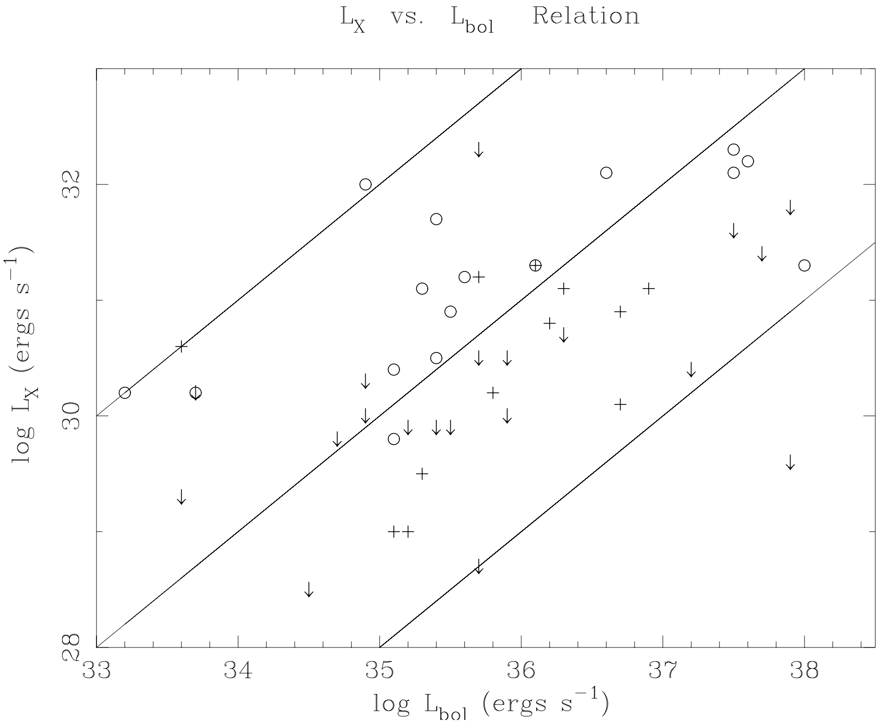

Figure 7.3: L_X *vs.* $L_{\rm bol}$ relation. Circles represent the *ASCA* detected sources. Plus marks and arrows (upper-limit) represent the *ASCA* non-detected sources, whose L_X values are from the ROSAT estimates except for HD 76534, and the *ROSAT* survey sources (Zinnecker and Preibisch 1994). L_X values are converted to the *ASCA* band assuming $kT = 2$ keV. Solid lines show log $L_X/L_{\rm bol} = -3$, -5 and -7 from the top, respectively

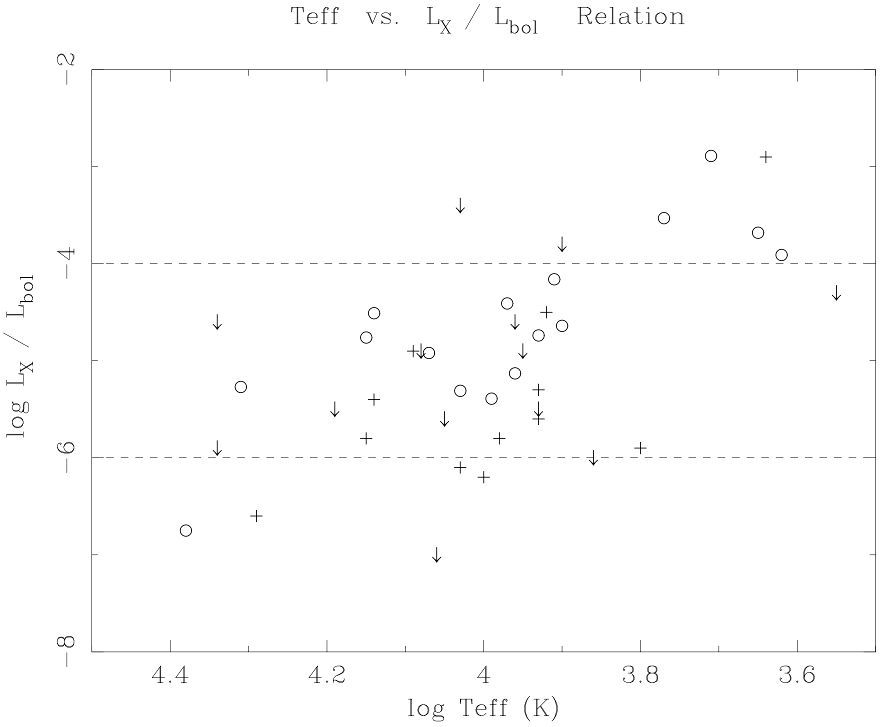

Figure 7.4: $T_{\rm eff}$ *vs.* L_X relation. Marks mean the same as the above.

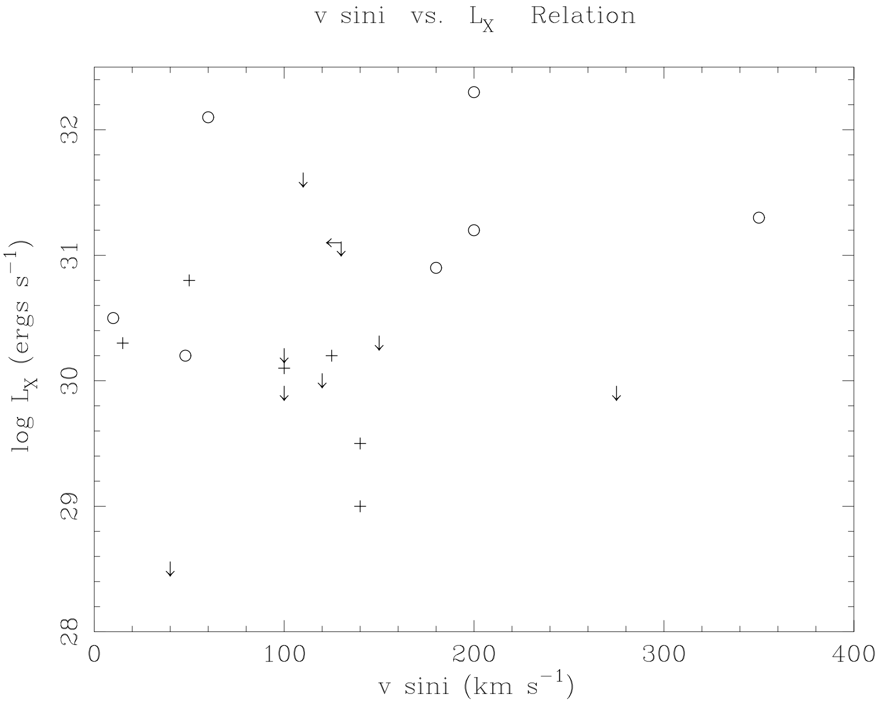

Figure 7.5: v sin i *vs.* L_X relation. Marks mean the same as Figure 7.3.

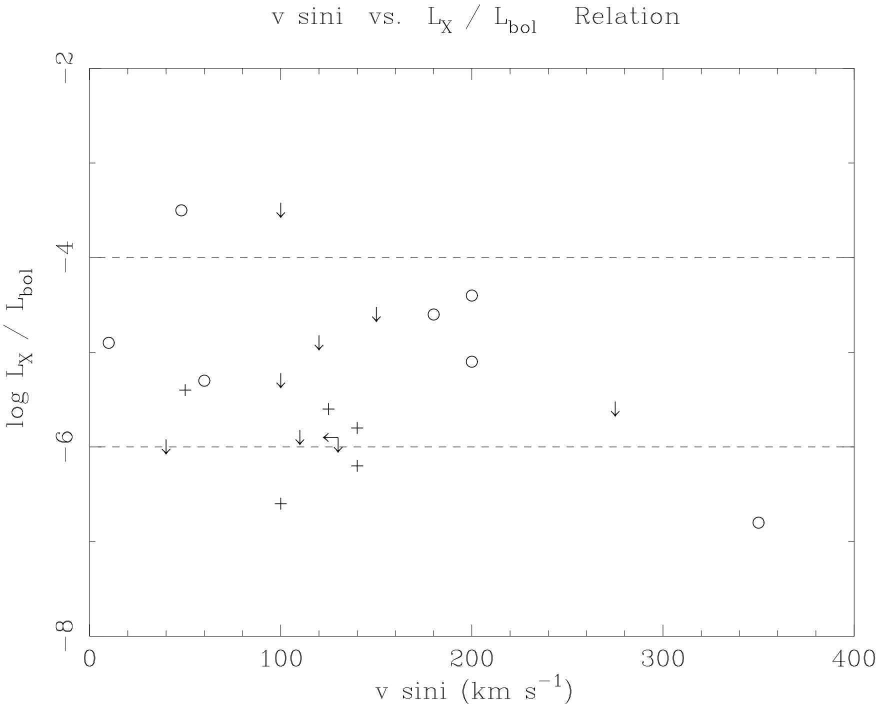

Figure 7.6: v sin i *vs.* log $L_\mathrm{X}/L_\mathrm{bol}$ relation. Marks mean the same as Figure 7.3.

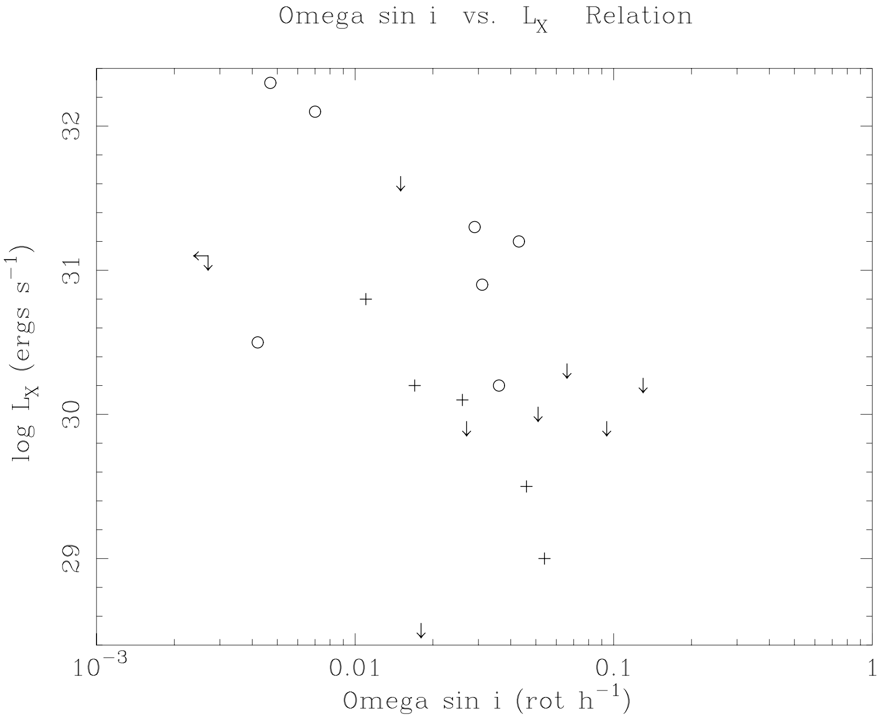

Figure 7.7: Ω sin *i vs.* log L_X relation. Marks mean the same as Figure 7.3.

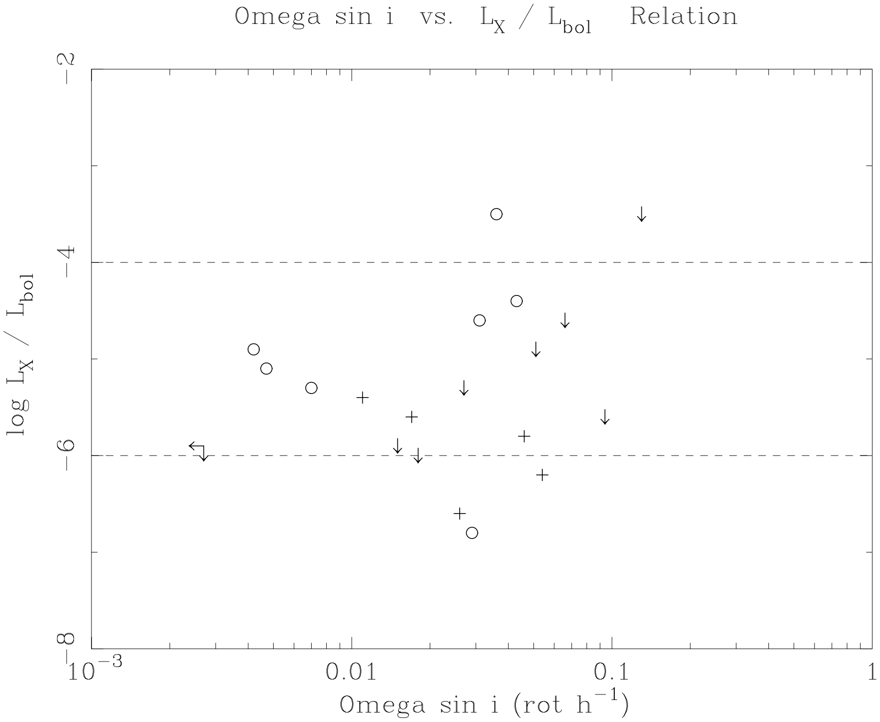

Figure 7.8: Ω sin *i vs.* log $L_\mathrm{X}/L_\mathrm{bol}$ relation. Marks mean the same as Figure 7.3.

Table 7.3: Fitting Results of Flare Light Curves

Source	Obs. ID	Det.	I_{qui} (10^{-2} cnts s^{-1})	I_{peak} (10^{-2} cnts s^{-1})	τ_{ris} (10^4s)	τ_{dec} (10^4s)
MWC 297	MWC297 2-3	SG	2.3 (2.1–2.4)	>12	–	5.6 (4.5–7.0)
HR 6000	Lupus3	G	3.3 (3.1–3.5)	5.8 (5.3–6.2)	< 0.2	< 0.2
VY Mon	PSRJ0631	G	0.25 (0.17–0.29)	> 0.38	–	3.6 (2.0–7.4)
TY CrA	R CrA3	G	3.6 (3.4–3.8)	~ 7.5	~ 1	2.4 (1.3–8.0)
Monoceros core	Mon R2	G			< 0.8	1.8
SSV 63E+W	a	G	2.0 (1.6–2.6)	1.8 (1.6–1.9)	1.7	1.2 (0.9–1.5)

Det.: Detector(S:SIS, G:GIS, SG: summed lightcurve of both detectors), I_{qui}: count rate of a constant level, I_{peak}: count rate of a flare peak, τ_{ris} (and τ_{dec} of HR 6000): a period between the constant level to the flux peak, τ_{dec}: e-folding time of a flare decay, a: Ozawa et al. (1999).

have a relation to the angular velocity ω. The stellar radius of low mass stars do not different so much, and threrefore the relation to v_{rot} sin$i$ is a good approximation of the relation to ω sin$i$. However the stellar radius of HAeBes is different up to an order (see Table 7.1) and the relations could be much different. We therefore estimate ω from the following equation and see the relation to $L_{\rm X}$ and $L_{\rm X}/L_{\rm bol}$.

$$L_{bol} = 4\pi R^2 \sigma T_{eff}^4$$

$$v = R\omega$$

where R is a stellar radius and σ is the Stefan-Boltzmann constant. The result is shown in Figure 7.7 and 7.8. We again do not find any correlation between these parameters.

7.3.3 Prominent X-ray Variability on HAeBes

The quiescent x-ray luminosity does not show any characteristics of the standard dynamo activity. We thus investigate x-ray variable features, which most indicates the magnetic activity on HAeBes. Among our HAeBe samples, MWC 297, HR 6000, VY Mon and TY CrA exhibited prominent time variations. All light curves but HR 6000 have similar time profiles to low mass stellar flares, though the rising phases of MWC 297 and VY Mon were lost. We fit these light curves with a conventional model of constant and exponential decay. The result is shown in Table 7.3. Most sources exhibited long decay timescales (a few $\times 10^5$ sec). This is much longer than the typical decay timescales of low mass MSs and TTS flares but comparable to those of protostars ($2-7$ ksec for MSs and TTSs and $10-30$ ksec for protostars, Tsuboi et al. 2000; Stelzer et al. 2000).

Assuming the radiative cooling model (the quasi-static cooling model), the plasma volumes of low mass stellar flares are extremely large, sometimes far exceed the stellar size. Though another model (see the appendix A.1) estimates smaller plasma volumes than the

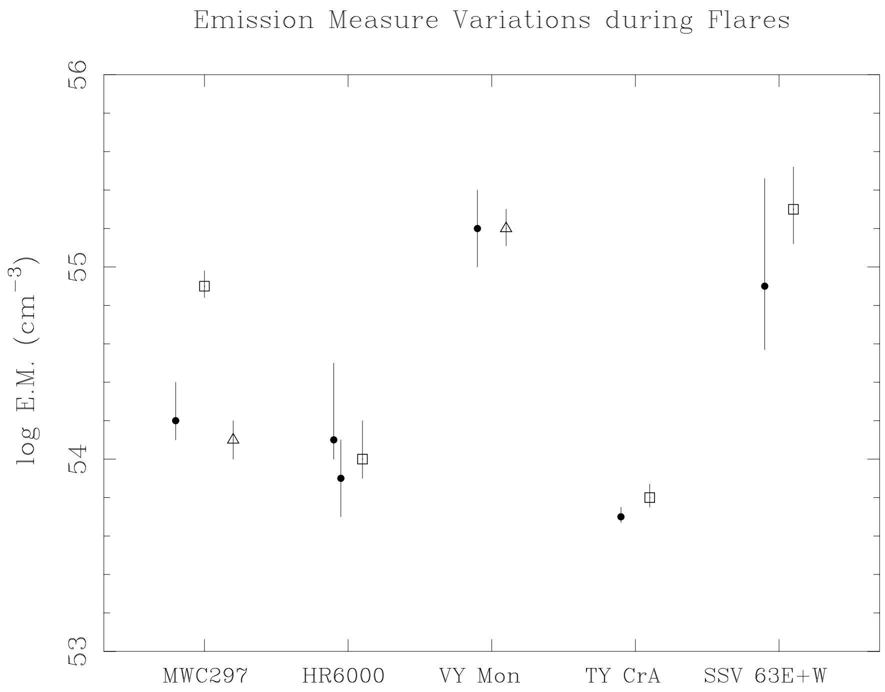

Figure 7.9: Variation of emission measure during flares. Dots, squares and triangles are the quiescent, flare and flare decay state, respectively.

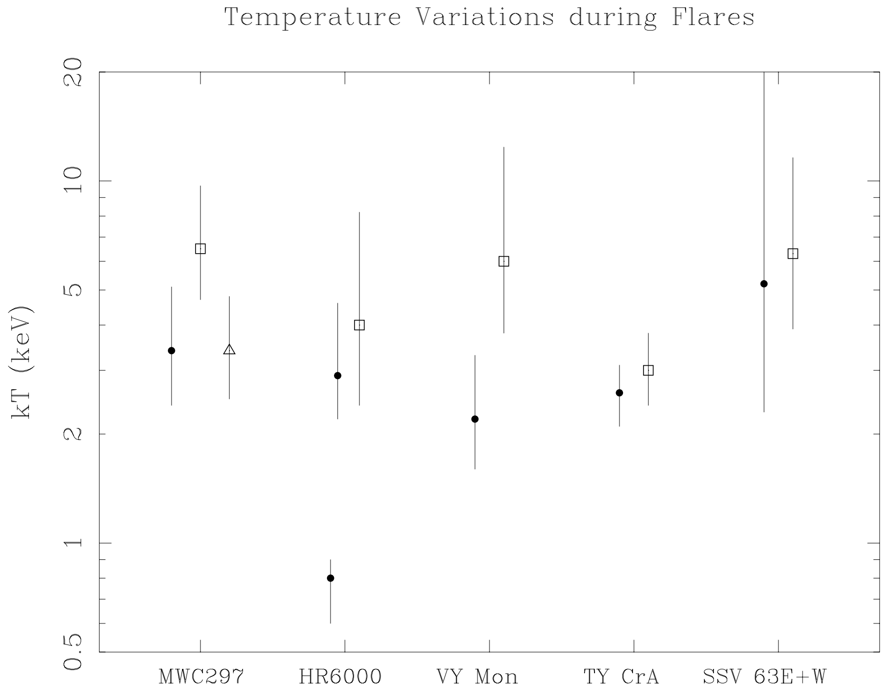

Figure 7.10: Variation of plasma temperature during flares. Symbols mean the same as the above.

Table 7.4: Physical parameters of the MWC 297 flare

n_e	$4.3\ 10^{10}\ \mathrm{cm}^{-3}$
V	$5.0\ 10^{33}\ \mathrm{cm}^{3}$
L (= $V^{1/3}$)	$1.7\ 10^{11}$ cm
$L_{\alpha=0.1}$	$8.6\ 10^{11}$ cm

$\alpha = d/L$. See Figure 7.11.

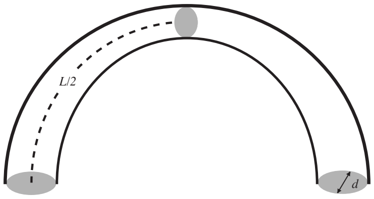

Figure 7.11: Assumed geometry of the flare magnetic field

quasi-static model in some cases, the quasi-static model is convenient for the order estimate of plasma volume. We thus apply this model to the x-ray flare on MWC 297. In this model, flare cooling timescales and luminosity is given by

$$\tau_{cool} = \frac{3n_{\mathrm{e}}k_B T}{n_{\mathrm{e}}^2 \Lambda(T)}$$

$$L_X = n_{\mathrm{e}}^2 \Lambda(T) V$$

where τ_{cool}: the cooling time scale of the plasma, n_{e}: electron density, $\Lambda(T)$: the emissivity in a unit volume. The derived parameters are shown in Table 7.4. The flare size L >10^{11-12} cm is significantly larger than those of solar radius and the typical flare size of low mass protostars. Because the radius of MWC 297 is about 10 times as large as the solar radius, a flare loop can be confined in just above the stellar surface of MWC 297. However, we only saw the decay phase of the MWC 297 flare. The maximum luminosity and plasma temperature could be much higher than the observed value. It is, therefore, too early to conclude that a magnetic loop size on MWC 297 flare is smaller than the stellar size.

We also investigated the kT and $E.M.$ variation in quiescent, flare and flare decay phases (Figure 7.9, 7.10). kT values of MWC 297 and VY Mon/G2 rise and $E.M.$ of MWC 297 increases during the flares. This supports that some heating mechanism like solar-type flares is working during the flare state. Other sources, however, do not show the prominent time variation within the limited photon statistics.

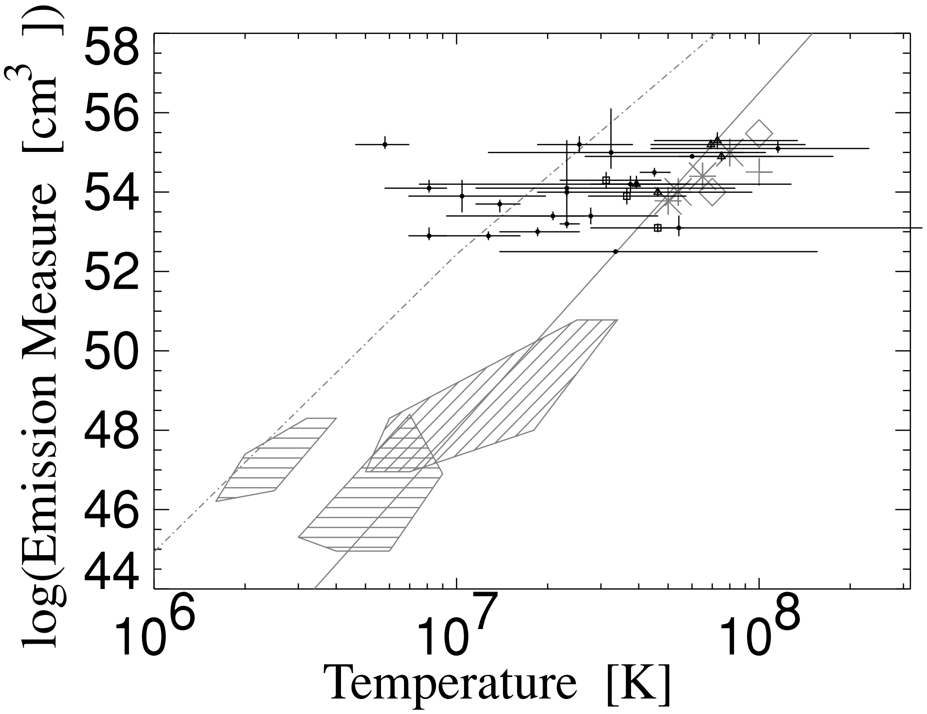

Figure 7.12: *kT vs. E.M.* relation (*black*), superimposed on the plots of solar and stellar x-rays (*grey*). Parameters in the quiescent state are shown by dots (1T or 2T low-temperature) or squares (2T high-temperature), and those in the flare state or high state are shown by triangles. Grey asterisks, pluses and diamonds are plots of a few stellar flares. Oblique hatched region (*upper right*) are solar flares and horizontal hatched regions are of solar micro flares (*bottom right*) and solar corona (*bottom left*). The solid line is the *E.M.-T* relation curve of stellar flares for B =50 gauss. The dotted bar line is the relation of stellar corona. See details in Shibata and Yokoyama (2001) and Shibata and Yokoyama (1999).

7.3.4 *kT vs. E.M.* Relation

Shibata and Yokoyama (1999) derived the universal correlation between flare temperature and emission measure for solar and stellar flares, which is based on a magnetic reconnection model with heat conduction and chromospheric evaporation. They extended this relation for coronal emission from a basic equation of heat generation, conduction and radiation (Shibata and Yokoyama 2001). In this theory, the *kT vs. E.M.* plots of quiescent and flare states are on a single line when strength of the magnetic field is given. We plot the observed *kT* and *E.M.* values on this graph (Figure 7.12). All components in the flare state are clearly on the *E.M.–T* relation curve for B =50 gauss. 2T high-temperature components in the quiescent state are also near this curve. These tendency suggests that HAeBe flares and hot components in the quiescent state are originated in the same types of magnetic activity as solar x-ray flares. 2T high-temperature components do not exhibit time variations so that they might be an assembly of microflares. 1T or 2T low-temperature components are distributed around the *E.M.*-T relation curve of coronal emission, and hence might be originated in a stellar corona. However, these values scatter in a very large range and some plots are on the flare curve. Because some sources are too weak to identify a time variation, a flaring state might be misidentified as a quiescent state.

7.4 Evolution of Stellar X-ray Activity

To find out the alternative mechanism to generate magnetic fields, we investigate the dependence of the quantity $L_{\rm X}$ and kT on the evolutional status of HAeBes. The stellar evolution is generally simulated in the HR diagram, but the spectral types and bolometric luminosities could have large uncertainties for a few HAeBes. We thus first see the relation with $N_{\rm H}$, and second we investigate the $L_{\rm X}$ dependence on the equivalent width of Hα lines. Finally, we see the kT and $L_{\rm X}$ dependence on the position in the HR diagram.

7.4.1 $N_{\rm H}$ *vs.* kT and $L_{\rm X}$ Relation

$N_{\rm H}$ is a good indicator of stellar evolutional status because the surrounding materials are gradually exhausted with age by gathering parts of these circumstellar materials and dissipating the rest by the UV radiation or stellar winds. $N_{\rm H}$ dependence on stellar masses or inclination to the line of sight is not clear, and hence this is a rough estimate of tracing the HAeBes evolution. Sources whose best-fit values is $N_{\rm H} = 0$ is fixed on the $A_{\rm V}$ converted $N_{\rm H}$ values because they have too large error bars. Then, kT values of 1T or low temperature components seem to steadily rise from 2 keV to 5 keV as $N_{\rm H}$ increases (Figure 7.13). Only MWC 1080 ($N_{\rm H}$ $\sim$1$\times$10^{22} cm^{-2}) lies above this line, but this might be the effect on a close HAeBe–HAeBe binary system (see the section 5.1.14). In contrast, high temperature component, which have small contribution to the x-ray luminosity, do not change around kT $\sim$2$-$4 keV. Low temperature plasma components of Large $N_{\rm H}$ sources are difficult to be detected due to suffer strong absorption. It is, however, obvious that HAeBes with smaller $N_{\rm H}$, ie elder HAeBes, tend to have lower plasma temperature.

Figure 7.14 shows the relation between $N_{\rm H}$ and $L_{\rm X}$ among the *ASCA* detected sources. Square plots means stars earlier than B and dotted plots later than A. $L_{\rm X}$ error bars are assumed to be the Poisson distribution of source counts. All sources with log $L_{\rm X}$ (ergs s^{-1}) $>$32 are B-type stars and have relatively large $N_{\rm H}$ ($>$10^{22} cm^{-2}). A-type stars are in the luminosity range between log $L_{\rm X}$ (ergs s^{-1}) = 30.5$-$31.5, being independent of $N_{\rm H}$ values. B-type stars with small $N_{\rm H}$ seem to have low x-ray luminosities, but the luminosities have large scatters between log $L_{\rm X}$ (ergs s^{-1}) = 30$-$32.

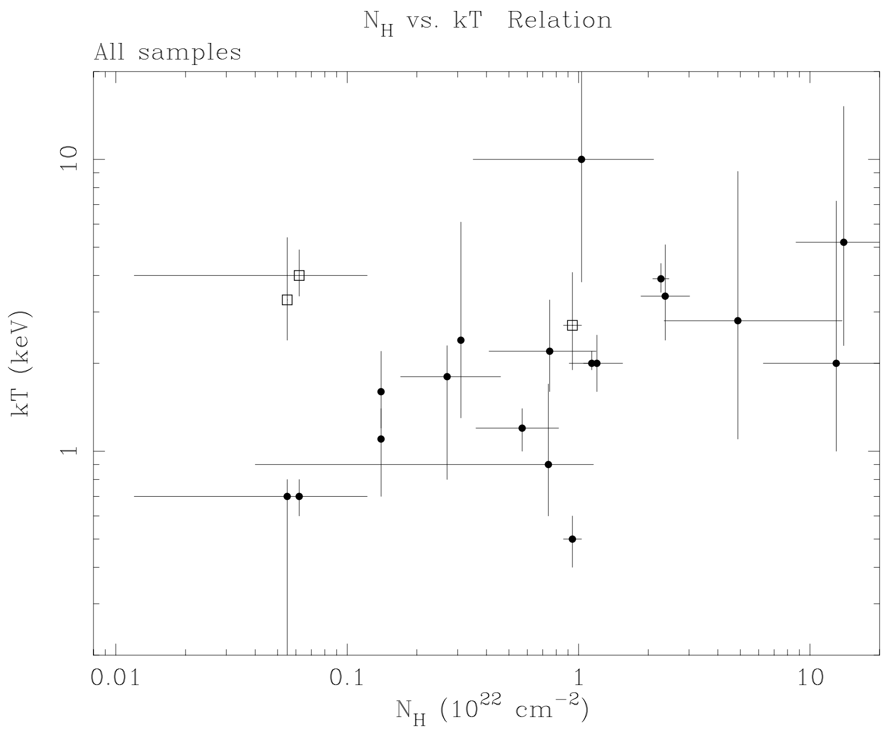

Figure 7.13: kT dependence on N_{H}. High temperature components in the 2T fitting models are shown by squares. Two observing data of TY CrA and HD 176386 (Obs. ID: RCrA 1 & RCrA 6) are plotted. S CrA is omitted because it would be a genuine low mass star.

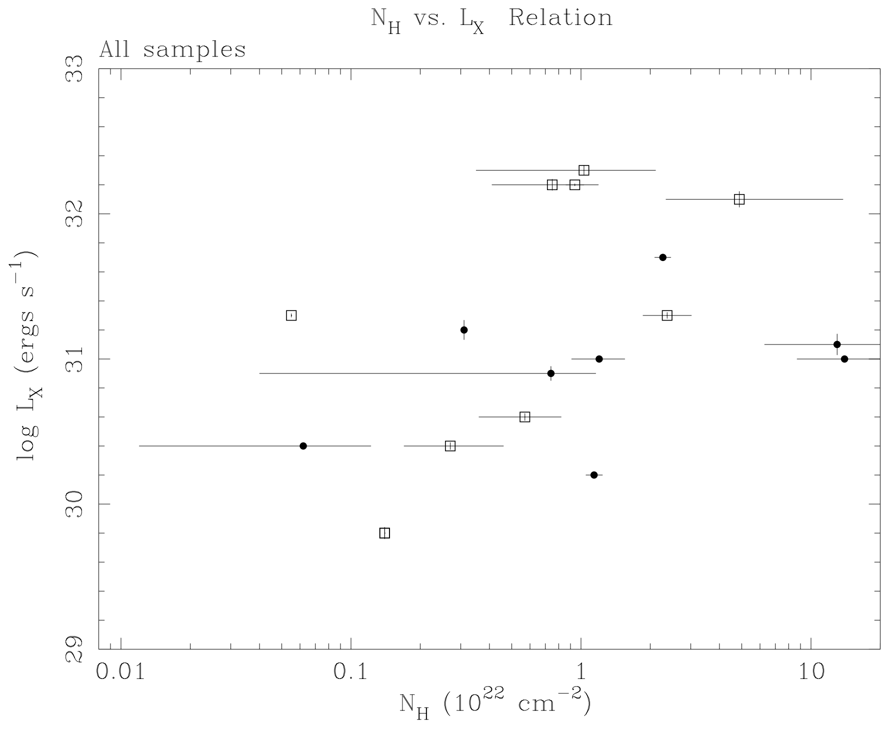

Figure 7.14: L_{X} dependence on N_{H} (square: earlier than B, dot: later than A). VY Mon is classified as spectral type B while V892 Tau is as A. Two observing data of TY CrA and HD 176386 (Obs. ID: RCrA 1 & RCrA 6) are plotted. S CrA is omitted because it would be a genuine low mass star.

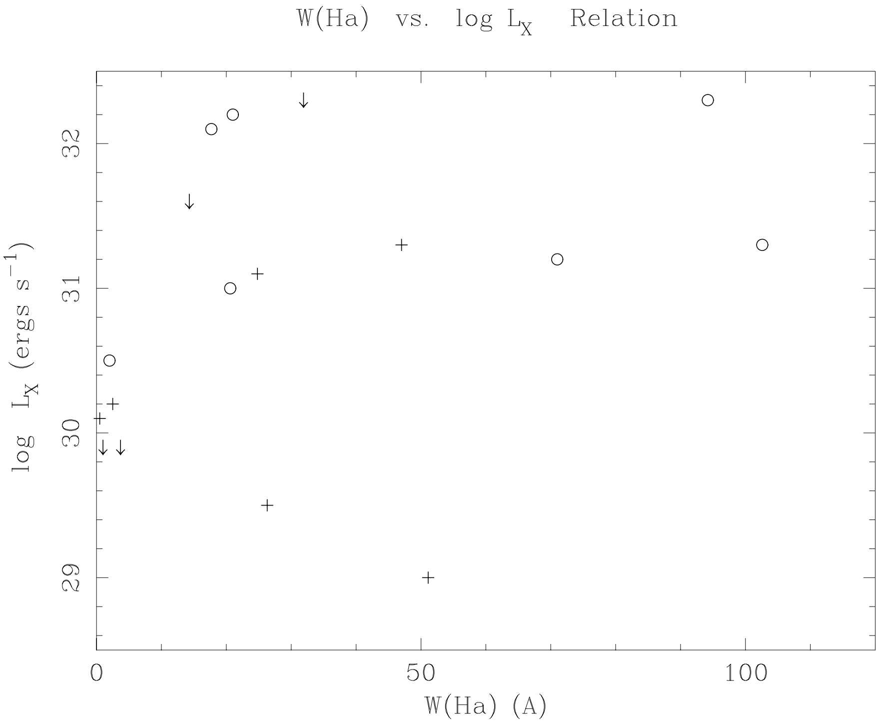

Figure 7.15: W(Hα) *vs.* log L_X relation. Marks mean the same as Figure 7.3.

7.4.2 Equivalent Width of Hα *vs.* L_X Relation

Equivalent width of Hα emission is used for the classification of low mass PMSs. This value is thought to trace the mass accretion rate, and hence the evolutional stage. We thus see the dependence of L_X on the equivalent width of Hα, W(Hα) (Figure 7.15). We refer equivalent width to the Corcoran and Ray (1998) and Damiani et al. (1994). Some objects have inconsistent W(Hα) values between articles, which could be the time variation or observing uncertainty. In this case, we applied the value in Corcoran and Ray (1998). We do not see any clear correlation between W(Hα) and log L_X. This might mean that the x-ray emission is irrelevant to the mass accretion, but it is too early to conclude it because the continuum levels are much different between stars and the Hα line luminosity might be a better to trace stellar evolution.

7.4.3 Evolutional Trends of kT and L_X in the HR Diagram

We estimated the kT and L_X evolution from the evolutional model provided by Palla and Stahler (1993) in the HR diagram. Figure 7.16 shows absorption corrected L_X and kT values of each HAeBe in the HR diagram. T_{eff}, L_{bol}, kT and L_X values of each source are seen in Tables 4.1 and 5.5. In this figure, circle size is proportional to logarithmic values of absorption corrected x-ray luminosity and the shade of circles means plasma temperature. Samples below the threshold luminosity log $L_{\rm X}$ (ergs s^{-1}) = 30, which is determined from the WTTS $L_{\rm X}$ function (see the section 7.1) are shown by crosses. We determine the position of SSV 63E+W in the HR diagram by combining the information that $L_{\rm bol}$ ~22.4 $L_\odot$, age <10^6 yrs and the mass 1.5 $M_\odot$ < M <5 $M_\odot$. The position in the HR diagram is then close to EC95.

We clearly see that samples on the upper right of Figure 7.16 has high temperature plasma kT >4 keV and samples closer to the main-sequence tend to have lower plasma temperature. The upper right in the HR diagram corresponds to the younger stars (see the subsection 2.1.3). These results are consistent with the relation with $N_{\rm H}$ values in the subsection 7.4.1. The similar trend seems to be present in $L_{\rm X}$. The luminosity on the upper right in the diagram is nearly $L_{\rm X} \sim 10^{32}$ ergs s^{-1} and gradually decreases as they close to the main-sequence. Nevertheless, the *ASCA* samples are limited to trace the overall picture of this $L_{\rm X}$ trend. We thus omit the information on temperature and add samples from *ROSAT* results (HAeBe:Zinnecker and Preibisch 1994, the Orion molecular cloud:Gagné et al. 1995). We collect source samples whose detection limit is log $L_{\rm X}$ (ergs s^{-1}) <30, We also include late-type samples with log $T_{\rm eff}$ (K) >3.65 (spectral type G) listed in Gagné et al. (1995) because some would be progenitors of A or late-B type stars. These samples do not have kT information for the lack of spectral resolution or the constraints on photon statistics. We calculate the *ASCA* band luminosity assuming the average kT ~2 keV of the *ASCA* detected sources, but the conversion factor only changes less than factor of two within the range of stellar plasma temperature, kT ~0.5−5 keV (see Table 4.8). Figure 7.17 shows the $L_{\rm X}$ map of HAeBes in the HR diagram. The $L_{\rm X}$ trend in the *ASCA* data is clearly seen in this picture. The most remarkable feature is that most sources elder than 10^6-year-old (3.8 < log $T_{\rm eff}$ < 4.1, 1.3 < log $L_{\rm bol}$ < 1.9) emit faint or no x-rays, ie log $L_{\rm X}$ (ergs s^{-1}) <30. We might say that the age 10^6-year-old would be at the end point of HAeBe x-ray activity.

Damiani et al. (1994) found a correlation between $L_{\rm X}$ and spectral type or $L_{\rm bol}$ but Zinnecker and Preibisch (1994) did not (see the subsection 2.2.2). We now see that this difference is simply due to the selection effect. Damiani et al. (1994) collected HAeBe samples close to the main-sequence so that they found a similar x-ray characteristics to MS stars. While Zinnecker and Preibisch (1994) collected young A-type samples such as V380 Ori and HR5999. Their x-ray luminosity is comparable to early B-type stars and thus no $L_{\rm X}$ dependence was seen.

7.5 Models to Generate the Magnetic Field on HAeBes

The large scale magnetic fields connecting a star and its disk seems to account for the x-ray activity on HAeBes (see the section 2.2.2 and the appendix A.3). In previous sections, we find

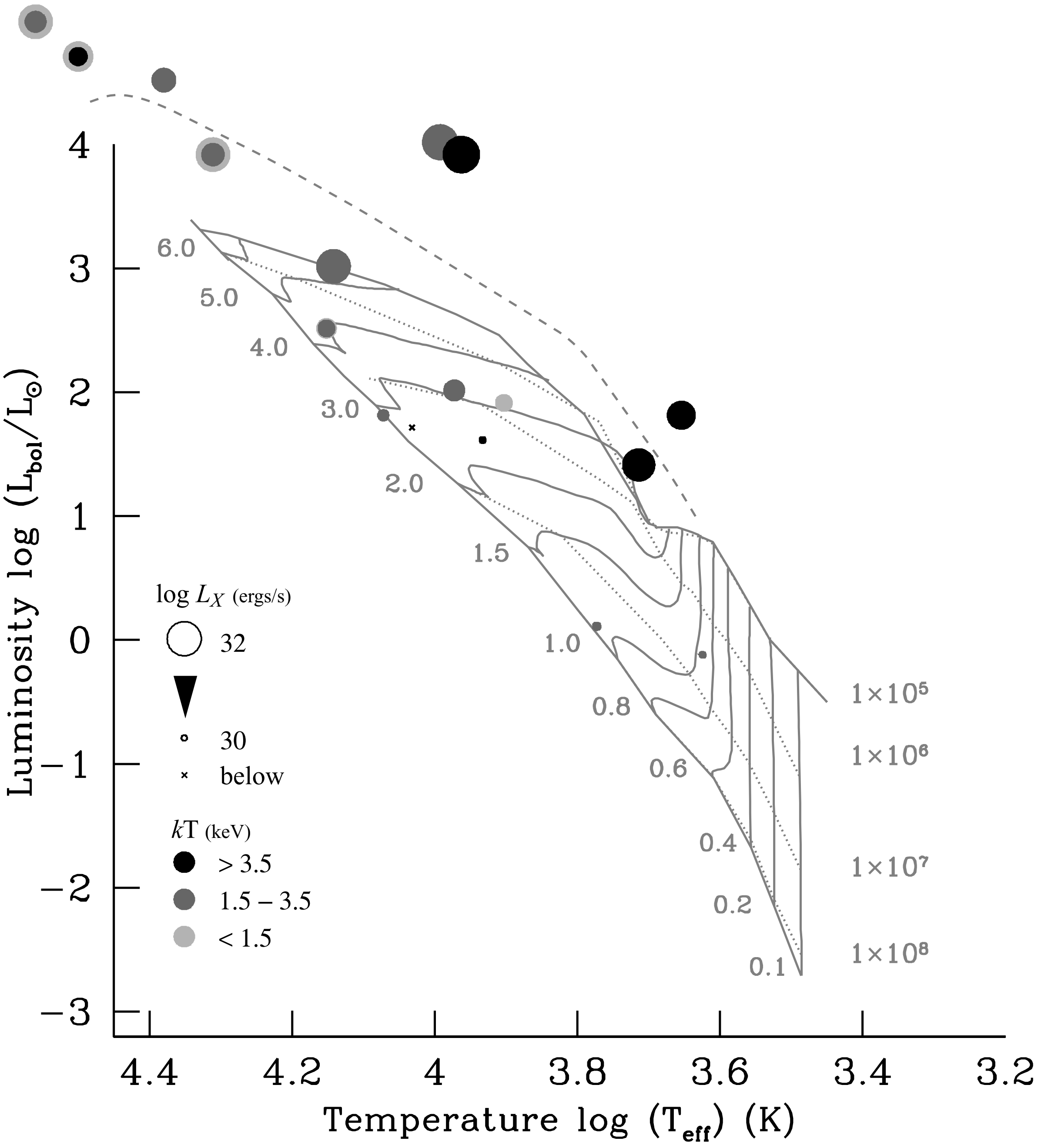

Figure 7.16: X-ray luminosity and plasma temperature of the HAeBe samples in the HR diagram. Circle size is proportional to log $L_{\rm X}$ and filled gray color indicates the plasma temperature. The threshold luminosity is set at log $L_{\rm X}$ (ergs s^{-1}) =30.0. Sources below this threshold are shown with crosses. The diagram is superimposed on a evolutional model by Palla and Stahler (1993). A dotted line means the birthline when accretion rate is $\dot{M} = 10^{-4}$ $M_{\odot}$ yr^{-1}.

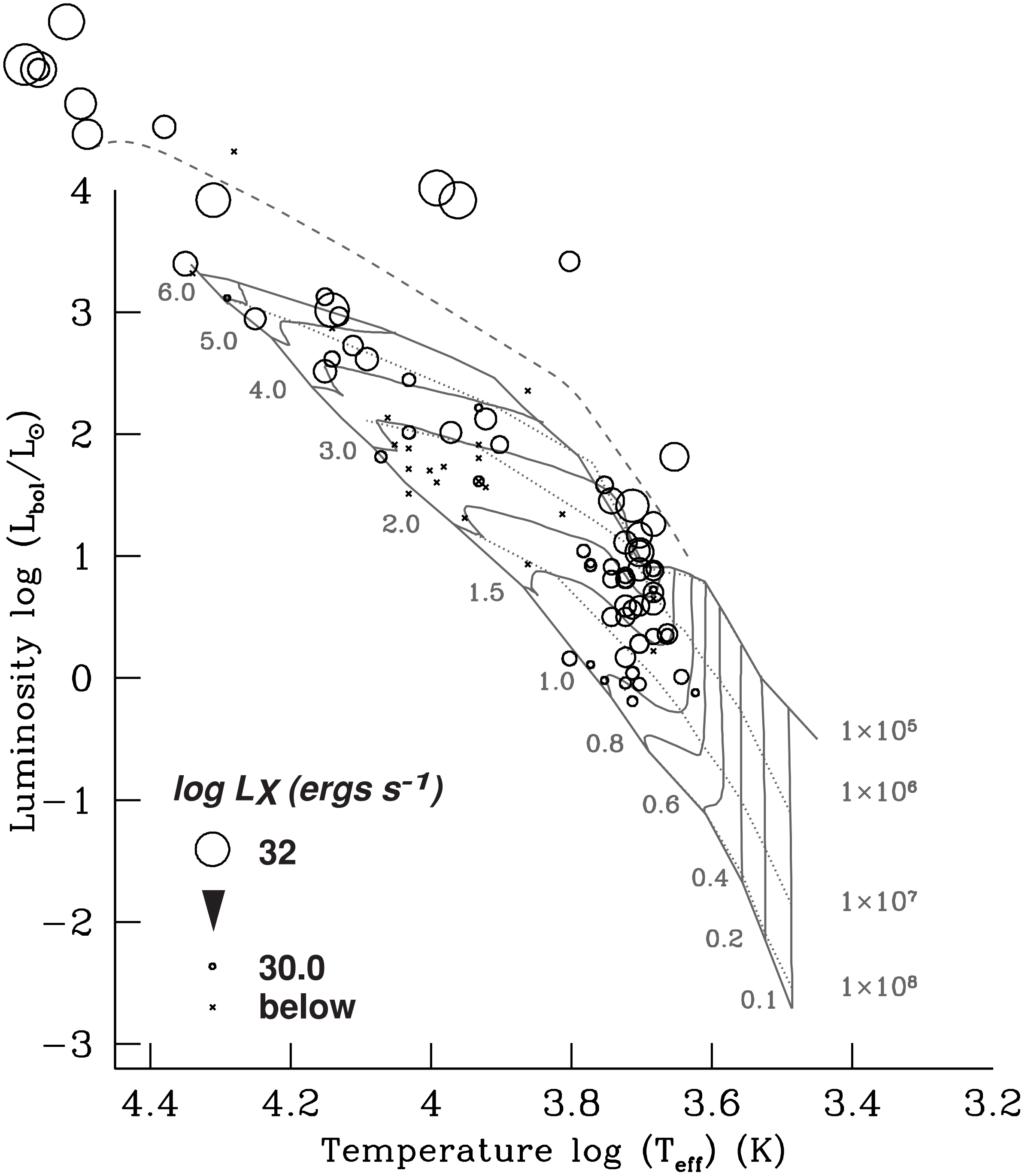

Figure 7.17: X-ray luminosity of the young stars in the HR diagram, including the *ROSAT* and *Einstein* samples. Details are the same as the previous figures but the information of plasma temperature is omitted.

Table 7.5: Young stars in the Orion cloud (Gagne et al. 1995)

Objects	T_{eff} log K	L_{bol} log $L_{\odot}$	$v \sin i$ km s^{-1}	L_{X} log ergs s^{-1}	$L_{\mathrm{X}}/L_{\mathrm{bol}}$ log	Objects	T_{eff} log K	L_{bol} log $L_{\odot}$	$v \sin i$ km s^{-1}	L_{X} log ergs s^{-1}	$L_{\mathrm{X}}/L_{\mathrm{bol}}$ log
P1491	4.03	2.43	–	30.6	−5.4	P1799	3.77	0.91	123	30.5	−4.0
P1623	3.93	1.79	171	<29.8	<−5.6	JW373	3.68	0.64	–	30.1	−4.2
P1671	3.92	1.55	–	<29.9	<−5.2	P1828	3.68	0.69	29	31.1	−3.2
P1712	4.03	2.00	75	30.6	−5.0	P1817	3.70	1.02	35	31.7	−2.9
P1708	4.14	2.85	–	<29.9	<−6.5	P1910	3.68	1.25	–	31.4	−3.4
P1795	4.03	1.87	–	29.9	−5.6	P1937	3.77	0.93	–	30.3	−4.2
P1798	4.25	2.93	50	31.2	−5.3	P1955	3.74	1.44	109	31.5	−3.5
P1891	4.58	5.01	140	32.7	−5.9	P1950	3.74	0.49	27	31.0	−3.0
P1889	4.49	4.44	145	31.9	−6.2	P1972	3.68	0.71	<20	30.2	−4.1
P2058	3.99	1.59	170	<29.7	<−5.4	P2001	3.72	0.16	<20	31.1	−2.7
P1393	3.72	0.49	<20	31.0	−3.0	P2033	3.72	0.80	56	31.1	−3.3
P1374	3.80	0.15	77	30.7	−4.1	P2032	3.75	−0.03	–	30.2	−3.7
P1409	3.72	0.80	29	30.9	−3.5	P2057	3.71	−0.20	–	30.4	−3.0
P1425	3.74	0.80	26	30.9	−3.5	P2069	3.68	0.60	38	31.3	−2.9
P1455	3.78	1.03	21	30.6	−4.0	P2086	3.81	1.33	72	<29.9	<−5.0
P1510	3.70	0.27	38	31.2	−3.3	P2084	3.68	0.88	<20	30.7	−3.7
P1518	3.70	−0.06	38	30.6	−2.9	P2100	3.72	0.83	72	30.8	−3.6
P1505	3.70	0.27	<20	31.0	−2.9	P2167	3.72	1.10	57	31.3	−3.4
P1541	3.71	0.55	<20	31.0	−3.2	P2152	3.66	0.35	–	31.1	−2.9
P1553	3.70	1.03	28	31.3	−3.4	P2181	3.70	0.58	–	31.1	−3.0
P1587	3.70	0.88	<20	31.3	−3.2	P2244	3.68	0.87	51	31.1	−3.3
P1659	3.70	1.16	<20	31.5	−3.3	P2253	3.72	−0.05	–	30.5	−3.0
P1736	3.75	1.57	41	30.9	−4.2	P2252	3.74	0.90	33	30.8	−3.7
P1773	3.68	0.33	–	30.9	−3.1	P2257	3.72	0.58	47	31.2	−2.9
P1760	3.68	0.21	–	<29.9	<−3.9	P2347	3.71	0.03	–	30.6	−3.0
P1785	3.72	0.80	<20	31.0	−3.4	P2368	3.66	0.34	47	30.6	−3.3

Objects in the right and below P1393 in the left are young stars in the Orion cloud (Gagné et al. 1995) – above cross: early type, below cross: late type.

the similarity of the x-ray property with low mass protostars (eg plasma temperature, flares). This fact lets us suppose that the x-ray emission mechanism is also the same as protostars, ie the magnetic activity linking a star and its disk. This model reconciles the lack of mechanism to generate the magnetic field on stellar surface. The magnetic fields are originated in the fossil field, remaining from the parent molecular cloud. The presence of circumstellar disks around HAes is widely accepted by the observation of *mm* radio continuum survey. The model also supports the origin of outflows. Hayashi et al. (1996) simulate that the reconnection accompanies a gas eruption, which might be seen as a jet or outflows. A certain HAe continues the outflow activity till a few Myrs (Devine et al. 2000), which correspond well with the decaying age of x-ray activity (see the subsection 7.4.3). The long flare duration of HAeBes might be due to the large plasma volume, which needs long propagation time of shocks. Moreover, this model explains the high velocity of accreting materials (Blondel et al. 1993, see also the subsection 7.2.2). Magnetic reconnection, which occurs at a mid-point between a star and its disk, accelerates gases and forces them to accrete onto a star.

A problem lies in that there seems no apparent change in the structure of circumstellar disks around 10^6-year-old. For example, AB Aur and HD 97048, older than 10^6-year-old, still have relatively massive disks. We see but do not find any correlation between the luminosity

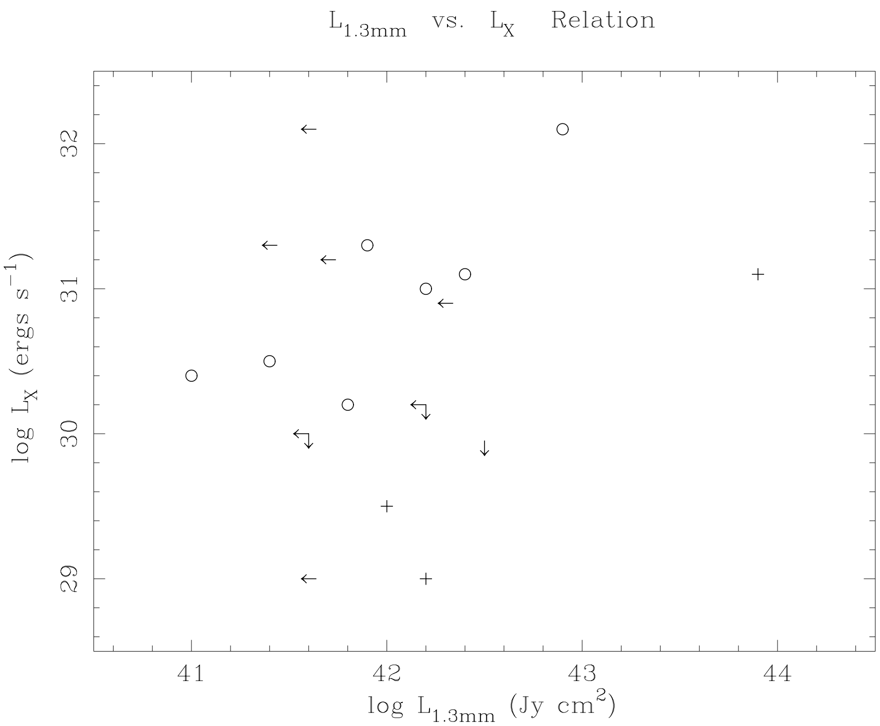

Figure 7.18: Radio continuum ($\lambda_{1.3mm}$) *vs.* $L_{\rm X}$ relation. Marks are the same as Figure 7.3.

of 1.3mm dust continuum emission, which is a good tracer of dense and cold circumstellar envelopes (Figure 7.18). These stars might already dissipate inner most of their disks, which cannot be resolved. On the contrary, even though there is no clear difference in the x-ray property between HAes and HBes, the circumstellar environment seems to be much different. HBes lack a compact continuum emission expected from a circumstellar disk and form large empty cavities. There are, however, a few pieces of supporting evidence for the star-disk magnetic field model. Drew et al. (1997) reports that even the very massive HBe MWC 297 shows the presence of an outflow phenomenon though they interpret its origin as radiative driven disk winds (Drew et al. 1998). Young massive MS star θ^1C Ori has an inverse P-Cygni profile in its spectrum, indicating the accretion flows (Conti 1972). Moreover, some early B-type MS stars are classified as β Pictoris type stars, having debris disks (eg Coulson et al. 1998, see the section 2.1.4).

Chapter 8

Discussion II – A Unified Picture of Stellar X-ray Activity

8.1 Evolution of the X-ray Activity to the Main-sequence Phase

One of the main conclusions in the previous section is that the x-ray activity of intermediate mass stars decays after 10^6-year-old. Massive stars larger than $4M_\odot$ reach ZAMS before this threshold age. It suggests that the massive stars could sustain the magnetic activity during the former phase of MS. Here, we demonstrate that this picture can solve most problems posed in the x-ray emission from high mass MS stars.

8.1.1 X-ray Emission from Late B Type Stars

From a RASS data survey of OB stellar x-rays, Berghoefer et al. (1997) reported that x-rays and bolometric luminosity relation of $L_\mathrm{X}/L_\mathrm{bol} \sim 10^{-7}$ was valid for massive stars down to a spectral type B1-1.5. Stars below this spectral type had no clear relation and have large scatters between these quantities. They also mentioned that the detection rate of these stars are very low (P $<$ 10%). These results suggest that the x-ray emission mechanism of massive stars, which is believed to be the stellar wind origin, changes at the spectral type B1-1.5. They invoked the x-ray origin of late B-type stars on extremely young low mass companion like CTTS, but some sources seem to have too large x-ray luminosities compared with low mass stellar x-rays. We therefore hypothesis that most sources detected in this survey are young and still possess the magnetic activity continuing from the PMS phase. There is the supporting evidence for the magnetic activity on young B-type MSs.

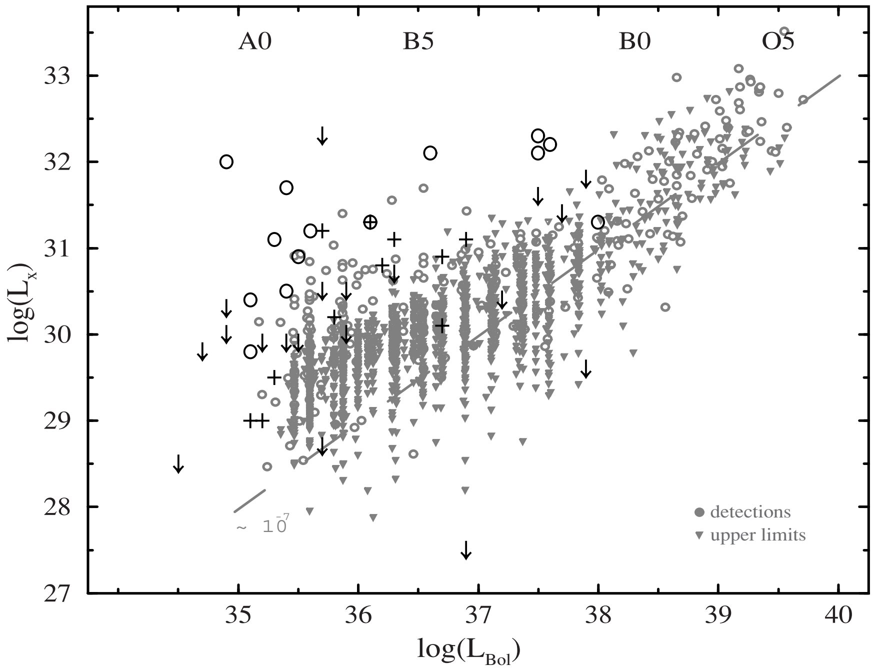

Figure 8.1: L_{X} *vs.* L_{bol} relation of Herbig Ae/Be stars superimposed on the plots of OB stars provided by Berghoefer et al. (1997). Plots of HAeBes are shown with black crosses while ones of OB stars are shown with grays.

L_{X} *vs.* L_{bol} **Relation** We superimposed HAeBe data on the L_{X} *vs.* L_{bol} graph of OB stars provided by Berghoefer et al. (1997) (see Figure 8.1). All HAeBe plots are just above the higher end of OB star. Considering the stellar evolution, $L_{\mathrm{X}}/L_{\mathrm{bol}}$ values decrease with age and the x-ray flux finally drop below the detection level. This is the reason why $L_{\mathrm{X}}/L_{\mathrm{bol}}$ values scatter in a wide range.

Detection Rate Berghoefer et al. (1997) reported that the detection rate continuously decreases toward later O and early B-type stars and drops to <10% between B2−B9. The transition age a few$\times 10^6$-year-old is roughly 10% of the life time of B2 stars (2.4×10^7 yrs, see also Table B.2).

Time Variability Smith et al. (1993) detected a giant x-ray flare on the MS B star λ Elidani (B2e) with *ROSAT* PSPC. They concluded that the flare arises on or related to λ Elidani itself because of no evidence of existing a companion star in IUE and optical spectra. They also suggested λ Elidani would not be a classical Be star. The fact that λ Elidani shows emission line then demonstrates its youth. It then has a characteristics of youth,

Table 8.1: X-ray characteristics of massive main-sequence stars

Target	Sp.T	ref.	Comp.	Temperature (keV)		Emission Measure (cm^{-3})		log L_{X} (ergs s^{-1})
δ Ori.	O8+B0.5	1	Cool	0.25	(0.21–0.30)	55.20	(55.03–55.37)	32.1
			Hot	0.60	(0.45–0.79)	54.73	(54.59–54.87)	31.6
λ Ori	O9.5+B0	1	Cool	0.29	(0.25–0.34)	55.09	(54.97–55.21)	32.1
			Hot	2.27	(1.14–4.52)	54.24	(54.01–54.47)	31.2
τ Sco.	B0V	2	Cool	0.62	(0.62–0.64)	54.54	(54.50–54.57)	31.8
			Hot	3.67	(2.59–)	53.77	(53.48–53.96)	30.9
			Hot2	1.06	(0.88–1.24)	53.91	(53.75–54.01)	31.0
ζ Oph.	O9.5V(e)	3	1T	0.54	(0.52–0.56)	54.20	(54.08–54.30)	31.2
ζ Ori.	O9.7Eb+O9.5IV	3	1T	0.43	(0.41–0.45)	54.34	(54.15–54.48)	31.2

The energy band of L_{X} is between 0.5 – 10 keV. References: 1.Corcoran et al. (1994), 2.Cohen et al. (1997), 3.Kitamoto et al. (2000)

8.1.2 X-ray Emission from O and Early B Type Stars

In Figure 8.1, stars earlier than B1-1.5 has a relation of log $L_{\mathrm{X}}/L_{\mathrm{bol}} \sim -7$, and the UV driven stellar wind seems to be the dominant activity. Nevertheless MS O-type stars are generally younger than B-type stars, and hence should possess the same kind of magnetic activity as late-type stars. We hypothesis that this component is seen as the hard tails in the x-ray spectra. The hard tails were believed to be emerged from the inverse Compton mechanism when the stellar UV photons were scattered by relativistic electrons, which is accelerated by the 1st order Fermi shocks (Chen and White 1991). However, the x-ray spectra of some O-type stars including the super massive star ζ Pup (Corcoran et al. 1993) can be reproduced by a simple one-component plasma model (see the discussion of Kitamoto and Mukai 1996). The inverse Compton model does not seem to explain the variety of this tail component.

We thus compared L_{X} and kT values of hot and cool components in O stars with those of HAeBes (Table 8.1, Figure 8.2). The reference papers only show *E.M.* and kT values so that we calculated the x-ray fluxes using xspec 9.0. We clearly see that the hard tails is quite similar to the values of HAeBes. In contrast, the soft x-ray component is on the other region, high L_{X} and low kT.

PMS natures in massive MS stars have never been predicted. However, a recent *Chandra* observation demonstrated the evidence of magnetic activity on O stars (see the subsection 2.2.1). On the other hand, the hottest star in the Orion cloud θ^1 Ori C showed a long term x-ray variation (Caillault et al. 1994). Because θ^1 Ori C also shows an inverse P-Cygni profile, this phenomenon might be associated with the accretion process linking to the magnetic activity.

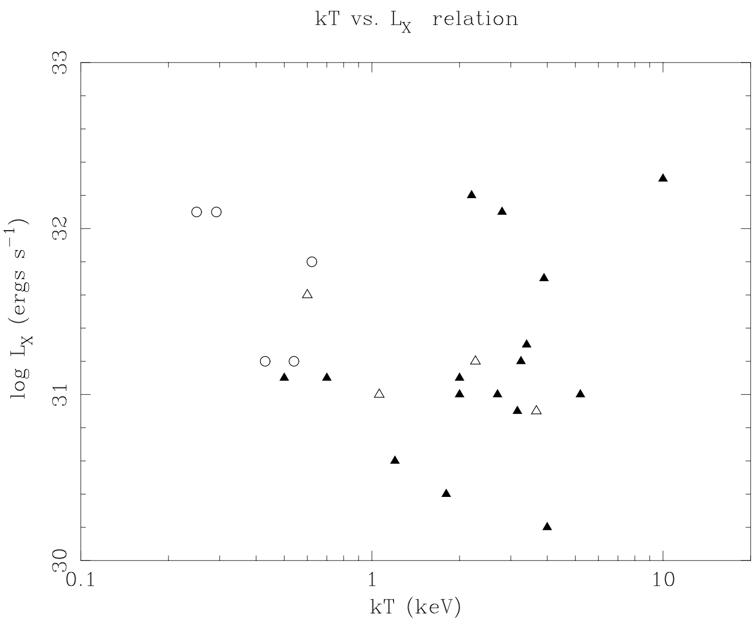

Figure 8.2: $kT\,vs.\ L_{\rm X}$ relation of MS massive stars and Herbig Ae/Be stars. Open squares and circles are soft and hard components in massive stellar spectra respectively. Filled squares and circles are those in HAeBes.

8.2 X-ray Emission from Giant Molecular Cloud Cores

GMC cores are the birth place of HAeBes (see the subsection 2.2.2). When we trace back the evolution of magnetic activity on HAeBes, we need to study the x-ray emission from GMC cores. These regions are generally very crowded and *ASCA* cannot clearly identify the x-ray sources, which probably include HAeBe progenitors, ie intermediate and high mass protostars. We find the presence of extremely high plasma components in Monoceros R2 region (see the section 6.1), which might be originated in high mass protostars.

Table 2.1 summarizes *ASCA* observations of five GMC cores. These x-ray properties are smeared over slightly large areas including surrounding soft x-ray sources, most of which are probably high mass MSs and low mass young stars. Therefore these $N_{\rm H}$ values are average on including x-ray sources. However, high kT values would represent x-ray emission from HAeBe progenitors because soft x-ray sources do not contribute the hard x-ray flux which determines kT. We thus compare these kT values with the HAeBe temperature (Figure 8.3). We omit the data of Orion trapezium where the x-ray emission from the massive MS star θ^1 Ori C is dominant. Then, the rising trend of kT values seen in HAeBe samples smoothly connects with kT of GMC cores. This result not only suggests that the hard x-ray flux comes from HAeBe progenitors but also implys that very young HAeBes have more violent x-ray activity. Of course, observations of GMCs with high spatial resolution are essential

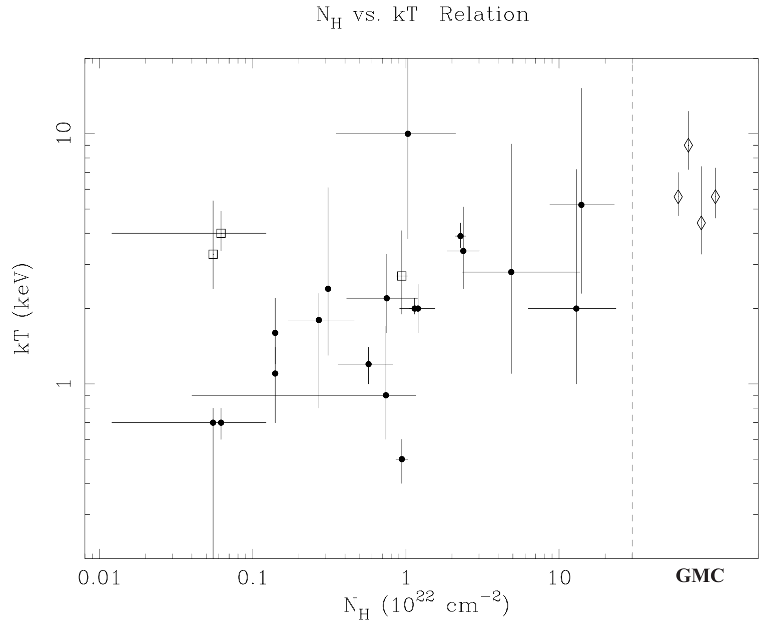

Figure 8.3: kT distribution of giant molecular cloud and Herbig Ae/Be stars. kT values of GMC are plotted on the right side of Figure 7.13.

to address this problem. *Chandra* will reveal the nature of intermediate and high mass protostars.

8.3 A Unified Picture of X-ray Activity on YSOs

We find that x-ray emission from intermediate to high mass YSOs is originated in the magnetic activity. This means that magnetic activity plays an important role on all types of YSOs from low mass to high mass stars. Here we describe the evolution of x-ray activity on YSOs.

Stellar x-ray emission begins in very young phase when stars are deeply embedded in molecular cloud cores, ie protostar phase. In this phase, stars possess 'fossil' magnetic fields inheritant from the parent clouds and exhibit violent magnetic activity linking a star and its disk, showing occasional x-ray flares. In this process, a part of infalling gases goes out from the system with large amount of angular momentum, which is later seen as molecular outflows or optical jets. The rest of infalling gases streams down to the stellar surface, accelerated by reconnection shocks. Accreting shocks heat gases up to the level of x-ray emission.

The link between a star and its disk fades around $\sim 10^6$ yrs. After decoupling the link, low mass stars continues magnetic activity on the stellar surface by operating $\alpha\Omega$ dynamo, but stars earlier than F5 do not have such mechanism and the x-ray activity rapidly decays. Because stars between A – F5 gradually evolve to the MS, 'dead zone' of the x-ray activity appears in the HR diagram. In contrast, earlier than B type stars reaches to the main-sequence before their x-ray activity ceases. Young MS stars - several percentage of all MS stars - still possess the x-ray activity. Stars earlier than B1-1.5 have enough UV photons to operate the wind driven x-ray activity. The x-ray emission by the magnetic activity becomes a minor component, but it is seen as hard tails.

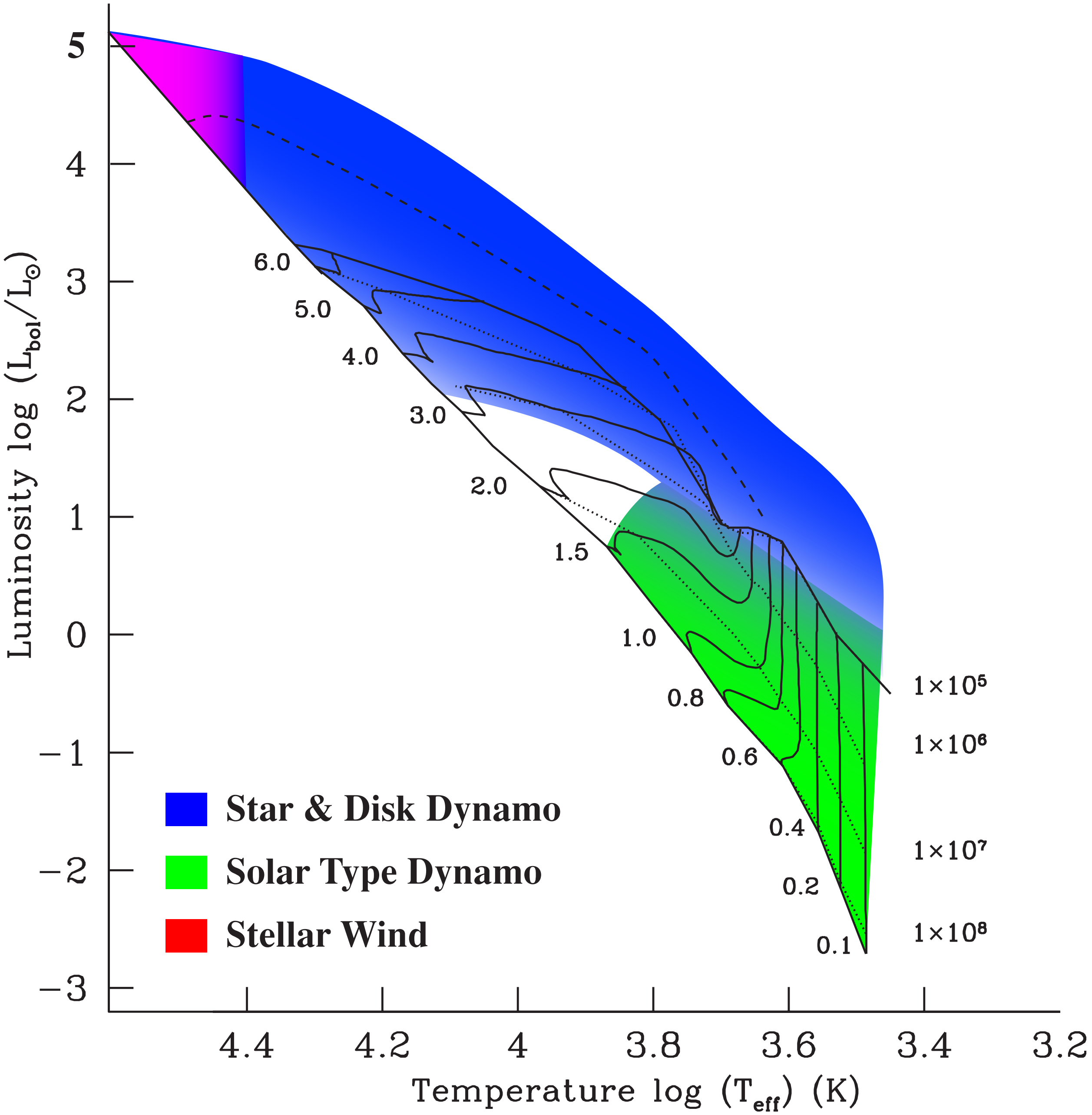

Figure 8.4: Unified picture of x-ray emission from stars.

Chapter 9

Conclusion & Future Problem

The x-ray emission from HAeBes has long been puzzled. This is partly because the proper x-ray emission mechanism is not known for these intermediate mass young stars and partly because the satisfying observing results have not been obtained. By combining our *ASCA* analyses with previous *ROSAT* and *Einstein* results, we find that the x-ray emission of HAeBes has its roots in the earliest phase of stars and continue to the former stage of the MSs. We list the results and implications below.

1. In the analyses of the *ASCA* data, 16 x-ray counterparts among 40 HAeBe candidates are detected. The x-ray luminosity is ranging between log $L_{\rm X}$ (ergs s^{-1}) = 30 − 32, which is significantly larger than the typical luminosity of low mass stars. The x-ray emission from low mass companions is unlikely.

2. 8 sources among the 16 detected sources (50%) exhibited time variation. Among 8 sources which have enough photon counts (above 1000 photons), 6 source showed time variation.

3. All x-ray spectra are successfully reproduced with absorbed one or two temperature thin-thermal (MeKaL) models. The plasma temperature ranges between $kT \sim 1-5$ keV, which is significantly higher than that of main-sequence OB stars ($kT < 1$ keV).

4. Several x-ray emission models are investigated for HAeBe x-rays. Stellar wind shock, wind-fed magnetosphere and accretion shock models cannot explain the HAeBe x-ray emission. Magnetic activity is the most probable x-ray emission mechanism.

5. There is no clear correlation between $L_{\rm X}$ and the rotational velocity (v sin i) or the angular velocity (ω sin i). The solar type dynamo mechanism does not seem to work on HAeBes.

6. Time profiles of sources showing prominent variability are investigated. All decay time scale is a few × 10^5 sec. This timescale is much longer than low mass TTSs and nearly the same as the timescale of low mass protostars. The flare size of an large x-ray flare from MWC 297, estimated with the radiative cooling model, is far larger than the solar radius but can be smaller than the radius of MWC 297.

7. The plasma temperature kT decreases as the observed $N_{\rm H}$ decreases whereas $L_{\rm X}$ depends more on stellar masses. This result indicates that the x-ray activity decays as stars evolve. By combining previous *ROSAT* and *Einstein* results, we find clear tendency that the x-ray activity of young stars decays after the stellar age $\sim 10^6$-year-old. Considering that the similarity of x-ray property and the circumstellar environment to low mass protostars, the x-ray emission from HAeBes seems to be originated in the magnetic activity linking a star and its accretion disk.

8. PMS x-ray activity continues to the former of the MS lifetime earlier than B-type stars. The x-ray emission driven by the stellar wind shocks seems to be dominant in stars earlier than spectral type B1-1.5, but the x-rays originated in the magnetic activity is still seen as hard tail component.

9. *ASCA* detected hard x-ray sources in the Monoceros R2 GMC core. The plasma temperature is very high $kT \sim 5$ keV. All GMC cores observed with *ASCA* have the similar temperature plasma. The rising trend of kT values seen as tracing back the HAeBe evolution smoothly connects to the kT of GMC cores. This suggests that hard x-rays from GMC cores are originated in HAeBe progenitors, ie high mass protostars.

In this study, a universal picture of the x-ray emission from higher mass YSOs are obtained for the first time. We think these three subjects as the next main problems.

- Can we obtain the definite evidence of magnetic activity on higher mass PMS? HAeBe samples showing time variation is still limited and the data quality is not high enough. A couple of x-ray variable sources with high signal-to-noise ratio are needed to address the dynamics of hot plasma. On the other hand, high resolution spectroscopy addresses the plasma density and temperature from atomic satellite lines. The information provides us the plasma geometry, for example, as whether the plasma is near or far from the stellar surface. This tool has already been utilized in the spectra of massive MSs (see the subsection 2.2.1). This will be a powerful tool for the analysis of PMSs.

- How is the structure of hot plasma around stars? There is no direct evidence to prove the structure of magnetic fields connecting a star and its disk. As we mentioned before, the x-ray flare could be strongly related to the jet formation. If the Doppler shift component in the PMS x-ray flare is detected, it will provide the important information on the jet acceleration mechanism and the structure of large scale magnetic fields.

- When does the x-ray activity begin in high mass young stars? Each x-ray source in the GMC core is not still resolved. By investigating x-ray properties of very young massive stars, the early evolution of x-ray activity, and hence magnetic activity, will be clear.

For statistical analyses of young higher mass stars, *Chandra* will provide sophisticated data without source contamination. Time profiles with high photon statistics can be obtained by *XMM-Newton* with very large effective area. On the other hand, high resolution grating spectroscopy onboard both *Chandra* and *XMM-Newton* is limited to soft x-rays around 1 keV. Micro calorimeter onboard Astro-E II will provide a powerful tool for performing high resolution spectroscopy of embedded sources. The x-ray emission from a young star provides important information close to the stellar body, but the study is now on the starting-point. In this ten years, the study will be greatly advanced with the new generation x-ray telescopes.

Appendix A

Models of the Stellar Magnetic Activity

A.1 Hydrodynamic Decay, Sustained Heating Model

Stellar x-ray flares provide the nature of the magnetic activity on stars. The Algol system is known to exhibit frequent x-ray flares and has been intensively studied. Flare decay is conventionally regarded as the cooling phase of thermalized plasma - the radiative cooling model. On this assumption, a flare volume becomes a few times as large as the stellar size (eg White et al. 1986). This result is supported by a detailed analysis containing an effect of heat conduction (the quasi-static cooling model, van den Oord and Mewe 1989). Schmitt and Favata (1999) however indicated that the real flare volume directly measured from an eclipsing event was much smaller than the volume in the conventional estimate. This suggests the presence of continuous heating during the flare. Reale and Micela (1998) applied a model of continuous heating during flares to a stellar x-ray flare with the *ROSAT* data. Favata et al. (2000) developed this method into an *ASCA* result and derived the flare volume is much smaller than the result of the radiative cooling model. According to these papers, the presence of additional heating is investigated by a slope of the locus of the flare decay in the log $E.M.$ – log T plane. This model describes flare parameters as the following equations.

$$\frac{\tau_{LC}}{\tau_{th}} = F(\zeta) = c_a e^{-\zeta/\zeta_a} + q_a \tag{A.1}$$

$$L = \frac{\tau_{LC}\sqrt{T_{max}}}{\alpha F(\zeta)} \tag{A.2}$$

where τ_{th}: the cooling time scale of plasma, τ_{LC}: a decay time scale of a light curve, and ζ: a slope of a flare decay in the log $E.M.$ – log T plane, and $\alpha = 3.7 \times 10^{-4}$ cm$^{-1}s^{-1}K^{1/2}$. The values c_a, ζ_a and q_a depend on a response of observed detectors, and $c_a = 10.9$, $\zeta_a =$

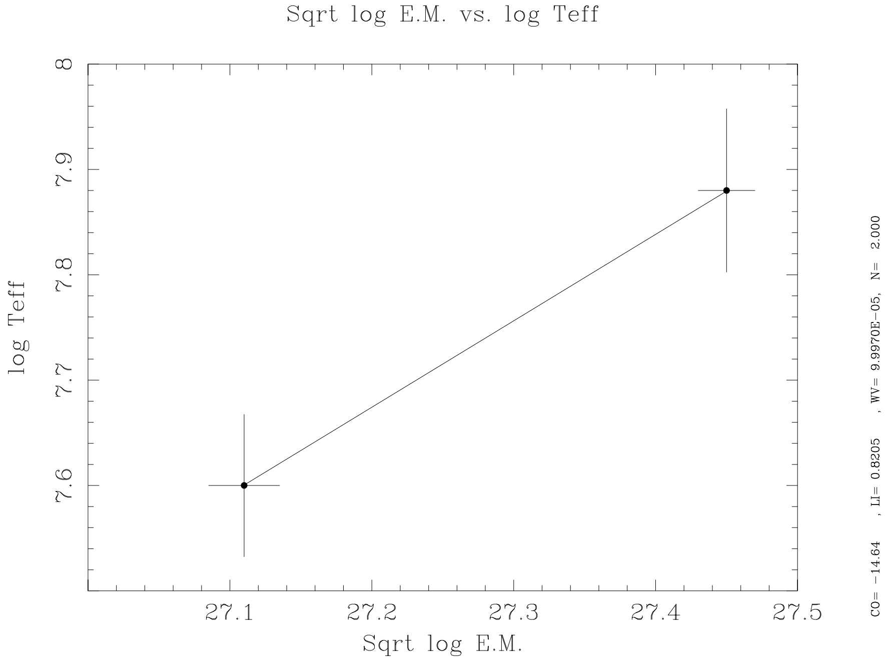

Figure A.1: Evolution of the MWC 297 flare parameters in the log $\sqrt{E.M.}$ – log T plane. The data points of the 2nd and 3rd observations are plotted in the plane. The solid line shows the slope of these plots.

0.56 and $q_a = 0.6$ for GIS. T_{max} is the maximum temperature of a flaring loop and Favata et al. (2000) derived an empirical relation to the observed maximum temperature T_{obs}.

$$T_{max} = 0.085 \times T_{obs}^{1.176} \tag{A.3}$$

The data of MWC 297 (the 2nd and 3rd observations) are plotted on the log $E.M.$ –log T plane (Figure A.1 and Table A.1). Because our plots have large errors, the uncertainty of ζ is very large. The semi-length L derived from the best-fit ζ value is as same as $\mathrm{L}_{\alpha=0.1}$ (see the subsection 7.3.3) in the radiative cooling model though the uncertainty of ζ is too large.

Table A.1: Physical parameters of the MWC 297 flare in the hydrodynamic model

ζ	0.82 (0.32–1.32)
T_{max}	1.5 $\times 10^8$ °K
F(ζ)	3.1
τ_{th}	1.78 $\times 10^4$ °K
L	5.9 $\times 10^{11}$ cm

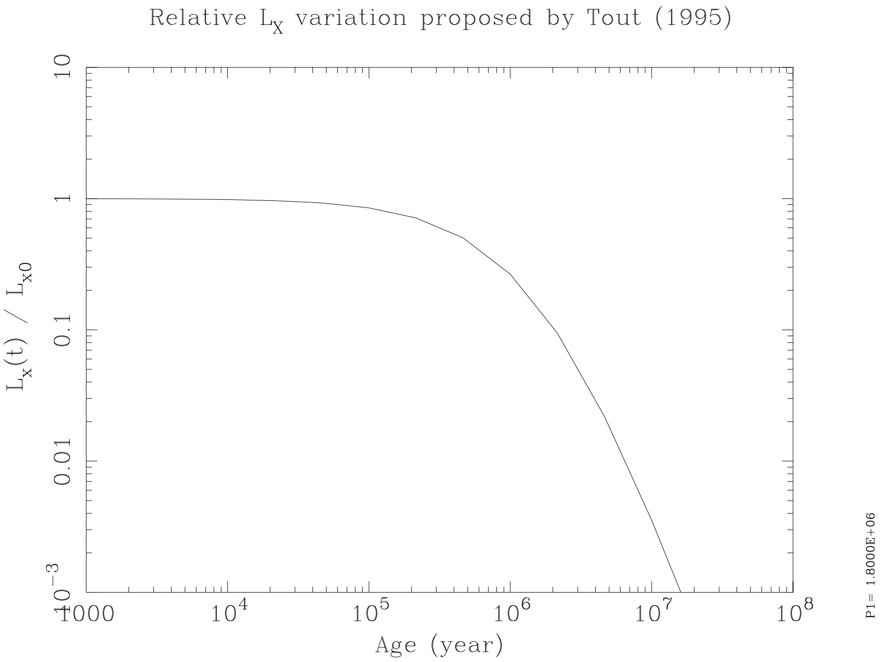

Figure A.2: Evolution of relative x-ray luminosity proposed by Tout et al. (1995).

A.2 Shear Dynamo Model

Tout and Pringle (1995) proposed a dynamo mechanism on HAeBes which is driven by a shear component holding in very young stars. In this model, HAeBe x-ray emission comes from a corona heated by this magnetic activity. It predicts that x-ray luminosity varies with age as follows (see also Figure A.2),

$$L_X(t) = L_{X0}(1 + t/t_0)^{-3} \tag{A.4}$$

where

$$\frac{L_{X0}}{L_\odot} \sim 8 \times 10^2 \varepsilon (\frac{\Delta\Omega_0}{\Omega_K})^3 (\frac{\gamma}{10^{-4}})^3 (\frac{M_*}{10 M_\odot})^{5/2} (\frac{R_*}{3 \times 10^{11}})^{-5/2} \tag{A.5}$$

$$t_0 \sim 4.8 \times 10^4 (\frac{\Delta\Omega_0}{\Omega_K})^{-1} (\frac{k^2}{0.1}) (\frac{\gamma}{10^{-4}})^{-3} (\frac{M_*}{10 M_\odot})^{-1/2} (\frac{R_*}{3 \times 10^{11}})^{3/2} yr \tag{A.6}$$

and $\Delta\Omega_0/\Omega_K$: ratio of the initial value of the rotational shear in the star to its breakup velocity, γ: efficiency of field generation, and k: proportionality factor between the stellar moment of inertia and $M_* R_*^2$. In this formula, there are several unknown parameters. Tout and Pringle (1995) suggest that this luminosity variation is consistent with the HAeBe luminosity provided by Zinnecker and Preibisch (1994) if these parameters are $\Delta\Omega_0/\Omega_K \sim 1$, $\gamma \sim 3 \times 10$ and $\epsilon \sim 10^{-3}$.

This model seems to have a few weak points. It does not predict the time evolution of the plasma temperature. The result in the subsection 7.4.1 indicates that the plasma temperature decreases as stars evolve, but this model assumes that energy is constantly supplied to a corona, and does not seem to predict a systematic change of plasma temperature. Second, x-ray luminosity only depends on stellar mass, radius and age except for its dynamo parameters (see the equation A.4, A.5). Some sources however have significantly small x-ray luminosity compared with sources on a similar evolutional tracks (see Figure 7.17) although the difference might be due to the uncertainty of the distance.

A.3 Diffusion Time Scale of the Magnetic Field

The star-disk magnetic field model assumes the presence of fissile magnetic fields inherited from the parent molecular cloud so that we check the dissipating time scale of the magnetic field on stars (Ref. Kato 1989).

When plasma gases are stable (v = 0), 4th Maxwell equation can be written as

$$\frac{\partial B}{\partial t} = \eta \nabla^2 B \tag{A.7}$$

This corresponds to the diffusion equation. Magnetic field therefore dissipates without plasma motion. The diffusion time scale (τ_D) approximates as

$$\tau_D \sim L^2/\eta \tag{A.8}$$

where η is the magnetic diffusivity. The convection zone on the sun (L ~1000 km) is about 10^8 yrs. Because stellar magnetic fields are generally larger than this scale, the diffusion of the magnetic field is negligible during PMS phases. This also suggests that the decay of x-ray activity is not caused by the dissipation of magnetic fields.

Appendix B

Stellar Physical Parameters

We list the typical stellar parameters and timescales of a stellar evolutional model.

Table B.1: Stellar parameters

Sp. type	T_{eff} (K)	B−V	Mass ($M_\odot$)	Radius ($R_\odot$)	v$_{rot}$ Type V (km/s)	v$_{rot}$ Type III (km/s)	v$_{rot}$ Type I (km/s)
O3	–	–	120	15			
O5	42000	−0.31	60	12			
O6	–	–	37	10			
O8			23	8.5	200		125
B0	30000	−0.30	17.5	7.4	170	120	102
B3	–	–	7.6	4.8			
B5	15200	−0.17	5.9	3.9	240	130	40
B8	11400	−0.11	3.8	3.0			
A0	9790	−0.02	2.9	2.4	180	100	40
A5	8180	+0.15	2.0	1.7	170		38
F0	7300	+0.30	1.6	1.5	100		30
F5	6650	+0.44	1.4	1.3	30		< 25
G0	5940	+0.58	1.05	1.1	10		< 25
G5	5560	+0.68	0.92	0.92	< 10	< 20	< 25

Case of class V (main sequence) except for v$_{rot}$ (Drilling and Landolt 2000).

Table B.2: ZAMS age & MS life time

Mass $M_\odot$	ZAMS age (yrs)	MS life time (yrs)
30.0	–	5.9×10^{6}
15.0	–	1.1×10^{7}
9.0	–	2.4×10^{7}
6.0	4.00×10^{5}	–
5.0	2.32×10^{5}	7.8×10^{7}
4.0	8.16×10^{5}	–
3.0	2.02×10^{6}	–
2.0	8.35×10^{6}	8.0×10^{8}
1.5	1.20×10^{7}	1.8×10^{9}
1.0	3.16×10^{7}	1.0×10^{10}

ZAMS age referred to a model provided by Palla and Stahler (1993). Life time on the MS is referred to a model, assuming the initial condition of the main sequence phase with the typical chemical composition of Population I (H: 70%; He: 27%; Heavy elements 3%, Audouze 1994).

Bibliography

Alcala, J. M., E. Covino, M. Franchini, J. Krautter, L. Terranegra, and R. Wichmann (1993). *Astron. Astrophys.* ***272***, 225.

Alcala, J. M., J. Krautter, J. H. M. M. Schmitt, E. Covino, R. Wichmann, and R. Mundt (1995). *Astron. Astrophys. Suppl.* ***114***, 109.

Ali, B. and D. L. Depoy (1995). *Astron. J.* ***109***, 709.

Allen, D. A. and J. P. Swings (1976). *Astron. Astrophys.* ***47***, 293.

Andersen, J., M. Jaschek, and C. R. Cowley (1984). *Astron. Astrophys.* ***132***, 354.

Andre, P., T. Montmerle, E. D. Feigelson, P. C. Stine, and K. Klein (1988). *Astrophys. J.* ***335***, 940.

Andre, P., R. B. Phillips, J. Lestrade, and K. Klein (1991). *Astrophys. J.* ***376***, 630.

Arida, M. and ASCA team (2000). http://heasarc.gsfc.nasa.gov/docs/asca/abc/abc.html.

Audouze, J. (1994). *"The Cambridge Atlas of ASTRONOMY"* (3 ed.)., Chapter The stars and the Galaxy, pp. 268. Cambridge.

Babel, J. and T. Montmerle (1997). *Astron. Astrophys.* ***323***, 121.

Beckwith, S., N. J. Evans, E. E. Becklin, and G. Neugebauer (1976). *Astrophys. J.* ***208***, 390.

Benedettini, M., B. Nisini, T. Giannini, D. Lorenzetti, E. Tommasi, P. Saraceno, and H. A. Smith (1998). *Astron. Astrophys.* ***339***, 159.

Berghöfer, T. W., J. H. M. M. Schmitt, and M. Hünsch (1999). *Astron. Astrophys.* ***342***, L17.

Berghoefer, T. W. and J. H. M. M. Schmitt (1994). *Astron. Astrophys.* ***290***, 435.

Berghoefer, T. W., J. H. M. M. Schmitt, and J. P. Cassinelli (1996). *Astron. Astrophys. Suppl.* ***118***, 481.

Berghoefer, T. W., J. H. M. M. Schmitt, R. Danner, and J. P. Cassinelli (1997). *Astron. Astrophys.* ***322***, 167.

Berghofer, T. W. and J. H. M. M. Schmitt (1994). *Science* ***265***, 1689.

Berrilli, F., G. Corciulo, G. Ingrosso, D. Lorenzetti, B. Nisini, and F. Strafella (1992). *Astrophys. J.* ***398***, 254.

Bertout, C., N. Robichon, and F. Arenou (1999). *Astron. Astrophys.* ***352***, 574.

Bibo, E. A., P. S. The, and D. N. Dawanas (1992). *Astron. Astrophys.* ***260***, 293.

Blondel, P. F. C., A. Talavera, and H. R. E. T. A. Djie (1993). *Astron. Astrophys.* ***268***, 624.

Boehm, T. and C. Catala (1995). *Astron. Astrophys.* ***301***, 155.

Boehm, T., C. Catala, J. . Donati, A. Welty, J. Baudrand, C. J. Butler, B. Carter, A. Collier-Cameron, J. Czarny, B. Foing, K. Ghosh, J. Hao, E. Houdebine, L. Huang, S. Jiang, J. E. Neff, D. Rees, M. Semel, T. Simon, A. Talavera, D. Zhai, and F. Zhao (1996). *Astron. Astrophys. Suppl.* ***120***, 431.

Bohm, T. and C. Catala (1993). *Astron. Astrophys. Suppl.* ***101***, 629.

Briceño, C. ., L. Hartmann, J. Stauffer, and E. Martín (1998). *Astron. J.* ***115***, 2074.

Briel, U., B. Aschenbach, G. Hasinger, H. Hippmann, E. Pfeffermann, P. Predehl, J. Schmitt, W. Voges, U. Zimmermann, I. George, S. Snowden, T. Turner, L. David, F. Harnden Jr, K. Kearns, M. Zombeck, M. Barstow, J. Osborne, J. Pye, M. Watson, R. West, and R. Willingale (1994). *"The ROSAT Users' Handbook"*. Max-Plank-Institut fur Extraterrestrische Physik.

Brooke, T. Y., A. T. Tokunaga, and S. E. Strom (1993). *Astron. J.* ***106***, 656.

Caillault, J., M. Gagné, and J. R. Stauffer (1994). *Astrophys. J.* ***432***, 386.

Cambresy, L., E. Copet, N. Epchtein, B. de Batz, J. Borsenberger, P. Fouque, S. Kimeswenger, and D. Tiphene (1998). *Astron. Astrophys.* ***338***, 977.

Canto, J., L. F. Rodriguez, N. Calvet, and R. M. Levreault (1984). *Astrophys. J.* ***282***, 631.

Cardelli, J. A., G. C. Clayton, and J. S. Mathis (1988). *Astrophys. J. Letters* ***329***, L33.

Cardelli, J. A. and G. Wallerstein (1989). *Astron. J.* ***97***, 1099.

Carkner, L., J. A. Kozak, and E. D. Feigelson (1998). *Astron. J.* ***116***, 1933.

Casanova, S., T. Montmerle, E. D. Feigelson, and P. Andre (1995). *Astrophys. J.* ***439***, 752.

Casey, B. W., R. D. Mathieu, N. B. Suntzeff, C. Lee, and J. A. Cardelli (1993). *Astron. J.* ***105***, 2276.

Casey, B. W., R. D. Mathieu, N. B. Suntzeff, and F. M. Walter (1995). *Astron. J.* ***109***, 2156.

Casey, B. W., R. D. Mathieu, L. P. R. Vaz, J. Andersen, and N. B. Suntzeff (1998). *Astron. J.* ***115***, 1617.

Casey, S. C. and D. A. Harper (1990). *Astrophys. J.* ***362***, 663.

Cassinelli, J. P., D. H. Cohen, J. J. Macfarlane, W. T. Sanders, and B. Y. Welsh (1994). *Astrophys. J.* ***421***, 705.

Castelli, F., M. Cornachin, C. Morossi, and M. Hack (1985). *Astron. Astrophys. Suppl.* ***59***, 1.

Catala, C., J. F. Donati, T. Böhm, J. Landstreet, H. F. Henrichs, Y. Unruh, J. Hao, A. Collier Cameron, C. M. Johns-Krull, L. Kaper, T. Simon, B. H. Foing, H. Cao, P. Ehrenfreund, A. P. Hatzes, L. Huang, J. A. de Jong, E. J. Kennelly, E. T. Kulve, C. L. Mulliss, J. E. Neff, J. M. Oliveira, C. Schrijvers, H. C. Stempels, J. H. Telting, N. Walton, and D. Yang (1999). *Astron. Astrophys.* ***345***, 884.

Chelli, A., I. Cruz-Gonzalez, and B. Reipurth (1995). *Astron. Astrophys. Suppl.* ***114***, 135.

Chen, P. S., H. Gao, and G. Z. Xiong (1995). *Astrophys. J. Suppl.* ***100***, 389.

Chen, W. and R. L. White (1991). *Astrophys. J.* ***366***, 512.

Chlebowski, T., F. R. Harnden, and S. Sciortino (1989). *Astrophys. J.* ***341***, 427.

Cohen, D. H., J. P. Cassinelli, and W. L. Waldron (1997). *Astrophys. J.* ***488***, 397.

Cohen, M. and L. V. Kuhi (1979). *Astrophys. J. Suppl.* ***41***, 743.

Cohen, M. and R. D. Schwartz (1987). *Astrophys. J.* ***316***, 311.

Comerón, F., G. H. Rieke, and R. Neuhäuser (1999). *Astron. Astrophys.* ***343***, 477.

Conti, P. S. (1972). *Astrophys. J. Letters* ***174***, L79.

Corcoran, M. and T. P. Ray (1998). *Astron. Astrophys.* ***331***, 147.

Corcoran, M. F., J. H. Swank, P. J. Serlemitsos, E. Boldt, R. Petre, F. E. Marshall, K. Jahoda, R. Mushotzky, A. Szymkowiak, K. Arnaud, A. P. Smale, K. Weaver, and S. S. Holt (1993). *Astrophys. J.* ***412***, 792.

Corcoran, M. F., W. L. Waldron, J. J. Macfarlane, W. Chen, A. M. T. Pollock, K. Torii, S. Kitamoto, N. Miura, M. Egoshi, and Y. Ohno (1994). *Astrophys. J. Letters* ***436***, L95.

Corporon, P. and A. . Lagrange (1999). *Astron. Astrophys. Suppl.* ***136***, 429.

Coulson, I. M., D. M. Walther, and W. R. F. Dent (1998). *Monthly Notices Roy. Astron. Soc.* ***296***, 934.

Damiani, F., G. Micela, S. Sciortino, and F. R. Harnden (1994). *Astrophys. J.* ***436***, 807.

de Winter, D., C. A. Grady, M. E. van den Ancker, M. R. Pérez, and C. Eiroa (1999). *Astron. Astrophys.* ***343***, 137.

de Zeeuw, P. T., R. Hoogerwerf, J. H. J. de Bruijne, A. G. A. Brown, and A. Blaauw (1999). *Astron. J.* ***117***, 354.

Devine, D., C. A. Grady, R. A. Kimble, B. Woodgate, F. C. Bruhweiler, A. Boggess, J. L. Linsky, and M. Clampin (2000). *Astrophys. J. Letters* ***542***, L115.

di Francesco, J., N. J. Evans, P. M. Harvey, L. G. Mundy, S. Guilloteau, and C. J. Chandler (1997). *Astrophys. J.* ***482***, 433.

Dong, Y. S. and J. Y. Hu (1991). *Chin. A&A* ***15***, 275.

Dotani, T., A. Yamashita, H. Ezuka, K. Takahashi, G. Crew, K. Mukai, and the SIS team (1997). "Recent Progress of SIS Calibration and Software". Technical Report 5, ISAS, MIT, NASA/GSFC.

Downes, D., A. Winnberg, W. M. Goss, and L. E. B. Johansson (1975). *Astron. Astrophys.* ***44***, 243.

Drake, S. A., D. C. Abbott, T. S. Bastian, J. H. Bieging, E. Churchwell, G. Dulk, and J. L. Linsky (1987). *Astrophys. J.* ***322***, 902.

Drake, S. A., J. L. Linsky, J. H. M. M. Schmitt, and C. Rosso (1994). *Astrophys. J.* ***420***, 387.

Drew, J. E., G. Busfield, M. G. Hoare, K. A. Murdoch, C. A. Nixon, and R. D. Oudmaijer (1997). *Monthly Notices Roy. Astron. Soc.* ***286***, 538.

Drew, J. E., D. Proga, and J. M. Stone (1998). *Monthly Notices Roy. Astron. Soc.* ***296***, L6.

Drilling, J. S. and A. U. Landolt (2000). *"Allen's Astrophysical Quantities"* (4 ed.)., Chapter 15, pp. 381. Springer-Verlag.

Eiroa, C. and M. M. Casali (1989). *Astron. Astrophys.* ***223***, L17.

Favata, F., F. Reale, G. Micela, S. Sciortino, A. Maggio, and H. Matsumoto (2000). *Astron. Astrophys.* ***353***, 987.

Feast, M. W. and I. S. Glass (1973). *Monthly Notices Roy. Astron. Soc.* ***164***, 35P.

Feigelson, E. D., S. Casanova, T. Montmerle, and J. Guibert (1993). *Astrophys. J.* ***416***, 623.

Feigelson, E. D. and W. M. Decampli (1981). *Astrophys. J. Letters* ***243***, L89.

Finkenzeller, U. and R. Mundt (1984). *Astron. Astrophys. Suppl.* ***55***, 109.

Fleming, T. A., I. M. Gioia, and T. Maccacaro (1989). *Astrophys. J.* ***340***, 1011.

Fuente, A., J. Martin-Pintado, R. Bachiller, R. Neri, and F. Palla (1998). *Astron. Astrophys.* ***334***, 253.

Fuente, A., J. Martin-Pintado, A. Rodriguez-Franco, and G. D. Moriarty-Schieven (1998). *Astron. Astrophys.* ***339***, 575.

Gagné, M., J. Caillault, and J. R. Stauffer (1995). *Astrophys. J.* ***445***, 280.

Garmire, G., E. D. Feigelson, P. Broos, L. A. Hillenbrand, S. H. Pravdo, L. Townsley, and Y. Tsuboi (2000). *Astron. J.* ***120***, 1426.

Geier, S., H. J. Wendker, and L. Wisotzki (1995). *Astron. Astrophys.* ***299***, 39.

Gotthelf, E. (1996). "The ASCA Source Position Uncertainties". Technical Report 4, LHEA GSFC.

Gotthelf, E. V., Y. Ueda, R. Fujimoto, T. Kii, and K. Yamaoka (2000). *Astrophys. J.* ***543***, 417.

Grady, C. A., M. R. Perez, A. Talavera, K. S. Bjorkman, D. de Winter, P. . The, F. J. Molster, M. E. van den Ancker, M. L. Sitko, N. D. Morrison, M. L. Beaver, B. McCollum, and M. W. Castelaz (1996). *Astron. Astrophys. Suppl.* ***120***, 157.

Grady, C. A., M. R. Perez, and P. S. The (1993). *Astron. Astrophys.* ***274***, 847.

Grady, C. A., B. Woodgate, F. C. Bruhweiler, A. Boggess, P. Plait, D. J. Lindler, M. Clampin, and P. Kalas (1999). *Astrophys. J. Letters* ***523***, L151.

Graham, J. A. (1991). "Star Formation in the Corona Australis Region". Technical Report 11, ESO.

Grankin, K. N., V. S. Shevchenko, A. V. Chernyshev, M. A. Ibragimov, W. B. Kondratiev, S. Y. Melnikov, S. D. Yakubov, N. D. Melikian, and G. V. Abramian (1992). *Informational Bulletin on Variable Stars* ***3747***, 1.

Gregorio-Hetem, J., T. Montmerle, S. Casanova, and E. D. Feigelson (1998). *Astron. Astrophys.* ***331***, 193.

Grillo, F., S. Sciortino, G. Micela, G. S. Vaiana, and F. R. Harnden (1992). *Astrophys. J. Suppl.* ***81***, 795.

Gullbring, E., N. Calvet, J. Muzerolle, and L. Hartmann (2000). *Astrophys. J.* ***544***, 927.

Haffner, L. M. and D. M. Meyer (1995). *Astrophys. J.* ***453***, 450.

Hamaguchi, K., H. Terada, A. Bamba, and K. Koyama (2000). *Astrophys. J.* ***532***, 1111.

Hamaguchi, K., Y. Tsuboi, and K. Koyama (2000). *Advances in Space Research* ***25***, 531.

Hanner, M. S., T. Y. Brooke, and A. T. Tokunaga (1994). *Astrophys. J. Letters* ***433***, L97.

Harnden, F. R., G. Branduardi, P. Gorenstein, J. Grindlay, R. Rosner, K. Topka, M. Elvis, J. P. Pye, and G. S. Vaiana (1979). *Astrophys. J. Letters* ***234***, L51.

Hartmann, L., S. J. Kenyon, and N. Calvet (1993). *Astrophys. J.* ***407***, 219.

Hauck, B. and C. Jaschek (2000). *Astron. Astrophys.* ***354***, 157.

Havnes, O. and C. K. Goertz (1984). *Astron. Astrophys.* ***138***, 421.

Hayashi, M. R., K. Shibata, and R. Matsumoto (1996). *Astrophys. J. Letters* ***468***, L37.

Henning, T., A. Burkert, R. Launhardt, C. Leinert, and B. Stecklum (1998). *Astron. Astrophys.* ***336***, 565.

Herbig, G. H. (1960). *Astrophys. J. Suppl.* ***4***, 337.

Herbig, G. H. and K. R. Bell (1988). *"Catalog of emission line stars of the orion population : 3 : 1988". Lick Observatory Bulletin, Santa Cruz: Lick Observatory, —c1988.*

Herbst, W. and V. S. Shevchenko (1999). *Astron. J.* ***118***, 1043.

Herbst, W., J. W. Warner, D. P. Miller, and A. Herzog (1982). *Astron. J.* ***87***, 98.

Hillenbrand, L. A. (1995). Ph. D. thesis, Univ. of Massachusetts Amherst.

Hillenbrand, L. A., S. E. Strom, F. J. Vrba, and J. Keene (1992). *Astrophys. J.* ***397***, 613.

Hofner, P. and E. Churchwell (1997). *Astrophys. J. Letters* ***486***, L39.

Hou, J. ., D. . Jiang, and C. . Fu (1997). *Astron. Astrophys.* ***327***, 725.

Howarth, I. D., R. K. Prinja, and D. Massa (1995). *Astrophys. J. Letters* ***452***, L65.

Hu, J. Y., P. F. C. Blondel, P. S. The, H. R. E. Tjin A Djie, D. de Winter, C. Catala, and A. Talavera (1991). *Astron. Astrophys.* ***248***, 150.

Hubrig, S., P. North, and G. Mathys (2000). *Astrophys. J.* ***539***, 352.

Hughes, J., P. Hartigan, and L. Clampitt (1993). *Astron. J.* ***105***, 571.

Hughes, J. D., J. P. Emerson, H. Zinnecker, and P. A. Whitelock (1989). *Monthly Notices Roy. Astron. Soc.* ***236***, 117.

Hughes, J. D., P. Hartigan, J. A. Graham, J. P. Emerson, and F. Marang (1991). *Astron. J.* ***101***, 1013.

Hutsemekers, D. and E. van Drom (1990). *Astron. Astrophys.* ***238***, 134.

Iben, I. J. (1965). *Astrophys. J.* ***142***, 1447.

Imanishi, K., K. Koyama, and Y. Tsuboi (2001). *Astrophys. J.*. in preparation.

Irvine, N. J. and N. Houk (1977). *Pabl. Astron. Soc. Pacific* ***89***, 347.

Ishisaki, Y., Y. Ueda, H. Kubo, Y. Ikebe, K. Makishima, and the GIS team (1997). "Reproducibility of the GIS Non X-Ray Background". Technical Report 5, ISAS.

Kahn, S. M., M. A. Leutenegger, J. Cottam, G. Rauw, J. . Vreux, A. J. F. den Boggende, R. Mewe, and M. Güdel (2001). *Astron. Astrophys.* ***365***, L312.

Kamata, Y., K. Koyama, Y. Tsuboi, and S. Yamauchi (1997). *Publ. Astron. Soc. Japan* ***49***, 461.

Kardopolov, V. I., V. V. Sahanionok, and G. K. Philipjev (1981). *Peremennye Zvezdy* ***21***, 589.

Kato, S. (1989). *"Fundamental theory for Astrophysics"* (1 ed.)., Chapter 10, pp. 83. Goto-shobo.

Kitamoto, S. and K. Mukai (1996). *Publ. Astron. Soc. Japan* ***48***, 813.

Kitamoto, S., S. Tanaka, T. Suzuki, K. Torii, M. F. Corcoran, and W. Waldron (2000). *Advances in Space Research* ***25***, 527.

Knapp, G. R. and R. L. Brown (1976). *Astrophys. J.* ***204***, 21.

Knee, L. B. G. and T. Prusti (1996). *Astron. Astrophys.* ***312***, 455.

Koyama, K., K. Hamaguchi, S. Ueno, N. Kobayashi, and E. D. Feigelson (1996). *Publ. Astron. Soc. Japan* ***48***, L87.

Kubo, S., T. Murakami, M. Ishida, and R. H. D. Corbet (1998). *Publ. Astron. Soc. Japan* ***50***, 417.

Kurtz, D. W. and F. Marang (1995). *Monthly Notices Roy. Astron. Soc.* ***276***, 191.

Lagrange, A. M., P. Corporon, and J. Bouvier (1993). *Astron. Astrophys.* ***274***, 785.

Lamers, H. J. G. L. M. and C. Leitherer (1993). *Astrophys. J.* ***412***, 771.

Leinert, C., A. Richichi, and M. Haas (1997). *Astron. Astrophys.* ***318***, 472.

Levreault, R. M. (1988). *Astrophys. J. Suppl.* ***67***, 283.

Li, W., N. J. Evans, P. M. Harvey, and C. Colome (1994). *Astrophys. J.* ***433***, 199.

Long, K. S. and R. L. White (1980). *Astrophys. J. Letters* ***239***, L65.

Loren, R. B. (1977). *Astrophys. J.* ***215***, 129.

Lucy, L. B. (1982). *Astrophys. J.* ***255***, 286.

Lucy, L. B. and R. L. White (1980). *Astrophys. J.* ***241***, 300.

Makishima, K., M. Tashiro, K. Ebisawa, H. Ezawa, Y. Fukazawa, S. Gunji, M. Hirayama, E. Idesawa, Y. Ikebe, M. Ishida, Y. Ishisaki, N. Iyomoto, T. Kamae, H. Kaneda, K. Kikuchi, Y. Kohmura, H. Kubo, K. Matsushita, K. Matsuzaki, T. Mihara, K. Nakagawa, T. Ohashi, Y. Saito, Y. Sekimoto, T. Takahashi, T. Tamura, T. Tsuru, Y. Ueda, and N. Y. Yamasaki (1996). *Publ. Astron. Soc. Japan* ***48***, 171.

Mannings, V. and A. I. Sargent (1997). *Astrophys. J.* ***490***, 792.

Marraco, H. G. and A. E. Rydgren (1981). *Astron. J.* ***86***, 62.

Matsumoto, H. (1998). Ph. D. thesis, Kyoto University.

McGregor, P. J., S. E. Persson, and J. G. Cohen (1984). *Astrophys. J.* ***286***, 609.

Meeus, G., C. Waelkens, and K. Malfait (1998). *Astron. Astrophys.* ***329***, 131.

Mewe, R., J. S. Kaastra, and D. A. Liedahl (1995). ***Legacy 6***, 16.

Montmerle, T., N. Grosso, Y. Tsuboi, and K. Koyama (2000). *Astrophys. J.* ***532***, 1097.

Montmerle, T., L. Koch-Miramond, E. Falgarone, and J. E. Grindlay (1983). *Astrophys. J.* ***269***, 182.

Morrison, R. and D. McCammon (1983). *Astrophys. J.* ***270***, 119.

Mundt, R. and T. P. Ray (1994). "Optical outflows from Herbig Ae/Be stars and other high luminosity young stellar objects". In *ASP Conf. Ser. 62: The Nature and Evolutionary Status of Herbig Ae/Be Stars*, p. 237.

Nakano, M., S. Yamauchi, K. Sugitani, and K. Ogura (2000). *Publ. Astron. Soc. Japan* ***52***, 437.

Natta, A., V. Grinin, and V. Mannings (2000). "Properties and Evolution of Disks around Pre-Main-Sequence Stars of Intermediate Mass". In *Protostars and Planets IV (Book - Tucson: University of Arizona Press)*, p. 559.

Natta, A., F. Palla, H. M. Butner, N. J. Evans, and P. M. Harvey (1993). *Astrophys. J.* ***406***, 674.

Neuhaeuser, R., M. F. Sterzik, G. Torres, and E. L. Martin (1995). *Astron. Astrophys.* ***299***, L13.

Neuhauser, R. and F. Comeron (1998). *Science* ***282***, 83.

Nisini, B., A. Milillo, P. Saraceno, and F. Vitali (1995). *Astron. Astrophys.* ***302***, 169.

Nordsieck, K. H., J. P. Cassinelli, and C. M. Anderson (1981). *Astrophys. J.* ***248***, 678.

Ohashi, T., K. Ebisawa, Y. Fukazawa, K. Hiyoshi, M. Horii, Y. Ikebe, H. Ikeda, H. Inoue, M. Ishida, Y. Ishisaki, T. Ishizuka, S. Kamijo, H. Kaneda, Y. Kohmura, K. Makishima, T. Mihara, M. Tashiro, T. Murakami, R. Shoumura, Y. Tanaka, Y. Ueda, K. Taguchi, T. Tsuru, and T. Takeshima (1996). *Publ. Astron. Soc. Japan* ***48***, 157.

Olofsson, G., M. Huldtgren, A. A. Kaas, S. Bontemps, L. Nordh, A. Abergel, P. André, F. Boulanger, M. Burgdorf, M. M. Casali, C. J. Cesarsky, J. Davies, E. Falgarone, T. Montmerle, M. Perault, P. Persi, T. Prusti, J. L. Puget, and F. Sibille (1999). *Astron. Astrophys.* ***350***, 883.

Otani, C. and T. Dotani (1994). "Echo and DFE in the SIS: How to Correct them". Technical Report 2, ISAS.

Owocki, S. P., J. I. Castor, and G. B. Rybicki (1988). *Astrophys. J.* ***335***, 914.

Owocki, S. P. and G. B. Rybicki (1984). *Astrophys. J.* ***284***, 337.

Owocki, S. P. and G. B. Rybicki (1985). *Astrophys. J.* ***299***, 265.

Owocki, S. P. and G. B. Rybicki (1986). *Astrophys. J.* ***309***, 127.

Ozawa, H., F. Nagase, Y. Ueda, T. Dotani, and M. Ishida (1999). *Astrophys. J. Letters* ***523***, L81.

Padgett, D. L., W. Brandner, K. R. Stapelfeldt, S. E. Strom, S. Terebey, and D. Koerner (1999). *Astron. J.* ***117***, 1490.

Palla, F. and S. W. Stahler (1990). *Astrophys. J. Letters* ***360***, L47.

Palla, F. and S. W. Stahler (1993). *Astrophys. J.* ***418***, 414.

Panzera, M. R., G. Tagliaferri, L. Pasinetti, and E. Antonello (1999). *Astron. Astrophys.* ***348***, 161.

Perryman, M. A. C., E. Hog, J. Kovalevsky, L. Lindegren, C. Turon, P. L. Bernacca, M. Creze, F. Donati, M. Grenon, and M. Grewing (1992). *Astron. Astrophys.* ***258***, 1.

Pezzuto, S., F. Strafella, and D. Lorenzetti (1997). *Astrophys. J.* ***485***, 290.

Pier, E. A. and ASCA Processing Team. *"ASCA Getting Started Guide for Revision 2 Data - Version 6.1 -"*. NASA Goddard Space Flight Center.

Pirzkal, N., E. J. Spillar, and H. M. Dyck (1997). *Astrophys. J.* ***481***, 392.

Porter, J. M., J. E. Drew, and S. L. Lumsden (1998). *Astron. Astrophys.* ***332***, 999.

Praderie, F., C. Catala, T. Simon, and A. M. Boesgaard (1986). *Astrophys. J.* ***303***, 311.

Prato, L. and M. Simon (1997). *Astrophys. J.* ***474***, 455.

Pravdo, S. H. and L. Angelini (1995). *Astrophys. J.* ***447***, 342.

Pravdo, S. H. and F. E. Marshall (1981). *Astrophys. J.* ***248***, 591.

Preibisch, T. (1997). *Astron. Astrophys.* ***324***, 690.

Preibisch, T. (1998). *Astron. Astrophys.* ***338***, L25.

Preibisch, T. (1999). *Astron. Astrophys.* ***345***, 583.

Prusti, T., A. Natta, and F. Palla (1994). *Astron. Astrophys.* ***292***, 593.

Reale, F. and G. Micela (1998). *Astron. Astrophys.* ***334***, 1028.

Reipurth, B., A. Pedrosa, and M. T. V. T. Lago (1996). *Astron. Astrophys. Suppl.* ***120***, 229.

Reipurth, B. and H. Zinnecker (1993). *Astron. Astrophys.* ***278***, 81.

Rodriguez, L. F., J. M. Moran, E. W. Gottlieb, and P. T. P. Ho (1980). *Astrophys. J.* ***235***, 845.

Rossi, C., L. Errico, M. Friedjung, F. Giovannelli, G. Muratorio, R. Viotti, and A. Vittone (1999). *Astron. Astrophys. Suppl.* ***136***, 95.

Ryter, C. E. (1996). *Astrophys. & Space Sci.* ***236***, 285.

Schmitt, J. H. M. M. and F. Favata (1999). *Nature* ***401***, 44.

Schulz, N. S., C. R. Canizares, D. Huenemoerder, and J. C. Lee (2000). *Astrophys. J. Letters* ***545***, L135.

Sekimoto, Y., K. Matsuzaki, T. Kamae, K. Tatematsu, S. Yamamoto, and T. Umemoto (2000). *Publ. Astron. Soc. Japan* ***52***, L31.

Serlemitsos, P. J., L. Jalota, Y. Soong, H. Kunieda, Y. Tawara, Y. Tsusaka, H. Suzuki, Y. Sakima, T. Yamazaki, H. Yoshioka, A. Furuzawa, K. Yamashita, H. Awaki, M. Itoh, Y. Ogasaka, H. Honda, and Y. Uchibori (1995). *Publ. Astron. Soc. Japan* ***47***, 105.

Seward, F. D., W. R. Forman, R. Giacconi, R. E. Griffiths, F. R. Harnden, C. Jones, and J. P. Pye (1979). *Astrophys. J. Letters* ***234***, L55.

Sharpless, S. (1959). *Astrophys. J. Suppl.* ***4***, 257.

Shevchenko, V. S., O. V. Ezhkova, M. A. Ibrahimov, M. E. van den Ancker, and H. R. E. Tjin A Djie (1999). *Monthly Notices Roy. Astron. Soc.* ***310***, 210.

Shevchenko, V. S., K. N. Grankin, M. A. Ibragimov, S. Y. Mel'Nikov, and S. D. Yakubov (1993). *Astrophys. & Space Sci.* ***202***, 121.

Shevchenko, V. S. and E. A. Vitrichenko (1994). "The eclipsing binary Herbig Ae/Be stars as protoalgols". In *ASP Conf. Ser. 62: The Nature and Evolutionary Status of Herbig Ae/Be Stars*, p. 55.

Shibata, K. and T. Yokoyama (1999). *Astrophys. J. Letters* ***526***, L49.

Shibata, K. and T. Yokoyama (2001). *Astrophys. J. Letters*.

Shu, F. H., H. Shang, and T. Lee (1996). ***Science*** ***271***, 1545.

Simon, T. and S. A. Drake (1989). *Astrophys. J.* ***346***, 303.

Skinner, S. L., A. Brown, and R. T. Stewart (1993). *Astrophys. J. Suppl.* ***87***, 217.

Skinner, S. L. and F. M. Walter (1998). *Astrophys. J.* ***509***, 761.

Skinner, S. L. and S. Yamauchi (1996). *Astrophys. J.* ***471***, 987.

Skrutskie, M. F., M. R. Meyer, D. Whalen, and C. Hamilton (1996). *Astron. J.* ***112***, 2168.

Slettebak, A. (1991). *"The Astronomy and Astrophysics Encyclopedia"*, pp. 710. Van Nostrand Reinhold.

Smith, K., M. Güdel, and A. O. Benz (1999). *Astron. Astrophys.* ***349***, 475.

Smith, M. A., C. A. Grady, G. J. Peters, and E. D. Feigelson (1993). *Astrophys. J. Letters* ***409***, L49.

Snell, R. L. and J. Bally (1986). *Astrophys. J.* ***303***, 683.

Stauffer, J. R., J. . Caillault, M. Gagné, C. F. Prosser, and L. W. Hartmann (1994). *Astrophys. J. Suppl.* ***91***, 625.

Stecklum, B., A. Eckart, T. Henning, and M. Loewe (1995). *Astron. Astrophys.* ***296***, 463.

Stelzer, B., R. Neuhäuser, and V. Hambaryan (2000). *Astron. Astrophys.* ***356***, 949.

Strom, K. M., G. Newton, S. E. Strom, R. L. Seaman, L. Carrasco, I. Cruz-Gonzalez, A. Serrano, and G. L. Grasdalen (1989). *Astrophys. J. Suppl.* ***71***, 183.

Strom, K. M. and S. E. Strom (1994). *Astrophys. J.* ***424***, 237.

Strom, S. E., F. J. Vrba, and K. M. Strom (1976). *Astron. J.* ***81***, 638.

Tagliaferri, G., S. Covino, T. A. Fleming, M. Gagné, R. Pallavicini, F. Haardt, and Y. Uchida (1997). *Astron. Astrophys.* ***321***, 850.

Tanaka, Y., H. Inoue, and S. S. Holt (1994). *Publ. Astron. Soc. Japan* ***46***, L37.

Testi, L., F. Palla, and A. Natta (1998). *Astron. Astrophys. Suppl.* ***133***, 81.

Testi, L., F. Palla, and A. Natta (1999). *Astron. Astrophys.* ***342***, 515.

Testi, L., F. Palla, T. Prusti, A. Natta, and S. Maltagliati (1997). *Astron. Astrophys.* ***320***, 159.

The, P. S., D. de Winter, and M. R. Perez (1994). *Astron. Astrophys. Suppl.* ***104***, 315.

The, P. S., M. R. Perez, N. V. Voshchinnikov, and M. E. van den Ancker (1996). *Astron. Astrophys.* ***314***, 233.

Tjin A Djie, H. R. E., P. S. The, J. Andersen, B. Nordstrom, U. Finkenzeller, and I. Jankovics (1989). *Astron. Astrophys. Suppl.* ***78***, 1.

Tokunaga, A. T. (2000). *"Allen's Astrophysical Quantities"* (4 ed.)., Chapter 7, pp. 143. Springer-Verlag.

Tout, C. A. and J. E. Pringle (1995). *Monthly Notices Roy. Astron. Soc.* ***272***, 528.

Tsuboi, Y. (1999). Ph. D. thesis, Kyoto University.

Tsuboi, Y., K. Imanishi, K. Koyama, N. Grosso, and T. Montmerle (2000). *Astrophys. J.* ***532***, 1089.

Tsuboi, Y., K. Koyama, H. Murakami, M. Hayashi, S. Skinner, and S. Ueno (1998). *Astrophys. J.* ***503***, 894.

Usov, V. V. and D. B. Melrose (1992). *Astrophys. J.* ***395***, 575.

Valenti, J. A., C. M. Johns-Krull, and J. L. Linsky (2000). *Astrophys. J. Suppl.* ***129***, 399.

van den Ancker, M. E., D. de Winter, and P. S. The (1996). *Astron. Astrophys.* ***313***, 517.

van den Ancker, M. E., D. de Winter, and H. R. E. Tjin A Djie (1998). *Astron. Astrophys.* ***330***, 145.

van den Ancker, M. E., P. S. The, H. R. E. Tjin A Djie, C. Catala, D. de Winter, P. F. C. Blondel, and L. B. F. M. Waters (1997). *Astron. Astrophys.* ***324***, L33.

van den Oord, G. H. J. and R. Mewe (1989). *Astron. Astrophys.* ***213***, 245.

Vaz, L. P. R., J. Andersen, B. W. Casey, J. V. Clausen, R. D. Mathieu, and I. Heyer (1998). *Astron. Astrophys. Suppl.* ***130***, 245.

Walker, H. J. and R. D. Wolstencroft (1988). *Pabl. Astron. Soc. Pacific* ***100***, 1509.

Walter, H. G. and O. J. Sovers (2000). *"Astrometry of Fundamental Catalogues"*, Chapter 3. A&A library. Springer-Verlag.

Warren, W. H. and J. E. Hesser (1977). *Astrophys. J. Suppl.* ***34***, 115.

Waters, L. B. F. M. and C. Waelkens (1998). *Ann. Rev. Astron. Astrophys.* ***36***, 233.

Weintraub, D. A. (1990). *Astrophys. J. Suppl.* ***74***, 575.

Welty, A. D., S. C. Barden, D. P. Huenemoerder, and L. W. Ramsey (1992). *Astron. J.* ***103***, 1673.

Wendker, H. J. (1995). *Astron. Astrophys. Suppl.* ***109***, 177.

Whitcomb, S. E., I. Gatley, R. H. Hildebrand, J. Keene, K. Sellgren, and M. W. Werner (1981). *Astrophys. J.* ***246***, 416.

White, N. E., J. L. Culhane, A. N. Parmar, B. J. Kellett, S. Kahn, G. H. J. van den Oord, and J. Kuijpers (1986). *Astrophys. J.* ***301***, 262.

Whittet, D. C. B., A. D. McFadzean, and T. R. Geballe (1984). *Monthly Notices Roy. Astron. Soc.* ***211***, 29P.

Whittet, D. C. B., T. Prusti, G. A. P. Franco, P. A. Gerakines, D. Kilkenny, K. A. Larson, and P. R. Wesselius (1997). *Astron. Astrophys.* ***327***, 1194.

Willner, S. P., F. C. Gillett, T. L. Herter, B. Jones, J. Krassner, K. M. Merrill, J. L. Pipher, R. C. Puetter, R. J. Rudy, R. W. Russell, and B. T. Soifer (1982). *Astrophys. J.* ***253***, 174.

Yamashita, A. (1995). Master's thesis, Tokyo University.

Yamashita, A. (2000). http://www.astro.isas.ac.jp/ ayamashi/htdocs/index.html.

Yamauchi, S., K. Hamaguchi, K. Koyama, and H. Murakami (1998). *Publ. Astron. Soc. Japan* ***50***, 465.

Yamauchi, S., K. Koyama, M. Sakano, and K. Okada (1996). *Publ. Astron. Soc. Japan* ***48***, 719.

Yoshida, S., T. Kogure, M. Nakano, K. Tatematsu, and S. D. Wiramihardja (1992). *Publ. Astron. Soc. Japan* ***44***, 77.

Yudin, R. V. and A. Evans (1998). *Astron. Astrophys. Suppl.* ***131***, 401.

Zealey, W. J., P. M. Williams, G. Sandell, K. N. R. Taylor, and T. P. Ray (1992). *Astron. Astrophys.* ***262***, 570.

Zinnecker, H. and T. Preibisch (1994). *Astron. Astrophys.* ***292***, 152.

Zombeck, M. V., M. Barbera, A. Collura, and S. S. Murray (1997). *Astrophys. J. Letters* ***487***, L69.

Acronyms & Abbreviations

ASCA	Advanced Satellite for Cosmology and Astrophysics
CCD	Charge Coupled Device
CTTS	Classical T-Tauri Star
DFE	Dark Frame Error
GIS	Gas Imaging Sepctrometer (onboard *ASCA*)
GMC	Giant Molecular Cloud
HAEBE	Herbig Ae/Be star
HEASARC	High Energy Astrophysics Science Archive Research Center
HRI	High Resolution Imager (onboard *ROSAT*)
IR	Infra-Red
IRAS	Infrared Astronomycal Satellite
ISAS	Institute of Space and Astronautical Science
ISM	InterStellar Medium
IUE	International Ultraviolet Explorer
KSC	Kagoshima Space Center
MS	Main Sequence
PI	Pulse height Invariant
PMS	Pre Main Sequence
PSF	Point Spread Function
PSPC	Position Sensitive Propotional Counter (onboard *Einstein* & *ROSAT*)
RASS	*ROSAT* All Sky Survey
ROSAT	Röntgensatellit (Germany)
RDD	Residual Dark Distribution
RDF	Rationalized Data Format
SAA	South Atlantic Anomaly
SED	Spectral Energy Distribution
SIS	Solid-state Imaging Spectrometer (onboard *ASCA*)
UKIRT	United Kingdom InfraRed Telescope
UV	Ultra Violet
WTTS	Weak-line T-Tauri Star
XRT	X-Ray Telescope
YSO	Young Stellar Object
ZAMS	Zero Age Main Sequence

Acknowledgment

I should be grateful to Prof. Koyama K. for guidance of my research and financial supports throughout my doctor course. His research into the x-ray activity of low-mass young stars have attracted me and drove me to the study of higher-mass stars. This research could not be successful without his warm advice and severe criticism. I should also be grateful to Assoc. Prof. Awaki H. and Tsuru T. of their useful suggestion and technical support. I learned how to research from them. I thank to other staffs Prof. Tanimori T., Prof. Maihara T., Dr. Tazawa Y. and Dr. Iwamuro F. Discussions with them helped me much to proceed my research. I also wish to thank all my colleagues. I was sometimes encouraged by them, and above all always very enjoyed chatting with them.

I especially express my thanks for persons directly supporting this research. Assoc. Prof. Yamauchi S. gave me much advice about the methods to analyze the ASCA data and information about latest results of stellar astrophysics. Prof. Kitamoto S. told me the recent understandings of the x-ray emission from massive MS stars. Assc. Prof. Nakano M. told me the information about stars in the Orion cloud. Prof. Feigelson E.D. and Prof. Montmerle T. kindly discussed the subject of star formation with me many times. I was always realized of the weakness of my hypothesis from them. Dr. Terada H. told me quick results of the *ASCA* data of a few HAeBes. Dr. Tsuboi Y. told me the *ASCA* results of many low-mass star forming regions. Mr. Imanishi K. told me the latest result of ρ-Oph cloud with *Chandra*. Dr. Ozawa H. told me the *ASCA* result of HH63E+W. Prof. Shibata K. and Dr. Yokoyama T. told me the basic mechanism of the magnetic reconnection and topics of solar physics. Assoc. Prof. Sakao T. told me the result of the *Yohkoh* satellite. Dr. Nishi R. told me problems of models of star formation. I would also like to thank others supporting me and all the members of the *ASCA* team.

This work is supported by the grants JSPS, research fellowships for young scientists, and made use of data obtained through the High Energy Astrophysics Division Online Service, provided by Institute of Space and Astronautical Science (ISAS) and the High Energy Astrophysics Science Archive Research Center Online Service, provided by the NASA/Goddard Space Flight Center.

Finally, I would like to thank my family and friends.